PULSARS AND THEIR ENVIRONMENTS: THE INTERACTIONS BETWEEN PULSAR EMISSION, MATTER, AND GRAVITATIONAL WAVES

A Dissertation

Presented to the Faculty of the Graduate School

of Cornell University

in Partial Fulfillment of the Requirements for the Degree of

Doctor of Philosophy

by

Ryan Marshall Shannon

January 2011

PULSARS AND THEIR ENVIRONMENTS: THE INTERACTIONS BETWEEN PULSAR EMISSION, MATTER, AND GRAVITATIONAL WAVES

Ryan Marshall Shannon, Ph.D.

Cornell University 2011

We investigate the interaction between radio pulsars, gravitational waves, warm plasma in the interstellar medium, and gravitationally bound matter, the latter three are liberally defined to comprise part of the pulsar environment. To examine the interactions between pulsars and their environments, we undertook observations at radio and infrared wavelengths which were supplemented by analytical and numerical modeling techniques.

We assess the sensitivity of an ensemble of ultra-stable millisecond pulsars (a pulsar timing array) to gravitational waves. We find that there are a number of sources of noise, both intrinsic and extrinsic to the pulsar that limit timing array sensitivity. We show that spin noise in millisecond pulsars is fundamentally similar to that in normal pulsars and is present at levels that limit the sensitivity of a timing array even though it is latent in current timing observations. We identify the presence of broad band pulse jitter in observations of the millisecond pulsar J1713+0747 that limits its timing precision when observed at high signal to noise ratio. The properties of a plausible debris disks around the millisecond pulsar B1937+21 are constrained and in this context pulsars are identified that are more suited to long term precision timing. Through simulation, the levels of most forms of interstellar timing noise are identified. We demonstrate that careful choice of observing strategies and more advanced modeling of pulse times of arrival can reduce markedly improve timing precision. We

conclude that observations of more pulsars, observed with higher throughput are required to make a significant detection of gravitational waves.

In addition, pulsar emission is studied through the lens of their environments. We use multi-path scattering of pulsar radio emission in the interstellar medium to form an effective interferometer and resolve the emission region of PSR B0834+06. We also test the theory that certain forms of pulsar modulation are caused by in-falling material by constraining the presence of debris disks around four variable pulsars.

We conclude that pulsars and their environments are inextricably linked and that detailed study of either necessarily requires intimate understanding of both.

BIOGRAPHICAL SKETCH

Ryan was born on 6 September 1981 in Oliver, British Columbia, Canada, the first child of Janet and Larry Shannon. He enjoyed his carefree childhood in rural British Columbia. Highlights of his youth include digging holes and building watercourses in the backyard beach on Vaseaux lake, skiing at Apex, and playing piano. When older, he still enjoyed skiing in the winter, but also enjoyed playing alto saxophone in the jazz supergroup/combo *Armadillo Jam*.

After graduation (as the top student) from Southern Okanagan Secondary School, Ryan enrolled in the Faculty of Science at the University of British Columbia in Vancouver. Ryan got interested in astronomy after taking an introductory astronomy class taught by the flamboyant Jaymie Matthews and more serious but equally interesting courses taught by Phil Gregory and Stéphane Courteau. The last three summers of his undergraduate education, Ryan enjoyed research, first at the University of Toronto (Lasers), and subsequently at l'Université de Montréal (L'étoiles naines blanches, avec Pierre Bergeron), and then at the University of British Columbia (Magnetars, with Jeremy Heyl). Ryan graduated with first class honours with distinction with a combined honours degree in Physics and Astronomy in 2004.

Ryan started graduate school at Cornell University in Astronomy and Space Sciences in the Fall of 2004 as the *only* matriculating astronomy graduate student. He quickly made friends with many entering physics students, a move he does not regret. Social highlights of his time at graduate school include dance parties; baking; baking things and then lighting them on fire; Abbey Road jam band; cooking; cooking Canadian thanksgiving for 28 people; building furniture; Halos 2, 3, and 4; karaoke; Pixel; swimming in the lake; and TGIF at the big red barn.

Not quite sure if he was interested in theoretical or observational astronomy, the then-director of graduate studies suggested he discuss research with Jim Cordes, who was known to work in both areas. Ryan ended up working with Jim, which is another decision Ryan does not regret. He worked on a number of projects (many of them presented here) that included observations of pulsars in radio, infrared, x-ray and gamma-ray wavelengths, and theoretical and numerical modeling of these pulsars.

Graduate school was definitely a defining time in life for Ryan.

In October 2010, Ryan became a postdoctoral fellow at CSIRO Astronomy and Space Sciences (né the ATNF) in the suburbs of Sydney, Australia.

To my parents and my sisters.

ACKNOWLEDGEMENTS

I thank my advisor, Jim Cordes. Jim inspired and shaped the content of this dissertation. I also greatly appreciate the space Jim gave me to develop my own ideas and turn them into research projects. It has been a privilege and a pleasure working with Jim over the last five years and I hope to continue collaborating with him in the future.

I thank my colleagues in the NANOGrav[1] collaboration. This dissertation was really focused through collaboration with them and the prospect of detecting gravitational waves with pulsars. I thank my other collaborators from other projects and in particular Glenn Jones for taking the lead on the Fermi-GAVRT project while I was writing this! I promise to write a giant pulse detection pipeline soon.

I thank my colleagues in the Astronomy Department at Cornell for providing an enriching experience over the last 6.1 years. I thank the staff at Arecibo for support of there observations and hospitality during my stays in Puerto Rico. I would particularly like to thank Tapasi Ghosh for staying up late and waking up early and running the `Mark5` observations while I observed remotely, Paulo Freire for showing me how to run timing backends, and Arun Venkataraman assistance with computing logistics and data storage. Arecibo is a very inspiring place for a radio astronomer!

I thank my special committee (Jim, Jamie Lloyd, Marina Romanova, and Ira Wasserman) for useful advice, administering examinations, and reading this dissertation. In addition I thank Jim Houck for serving as a temporary committee member during my A exam.

At NAIC, I thank Bob Brown and Don Campbell for financial support, and

[1] `www.nanograv.org`

Jill Tarbell and Wendy Turner for help with all things logistical and bureaucratic. I thank Sue Clark, Mary Mulvanerton, and Lynda Sovocool for helping administer NASA observing grants.

I am grateful for the wonderful friends I made in Ithaca, particularly my friends at *the Ranch* who provided a rich intellectual and social environment. John, Sharon, Matt, Phil, Rick, Briony, Laura: You guys rock! I also thank my friends in Vancouver, especially in Physsoc, and my friends growing up in Oliver.

I thank my family for supporting me through this adventure that keeps on going. Finally, thank you to my first teachers, my Dad and Mom, who nurtured my curiosity of all things from a very young age.

This work was supported the National Science Foundation through grants AST 0206036 and AST 0807151; by the National Astronomy and Ionosphere Center, which operates the Arecibo Observatory under a cooperative agreement with the National Science Foundation; by NASA through an awards issued by JPL/Caltech and the Fermi Science Center.

This work is based on observations made with the Arecibo Observatory; the Green Bank Telescope, operated by the National Radio Astronomy Observatory, which itself is a facility of the National Science Foundation operated under cooperative agreement by Associated Universities, Incorporated; and the Spitzer Space Telescope, which is operated by the Jet Propulsion Laboratory, California Institute of Technology under a contract with NASA.

Travel support during the course of this work was provided by the National Astronomy and Ionosphere Center; the National Radio Astronomy Observatory; the American Astronomical Society; the United States National Committee for the International Union of Radio Science; the Lorentz Center in Leiden, the

Netherlands; the Graduate School of Cornell University; and the International Astronomical Union.

This work made use of NASA's ADS system and the ATNF Pulsar Catalogue.

TABLE OF CONTENTS

LIST OF TABLES

LIST OF FIGURES

CHAPTER 1

INTRODUCTION

This dissertation comprises seven independent but complementary studies examining the relationship between pulsars and their environments. *Environment* is defined very liberally to be mass or energy to which pulsars are sensitive that lies between the pulsar magnetosphere (the region co-rotating with neutron star) and the Solar system. Using a variety of observations and theoretical techniques, we investigate how pulsars can be used to understand their environments and how pulsar environments can be used to understand pulsar emission, and come to the general conclusion that detailed study of either the pulsar or its environment requires intimate knowledge of both.

Particular attention is placed on investigating the relationships between pulsar emission and three aspects of the pulsar environment: debris and other matter orbiting pulsars, warm plasma on the interstellar medium (ISM), and gravitational waves passing through the interstellar space between the pulsar and the Earth. The relationships between the four broad themes and the main chapters (Chapters 2 through Chapter 8) are displayed in the Venn diagram in Figure 1.1. Most chapters investigate the interaction between two of the thematic areas.

One of the most notable properties of pulsars, particularly rapidly rotating millisecond pulsars, is their extreme stability. By comparing the average of many thousands of pulses with a template, arrival times can be modeled to extraordinary precision. The most stable pulsars show arrival times that can be modeled to a root mean square (rms) variation of $\approx$ 100 ns over many years, assuming a per-epoch integration time of 30 minutes on a 100-m class telescope.

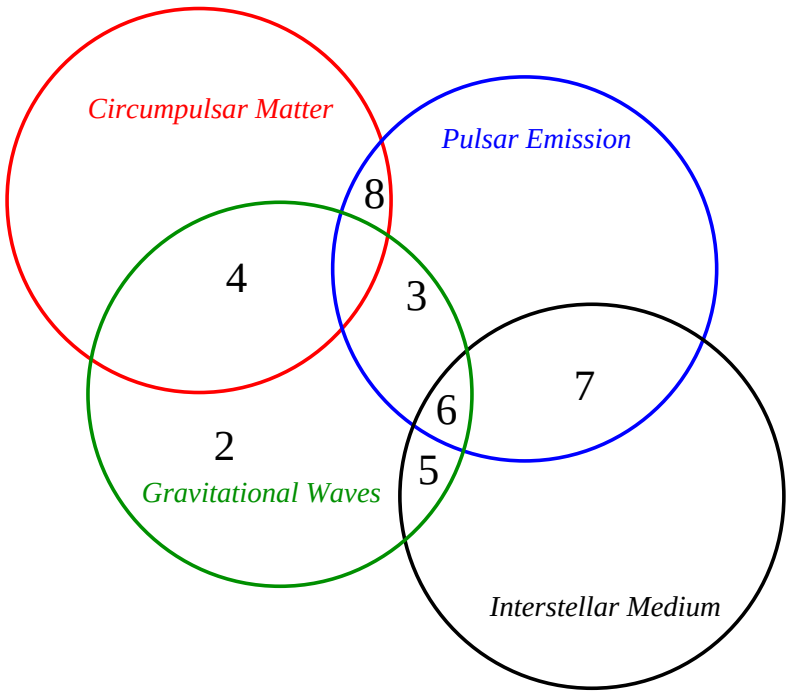

FIGURE 1.1.— Venn diagram of the work covered iu this dissertation. Four broad themes (printed in italics and denoted by the four circles) are covered. Typically the chapters (numbers printed listed non-italicized font) investigate the relationship between two of these themes. The titles of the chapters are: Chapter 2, *Minimum requirements for Detecting a Stochastic Background of Gravitational Waves*; Chapter 3, *Assessing the Role of Spin Noise in Precision Pulsar Timing*; Chapter 4, *Asteroids around Millisecond Pulsars*; Chapter 5, *Correcting Interstellar Propagation Delays in Precision Pulsar Timing*; Chapter 6, *Multi-frequency Precision Timing of PSR J1713+0747*; Chapter 7, *Resolving Pulsar Magnetospheres Using Interstellar Interferometry*; and Chapter 8, *A Search for Debris around Four Variable Pulsars*.

It is possible to exploit this precision and detect gravitational waves (GWs) passing through the solar neighbourhood by analyzing the variation in pulse arrival times from a set of millisecond pulsars (a pulsar timing array, PTA, Detweiler 1979; Foster & Backer 1990). A large portion of this dissertation examines the sensitivity of PTAs to GWs with a particular focus on astrophysical sources of noise that are likely present in pulsar times of arrival.

In Chapter 2 an assessment of the sensitivity of a pulsar timing array to a

stochastic background of gravitational waves is presented. The sensitivity is calculated in terms of a signal model (i.e., in terms of noise comprised of stationary *white* and non-stationary *red* components) with physical models for certain types of noise detailed in subsequent chapters[1], with a more comprehensive model presented in (Cordes & Shannon 2010). We find that for the expected strength of the gravitational wave background (Jaffe & Backer 2003), and expected levels of noise, a larger number of pulsars are needed than were estimated in previous studies. We show that the best way to improve sensitivity is by increasing observation throughput by either observing for longer at each epoch or by observing with a higher cadence.

One source of red noise in pulsar timing observations is associated with rotational instabilities of the pulsar and is referred to as spin noise or timing noise. These instabilities are presumably associated with either angular momentum transfer between the superfluid interior of the neutron star and its solid crust (Jones 1990) or torque variations associated with changes in magnetospheric currents (Cheng 1987; Kramer et al. 2006a; Cordes & Shannon 2008; Lyne et al. 2010). In either case, the manifestation is the same: relative to a model, TOAs show non-stationary excess that is independent of observing frequency. This behavior is prevalent in canonical pulsars, but is only seen in two MSPs. In Chapter 3 the levels of spin noise in different pulsar populations are assessed. We find that spin noise is likely present in MSPs at levels important to precision timing experiments and that this timing noise shows temporal variability similar to that expected of gravitational waves, the stochastic gravitational wave

[1]We note that this chapter is a bit of a *spoiler* because it reveals the conclusions of some of the other chapters. If the reader prefers to be surprised (unlike the authour of this dissertation), feel free to read this chapter after reading Chapters 3 through 6.

background.

Another source of red noise is associated with the orbital recoil of the pulsar due to a set of asteroidal mass companions, presumably in a disk. While single companions or a small number of planets will produce recoil with a well defined signature (Konacki & Wolszczan 2003), the recoil associated with a larger number will appear to be more stochastic, with the degree of non-stationarity dependent on the disk configuration. In Chapter 4, we demonstrate that asteroidal mass bodies can form around millisecond pulsars. We then apply this fact to explain the timing noise in the millisecond pulsar B1937+21. We show that a variety of asteroid belt configurations can explain the observed structure. If these disks were present MSPs, they create a fundamental timing noise floor for a particular pulsar because it is implausible to identify the signatures of the asteroids without removing the signature of gravitational waves.

Another potential source of noise in pulsar timing measurements is associated with the propagation of radio waves through warm turbulent plasma along the line of sight. As the emitted radio waves refract through electrons in the plasma, the group delay and path length of radiation is altered away from the direct line of sight. This alteration, which is time and frequency dependent, modifies the arrival time and shape of the observed pulsar signal. In Chapter 5, we present simulations that model interstellar propagation effects on times of arrival and describe improved techniques for mitigating these propagation effects.

To investigate fundamental limits of timing precision, a timing campaign of the highly stable millisecond pulsar J1713+0747 was completed using the 305-m Arecibo telescope. Observations were conducted over a wider range of frequen-

cies and a wider ranger of time scales than conducted in standard precision timing observations, using a variety of signal processing equipment (i.e., backends) simultaneously to best distinguish different perturbations to TOAs. This unique data set was used to examine the wide range of phenomena discussed in the previous chapters. In Chapter 6, two preliminary studies of these observations are presented. In the first we demonstrate that intrinsic radio pulse variations (pulse phase jitter) on pulse-to-pulse time scales limits timing precision on short time scales. In the second study we examine the efficacy of the multi-frequency TOA fitting methods presented in Chapter 5 to improve the precision of TOAs. We find hints that these methods improve timing precision.

Chapter 6 concludes the portion of the dissertation focused on the limits of precision pulsar timing. In the final two main-body chapters, we present studies related to how pulsar environments can be used to understand pulsars.

Pulsar emission and in particular the radio emission mechanism is only heuristically understood and the location this emission region is poorly constrained. In Chapter 7, the radio emission region of the pulsar B0834+06 is resolved by exploiting by using the ISM as an interferometer that provides sub-nanoarcsecond resolving power. Our results suggest that the emission region is higher in the magnetosphere than suggested by other methods.

Pulsar radio emission shows variability in intensity on a time scales ranging from nanoseconds (Hankins et al. 2003) to years (Kramer et al. 2006a). The longest time scales are highly inconsistent with most time scales conceivable in the pulsar magnetosphere. Cordes & Shannon (2008) suggest that in-falling debris from a circumpulsar asteroid belt or debris disk can explain this variability. Compact debris disks are irradiated by both thermal and non-thermal emission

from the pulsar and re-radiate predominantly in the mid-infrared. In Chapter 8, we present results of a survey for infrared companions with the *Spitzer* Space telescope for four pulsars that show radio variability. We constrain the masses of debris disks by placing upper limits on the infrared emission from these objects. This chapter demonstrates both the promise and challenges facing future studies of pulsars in the infrared with larger aperture space-borne telescopes such as the James Webb Space Telescope.

We conclude in Chapter 9 by discussing future work related to this dissertation that is in progress or ought to be conducted.

Note to the readers: Throughout this work *frequency* is used in a three major and distinct contexts. The observing frequency is the *radio frequency* at which observations were conducted. In Fourier or other power spectra analysis of a time series, *fluctuation frequency* is the Fourier conjugate variable to time. The rotation rate of a pulsar is the *spin frequency*. The context for all three should be obvious but notation for each varies from chapter to chapter.

CHAPTER 2

MINIMUM REQUIREMENTS FOR DETECTING GRAVITATIONAL WAVES WITH PULSARS

The detection of nanohertz-frequency gravitational waves with a set of millisecond pulsars (a pulsar timing array) will provide another confirmation of Einstein's theory of general relativity and a new window through which to study the universe. Here we assess the requirements for a significant detection of a stochastic gravitational wave background with a pulsar timing array. We present the expected signal to noise ratio for a general cross-correlation detection statistic. We find that current observing procedures are unlikely to make a highly significant detection of a gravitational wave background at cosmologically significant levels because the presence of both non-stationary and white noise in pulsar times of arrivals severely limits the signal to noise ratio. To make a significant detection and perform follow-up characterization of any graviational wave signal requires the observations of a larger number of pulsars with much higher throughput than presently conducted; hence detection requires larger amounts of telescope time on current facilities or perhaps a dedicated pulsar timing telescope.[1]

2.1 Introduction

The direct detection of gravitational waves (GWs) will usher in a new era for astrophysics. Not only will this detection[2] provide another way to test Einstein's

[1] R. M. Shannon & J. M. Cordes., in preparation.

[2] There is *indirect* evidence for the existence of gravitational waves from the decay of the orbits of compact object binary systems (Hulse & Taylor 1975; Taylor & Weisberg 1982; Kramer et al. 2006b).

theory of general relativity, GWs can be used as astrophysical probes to examine environments inaccessible to electromagnetic observations. For example GWs can be used to examine systems where electromagnetic emission is too faint to be detected or is obscured by source confusion or high levels of opacity. In addition they provide complementary tools for electromagnetic observations (the so-called *multi-messenger astronomy*), by providing unique constraints on system observation geometry.

Long wavelength[3] GWs can be detected through the precision timing of the highly stable millisecond pulsars (MSPs). Gravitational waves passing within 10 to 20 ly of the solar system (with comparable GW wavelengths, and wave periods; and frequencies in the 3 30 nanohertz range) can be detected by analyzing the correlated variability in times of arrivals (TOAs) from a set MSPs (a pulsar timing array, PTA). The strongest GW signal in the PTA band is expected to be associated with a stochastic background of gravitational waves, which is a superposition of GW radiation from the early stages of in-spiral of massive black hole binaries spread across the universe (Jaffe & Backer 2003). However there are possibly more exotic contributions to this stochastic background, such as radiation from a network of cosmic strings (Damour & Vilenkin 2005). In addition, it may be possible to detect GW signals from single sources (Jenet et al. 2004; Finn & Lommen 2010), though the strength of these signals are less constrained.

The viability of the PTA method has recently increased because of improvements to pulsar timing precision (Demorest 2007). These improvements are

[3]Note that extremely long wavelength GWs produced during the inflationary period in the early universe can potentially be detected through analysis of the polarization of the cosmic microwave background.

mostly due to more advanced signal processing hardware (Ransom et al. 2009) but also of the discovery of pulsars that intrinsically provide more stable TOAs (Jacoby et al. 2003). As a result there has been a burst of recent work that describes methods for detecting GW signals in pulsar timing observations, and, in particular, methods for detecting stochastic gravitational wave backgrounds. Jenet et al. (2005) present a method for detecting gravitational wave backgrounds based on a cross correlation coefficient. Anholm et al. (2009) integrated this cross correlation detection statistic in the framework of ground based detection methods presented by Allen & Romano (1999), while van Haasteren et al. (2009) integrates it into a Bayesian methodology. These studies generally come to the same conclusion: to make a detection of a GWB, 20 to 40 pulsars, having stationary timing errors of 100 ns timed with monthly cadence over 5 to 10 years are required to detect the GWB. However, these previous studies do not address the sensitivity of a PTA in the presence of the diversity of noise that plausibly exist in pulsar timing observations.

Here we assess the requirements for making a significant detection of correlated gravitational waves in the presence of diverse astrophysical noise realistically contained in precision timing observations. In §2.2 we discuss the contributions to pulsar times of arrival and present the signal model necessary to fully assess the sensitivity of a PTA to GWs. In §2.3 we present the most optimistic signal to noise ratio (SNR) for a PTA and then assess the minimum requirements for detecting GWBs. In §2.4 we discuss methods to improve PTA sensitivity. From this analysis we conclude that observations of more pulsars with higher throughput are necessary to make a significant detection of a GWB.

2.2 Signal Model

Gravitational waves are detected in pulsar observations through analysis of the time of arrival of pulses (TOAs). TOAs themselves are calculated by comparing an average pulse (formed by averaging many pulses over a single observation epoch together to increase the signal to noise ratio) to a template pulse. The total perturbation $R_\alpha(t_i)$ to the TOA from pulsar α at time t_i is completely modeled as

$$T_\alpha(t_i) = D_\alpha(t_i) + E_\alpha(t_i) + P_\alpha(t_i) + W_\alpha(t_i) + R_\alpha(t_i) + C(t_i), \tag{2.1}$$

where D_α are deterministic contributions to the TOA, E_α is the correlated portion of GWB, P_α is the uncorrelated portion of the GWB (the so-called pulsar end term), W_α is uncorrelated white noise, R_α is uncorrelated non-stationary red noise, and C is correlated noise. The goal of PTA observations is of course to significantly detect the signal E_α, in the presence of all the other perturbations, which we describe next.

Deterministic contributions to TOAs include the unknown spin down of the pulsar, motion of the Earth about the solar system barycenter, and motion of the pulsar about a companion and through the Galaxy (Backer & Hellings 1986; Edwards et al. 2006).

Gravitational waves contribute both correlated and uncorrelated perturbations to the TOAs. Between different lines of sight, the amplitude of the correlated term depends on the relative angle between of pulsars (Detweiler 1979). The uncorrelated term is associated with GWs crossing the pulsar-earth lines of sight outside of the solar neighborhood. The signal from these GWs cannot be included because the distances to pulsars are not known to sufficient precision. The expected amplitude and variability are the same for both the correlated and

uncorrelated terms; therefore, in the ensemble average, the signal to noise ratio is at most unity for a single pulsar-earth baseline.

There are a large number of additional noise sources in pulsar timing observations. A comprehensive list of these stochastic TOA perturbations is presented in Cordes & Shannon (2010). These perturbations have a range of origins spanning the entire pulsar-earth line of sight and contribute both stationary (white noise) and nonstationary (red noise) TOA perturbations. For example, there are white noise terms is associated with the finite signal to noise ratio of observations, intrinsic pulse phase jitter, and short-term modulation of pulsar signal by the interstellar medium (ISM) (Cordes & Shannon 2010). Red noise is associated with intrinsic spin instabilities of the pulsar (Chapter 3) and long-term modulation of the ISM caused by relatively large scale structures (Chapter 4).

Correlated noise $C(t)$ is associated with clock correction errors and uncertainties in the solar system barycenter (Champion et al. 2010). In subsequent discussion we will assume that this term is negligible. In a future paper, we will discuss strategies for confirming that this is the case (J. Cordes & R. Shannon, in preparation).

GW detection algorithms are implemented on residual TOAs after (or, perhaps during) a necessary fit that models the many deterministic TOAs perturbations, and a fit versus radio frequency to account for the effects of interstellar propagation. This model includes a quadratic polynomial that accounts for the unknown pulsar spin phase, spin frequency and spin frequency derivative. This fit of course remove other perturbations, including a large fraction of many types of red noise perturbations (Cordes 1980) such as that associated

with stochastic GWBs. The level of power removed depends strongly on the degree of non-stationarity to the process.

The residual time series after a model fit is defined as

$$t_{\mathscr{M},\alpha}(t_i) = e_{\mathscr{M},\alpha}(t_i) + p_{\mathscr{M},\alpha}(t_i) + w_{\mathscr{M},\alpha}(t_i) + r_{\mathscr{M},\alpha}(t_i), \tag{2.2}$$

where lower case symbols are used to indicate notational indicate that the contributions are associated with the residual time series after a fit to a model $\mathscr{M}$. The model fit changes the nature of the perturbations and augments to the non-stationarity of the time series. The post-fit rms variance depends strongly on the length and number of samples in the time series.

2.3 Minimum Array Configuration

The most optimistic requirements on pulsar stability are placed by estimating PTA sensitivity when all the PTA pulsars are located in the same direction in the sky at different distances from the observer. This configuration maximizes the level of correlated signal between objects while appropriately suppressing the level of uncorrelated gravitational waves.

Detection sensitivity is assessed by analyzing the signal to noise ratio (SNR) of a pairwise correlation coefficient, similar to the correlation coefficient presented in Jenet et al. (2005). The correlation coefficient for a PTA comprised of N_p pulsars, constructed from N_t TOAs at times t_i is

$$C(T) = \frac{2}{N_p(N_p-1)} \frac{1}{N_t} \sum_{i=1}^{N_t} \sum_{\alpha=1}^{N} \sum_{\beta=1}^{\alpha-1} t_\alpha(t_i) t_\beta(t_i) \tag{2.3}$$

This statistic is further described in the Appendix of this Chapter, which is

§2.6. That section includes a derivation of the statistics signal to noise ratio $S_{\rm PW}$. The total time series of length T is subdivided into consecutive sub-blocks of length T/M to mitigate the saturation of the detection SNR when the signal is self-noise limited. This is analogous to the *pre-whitening* method presented in Jenet et al. (2005). Based on the signal model of equation (2.2), the SNR for the correlation coefficient is

$$S_{\rm PW} = \sqrt{M}\left[\frac{4}{GN_p}\frac{\sigma_n^2(T/M)}{\sigma_e^2(T/M)} + \frac{2\sigma_n^4(T/M)}{G^2N_p(N_p-1)\sigma_e^4(T/M)}\right]^{-1/2}, \tag{2.4}$$

where $\sigma_e^2(T/M)$ is the ensemble average mean squared amplitude of the correlated signal in the sub-block of length T/M and G is the relative amplitude of the single realization to the ensemble average. The uncorrelated noise σ_n^2 comprises contributions from uncorrelated GWs (the pulsar-end term), other red noise, and white noise:

$$\sigma_n^2(t) = \sigma_p^2(t) + \sigma_r^2(t) + \sigma_w^2(t). \tag{2.5}$$

The rms contribution of the pulsar-end term, over a time span t is defined to be

$$\sigma_p(t) = \sigma_e(t) = \sigma_{g,0}\left(\frac{t}{t_0}\right)^{\beta}, \tag{2.6}$$

where $\beta = 5/3$ and $\sigma_t \approx 20$ ns for $t_0 = 5$ yr for the expected perturbations from a massive black hole binary background (Jaffe & Backer 2003; Shannon & Cordes 2010; Chapter 3).

The major source of uncorrelated red noise is intrinsic spin noise. Spin noise is associated with rotational instabilities of the NS caused by torque variations in the magnetosphere or the transfer of angular momentum between the rigid crust and core of neutron star. If the spin noise is associated with a random walk

or similar power-law processes, the rms amplitude can be modeled as

$$\sigma_r(t) = \sigma_{r,0} \left(\frac{t}{t_0} \right)^{\gamma}, \tag{2.7}$$

where $\sigma_{r,0} = 20$ ns at $t_0 = 5$ yr and $\gamma \approx 1.8$ (Shannon & Cordes 2010; Chapter 3) for most millisecond pulsars.

We parameterize white noise contributions over a total observing span of T

$$\sigma_w(T) = \frac{\sigma_{w,0}}{R_{\rm obs} T}, \tag{2.8}$$

where $\sigma_{w,0}$ is the rms error in a single TOA estimate, and $R_{\rm obs}$ is the observation rate. Presently, for the best pulsars $\sigma_{w,0} = 100$ ns, and observations are typically conducted at a monthly rate ($R \approx 10$ yr^{-1}).

We note that when the signal is larger than the noise $\sigma_e^2 \gg \sigma_n^2$, and the SNR of the correlation coefficient is $S_{\rm PW} \propto \sqrt{N_p}$. In the low signal to noise limit ($\sigma_n^2 \gg \sigma_e^2$), $S_{\rm PW} \propto \sqrt{N_p(N_p - 1)}$.

We investigated the signal to noise ratio (equation 2.4) of the detection statistic in the presence of varying compositions of noise with PTAs comprising varying numbers of pulsars. Unless otherwise noted, the rms amplitude of the GWs and the red noise are assumed to respectively scale proportional to $T^{5/3}$ and T^2. Unless otherwise noted, we assume the default PTA observing configuration is an observing span of $T = 10$ yr; the white noise per observing epoch is $\sigma_{\rm WN} = 100$ ns; the timing noise at $T = 5$ years is $\sigma_{\rm TN,0} = 20$ ns; the ensemble average strength of the GWB is $\sigma_{\rm GW,0} = 20$ ns; and the relative rms amplitude of the realization of the GWB to its rms ensemble average is unity ($G = 1$).

We first investigate the optimal number of subdivisions for the data. In Figure 2.1 the SNR is plotted versus the number of subdivisions M. The optimal

number depends on the relative strengths of the white noise, red noise and the GW signal, but for nominal PTA observing configurations the best value M is between 3 and 10. In subsequent discussion M has been chosen to maximize the SNR.

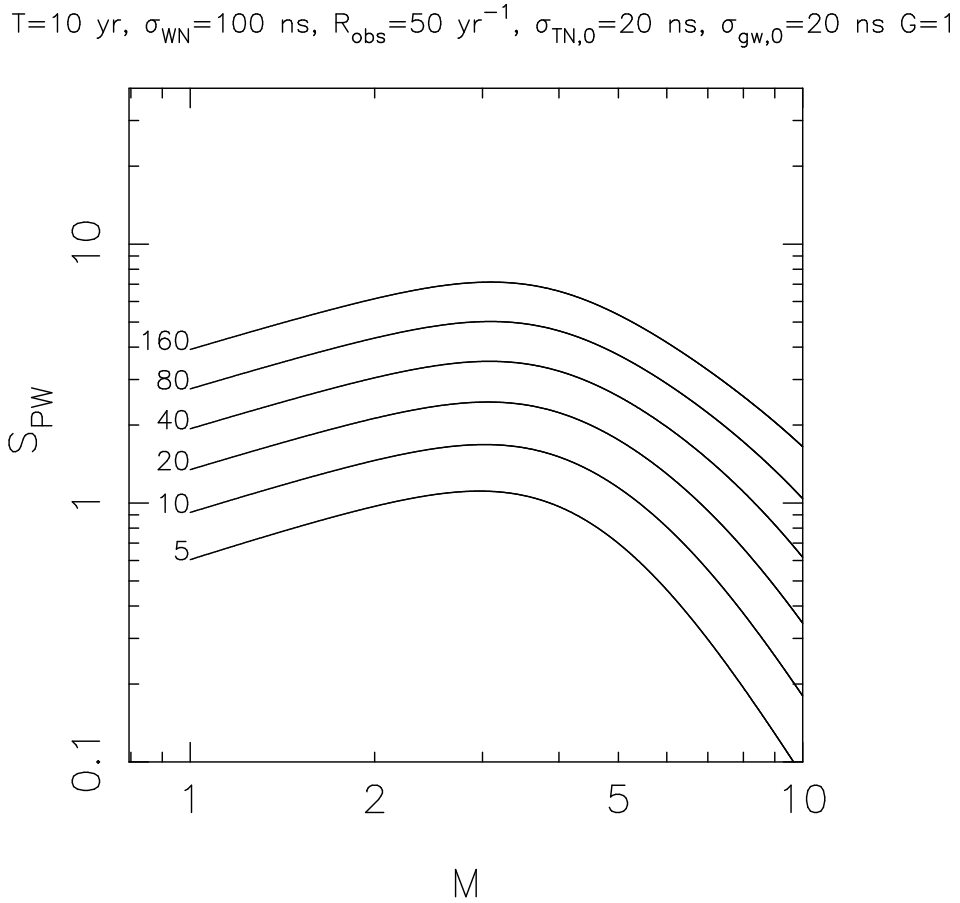

FIGURE 2.1.— Signal to noise ratio $S_{\rm PW}$ versus number of sub-blocks M, for PTAs comprised of different numbers of pulsars. The number of pulsars in the PTA is listed to the left of each curve. Above the plot, the stability properties of the pulsars and the observation rate and duration are listed.

In Figure 2.2 the signal to noise ratio of the pairwise CCF is plotted versus the amplitude of the timing noise for PTAs comprised of different numbers of pulsars. When the strength of the timing noise is low, the SNR is constant because it is limited by white noise. When $\sigma_{\rm TN,0} = 0$ the SNR is close to that of the detection statistic presented in Figure 1.b of Jenet et al. (2005).

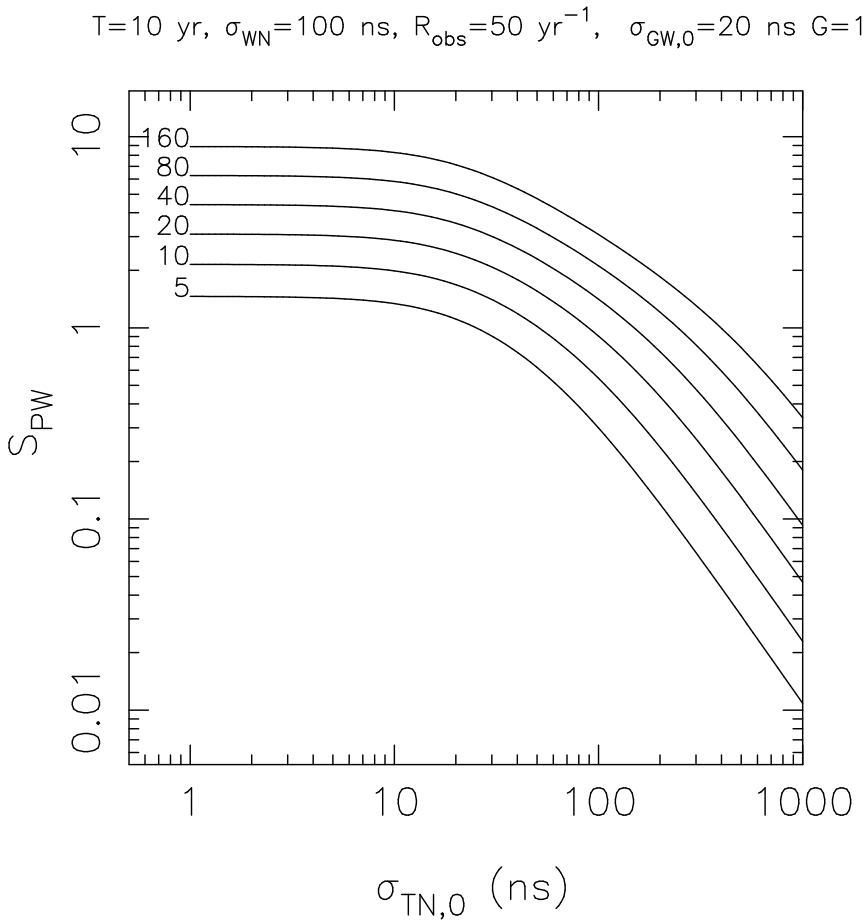

FIGURE 2.2.— Signal to noise ratio $S_{\rm PW}$ versus strength of the timing noise $\sigma_{\rm TN,0}$ for PTAs comprised of different numbers of pulsars. The number of pulsars in the PTA are listed to the left of each curve. Above the plot the stability properties of the pulsars and the observation rate and duration are listed.

In Figure 2.3 the variation of the signal to noise ratio with the rms strength of the gravitational wave background is displayed. When the signal is much weaker than intrinsic noise, the SNR scales $\propto \sigma^2_{\rm GW,0}$. When the signal is much larger than the intrinsic noise, the SNR is self-noise limited and scales directly proportional to $\sigma_{\rm GW,0}$.

In Figure 2.4 the SNR of the detection statistic $S_{\rm PW}$ is plotted versus the observing rate R. Increasing the observing rate improves the SNR, but does not completely mitigate the loss of SNR associated with the presence of timing

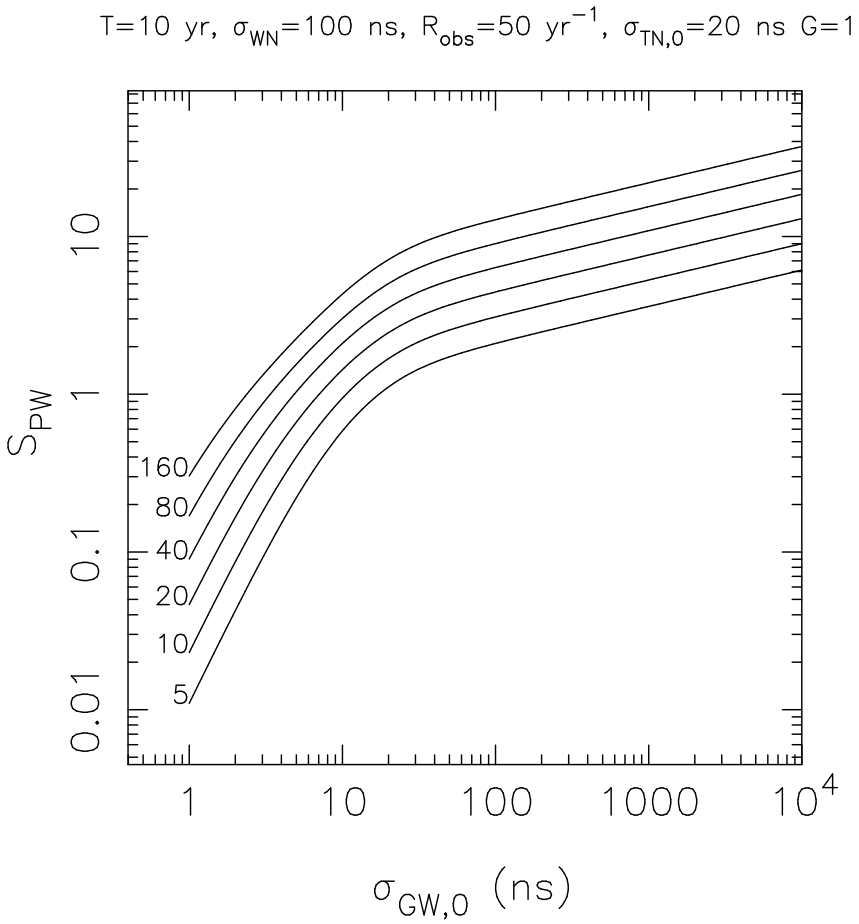

FIGURE 2.3.— Signal to noise ratio $S_{\rm PW}$ versus strength of the gravitational wave perturbations $\sigma_{\rm GW,0}$ for different numbers of pulsars. The number of pulsars in the PTA are listed to the left of each curve. Above the plot the stability properties of the pulsars and the observation rate and duration are listed.

noise.

In Figure 2.5 $S_{\rm PW}$ is plotted versus the white noise level. The SNR is better when there is lower levels of white noise because the effective number of available sub-blocks is larger.

In Figure 2.6, $S_{\rm PW}$ is plotted versus the amplitude of the signal relative to its expected ensemble average value. The SNR only increases proportional to G in the low SNR regime where white noise dominates. In the high SNR regime the

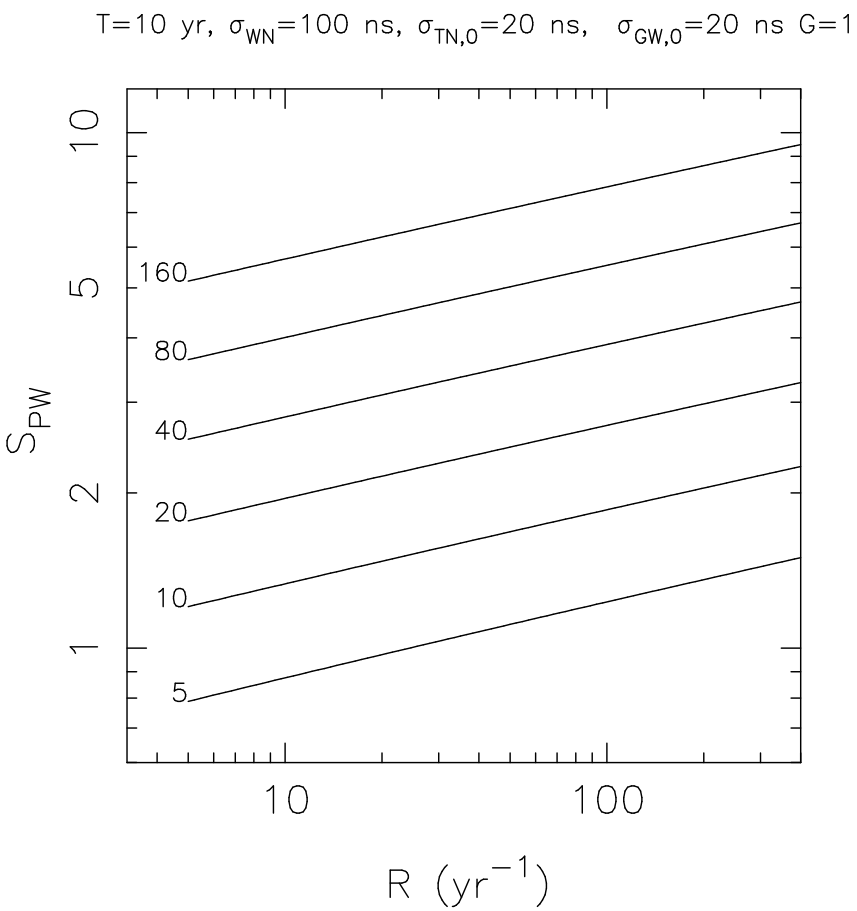

FIGURE 2.4.— Signal to noise ratio $S_{\rm PW}$ versus the observing rate R for different numbers of pulsars. The number of pulsars in the PTA are listed to the left of each curve. Above the plot the stability properties of the pulsars and the observation rate and duration are listed.

$S_{\rm PW} \propto G^{1/2}$.

The expected values of G was examined through simulation. In Figure 2.7 a histogram of the rms amplitudes of time series relative to the average for the massive black hole GWB and for other non-stationary processes that may be present in pulsar timing residuals (but uncorrelated between pulsars). The strength of the GW signal shows a wide variation about its ensemble average strength. This variation is somewhat suppressed because the SNR scales $\propto G^{1/2}$.

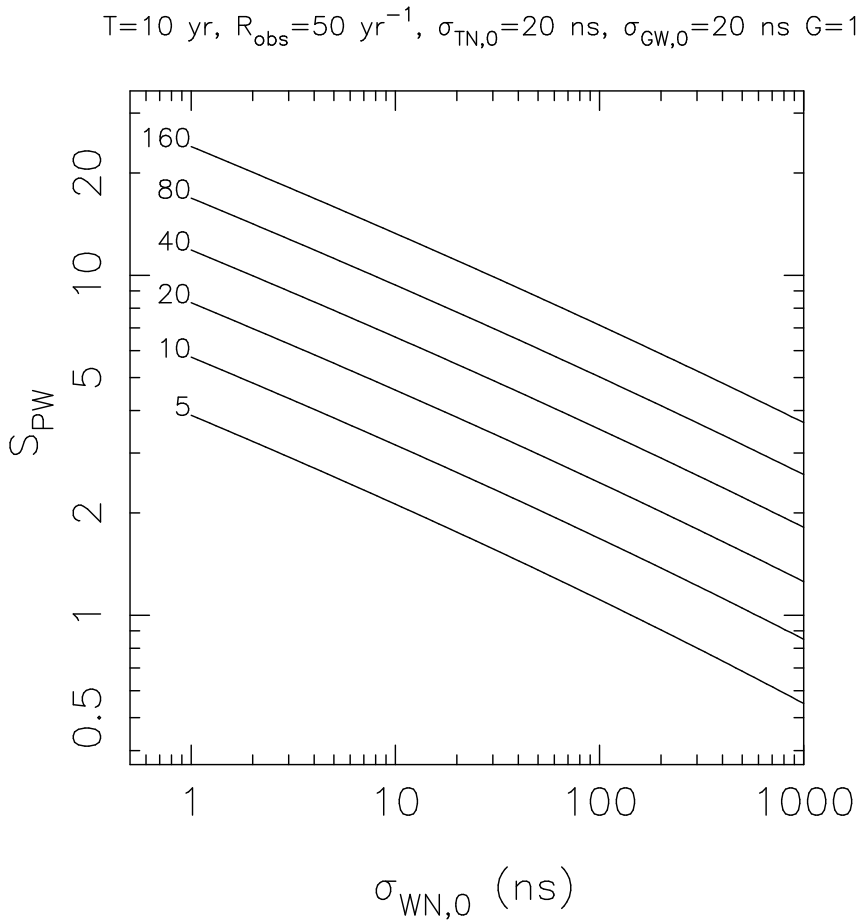

FIGURE 2.5.— Signal to noise ratio versus level of white noise for different numbers of pulsars. The number of pulsars in the PTA are listed to the left of each curve. Above the plot the stability properties of the pulsars and the observation rate and duration are listed.

2.4 Improving PTA Sensitivity

Current PTA observations are not likely to detect gravitational wave background of astrophysically or cosmologically relevance at a high significance level. If timing noise is much weaker than predicted, a low SNR detection is possible with 40 pulsars. However this low SNR detection is difficult to confirm because any diagnostic that is sued to verify a detection requires subdivision of the data (e.g., by dividing into different time intervals, or into sub-arrays of pul-

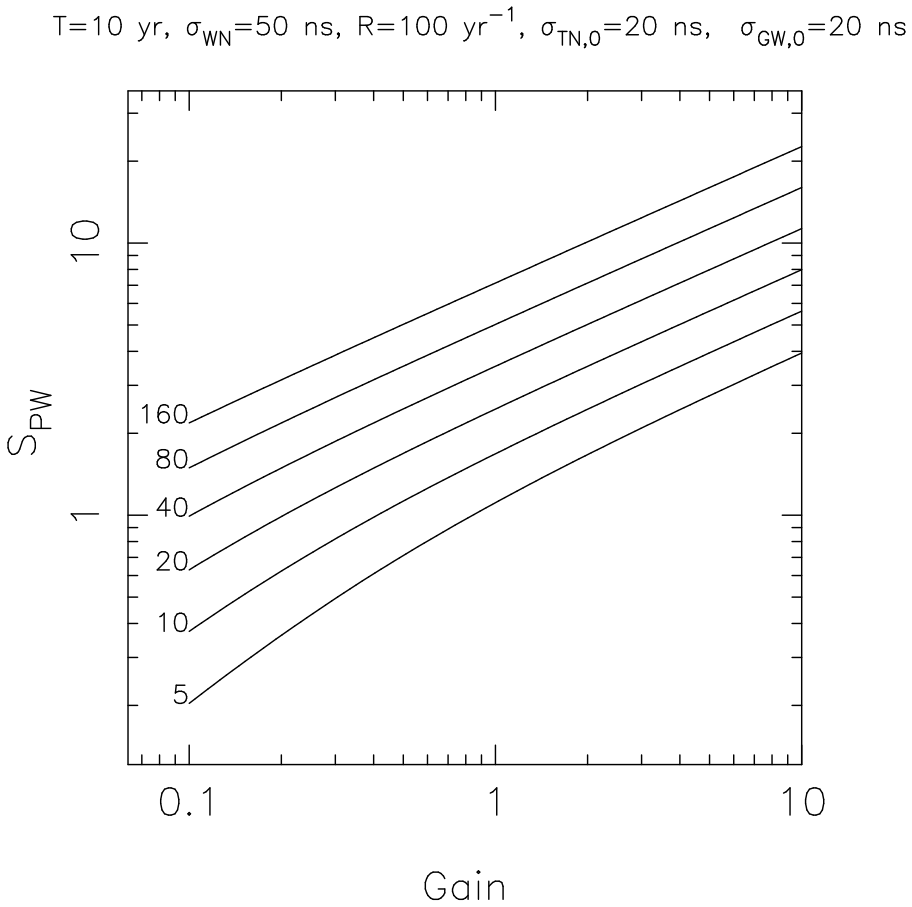

FIGURE 2.6.— Signal to noise ratio versus relative amplitude (referred to as Gain, G) of the signal. The number of pulsars in the PTA are listed to the left of each curve. Above the plot the stability properties of the pulsars and the observation rate and duration are listed.

sars) which decreases the SNR. For similar reasons higher sensitivity is certainly necessary to characterize any detected GWB. Broadly speaking, the sensitivity of a PTA can be increased by reducing white noise levels, decreasing red noise levels, and increasing the number of pulsars or increasing the length of the observing campaign.

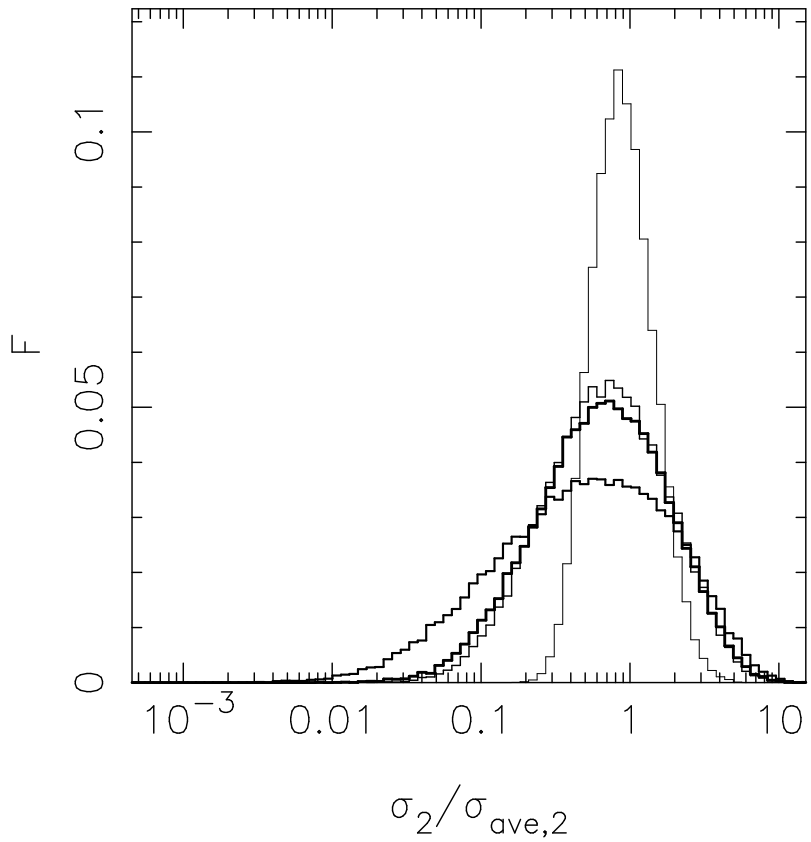

FIGURE 2.7.— Histogram of the realization to realization variation rms amplitude of the time series relative to its ensemble average G for various stochastic processes, including gravitational wave background. From thinnest to thickest lines, the curves are histograms of the strength of random walks in phase (RW_0), random walk in frequency (RW_1), random walk in frequency derivative (RW_2), and gravitational wave background, based on 2000 realizations of each process. The gravitational wave background has similar statistics to RW_2 because both share similar time variability (Shannon & Cordes 2010).

2.4.1 Decreasing White Noise

White noise is comprised predominantly of three terms that affect the template matching used to determine TOAs from observed average pulses. The first is associated estimation error associated with radiometer noise, The second is associated with diffractive interstellar scintillation is referred to as the *finite scintle effect* (Cordes & Shannon 2010). The third effect is intrinsic variability of radio

emitting region of the pulsar and is referred to as pulse phase jitter (Cordes & Shannon 2010; Chapter 6). Individual pulses have variable pulse phase and amplitude. All pulsars appear to possess this variability with perhaps one exception (Jenet et al. 2001).

Improve Calibration and Time Tagging Methodology: Some fraction of white noise is likely associated with poor calibration of the radio observations. There are small ($\sim$ 10% to 20%) improvements in the measurement error by improving polarmetric calibration and preforming timing on total intensity Stokes profiles (van Straten 2006). In addition, it may be possible to use phase retrieval methods can be used to mitigate some fraction of diffractive interstellar propagation delays under certain circumstances (P. Demorest & M. Walker, private communication).

Observe with higher-gain telescopes: The TOA estimation error associated with radiometer noise can be reduced by increasing telescope gain (i.e, observing with a larger telescope) or reducing telescope system temperature. However, there other forms of white noise associated with the finite scintle effect and pulsar phase jitter are not mitigated by increasing telescope gain (Cordes & Shannon 2010; Chapter 6).

Observe with wider bandwidths: Wider bandwidth observations mitigate radiometer noise and the finite scintle effect. However wider bandwidth observations do not mitigate pulse phase jitter because it produces correlated TOA errors over a wide frequency range. In addition with wider bandwidth observation it is necessary to properly account with the frequency evolution of the pulse profile; this consists of both intrinsic and ISM-induced terms.

Observe at optimal observing radio frequencies: Radiometer noise is typically lowest near 1 GHz where pulsars are the brightest relative to the sky background. However, the finite scintle effect is much weaker at higher observing frequencies. Jitter is only weakly frequency dependent. There is a trade-off between the finite scintle effect and radiometer noise, which is lowest at frequencies where ISM-associated timing noise is significant (Cordes & Shannon 2010). By optimizing observing bands these two effects can be balanced. However, there are other longer term effects that may require a wider range of frequencies to mitigate (Chapter 5).

Increase telescope throughput: By increasing the total integration time (by either increasing the observing time per epoch or increasing the observing rate R) the level of white noise by definition is reduced.

2.4.2 Decrease Red Noise

There are three major contributions to red noise: GW perturbations that are uncorellated between lines of sight, intrinsic spin noise, and arrival time variability associated with refractive interstellar scintillation.

Remove Spin Noise: Recently Lyne et al. (2010) identified a correlation between pulse shape and spin-down state in a small sample of slow period canonical pulsars, indicating that some timing noise was magnetospheric in origin. By identifying this correlation a large portion of the timing noise in these pulsars could be removed. If *all* timing noise was associated with this magnetospheric processes, it would be possible to significantly improve the timing stability of the pulsars.

Remove Refractive Propagation Effects: Improved TOA fitting algorithms reduce the levels of red ISM noise associated with refractive interstellar scintillation (Cordes & Shannon 2010; Chapter 5). Like short-timescale ISM effects, the most effective way to remove refractive propagation effects is through observations at higher frequencies.

Determine accurate distances to pulsars: If pulsars distances were determined to < 1 lyr the pulsar-end term could be included in phase with the earth term. This level of precision is not plausible in the near future (S. Chatterjee, private communication).

2.4.3 Increase Number of Pulsars

In the regime relevant to a detection of the GWB with PTAs, the sensitivity of a PTA is proportional to $\sqrt{N_p}$. New pulsars can be found through wide field surveys a radio wavelengths (e.g., Cordes et al. 2006b) or targeted searches of candidate radio pulsars discovered at other wavelenghts (e.g., targeted searchesT of Fermi point sources).

2.4.4 Increase Length of the Observing Campaign

If the observing span is lengthened the SNR will increase. The improvement in SNR depends on the strength and temporal variability of the red noise relative to the gravitational wave background. This is obviously a less desirable option. In Figure 2.8 the SNR of the detection statistic versus total observing span T is displayed. When the total observing span is short, the error is dominated by

white noise and the total SNR grows strongly with T. However, in this regime, the SNR is low and a detection cannot be made. When the observing span is longer and the SNR is higher > 1, the SNR increases much more slowly with T.

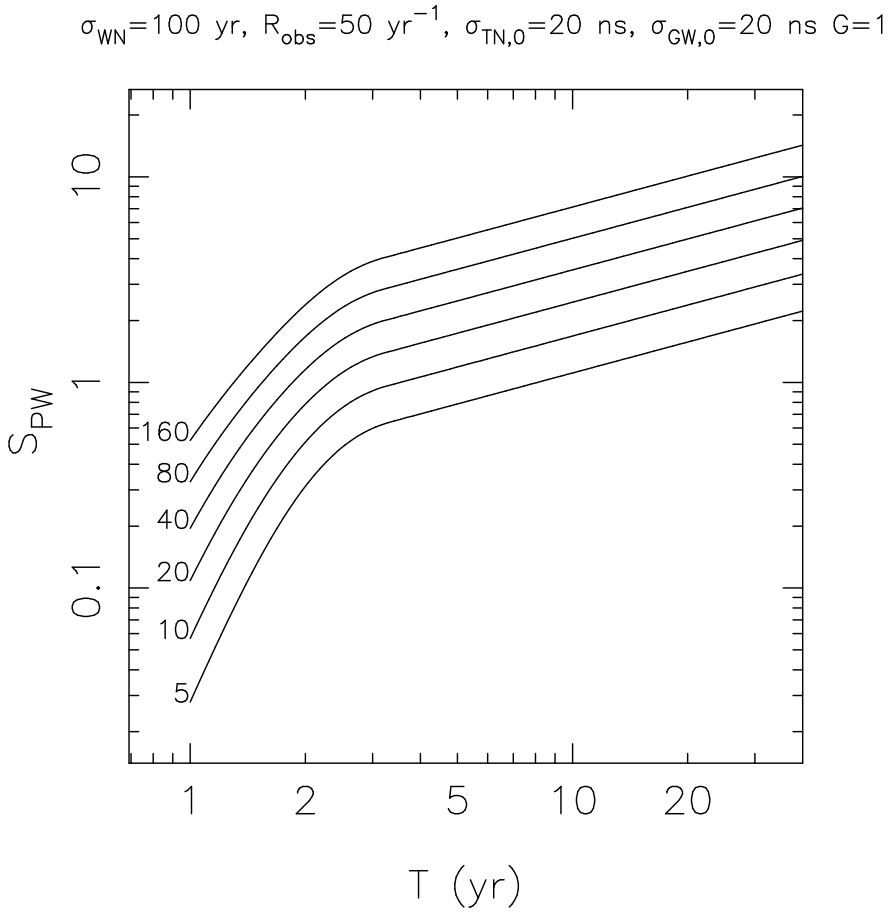

FIGURE 2.8.— Signal to noise ratio of a detection statistic $S_{\rm PW}$ versus total observing span T. The number of pulsars in the PTA is listed to the left of each curve. Above the plot, the stability properties of the pulsars and the observation rate and duration are listed.

2.5 Discussion and Conclusions

The only guaranteed way to improve the sensitivity of PTA observations to GWs is to increase throughput: either by increasing observing time at each epoch, or

increase the number of observing epochs. Wider bandwidths and higher gain telescopes may benefit the observations of some pulsars, but a few MSPs already jitter dominated.

In the long term, additional pulsars need to be incorporated into PTAs to improve the sensitivity to levels required to characterize the gravitational wave background.

2.5.1 Acknowledgements

This work was supported by the NSF through grant AST-0807151 and by NAIC, which is operated by Cornell University under a cooperative agreement with the NSF.

2.6 Appendix: Cross Correlation Detection Signal to Noise Ratio

The correlated component of the GWB signal in pulsar TOAs can be detected using many techniques, the most straightforward of which is a cross correlation method, described below. To calculate the SNR we simplify the signal model presented in equation (2.2) by first consolidating the noise terms. In addition we assume the most optimistic PTA configuration with all pulsar located in the same direction of the sky but at different distances, so that the earth-end term is 100% correlated. Thus, for each pulsar $\alpha = 1, N_p$ at times $t_i, i = 1, N_t$ the residual

time of arrival is

$$t_{i\alpha} = e_i + n_{i\alpha}, \tag{2.9}$$

The noise is a zero-mean random variable

$$\langle n_{\alpha i} n_{\beta j} \rangle = \sigma_n^2(T) c_n(t_i, t_j) \delta_{\alpha\beta}, \tag{2.10}$$

where $\delta_{\alpha\beta}$ is a Kronecker delta function, $c_n(t_i, t_j)$ is the cross correlation function for the noise, and we have assumed the same ensemble average noise for all pulsars.

The cross correlation function detection statistic is defined by combining the residuals of all $N_p(N_p - 1)/2$ pairs of pulsars

$$C = \frac{2}{N_p(N_p - 1)} \frac{1}{N_t} \sum_{\alpha=1}^{N_p} \sum_{\beta=1}^{\alpha} t_\alpha(t_i) t_\beta(t_i). \tag{2.11}$$

We now define the expected values of the perturbations relative to correlation functions

$$\langle C_e \rangle = \mu_{C,e} = \frac{1}{N_t} \sum_i e_i e_j = G^2 \sigma_e^2 \sum_i \frac{c_e(t_i, t_i)}{N_t}, \tag{2.12}$$

where G is gain of the earth-end time series relative to its expected ensemble average value,

The variance of C is

$$\sigma_{C,e}^2 = \frac{4}{N_p N_t^2} \sum_{ij} \langle e_i e_j n_i n_j \rangle + \frac{2}{N_p(N_p - 1) N_t^2} \sum_{ij} \langle n_i^2 n_j^2 \rangle. \tag{2.13}$$

Where the expectated values are

$$\langle e_i e_j n_i n_j \rangle = G^2 \sigma_e^2 \sum_{ij} \sigma_n^2 c_{ne}(t_i, t_j), \tag{2.14}$$

and

$$\langle n_i^2 n_j^2 \rangle = \sigma_n^4 \sum_{ij} c_{nn}(t_i, t_j). \tag{2.15}$$

Note that in general the perturbations are non-stationary and hence the correlation coefficients depend the many properties of the time series, including the GW signal and the fitting process.

Substituting in these expressions, the SNR of the detection statistic is

$$S_{C,e} = \frac{\sqrt{N_p/2}\sum_i c_e(t_i,t_i)/N_t}{\left\{2(\sigma_n^2/G^2\sigma_e^2)\sum_{ij} c_{ne}(t_i,t_j)/N_t^2 + [1/(N_p-1)](\sigma_n^4/G^4\sigma_e^4)\sum_{ij} c_{nn}(t_i,t_j)/N_t^2\right\}^{1/2}}. \tag{2.16}$$

Realization to realization variation will cause e to vary, which is incorporated through the relative amplitude factor G. To assess the likelihood of detecting a background with particular ensemble average quantities, it is necessary to marginalize over G using its expected probability distribution displayed in Figure 2.7. If the data are sub-blocked (discussed in the main text), some averaging is being conducted, the effects of realization to realization variation are at least partially suppressed. The summations involving the correlation function are ≈ 1 (J. Cordes & R. Shannon in preparation). Applying this last approximation to equation (2.16), we find equation (2.4).

CHAPTER 3

ASSESSING THE ROLE OF SPIN NOISE IN THE PRECISION TIMING OF MILLISECOND PULSARS

We investigate rotational spin noise (referred to as timing noise) in non-accreting pulsars: millisecond pulsars, canonical pulsars, and magnetars. Particular attention is placed on quantifying the strength and non-stationarity of timing noise in millisecond pulsars because the long-term stability of these objects is required to detect nanohertz gravitational radiation. We show that a single scaling law is sufficient to characterize timing noise in millisecond and canonical pulsars while the same scaling law underestimates the levels of timing noise in magnetars. The scaling law, along with a detailed study of the millisecond pulsar B1937+21, leads us to conclude that timing noise is latent in most millisecond pulsars and will be measurable in many objects when better arrival time estimates are obtained over long data spans. The sensitivity of a pulsar timing array to gravitational radiation is strongly affected by any timing noise. We conclude that detection of proposed gravitational wave backgrounds will require the analysis of more objects than previously suggested over data spans that depend on the spectra of both the gravitational wave background and of the timing noise. It is imperative to find additional millisecond pulsars in current and future surveys in order to reduce the effects of timing noise.[1]

3.1 Introduction

In most pulsars the residual times of arrival (TOAs) show structure that differs greatly from what is expected from measurement error alone and is typically

[1]R. M. Shannon & J. M. Cordes, accepted by ApJ.

consistent with having a red power spectrum. This structure is generically referred to as spin noise or timing noise (TN).

Rotational irregularities of the neutron star appear to be the dominant source of TN in most pulsars. Timing noise is thought to arise from either changes in coupling between the neutron star crust and its superfluid core (Jones 1990) or magnetospheric torque fluctuations (Cheng 1987; Kramer et al. 2006a; Cordes & Shannon 2008; Lyne et al. 2010). Thus the study of TN provides valuable insight into the structure of the neutron star and its magnetosphere.

The observed strength of timing noise varies by more than eight orders of magnitude over the known non-accreting pulsars, which we subdivide into three classes: the magnetars, with spin frequencies $\nu < 1/6$ s^{-1} and relatively high magnetic fields; the rapidly-spinning and relatively weakly magnetized millisecond pulsars (MSPs), with spin frequencies $\nu > 50$ s^{-1}; and the canonical pulsars (CPs) with both spin frequencies and magnetic field strengths between the two other classes. Some magnetars show root mean square (rms) TOA variations of many tens of seconds on time scales of years, whereas the most stable MSPs have not shown evidence of TN at the 200 ns level over decade-long time scales.

Millisecond pulsars, which have stability comparable to the best terrestrial clocks, continue to be intensely studied. Their low levels of TN enable other TOA perturbations to be quantified, such as the relativistic effects in pulsars with massive (white dwarf) companions (Verbiest et al. 2008), recoil from planetary-mass companions (Konacki & Wolszczan 2003), and the presently undetected stochastic gravitational wave background (GWB Detweiler 1979; Hellings & Downs 1983; Jenet et al. 2006). Interest in the detection of gravi-

tational waves with pulsars has intensified in recent years due to the improvement in MSP timing precision. This improvement can be attributed to technological advancements in telescope receivers and signal processing equipment (Demorest 2007), improved analysis methods (van Straten 2006), and the discovery of new pulsars that appear to possess intrinsically superior timing stability (Ord et al. 2006).

Long-term timing stability of millisecond pulsars is necessary to detect the small correlated perturbations in the TOAs associated with passage of gravitational waves through the solar system. It has been suggested that if sub−100 ns stability over $5 - 10$ years can be achieved for a number of millisecond pulsars (currently estimated at $N_{\rm PTA} = 20 - 40$) in a pulsar timing array (PTA), a stochastic background of gravitational waves at a cosmologically significant level can be detected (Jenet et al. 2005). Only two MSPs have shown any measurable TN, making characterizing as well as forecasting TN in MSPs difficult. However, the strength and properties of TN will certainly affect the detection of gravitational waves, even if TN is latent in most objects at present.

In this paper we analyze TN throughout the pulsar population and assess the strength of TN in MSPs. In §3.2 we summarize the phenomenology of TN and show that random walk models and related non stationary processes can be used to model most observed TN. In §3.3 we suggest two tools for diagnosing TN: one that is appropriate for assessing the long-term stability of MSPs and another that can be used to classify and compare TN throughout the pulsar population. In §3.4, we derive scaling relationships for TN in canonical pulsars, millisecond pulsars, and magnetars. We find that millisecond pulsars have TN that is consistent with that observed in canonical pulsars. We further link

MSPs to CPs by showing that the behavior of the MSP B1937+21 is similar to that found in the canonical pulsar population. In contrast, magnetars are found to possess TN that exceeds the amount expected from extrapolation from the other populations. In §3.5 we conclude that TN is present at levels that affect the observation strategies employed in pulsar timing arrays and suggest detecting gravitational radiation requires timing observations of more pulsars than previously estimated. In that section we also discuss techniques for mitigating TN and improving the sensitivity of a PTA to gravitational waves.

3.2 Timing Noise: Phenomenology

Timing noise is manifested as structure in the residuals of a fit to pulsar TOAs. A single TOA is determined by comparing a profile formed from averaging a large number of pulses with a template profile. The averaging is conducted to both increase the signal to noise ratio and decrease the effects of jitter associated with intrinsic pulse-to-pulse phase and amplitude variations. The TOAs are then compared to a model that accounts for the propagation of the pulse from the pulsar to the earth and refers the arrival times to the solar system barycenter (Edwards et al. 2006). The fit includes terms accounting for periodic variations associated with the motion of the earth about the solar system barycenter and the reflex motion of the pulsar due to a companion, if the pulsar is in a binary system. The fit also includes secular terms that account for the unknown spin-down of the pulsar, and secular, but frequency-dependent terms that correct for the propagation of the radio pulses through plasma in the interstellar medium. It is essential to fit for the pulsar spin frequency ν and frequency derivative $\dot{\nu}$ because these quantities are intrinsic to the pulsar and cannot be predicted us-

ing any other technique. With the exception of a few young pulsars (such as the Crab and Vela pulsars) the values of the higher order frequency derivatives associated with pulsar braking are not measurable on the year to decade observing spans over which pulsars have presently been observed.

The residuals $\mathscr{R}(t)$ of the fit are used to assess the validity of the timing model and identify the presence of unmodeled periodic and secular trends. The rms of the residuals over an observing span of length T, after a second-order polynomial fit is given by

$$\sigma^2_{\mathscr{R},2}(T) = \frac{1}{N_t} \sum_{i}^{N_t} \mathscr{R}^2(t_i), \tag{3.1}$$

for an observation comprising N_t samples at times t_i, with $i = 1, N_t$.

The variance $\sigma^2_{\mathscr{R},2}$ can be subdivided into a white component σ^2_W and a red component $\sigma^2_{\mathrm{TN},2}$ that in canonical pulsars is usually dominated by TN:

$$\sigma^2_{\mathscr{R},2}(T) = \sigma^2_{\mathrm{TN},2}(T) + \sigma^2_W. \tag{3.2}$$

In this discussion *red* is used to label processes which have ensemble average power spectra that have greater power at lower fluctuation frequencies (red spectra) and *white* for processes that have equal levels of power at all fluctuation frequencies (white or flat spectra).

There are a number of TN models that are distinguished by the time evolution of the residuals, or equivalently the shape of the power spectrum of the residuals.

One set of models is based on random walks of the spin properties of the pulsar. We consider random walks in pulse phase (RW_0), frequency (RW_1), and frequency derivative (RW_2) as useful archetypal processes. Because the

processes correspond to white noise in ν, $\dot{\nu}$, and $\ddot{\nu}$, they produce rms residuals that scale proportional to $T^{1/2}$, $T^{3/2}$, and $T^{5/2}$, respectively (Boynton et al. 1972), and ensemble average power spectra with spectral indices of -2, -4, and -6, respectively (Harding et al. 1990). For these processes the residuals have non-stationary statistics. For reference, we note that a gravitational wave background from merging massive black holes produces rms residuals that scale proportional to $T^{5/3}$ and a power spectrum with a spectral index of $-13/3$ (Jaffe & Backer 2003).

Band-limited noise (BL) is associated with processes that have low and high frequency cut-offs, in which the rms residuals increase for some time with a slope dependent on the particular spectral shape of the process. After a time associated with the low-frequency cut-off of the band $T_{\rm out} = 1/f_{\rm low}$, the rms timing noise will plateau. An example of a BL process is the perturbation induced by a wide asteroid belt around a pulsar (R. Shannon et al., in preparation).

In many pulsars it appears that multiple types of TN occur at once. However, random walks provide a good basis for modeling non-stationary components of timing noise. Cordes & Downs (1985) and D'Alessandro et al. (1995) conducted detailed analyses of complementary sets of canonical pulsars. While they found that TN in most canonical pulsars cannot be explained by a single random walk process, both suggest that a mixture of random walks in ν and $\dot{\nu}$ and discrete jumps in ϕ, ν, and $\dot{\nu}$ were compatible with the TN.

Alternative models for timing noise include periodic and quasiperiodic processes. These models have gained favor because of recent reports of periodic and quasiperiodic contributions the the residual TOAs for a few pulsars. For example, PSR B1931+24 (Kramer et al. 2006a) shows jumps between two states

with distinct spin down rates $\dot{\nu}$ at quasiperiodic times. In a study of 366 pulsars, Hobbs et al. (2010) and Lyne et al. (2010) identify a few pulsars ($\approx$ 2% of their sample) that contain periodic or quasiperiodic components in residual time series and switches between distinct states of $\dot{\nu}$. They also found that the different levels of $\dot{\nu}$ have unique average pulse profiles and they propose that this form of timing noise can be corrected. In a substantial fraction of the identified cases of periodicity or quasiperiodicity, the model included a significant $\ddot{\nu}$ that is attributed to non-stationary timing noise that augments any periodic or quasiperiodic component. We discuss the possibility of mitigating timing noise further in §3.5.3.

While in some cases, there is clear evidence of a periodic or quasiperiodic contribution to the TOAs, in other cases, realization to realization variation can mimic quasiperiodic behavior. To demonstrate this we simulated residual curves for RW_0, RW_1, and RW_2 random walks. In the top panel of Figure 3.1, we show four realizations of quadratic-subtracted residual TOAs for the same RW_1 process. In the plots residual curves show behavior that mimic quasiperiodicity, irregular behavior in which higher order polynomials dominate the TN, and cubic-dominated behavior with both $\ddot{\nu} > 0$ and $\ddot{\nu} < 0$.

We use the number of zero crossings to quantify the morphological variations in single realizations of RW processes. Realizations that have a large number of zero crossings will appear quasiperiodic or irregular. In contrast, realizations that have three zero crossings will appear cubic and match what is expected from ensemble average statistics. In the bottom panel of Figure 3.1 we show a histogram of the number of zero crossings for each quadratic-subtracted polynomial for 4000 realizations of RW_1, and RW_2 processes. A significant frac-

tion of the realizations of both RW_1 and RW_2 processes show > 3 zero crossings and a few show > 6 zero crossings. The number of zero crossings for residuals of RW_0 random walks is not displayed, because this random walk has a shallow spectrum and thus single realizations show very irregular behavior that typically have > 10 zero crossings.

3.3 Timing Noise: Diagnostics

Two approaches have been used to characterize the strength of timing noise in radio pulsars. The first uses the total TN after a second order fit $\sigma_{\mathrm{TN},2}$. Cordes & Helfand (1980) define the activity parameter as

$$A = \log\left[\frac{\sigma_{\mathrm{TN},2}(T)}{\sigma_{\mathrm{TN},2}(T)_{\mathrm{Crab}}}\right], \tag{3.3}$$

which measures levels of TN relative to the Crab pulsar and represents a time-independent measure of the strength of the TN, assuming that pulsars show TN with similar time variability to the Crab pulsar.

A second set of methods characterizes timing noise using the frequency second derivative $\ddot{\nu}$ calculated from a cubic fit to the TOAs. Some groups have directly used $\ddot{\nu}$ to assess the strength of the TN (Urama et al. 2006; Chukwude 2007) and correlated it with other pulsar parameters. Arzoumanian et al. (1994) assessed the strength of TN using a parameter

$$\Delta_8 = \log\left(\frac{|\ddot{\nu}|}{6\nu}T_8^3\right), \tag{3.4}$$

where $\ddot{\nu}$ is measured over an observing span of $T_8 = 10^8$s. While the cubic term will dominate the variance of TN in the ensemble average of any red process with a monotonically decaying spectrum, in a single realization higher order

terms may contain a large portion of the TN. Thus statistics based on $\ddot{\nu}$ tend to underestimate the amount of TN in these processes. Additionally, the statistic Δ_8 is model-dependent because $\ddot{\nu}$ on average increases with length of observing span for red noise processes, much like the total rms residuals. Therefore to properly compare values of Δ_8 or $\ddot{\nu}$ in observations of different lengths a model-dependent time scaling needs to be included.

A dimensionless Allan variance-like parameter σ_z is described in Matsakis et al. (1997) that can be used to estimate pulsar stability,

$$\sigma_z(T) = \frac{1}{2\sqrt{5}} \left[\frac{\sigma_{\ddot{\nu}}(T)}{\nu} \right] T^2, \tag{3.5}$$

where $\sigma_{\ddot{\nu}}(T)$ is the rms of $\ddot{\nu}$ over observing spans of length T. Because the parameter uses $\ddot{\nu}$ to estimate TN, it also will in general underestimate the total TN.

Previous methods do not provide satisfactory diagnostics for TN. We therefore suggest that the rms timing noise (after a second order fit) is the basis for any proper diagnostic of TN, and propose two closely-related tools for diagnosing TN in pulsars.

To estimate the timing stability of a pulsar we use the post-fit rms TN scaled to ν, $\dot{\nu}$, and time span T,

$$\hat{\sigma}_{\mathrm{TN},2} = C_2 \nu^{\alpha} |\dot{\nu}|^{\beta} T^{\gamma}, \tag{3.6}$$

where the parameters C_2, α, β, and γ are estimated over the entire pulsar population.

A diagnostic suitable for comparing timing noise across the pulsar popula-

tion is the relative TN parameter

$$\zeta = \frac{\sigma_{\mathrm{TN},2}(T)}{\hat{\sigma}_{\mathrm{TN},2}(T)} = \frac{\sigma_{\mathrm{TN},2}(T)}{C_2 \nu^{\alpha} |\dot{\nu}|^{\beta} T^{\gamma}}, \tag{3.7}$$

which is the measured TN $\sigma_{\mathrm{TN},2}$, normalized by the global fit $\hat{\sigma}_{\mathrm{TN},2}$ from equation (3.6). The relative TN parameter is similar to the activity parameter A, but instead of normalizing to the properties of one pulsar (i.e., the Crab pulsar), the TN is compared to the best fit across all objects. This statistic can be used to identify outlying objects. If a pulsar shows $\zeta \ll 1$ it has smaller levels of TN than expected. If a pulsar shows $\zeta \gg 1$, it produces larger levels of TN than expected. We note that because this parameter depends on the modeled timing noise it depends on the observations included in the fit. The parameter values will change when more objects are included in the fit, or objects are included over longer observing spans. As a result ζ will change when additional observation of TN are included. If the new observations have statistically similar behavior as the present observations of TN, the fit will not change in a significant way. If the additional objects have different behavior (for example, if timing noise became stationary over very large T), the revised values of ζ will better identify the outlying objects.

3.4 Timing Noise across Neutron Star Populations

In this section, we show how rotational TN varies across the canonical pulsar, millisecond pulsar and magnetar populations. Previous analyses of TN have focused on canonical pulsars and fit for only a limited number of parameters using the statistical tools described in the previous section. Instead we will use $\hat{\sigma}_{\mathrm{TN},2}$ and ζ, which are defined in equations (3.6) and (3.7), respectively.

For our analysis we compiled observations of TN from many sources in the literature. In Appendix 3.7 we present the observing campaigns that we use and describe our methods for calculating $\sigma_{\rm TN,2}$. Our analysis includes $N_t = 1213$ time series, from approximately 450 distinct pulsars, which include $N_D = 591$ detections of TN and $N_{\rm UL} = 622$ upper limits. Our analysis excludes young objects that have measured frequency second derivatives $\ddot{\nu}$ that are attributed to pulsar braking. Plots displaying the rms timing noise $\sigma_{\rm TN,2}$ versus ν and $\dot{\nu}$ are displayed in Figure 3.2.

3.4.1 Maximum Likelihood Analysis

We use a maximum likelihood approach following Dewey & Cordes (1989) to find the best fit parameters for equation (3.6) in logarithmic space

$$\ln(\hat{\sigma}_{\rm TN,2}) = \ln C_2 + \alpha \ln(\nu) + \beta \ln|\dot{\nu}_{-15}| + \gamma \ln(T_{\rm yr}), \tag{3.8}$$

with $\sigma_{\rm TN,2}$ expressed in μs, ν expressed in $\rm s^{-1}$, $\dot{\nu}_{-15}$ expressed in 10^{-15} $\rm s^{-2}$, and $T_{\rm yr}$ expressed in years.

A fifth parameter δ is incorporated in the analysis to account for the large scatter in the strength of the timing noise. This scatter is associated with both realization-to-realization variation and non-modeled parameters that are assumed to be independent of ν and $\dot{\nu}$, such as neutron star mass and other physical elements of TN.

We assume that $\sigma_{\rm TN,2}$ is log-normally distributed; therefore the probability density function (PDF) of measuring rms residuals $\sigma_{{\rm TN,2},i}$ is

$$f_{\sigma_{\rm TN}}(\sigma_{{\rm TN,2},i}) = \frac{1}{\sqrt{2\pi\delta^2}} \exp\left[-\left(\frac{\ln(\hat{\sigma}_{{\rm TN,2},i}/\sigma_{{\rm TN,2},i})^2}{2\delta^2}\right)\right], \tag{3.9}$$

where $\hat{\sigma}_{\mathrm{TN},2,i} = \hat{\sigma}_{\mathrm{TN},2,i}(C_2, \alpha, \beta, \gamma, \delta)$ is the modeled red noise component. We define the probability P_i as the product of the PDF and the measurement error

$$P_i = f_{\sigma_{\mathrm{TN}}}(\sigma_{\mathrm{TN},i})\Delta(\ln \sigma_{\mathrm{TN},i}) = f_{\sigma_{\mathrm{TN}}}(\sigma_{\mathrm{TN},i})\frac{\Delta\sigma_{\mathrm{TN},i}}{\sigma_{\mathrm{TN},i}}, \tag{3.10}$$

which assumes that the measurement error is small relative to δ, a situation that is confirmed below.

We also incorporate upper limits from many observations using the probability

$$P_{\mathrm{UL},i} = 1 - \frac{1}{2}\mathrm{erfc}\left[\frac{\ln(\hat{\sigma}_{\mathrm{TN},i}/\sigma_{\mathrm{TN},i})}{\delta\sqrt{2}}\right], \tag{3.11}$$

where erfc is the complementary error function. The total probability for N_D detections of timing noise and N_{UL} upper limits is then

$$P(C_2, \alpha, \beta, \gamma, \delta) = \prod_i^{N_D} P_i \prod_j^{N_{\mathrm{UL}}} P_{\mathrm{UL},j}. \tag{3.12}$$

For each population, the probability space was examined using a series of grid searches. An initial search was conducted with a coarse grid and a wide range of values in each parameter to identify the best-fit location and determine if multiple values of any of the parameters were allowed. Refined grid searches were conducted with much narrower ranges in values with fine gridding to calculate parameter estimation error and covariance.

3.4.2 Canonical Pulsars

A fit restricted to only the canonical pulsars yields well determined values of the parameters in equation (3.6). We find significant correlation of the strength

of timing noise with ν, $\dot{\nu}$, and T. The estimated parameter values and their respective $\pm 2\sigma$ (95%) confidence intervals are presented in Table 3.1. The scaling of timing noise with observing span ($\gamma = 1.9 \pm 0.2$) is found to be intermediate to scalings expected from RW_1 and RW_2, for which we would expect $\gamma = 3/2$, and $\gamma = 5/2$, respectively.

Realization to realization variation associated with a stochastic process provides insufficient scatter account for the spread in timing noise that is characterized by the fit parameter $\delta = 1.6 \pm 0.1$. We simulated a large number of realizations of random walks RW_0, RW_1, and RW_2 and determined that realization to realization variation will induce a scatter in each process of $\delta = 0.23$, 0.46, and 0.60, respectively. We conclude that the inferred value of δ include additional contributions from the actual TN processes that are not captured by single idealized random walk models.

These findings generally agree with previous studies of timing noise in canonical pulsars that have concluded both that TN typically shows non-stationary behavior characterized by a red power spectrum and have established correlations between timing noise and other spin parameters. Cordes & Helfand (1980) found a correlation between the activity parameter A and period derivative $\dot{P} = -\dot{\nu}/\nu^2$ in 50 pulsars. Dewey & Cordes (1989) found a correlation between this activity parameter and P and $\dot{P}$ in observations of 40 canonical pulsars.

The scaling law models the timing noise over the entire range of observing spans and we find no evidence for band-limited timing noise. In Figure 3.3 we display the relative TN parameter ζ versus observing span. If timing noise was band-limited over current observing spans, the amount of timing noise would

plateau, and at large T, the fit would be poor and $\zeta \ll 1$. In addition we found consistency between fits to CP observations with $T < 10$ yr and $T > 10$ yr.

Analysis of a large on-going timing campaign of 366 pulsars at the Jodrell Bank Observatory with observing spans of 10 to 36 years is presented in Hobbs et al. (2010). They calculated a scaling relation between $\sigma_z(10\text{ yr})$ and ν and $\dot{\nu}$

$$\hat{\sigma}_z(10\text{ yr}) = 10^{-11.5}\nu^{-0.4}|\dot{\nu}_{-15}|^{0.8}, \tag{3.13}$$

where ν is measured in s^{-1} and $\dot{\nu}_{-15} = 10^{-15}$ s^{-2}. Our scaling relationship $\sigma_{\text{TN},2} \propto \nu^{-0.9\pm0.2}|\dot{\nu}|^{1.0\pm0.05}$ is inconsistent with this. In their analysis, σ_z includes contributions from additive white noise. If we conduct our analysis with $\sigma_{\mathscr{R},2}$ (i.e., include the white noise) instead of only to the red component $\sigma_{\text{TN},2}$, we find a more consistent scaling relationship of $\sigma_{\mathscr{R},2} \propto \nu^{-0.7\pm0.1}|\dot{\nu}|^{0.76\pm0.02}$.

3.4.3 Millisecond Pulsars

Only two MSPs have shown significant levels of timing noise: PSR B1937+21 (discussed in detail below), and PSR B1821−24. (Verbiest et al. 2009). The model for canonical pulsars over-predicts the level of timing noise observed in PSRs B1937+21 and B1821−24, as displayed in Figure 3.4. For both of these objects, the observed levels of TN are below the levels expected from the CP-only fit by a factor of one to two times δ.

The best fit to the MSP population, listed in Table 3.1, has larger fitting uncertainties because the few observations of TN and constraining upper limits are restricted to smaller ranges in ν, $\dot{\nu}$, and T. The fit is dominated by the many observations of timing noise in PSR B1937+21. For a few MSPs, observations

provide restrictive upper limits, but for many the expected levels of timing noise are not constraining at the levels predicted by the CP-only fit.

We also conducted a joint fit of the MSP and CP populations. In Figure 3.5 we plot the observed levels of TN versus the levels predicted from the joint fit. Visual inspection suggests that this fit provides a good model of the timing noise in the MSP population because the levels of timing noise observed are within the $\pm 1\delta$ band and the upper limits exceed levels predicted by the model.

The quality of fit is quantified by comparing observed and predicted levels of timing noise using a χ^2 statistic

$$\hat{\chi}^2 = \sum_{i}^{N_D} \frac{(\ln \sigma_{\mathrm{TN},2,i} - \ln \hat{\sigma}_{\mathrm{TN},2,i})^2}{\hat{\delta}^2}, \tag{3.14}$$

where only the N_D observations of detected timing noise are included and upper limits are excluded. If a model provides a good fit to the data, $\hat{\chi}^2$ follows a χ^2 distribution. For a fit to any population, the number of degrees of freedom is $N_{\mathrm{DOF}} = N_D - 5$ if the population included in the fit (because 5 parameters are included in the fit), and $N_{\mathrm{DOF}} = N_D$ if the population was not included in the fit. In Table 3.2, we list the values of $\hat{\chi}^2$ and corresponding probabilities P that each fit models the individual populations. This analysis confirms that the joint CP+MSP fit is a good model for both the CP and MSP populations.

The similarity of timing noise in MSPs to that in canonical pulsars is strengthened by examining the timing residuals of PSR B1937+21 in greater detail. In terms of statistical precision, PSR B1937+21 is the best MSP in which to study timing noise because it shows the largest levels of TN of any MSP.

In order to assess the strength and type of timing noise in PSR B1937+21, we investigate how $\sigma_{\mathrm{TN},2}$ scales with observing span by combining the results

of many timing programs presented in Appendix 3.7. In Figure 3.6, the rms residual timing noise is plotted versus observing span length for the various campaigns. In this figure we also show model curves for random walks RW_0, RW_1, and RW_2 scaled to an ensemble-average rms of 2 μs over an 8 year observing span, combined in quadrature with a 0.15 μs white noise component, which matches the levels of noise in the short time span observations displayed in Figure 3.6. Over short time spans, the residuals are dominated by white noise associated with instrumental sensitivity, pulse averaging effects, and diffractive interstellar scintillation (Cordes et al. 1990).

Inspection of this plot shows that the scaling of $\sigma_{\rm TN,2}$ with T is intermediate to RW_1 and RW_2 and therefore the scaling of TN with time is consistent with the observed scaling in the CP population ($\sigma_{\rm TN} \propto T^{2\pm0.2}$). This scaling is inconsistent with RW_1 or RW_2 random walks. We note however that the power law scaling is altered if the amplitude of the RW steps have a power-law distribution (for further discussion see Appendix C of Cordes & Downs 1985). The level of TN does not plateau over large T so we conclude that the timing noise shows no sign of being band-limited on the current observation time scales.

Observational bias has lead to detection of TN in only two MSPs. The expected levels of timing noise in the other MSPs are below current observing sensitivity. Timing noise is observed in PSR B1937+21 because it has a considerably larger $\dot{\nu}$ than other intensely studied MSPs.

TABLE 3.1
BEST FIT PARAMETERS

Fit	$\ln(C_2)$	α	β	γ	δ	$N_D(N_{\rm UL})$
CP	2.0 ± 0.4	-0.9 ± 0.2	1.00 ± 0.05	1.9 ± 0.2	1.6 ± 0.1	563 (470)
MSP	-20 ± 20	1 ± 2	2 ± 1	2.4 ± 0.6	1.2 ± 0.5	12 (147)
CP+MSP	1.6 ± 0.4	-1.4 ± 0.1	1.1 ± 0.1	2.0 ± 0.2	1.6 ± 0.1	575 (617)
MAG	3 ± 7	-1 ± 3	1.5 ± 0.6	3 ± 1	2.1 ± 0.7	15 (7)
CP+MAG	2.4 ± 0.5	-1.4 ± 0.2	1.13 ± 0.07	1.7 ± 0.2	1.7 ± 0.2	578 (477)
ALL	2.2 ± 0.4	-1.5 ± 0.1	1.2 ± 0.1	1.8 ± 0.1	1.7 ± 0.1	590 (624)

NOTE.—Best fit parameters and $\pm 2\sigma$ confidence limits for different populations of pulsars. N_D is the number of time series with detected timing noise used in the fit. $N_{\rm UL}$ is the number of time series with upper limits of timing noise used in the fit.

3.4.4 Magnetars

The probabilities that the models fit the observed TN in the magnetar population are displayed in Table 3.2. We find that the magnetar-only model provides a good fit to the observations (not surprisingly) but all other models underpredict the timing noise in the magnetar population. We conclude that magnetars show timing noise levels in excess of those found in the other populations of neutron stars.

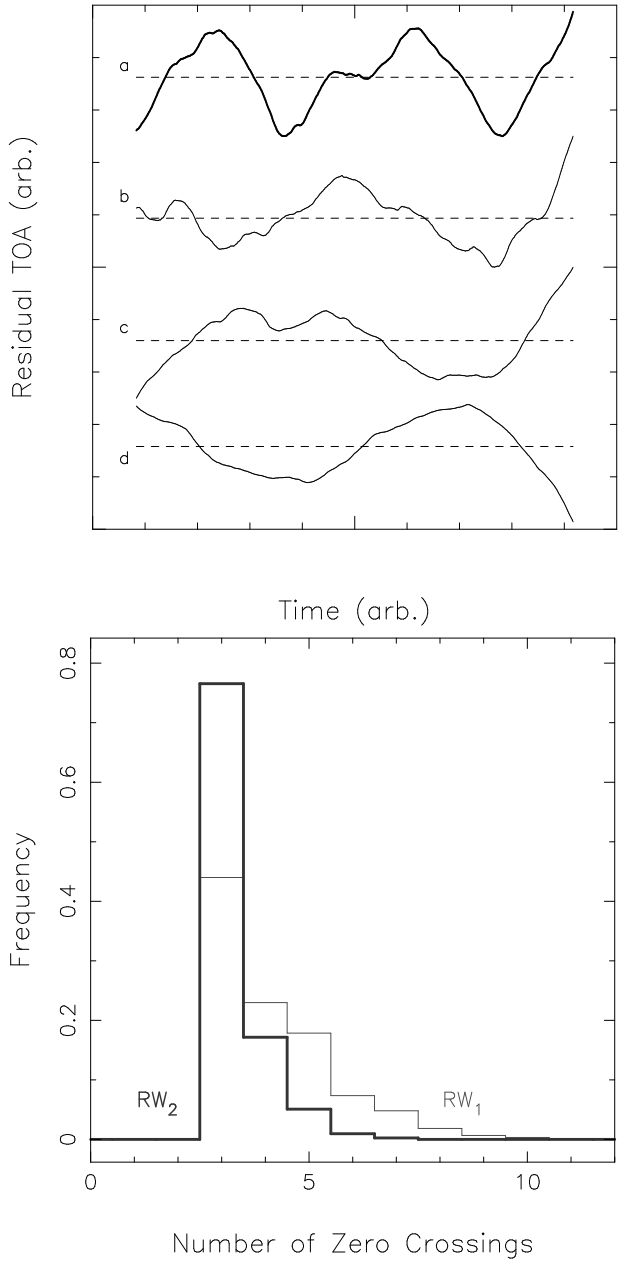

FIGURE 3.1.— *Upper panel:* Four realizations of RW_1 timing noise. Curve *a* has a large number of zero crossings and behavior that could be misidentified as quasi-periodic in spectral analysis. Curves *b* shows behavior that is irregular. Curves *c* and *d* show behavior in which the cubic term is dominant, with $\dddot{\nu} > 0$ in curve *c* and $\dddot{\nu} < 0$ in curve *d*. *Bottom panel:* Histogram of the number of zero crossings for processes RW_1 (thick lines) and RW_2 (thin lines) after including a quadratic fit. Both processes show realizations where the number of zero crossings is much larger than 3 that mimic quasiperiodicity in spectral analyses. The number of zero crossings for RW_0 is off the scale of the graph.

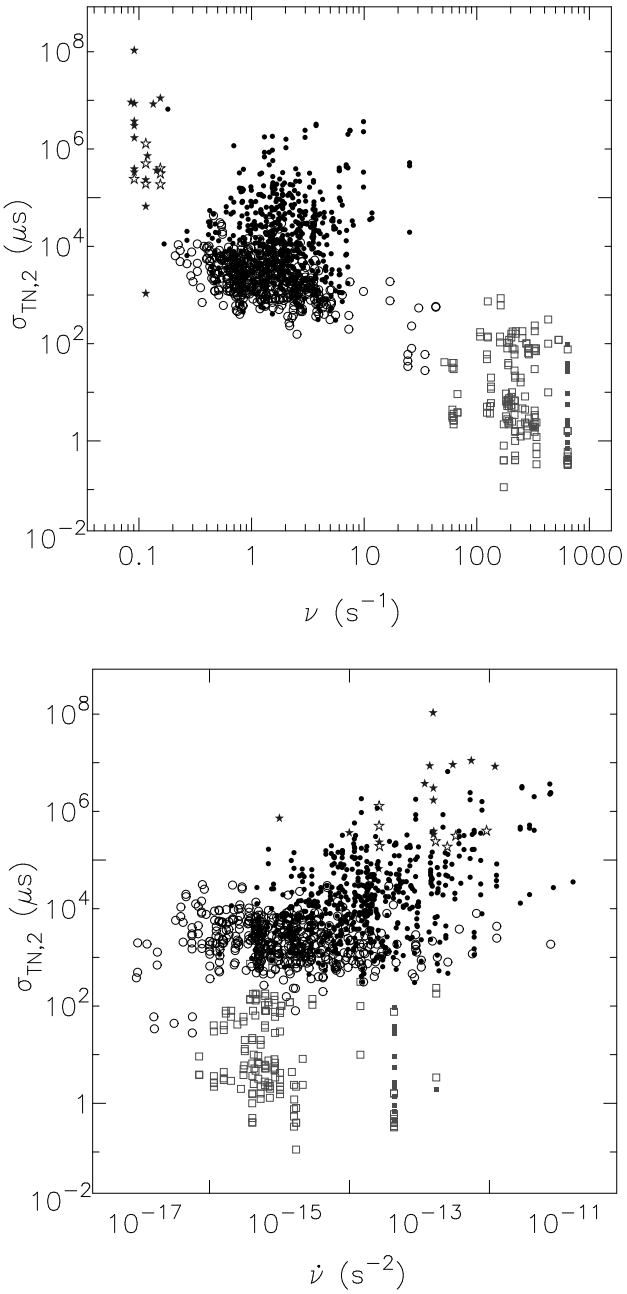

FIGURE 3.2.— Scatter plots showing the correlation between measured rms timing noise $\sigma_{TN,2}$ with spin frequency ν (top panel) and frequency derivative, $\dot{\nu}$ (bottom panel). Filled symbols represent detections of timing noise, and open symbols represent 2σ upper limits. Magnetars ($\nu < 1/6$ s^{-1}) are identified by stars, canonical pulsars (50 s^{-1} $< \nu <$ 1/6 s^{-1}) are identified by circles, and millisecond pulsars ($\nu > 20$ s^{-1}) are identified by squares. The observations encompass a wide range of observing spans 0.1 yr $< T <$ 30 yr.

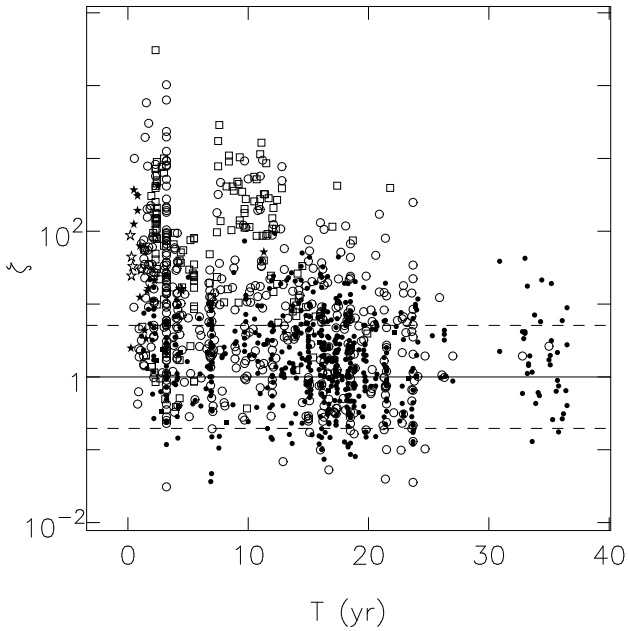

FIGURE 3.3.— Scatter plot showing the timing noise parameter ζ versus observing span T. We have used the timing noise model of the joint CP+MSP fit to calculate ζ. There is no evidence for a change in timing noise characteristics over longer observing spans. Filled symbols represent detections of timing noise, and open symbols represent 2σ upper limits. Magnetars ($\nu < 1/6$ s^{-1}) are identified by stars, canonical pulsars (50 s^{-1} $< \nu <$ 1/6 s^{-1}) are identified by circles, and millisecond pulsars ($\nu > 20$ s^{-1}) are identified by squares. The solid lines indicates $\zeta = 1$. The dashed lines are the $\pm 1\sigma$ variation of ζ, as inferred from value of δ inferred from the joint CP+MSP fit.

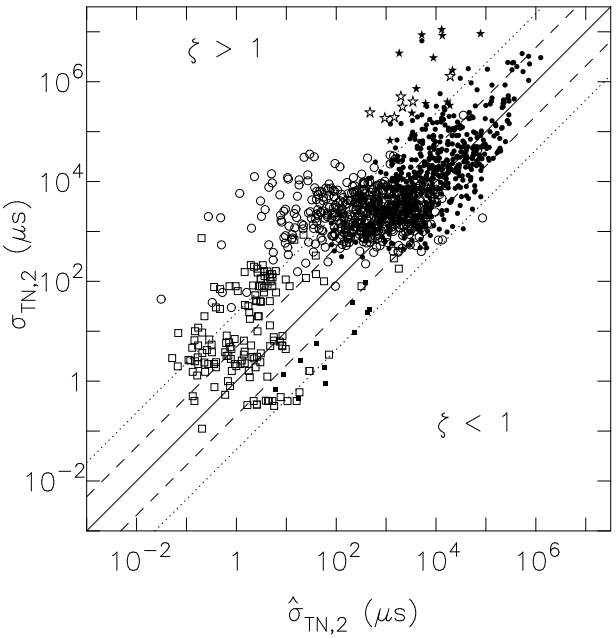

FIGURE 3.4.— Correlation between predicted rms TN $\hat{\sigma}_{\rm TN,2}$ and measured rms TN $\sigma_{\rm TN,2}$ for the CP-only model fit. Filled symbols represent detections of timing noise, and open symbols represent 2σ upper limits. Magnetars ($\nu <$ 1/6 s^{-1}) are identified by stars, canonical pulsars (50 s^{-1} $< \nu <$ 1/6 s^{-1}) are identified by circles, and millisecond pulsars (MSPs) are identified by squares. The solid line indicates complete correlation between observed and predicted levels of TN (i.e, $\hat{\sigma}_{\rm TN,2} = \sigma_{\rm TN,2}$). Points below this line are observations that have levels of TN less than expected by the model ($\zeta < 1$). The dashed lines show the expected width as estimated by the parameter $\hat{\delta}$, corresponding the $\pm 1\sigma$ (67%) width. The dotted lines show $\pm 2\sigma$ (95%) width. The CP-only model overestimates the strength of the timing noise in the MSPs and underestimates the levels of timing noise in the magnetars.

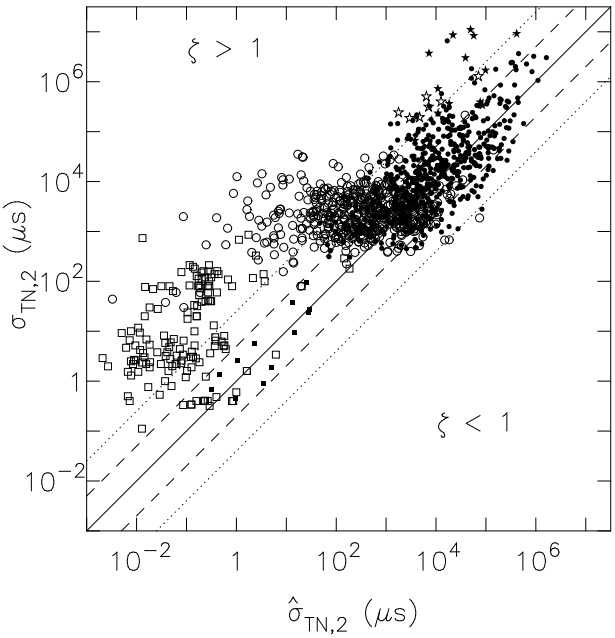

FIGURE 3.5.— Correlation between predicted rms TN $\hat{\sigma}_{TN,2}$ and measured rms TN $\sigma_{TN,2}$ for the CP+MSP Fit. Filled symbols represent detections of timing noise, and open symbols represent 2σ upper limits. Magnetars ($\nu < 1/6$ s^{-1}) are identified by stars, canonical pulsars (50 s^{-1} $< \nu <$ 1/6 s^{-1}) are identified by circles, and millisecond pulsars (MSPs) are identified by squares. The solid line indicates complete correlation between observed and predicted levels of TN (i.e, $\hat{\sigma}_{TN,2} = \sigma_{TN,2}$). Points below this line are observations that have levels of TN less than expected by the model ($\zeta < 1$). The dashed lines show the expected width as estimated by the parameter $\hat{\delta}$, corresponding the $\pm 1\sigma$ (67%) width. The dotted lines show $\pm 2\sigma$ (95%) width. The CP+MSP model models well the timing noise in MSP but underestimates the level of timing noise in the magnetars.

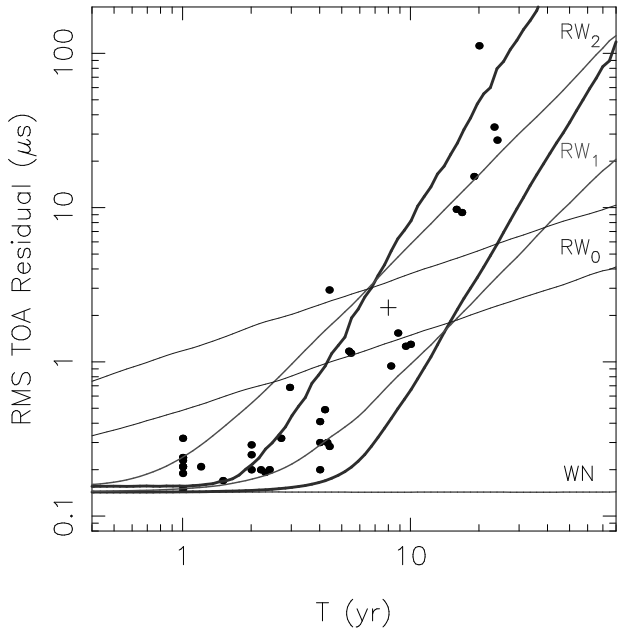

FIGURE 3.6.— The RMS residuals $\sigma_{\mathscr{R},2} = \sqrt{\sigma^2_{\rm TN,2} + \sigma^2_W}$ versus observing span T for PSR B1937+21 and simulated random walks. The large scatter in the observations at $T = 1$ yr is associated with variable levels of white noise across timing programs. The expected variation for random walks in phase ϕ ($\rm RW_0$, thinnest lines), frequency ν ($\rm RW_1$, medium thickness lines), and frequency derivative $\dot{\nu}$ ($\rm RW_2$, thickest lines) are also displayed. The 95% confidence limits (based on simulations of a large number of realizations) are shown for each process. The strength of the random walks are normalized to $\sigma_{\rm TN,2} = 2$ μs at $T = 8$ yr, which is indicated by the cross on the plot. To each curve, white noise with rms strength of $\sigma_W = 0.15$ μs is added. This level is denoted by the horizontal line marked WN.

TABLE 3.2
FIT COMPARISONS

		Model Fit											
		CP		MSP		MAG		CP+MSP		CP+MAG		ALL	
Family	N_D	χ^2	P	χ^2	P	χ^2	P	χ^2	P	χ^2	P	χ^2	P
CP	563	532	0.8	$10^{5.2}$	(10^{-20})	1996	(10^{-20})	538	0.72	477	0.99	493	0.98
MSP	12	37	$10^{-3.6}$	14	0.05	38	$10^{-3.8}$	3.8	0.8	3.7	0.99	7.0	0.4
MAG	15	176	(10^{-20})	$10^{4.1}$	(10^{-20})	10	0.4	98	(10^{-10})	63	$10^{-7.1}$	54	$10^{-7.5}$

NOTE.—Goodness of fit estimates for the canonical pulsars (CP), millisecond pulsars (MSP), and the magnetars (MAG) for models of sub-populations. For the model fits the N_D detected time series were used to calculate a χ^2 statistic to assess the goodness of fit for the subgroups of the pulsar population. Using this statistic, we calculated the probability P that a fit modeled the observed levels of timing noise. Probabilities in parentheses are upper limits.

3.4.5 Discussion: Timing Noise in Pulsar Populations

There are physical reasons to expect timing noise in MSPs and CPs to be consistent and follow a combined power law. Magnetic fields almost certainly play a role in the mechanism causing the timing noise, whether TN is associated with superfluid in the core or currents in the magnetosphere. Differences in the relationship between magnetic field strengths and the spin parameters ν and $\dot{\nu}$ between the populations would cause a break-down in the scaling relations.

Ultra-strong magnetic fields may cause the excess timing noise observed in magnetars. Unlike canonical pulsars and millisecond pulsars, magnetar radiation appears to be driven by the decay of magnetic fields, with some theories suggesting that the radiation is associated with crust cracking (Hurley et al. 2005) that may be enhanced compared to CPs. This cracking could drive rotational irregularities that contribute to the observed excess in timing noise.

Many radio pulsars have been discovered that have ν and $\dot{\nu}$ approaching those of the magnetars. Additional timing observations of high magnetic field radio pulsars are needed to properly assess the difference between radio pulsars and magnetars.

3.5 Implications for Gravitational Wave Detection

The presence of timing noise will significantly affect the sensitivity of a pulsar timing array to gravitational radiation. At present, most MSPs show residuals consistent with white noise. Based on the scaling laws derived in §3.4, we predict that TN will be identified in many objects when they are monitored over

longer time spans or observed with higher precision.

In Table 3.3, we list the MSPs that at present show the best timing stability. We show the expected rms timing noise over 2 yr, 5 yr, and 10 yr observing spans, based on the scaling relationships discussed in §3.4. We also show the $\pm 1\sigma$ variation that would be expected based on the observed spread of timing noise, and measured limits on the amount of TN over 10 yr observing spans. For these pulsars TN is likely present at the 10 ns to 100 ns level and will therefore affect the detection of other TOA perturbations with amplitudes at these levels, such as a gravitational wave background. In addition, we show predicted and measured levels of timing noise for PSR B1937+21. The large levels of timing noise imply this object will not contribute to the sensitivity of a PTA to GWs.

In the following we examine in detail the effect of the presence of timing noise on the properties of the PTA.

TABLE 3.3
EXPECTED LEVELS TIMING NOISE FOR PTA PULSARS

Object	ν (s^{-1})	$\dot{\nu}$ ($10^{-15}s^{-2}$)	T = 2 yr $\hat{\sigma}_{TN}$ (ns)	T = 2 yr $\hat{\sigma}_{TN,L}$ (ns)	T = 2 yr $\hat{\sigma}_{TN,U}$ (ns)	T = 5 yr $\hat{\sigma}_{TN}$ (ns)	T = 5 yr $\hat{\sigma}_{TN,L}$ (ns)	T = 5 yr $\hat{\sigma}_{TN,U}$ (ns)	T = 10 yr $\hat{\sigma}_{TN}$ (ns)	T = 10 yr $\hat{\sigma}_{TN,L}$ (ns)	T = 10 yr $\hat{\sigma}_{TN,U}$ (ns)	$\sigma_{TN,meas}$ (ns)
J0437−4715	174	-1.73	35	7	180	210	41	1100	830	160	4300	< 200
J1713+0747	219	-0.41	5	1	26	31	6	160	120	23	630	< 200
J1744−1134	245	-0.54	6	1	31	36	7	190	140	27	730	< 620
J1909−3744	339	-1.62	13	2	68	79	15	410	310	60	1600	< 170
B1937+21	623	-43.30	230	44	1200	1400	270	7200	5500	1100		1500

NOTE.—Estimated strength of timing noise for selected PTA pulsars and PSR B1937+21 over 2 yr, 5 yr, and 10 yr observing spans based on the best-fit model to the canonical pulsars and the millisecond pulsars (as defined in Table 3.1). For each pulsar we list the spin frequency ν and spin frequency derivative $\dot{\nu}$. For each observing span we show the expected values $\hat{\sigma}_{TN}$ and the 1σ upper and lower limits: $\hat{\sigma}_{TN,L}$ and $\hat{\sigma}_{TN,U}$, respectively. The limits are formally the quadrature sum of the parameter that quantifies the scatter of the distribution $\hat{\delta}$ and the estimation error associated with the model, but are dominated by $\hat{\delta}$. We also present the measured timing noise $\sigma_{TN,meas}$ (or upper limits) over $\approx$ 10 yr observing span.

3.5.1 Timing Noise and PTA Sensitivity

To estimate the level of timing stability required to detect GWs, we calculate the GW detection signal to noise ratio (SNR) using a particular detection scheme. We note the resulting conclusions are general and are relevant to all detection methods, including methods that are implemented using either frequentist or Bayesian approaches (Jenet et al. 2005; van Haasteren et al. 2009).

Best Case: Gravitational Waves and Timing Noise Only

In order to assess the best possible case, we first consider TOAs that contain *only* perturbations associated with gravitational waves and timing noise. For each pulsar k at observation epoch i, the time of arrival perturbation (before any fit) s_{ki} is altered by the correlated component of the GWB passing through the solar neighborhood e_{ki}, the uncorrelated component of the GWB outside of the solar neighborhood p_{ki}, and uncorrelated TN r_{ki}:

$$s_{ki} = e_{ki} + p_{ki} + r_{ki}. \tag{3.15}$$

The perturbations e and p have the same rms strength. We define the SNR in the time series to be the ratio of the rms amplitudes (after a second order fit) of the correlated portion of the signal (i.e., e_{ki}) to the uncorrelated portion of the signal ($p_{ki} + r_{ki}$). Thus in the residuals from a single pulsar the SNR is at most unity and is smaller if TN is present.

We now consider one approach to GW detection that involves forming a coherent sum (R. Shannon & J. Cordes, in preparation) of the residuals for $N_{\rm PTA}$ pulsars, which increases the SNR. The best case configuration is when all the

pulsars are located in a small patch of the sky, but at different distances away from the observer. In this case e_{ki} is completely correlated between pulsars and p_{ki} and e_{ki} are uncorrelated. As a result, e_{ki} is amplified relative to p_{ki} and r_{ki} by a factor $\sqrt{N_{\rm PTA}}$. The combined SNR in a single data block of span T of observations from $N_{\rm PTA}$ pulsars is

$$\left(\frac{S}{N}\right)_{T,1} = \sqrt{\frac{N_{\rm PTA}\sigma^2_{\rm GW,2}(T)}{\sigma^2_{\rm TN,2}(T) + \sigma^2_{\rm GW,2}(T)}}, \tag{3.16}$$

where the rms strengths of the GWB and the TN are characterized by $\sigma_{\rm GW,2}(T)$ and $\sigma_{\rm TN,2}(T)$, respectively.

A test statistic based on the coherent sum has an SNR of

$$\left(\frac{S}{N}\right)_{{\rm TS},M} = \sqrt{\frac{MN_{\rm PTA}}{1 + \sigma^2_{\rm TN,2}(T_M)/\sigma^2_{\rm GW,2}(T_M)}}, \tag{3.17}$$

where we have assumed the data set can be subdivided and M independent estimates of the TS can be calculated (for example by using data blocks of length $T_M = T/M$), resulting in an enhancement of the SNR by a factor of $\sqrt{M}$. We note that there are alternative ways to subdivide the time series. Jenet et al. (2006) decompose the residuals using a set of orthonormal polynomials and calculate a TS using each polynomial, while Verbiest et al. (2009) conduct an analysis in the Fourier transform domain. In all cases the optimal value of M is limited by other sources of noise (like white noise), which we discuss further in §3.5.1.

The scaling relationship of equation (3.17) is used to establish the properties of a PTA sufficient to detect the GWB. To detect the gravitational wave background with a strength $\sigma_{\rm GW,2}(T)$ with ${\rm SNR}_{{\rm TS},M} > S_{\rm min}$ requires that the TN in an individual pulsar satisfy

$$\sigma_{\rm TN,2}(T_M) < \sigma_{\rm GW,2}(T_M)\sqrt{\frac{MN_{\rm PTA}}{S^2_{\rm min}} - 1}. \tag{3.18}$$

The number of pulsars required to detect a GWB of strength $\sigma_{\rm GW,2}(T)$ with an SNR greater than $S_{\rm min}$ with TN at a level $\sigma_{\rm TN,2}(T)$ is

$$N_{\rm PTA} > \frac{S_{\rm min}^2}{M}\left[1+\left(\frac{\sigma_{\rm TN,2}(T_M)}{\sigma_{\rm GW,2}(T_M)}\right)^2\right]. \quad (3.19)$$

Here we make two preliminary estimates of the requirements for GW detection using equations (3.18) and (3.19). In §3.5.2 we give a more detailed assessment that uses the model of TN in the pulsar population presented in §3.4.

As a first example, we estimate pulsar stability requirements to detect the expected stochastic background of merging massive black hole (MBH) binaries. Stochastic GWBs are typically characterized by their expected strain response $h_c(f)$ and not $\sigma_{\rm GW,2}$. In Appendix 3.9 we show how to calculate $\sigma_{\rm GW,2}$ from $h_c(f)$. The MBH background is presently considered the strongest plausible GWB, and is expected to induce a strain response of $h_c(f) = A_0(f/1\ {\rm yr}^{-1})^{-2/3}$, where the value of A_0 is estimated to be between 10^{-16} and 10^{-15} (Jaffe & Backer 2003; Sesana & Vecchio 2010). Over a $T = 5$ yr observing span, the MBH GWB will contribute $\sigma_{\rm GW,2} = 19$ ns $(A_0/10^{-15})$ to the times of arrival, as indicated in Table 3.4, which presents results for this section and §3.5.2. To achieve a signal to noise ratio in the detection statistic of $S_{\rm min} = 5$ for a PTA comprising $N_{\rm PTA} = 40$ pulsars using $M = 1$ observation blocks, timing noise must be limited to $\sigma_{\rm TN,2}(T = 5\ {\rm yr}) < (\sqrt{3/5})\sigma_{\rm GW,2}(T = 5\ {\rm yr}) \approx 15$ ns.

We can also estimate the number of pulsars required to detect a GWB if TN levels are equal to the amplitude $\sigma_{\rm TN,2} \approx 20$ ns over 5 years exhibited by the pulsars in Table 3.3. A PTA comprising $N_{\rm PTA} = 70$ pulsars would yield an SNR of $S_{\rm min} = 5$, assuming $M = 1$, and a GWB with the same properties as in the previous example. However, a number of MSPs are expected to have TN at levels below the scaling law and therefore the required number of pulsars may

be somewhat lower, which is described in §3.5.2

Effect of White Noise on the Number of Independent Sub-blocks

In general, the number of subdivisions M that maximizes the SNR of the TS depends on the amplitude of other noise contributions to the residuals, in particular white noise, which is guaranteed to be present in pulsar timing observations. We define a time scale T_M over which the expected GW signal exceeds the white noise levels $\sigma_{W,\mathrm{TS}}$ in the coherent time series by the same threshold as the TN, i.e., $\sigma_{\mathrm{GW},2}(T_M) = S_{\min}\sigma_{W,\mathrm{TS}}(T_M)$. For a total observing span of length T there are $M \approx T/T_{\mathrm{M}}$ independent data blocks if $T > T_M$; if not, there is $M = 1$ data block.

The random noise in the TS associated with the WN is given by

$$\sigma_{W,\mathrm{TS}}(T) = \frac{\sigma_n}{\sqrt{N_{\mathrm{PTA}} N_{\mathrm{obs}}(T)}}, \tag{3.20}$$

where σ_n is the level of white noise in a single observation and $N_{\mathrm{obs}}(T) = R_{\mathrm{obs}}T$ is the number of observation epochs in the interval of length T, and is characterized by an observation rate R_{obs} (or equivalently an observing cadence of R_{obs}^{-1}). For a background with $\sigma_{\mathrm{GW},2}(T) = \sigma_g T^{5/3}$, the minimum time is

$$T_M = \left(\frac{\sigma_n}{\sigma_g}\frac{S_{\min}}{\sqrt{N_{\mathrm{PTA}} R_{\mathrm{obs}}}}\right)^{6/13}. \tag{3.21}$$

For an array of 40 pulsars, with $N_{\mathrm{obs}}(T) = 10\ T_{\mathrm{yr}}$ (i.e., 10 observations per year), $\sigma_n = 100$ ns rms error per residual, and a GWB with strain spectrum $h_c(f) = 10^{-15}(f/1\ \mathrm{yr}^{-1})^{-2/3}$, the minimum block size is $T_{\min} \approx 2$ yr for $N_{\mathrm{PTA}} = 40$ to 100. The minimum block length $T_{\min}$ is approximately the same for both values of N_{PTA} because of the weak dependence of M on N_{PTA}, $M \propto N_{\mathrm{PTA}}^{3/13}$, for the assumed GWB background.

3.5.2 The Fraction of MSPs Suitable for PTAs

Using the stability requirements defined in equation (3.18), the fraction of MSPs suitable for inclusion in a PTA $f_{\rm MSP}$ can be evaluated. This fraction is equivalent to the probability that a pulsar within the population has rms timing noise less than some threshold amount σ_t over an observing span of length T. Based on our TN model, this probability is

$$P(\ln\sigma < \ln\sigma_t|T) = \int_{-\infty}^{\ln\sigma_t} d\ln\sigma \int d\boldsymbol{M}\rho_{\boldsymbol{M}}(\boldsymbol{M}) \times \int d\nu d\dot{\nu}\rho_{\nu,\dot{\nu}}(\nu,\dot{\nu})\rho_{\ln\sigma}(\ln\sigma|\boldsymbol{M},\nu,\dot{\nu},T), \quad (3.22)$$

where $\rho_{\boldsymbol{M}}(\boldsymbol{M})$ is the PDF of the parameter distribution, $\rho_{\nu,\dot{\nu}}$ is the PDF of the pulsar distribution in ν and $\dot{\nu}$, and $\rho_{\ln\sigma}$ is the PDF of the level of timing noise, given the model parameters.

In Appendix 3.8, we present methods for evaluating equation (3.22). The sensitivities of PTAs comprising $N_p = 40$ and 100 pulsars with a variety of observing spans T are investigated with the same conditions as in §3.5.1. We have modeled timing noise $\sigma_{\rm TN,2}$ using the joint CP and MSP model as presented in Table 3.1 and equation (3.6).

In Table 3.4 we show the fraction of pulsars suitable for inclusion in these PTAs. The fraction of suitable pulsars is smaller at $T = 5$ yr than $T = 2$ yr because the level of expected timing noise has increased relative to the GW signal but the number of sub-blocks M has not changed. To produce a PTA comprising $N_{\rm PTA}$ pulsars requires the investigation of a total sample of MSPs, $N_{\rm MSP} = N_{\rm PTA}/f_{\rm MSP}$ pulsars. To calculate M we have again assumed that the pulsars are observed 10 times per year with an rms precision on a single TOA of 100 ns. For a PTA comprising 40 to 100 high quality MSPs and data spans of 5

TABLE 3.4
TIMING NOISE CONSTRAINTS ON MSPS SUITABLE FOR A PTA

		$N_{\rm PTA} = 40$			$N_{\rm PTA} = 100$		
T (yr)	$\sigma_{\rm GW,2}$ (ns)	M	$\sigma_{{\rm TN},2,t}$ (ns)	$f_{\rm MSP}$ (%)	M	$\sigma_{{\rm TN},2,t}$ (ns)	$f_{\rm MSP}$ (%)
2	4	1	3	30 ± 7	1	7	46 ± 8
5	19	1	14	25 ± 6	1	32	40 ± 7
10	59	2	28	37 ± 7	3	31	56 ± 7
20	187	5	34	50 ± 7	6	45	64 ± 7
5	19	2	9	41 ± 7	2	15	53 ± 7
5	19	4	4	55 ± 8	4	7	65 ± 7

NOTE.—Fraction of pulsars suitable for inclusion in a PTA, $f_{\rm MSP}$, for arrays comprising $N_{\rm PTA} = 40$ and 100 pulsars, over observing spans ranging from $T = 2$ yr to $T = 20$ yr. We have assumed a background with characteristic strain spectrum of $h_c(f) = 10^{-15}(f/1\ {\rm yr}^{-1})^{-2/3}$. We have also assumed a detection signal to noise ratio of $S_{\rm min} = 5$, using equation (3.18), with M independent data blocks,as described in the main text. Also listed are the quadratic-corrected rms contribution of the gravitational wave background $\sigma_{\rm GW,2}(T)$ for the total observing span T and the threshold TN level $\sigma_{{\rm TN},2,t}(T_M)$ for the sub-block length $T_M = T/M$.

to 10 years, our analysis indicates that a total MSP sample that is two to three times larger than $N_{\rm PTA}$ needs to be investigated in order to identify high quality objects.

3.5.3 Mitigating Timing Noise

It has been previously noted that applying a low-pass spectral filter to the residual TOA time series can improve the signal-to-noise ratio in a PTA (Jenet et al.

2005). The presence and diversity of red noise in the MSPs necessitates filtering that is tailored to the properties of each individual pulsar. Schematic power spectra for RW_0, RW_1, and RW_2 random walks and the gravitational wave background are displayed in Figure 3.7. For systems in which RW_2 is the dominant form of TN high-pass filtering (i.e., removing the lowest frequency components of the signal) can be used to mitigate the contribution of TN to the TOAs. It is not possible to develop a filter that mitigates RW_1 timing noise without also removing the gravitational wave signal because they have very similar spectral shapes.

There is evidence that pulse profile information can be used to correct residual time series. Lyne et al. (2010) identify a link between changes in pulse shape (probably connected to mode changing) and changes in $\dot{\nu}$, and demonstrate that some timing noise can be corrected by identifying the time of the mode changes and the estimated values of $\dot{\nu}$. Even if all TN was associated with mode changing, incomplete sampling results in an uncertainty in the precise time that the pulsar changes modes and hence spin down rates. This uncertainty is manifested as timing noise in the corrected time series, and will have an amplitude proportional to the uncorrected level of timing noise. As noted in §3.3, in half of the cases presented in Lyne et al. (2010), the correlation was found after a fit for $\ddot{\nu}$ that removes non-stationary TN that could not be corrected.

3.5.4 Future Prospects

A large number of pulsars need to be studied because timing noise will limit the utility of many objects and MSP timing stability cannot be fully constrained

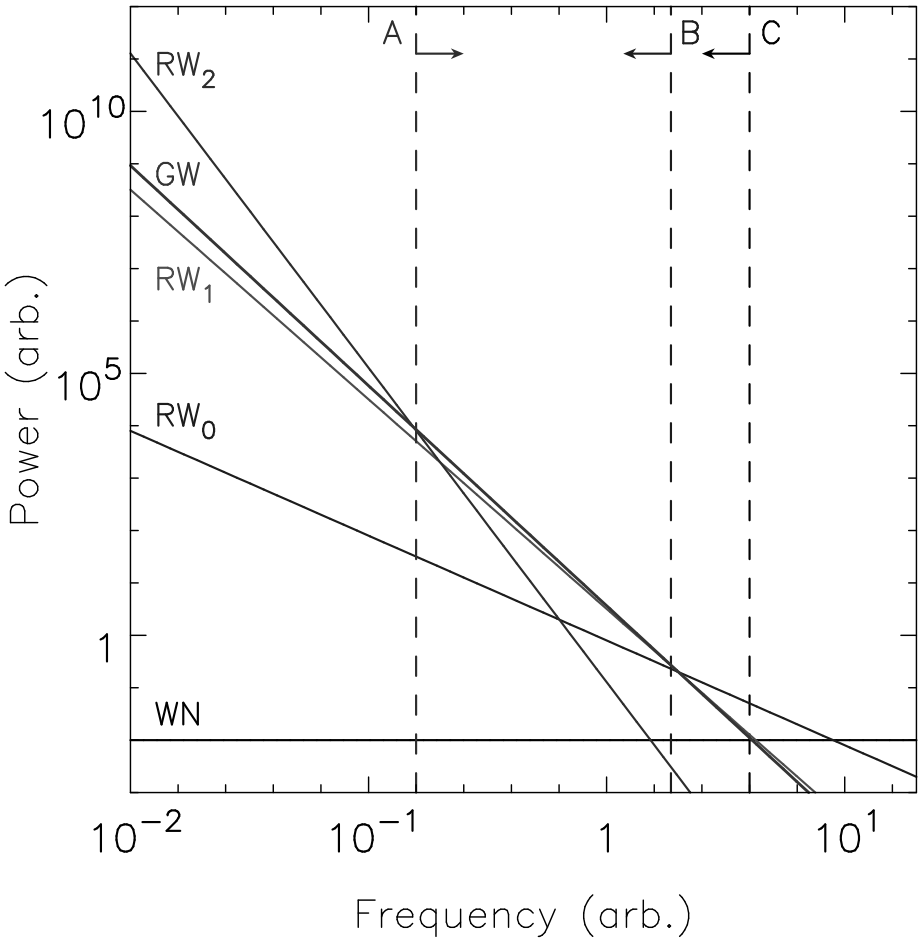

FIGURE 3.7.— Schematic power spectra for stochastic processes that contribute to pulsar timing residuals. The dashed lines indicate fluctuation frequencies at which the TN exceeds the GWB for various processes and the arrows associated with these lines identify region in which the GWB signal is accessible. Vertical dashed line *A* identifies the region in which the spin frequency noise (RW_2) exceeds the gravitational wave background. Vertical dashed line *B* identifies the region in which phase noise (RW_0) exceeds the gravitational wave background. Vertical dashed line *C* identifies the region in which white noise (WN) exceeds the gravitational wave background.

with spin parameters ν and $\dot{\nu}$. As a result, if $N_{\rm PTA}$ pulsars are required for a significant detection of the GWB, a much larger number of pulsars ($N_{\rm MSP} = N_{\rm PTA}/f_{\rm MSP}$, as outlined in §3.5.2) need to be discovered and characterized. To constrain the timing stability it is necessary to conduct timing observations with sufficient precision to detect the presence of TN at the threshold level, as set by equation (3.18). For realistic PTA configurations and a reasonable detection SNR, the required stability level will be at most a factor of a few greater than the anticipated strength of the gravitational wave background. An object is suitable for inclusion into the PTA if timing noise is not detected at this level.

Pulsar timing arrays can be expanded by both incorporating presently known objects with good intrinsic stability that are currently excluded due to low flux and discovering new MSPs with suitable timing stability.

Additional MSPs suitable for incorporation into a PTA are continually being discovered, with ongoing surveys with the Arecibo, Green Bank, and Parkes Telescopes; targeted searches for radio pulsar companions to *Fermi* gamma-ray point sources; and in the near future with the LOFAR Array (van Leeuwen & Stappers 2010). While occasionally bright MSPs have been discovered (Jacoby et al. 2003), selection effects generally bias new discoveries toward fainter pulsars, and thus suitable objects require longer observations with more sensitive telescopes to mitigate white radiometer noise.

The requirements for finding and timing ultra faint MSPs highlight the need to use high-gain telescopes such as the Arecibo telescope and the proposed Square Kilometre Array (SKA). The SKA is estimated to find up to ≈ 6000 MSPs (Smits et al. 2009). If we conservatively estimate that 10% of the MSPs are suitable, there will be ≈ 600 objects available for inclusion in a PTA. The very best

of these could comprise a PTA sufficient to *detect* the GWB while a much larger PTA could be used to study in detail the GWB and detect and examine individual GW sources. Large interferometers such as the SKA will be particularly important for improving throughput of timing campaigns because they can be divided into sub-arrays that can observe multiple objects simultaneously.

3.6 Conclusions

We have developed scaling relationships for timing noise in millisecond pulsars, canonical pulsars, and magnetars. We find that timing noise in MSPs is consistent with that observed in canonical pulsars. The timing behavior of the millisecond pulsar B1937+21 supports universality of TN in CPs and MSPs. Latent timing noise is predicted to be present in other MSPs with similar properties (but smaller) magnitudes to that in the CPs and PSR B1937+21, in accord with their smaller spin down rates. This timing noise may be measurable in many pulsars when either longer data sets or higher precision arrival times are obtained. Timing noise in magnetars is greater than that expected from extrapolation from the canonical pulsars.

3.6.1 Acknowledgements

We thank George Hobbs for providing a preprint of Hobbs et al. (2010) in advance of publication, and the referee for comments that improved the clarity of the text. This work made use of NASA's ADS System and the ATNF Pulsar Catalogue (Manchester et al. 2005). This work was supported by the NSF through

grant AST-0807151 and by NAIC, which is operated by Cornell University under a cooperative agreement with the NSF.

3.7 Appendix: Reduction Procedure and Timing Campaigns Used

We have synthesized the results of many timing observations to construct the scaling relationships for timing noise (TN) in canonical pulsars (CPs), millisecond pulsars (MSPs), and magnetars (MAGs), as described in §3.4; and to conduct the case study of the MSP B1937+21 (as described in §3.4.3). In Table 3.5 we summarize the timing campaigns used in the analyses, the average length of data span contained in the campaign, and the number and type of objects analyzed.

In the following sections we outline the procedure used to properly combine the results from all of the campaigns. In §3.7.1 we describe how the root mean square (rms) timing noise $\sigma_{\rm TN,2}$ is calculated from other TN diagnostics. In §3.7.2 we justify the threshold used for detecting the presence of red noise in timing data. In §3.7.3, we justify the exclusion of some timing observations from this study. In §3.7.4, we describe the observations used that form the basis of our study of PSR B1937+21.

3.7.1 Calculating $\sigma_{\rm TN,2}$

We use the rms timing noise after a second order polynomial fit $\sigma_{\rm TN,2}(T)$ as the primary observable property of TN, as justified in §3.3.

In Table 3.5, for each reference we identify the type of observations reported. While some timing campaigns report $\sigma_{\rm TN,2}$ (coded TN in Table 3.5), others report different but related measurements of TN. There are two notable conversions that are occasionally needed. Some campaigns report only the total rms residuals and the white noise level, and the red timing noise must be extracted from these quantities. For other campaigns, the timing noise is modeled in a functional form.

Calculating $\sigma_{\rm TN,2}$ from the total timing noise and the white noise (Code TW *in Table 3.5):* Many timing campaigns report the total rms residuals and the levels of white noise in the observations. In this case, the amount of timing noise is the quadrature difference between the rms residuals $\sigma_{\mathscr{R},2}$ and the white noise in the time series:

$$\sigma^2_{\rm TN,2} = \sigma^2_{\mathscr{R},2} - \sigma^2_W. \tag{3.23}$$

In these observations the the level of white noise σ_W reported comes from one of two sources: either the rms of residuals after the TN has been analytically modeled; or an estimate from the white noise in a single TOA.

Including modeled timing noise, (Codes S, STW, or H in Table 3.5): In some cases the fit includes terms $\mathcal{M}_{\rm TN}(t)$ that model the timing noise. The model is typically a series of polynomials or sinusoids. It is typically included to provide an estimate of $\ddot{\nu}$ (in which case $\mathcal{M}(t) = \ddot{\nu}(t - T_e)^3/6$, where T_e is the epoch at which the spin properties are defined) or to improve the determination of modeled param-

eters of interest such as astrometric terms. In these cases $\sigma_{\rm TN,2}$ is approximated as the quadrature sum of the rms of $\mathcal{M}_{\rm TN}(t)$ and the TN contained in the post-fit residuals:

$$\sigma^2_{\rm TN,2} = \sigma^2_{\rm TN,\mathcal{M}}(T) + \frac{1}{T}\int_{t_0}^{t_1} \mathcal{M}^2_{\rm TN}(t)dt, \tag{3.24}$$

where t_0 and $t_1 = t_0 + T$ are the starting and ending epochs of the observations.

For observations labeled *S*, polynomials have been used to model the timing noise. For observations labeled *H*, harmonically related sinusoids have been used to model the timing noise. For observations labeled *STW*, a fit including $\ddot{\nu}$ was completed that partially whitens the residuals. In addition to $\ddot{\nu}$, the total rms timing noise $\sigma_{\rm TOT,\mathcal{M}}$ and the whitened rms timing noise σ_W were reported. In this case, the rms timing noise is $\sigma^2_{\rm TN,\mathcal{M}}(T) = \sigma^2_{\rm TOT,\mathcal{M}} - \sigma^2_W$.

3.7.2 The Detection Threshold for $\sigma_{\rm TN,2}$

To determine if timing noise is detected in a time series, we conservatively require that the rms timing noise exceed twice the white noise floor (i.e., $\sigma_{\rm TN,2} > 2\sigma_W$), because we suspect that in many timing programs the residuals were not examined at sufficient detail to rule out TN below this level. If the measured TN in a time series does not meet the threshold we declare the time series to be an upper limit with a value of $2\sigma_W$. This is much larger than the formal detection threshold, $\sigma_{\rm TN,2} > \sigma_W/\sqrt{N_{\rm DOF}}$, where $N_{\rm DOF}$ is the number of degrees of freedom in the residual TOAs.

TABLE 3.5
PREVIOUS TIMING CAMPAIGNS

Reference	Objects	$T_{\rm typ}$ (yr)	Observation
Canonical Pulsars (CPs)			
Helfand et al. (1980)	37	4	TW
Cordes & Downs (1985)	27	10	TN
D'Alessandro et al. (1993)	45	4	TW
Arzoumanian et al. (1994)	96	3	TW
Foster et al. (1994)	1	6	T*
D'Alessandro et al. (1995)	45	7	TN
Hobbs et al. (2004)	346, 27 MSP	20	TSW
Zou et al. (2004)	2	1	T
Champion et al. (2005)	15, 1 MSP	2	T
Kaplan & van Kerkwijk (2005)	1	11	T
Chukwude (2007)	27	10	S
McLaughlin et al. (2009)	6 RRAT	6	T
Hobbs et al. (2010)	346, 30 MSP	25	TSW
Millisecond Pulsars (MSPs)			
Kaspi et al. (1994)	2	2	S
Bell et al. (1997)	4	3	T
Lommen (2002)	4, 2 CP	10	S
Hotan et al. (2006)	15	2	S
Ord et al. (2006)	1	4	S
Demorest (2007)	15	2	T
Verbiest et al. (2008)	1	10	T
Hobbs et al. (2009b)	20	4	T
Lazaridis et al. (2009)	1	14	T
Verbiest (2009)	19	10	H
Magnetars (MAGs)			
Woods et al. (2000)	1	1	S
Kaspi et al. (2001)	4	1	S
Gavriil & Kaspi (2002)	5	1	S
Gotthelf et al. (2002)	1	2	S
Camilo et al. (2007)	1	1	S
den Hartog et al. (2008)	3	1	S
Dib et al. (2008)	1	1	S

NOTE.—Timing campaigns used in this analysis. We list campaigns, class of objects studied, typical observing length $T_{\rm typ}$, and reported observable, as described in main text.

3.7.3 Excluded Observations

We excluded observations of globular cluster pulsars which show acceleration (and significant $\ddot{\nu}$) associated with these dense environments. We have also excluded some additional reports of timing noise from this analysis:

PSR J1012+5307. Lange et al. (2001) report a non-zero $\ddot{\nu}$ that they attribute to TN. However a more recent analysis by Lazaridis et al. (2009) that includes the previous data shows no evidence for $\ddot{\nu} \neq 0$. We therefore omit the measurement of Lange et al. (2001).

PSR J1713+0747. Splaver (2004) report a non-zero $\ddot{\nu}$ that they attribute to TN. However, a more recent analysis by Verbiest et al. (2009) shows no evidence for $\ddot{\nu} \neq 0$. We therefore exclude the measurement of Splaver (2004).

PSR B1937+21. We have also excluded a measurement of TN for PSR B1937+21 from this analysis, which is discussed in the next section.

3.7.4 PSR B1937+21

The observations used for the analysis of the scaling of the rms TN for PSR B1937+21 (discussed in §3.4.3) are presented in Table 3.6. We report the observing span of the observations the rms residuals $\sigma_{\mathscr{R},2}$, and, when available, the number of TOAs used in the analysis. In order to increase the number of independent observations at short observing spans, the publicly available residual TOAs from Kaspi et al. (1994) were subdivided into shorter observing spans of 1, 2, and 4 years. We note that many of the observations contain contemporaneous or common observations, and therefore many of the data points are not formally independent.

All the campaigns included have been corrected for dispersion measure (DM) variations, determined by measuring the arrival time difference contemporaneously in two frequency bands. The DM correction is more accurate in recent campaigns because of improved observation procedures. In early campaigns, the measurements at two frequencies were performed many days apart and changes in interstellar propagation over those times likely increase TOA uncertainty. In more recent campaigns, two-frequency observations often occur consecutively during the same observing session or simultaneously with dual-frequency receivers.

We have excluded the 12.5 yr measurements of timing noise in PSR B1937+21 reported in Verbiest et al. (2009) because the time series contained a long gap between observations with two different instruments. An arbitrary time offset between the two instruments (i.e., a jump) was included the fit. This jump removes a significant amount of TN from the residual time series.

3.8 Appendix: Estimating the fraction of suitable pulsars

In this section, we describe the methods for calculating the fraction of pulsars suitable for inclusion in the pulsar timing array. The fraction of pulsars that show TN below a threshold RMS $\sigma_{\mathrm{TN},t}$ is equivalent to the probability of finding a pulsar within the population with those properties,

$$P(\ln\sigma < \ln\sigma_t|T) = \int_{-\infty}^{\ln\sigma_t} d\ln\sigma \int d\boldsymbol{M}\rho_{\boldsymbol{M}}(\boldsymbol{M}) \int d\nu d\dot{\nu}\rho_{\nu,\dot{\nu}}(\nu,\dot{\nu})\rho_{\ln\sigma}(\ln\sigma|\boldsymbol{M},\nu,\dot{\nu},T) \quad (3.25)$$

where $\rho_{\boldsymbol{M}}$ is the probability density for observing fit parameters, where $\boldsymbol{M} = (C_1, \alpha, \beta, \gamma, \delta)$, as in equation (3.8); $\rho_{\nu,\dot{\nu}}$ is the probability density for the pulsar

TABLE 3.6
TIMING NOISE IN PSR B1937+21

T (yr)	$\sigma_{\rm RMS}$ (μs)	$N_{\rm TOA}$	Ref.
1.0	0.15	···	1
1.0	0.23	22	2
1.0	0.24	19	2
1.0	0.32	16	2
1.0	0.24	16	2
1.0	0.21	18	2
1.0	0.21	14	2
1.0	0.19	23	2
1.2	0.21	13	2
1.5	0.17	···	3
2.0	0.25	47	2
2.0	0.29	38	2
2.0	0.20	38	2
2.2	0.20	38	2
2.3	0.19	···	4
2.4	0.20	231	5
2.7	0.32	85	6
4.0	0.20	39	7
4.0	0.30	···	8
4.0	0.41	85	2
4.2	0.49	80	2
4.4	0.27	168	9
8.2	0.94	440	2
10.0	1.3	···	10
16.8	9.3	387	10
20.0	112.0	400	11
23.3	24.2	588	12
24.0	27.4	···	13

NOTE.— Root mean square times of arrival for PSR B1937+21 for different observing programs. Column T shows the observing span, column $\sigma_{\rm RMS}$ shows the total rms residuals, column $N_{\rm TOA}$ shows the number of times of arrival included in the analysis, and column Ref. shows the numbered references. The references are: (1) Manchester (2008); (2) Kaspi et al. (1994); (3) Manchester (2009); (4) You et al. (2007); (5) Hotan et al. (2006); (6) Demorest (2007); (7) Demorest (2008); (8) Thereau (2008); (9) Verbiest (2009); (10) Lommen (2002); (11) Hobbs et al. (2004); (12) Verbiest et al. (2009); (13) Janssen (2008).

spin distribution; and $\rho_{\ln\sigma}$ is the PDF for observing a value of TN, assuming fixed values for the fit parameters.

We will assume that the level of TN σ is log-normally distributed about the expected value:

$$\rho_{\ln\sigma}(\ln\sigma|C_1,\alpha,\beta,\gamma,\delta,\nu,\dot{\nu},T) = \frac{1}{\sqrt{2\pi\delta^2}}\exp\left[-\frac{(\ln\sigma/\hat{\sigma})^2}{2\delta^2}\right]. \quad (3.26)$$

This is consistent with the analysis of §3.4, and the large observed spread in TN for pulsars with similar spin parameters ν and $\dot{\nu}$.

To model the $\rho_{\nu,\dot{\nu}}$, we will use the observed distribution of MSPs:

$$\rho_{\nu,\dot{\nu}}(\nu,\dot{\nu}) = \frac{1}{N_p}\sum_{p}^{N_p}\delta(\nu-\nu_p)\delta(\dot{\nu}-\dot{\nu}_p). \quad (3.27)$$

For the analysis presented here, we use the 64 non-globular cluster MSPs listed in the ATNF pulsar catalogue (Manchester et al. 2005).

The parameter space PDF $\rho_{\boldsymbol{M}}$ is modeled using estimates of the best fit values and the fitting covariance matrix $\boldsymbol{C}$

$$\rho_{\boldsymbol{M}}(\boldsymbol{M}|\ln C_1,\alpha,\beta,\gamma,\delta_T) = \frac{1}{\sqrt{(2\pi)^5\det(\boldsymbol{C}^{-1})}}\exp\left[(\boldsymbol{M}-\hat{\boldsymbol{M}})^T\boldsymbol{C}^{-1}(\boldsymbol{M}-\hat{\boldsymbol{M}})\right], \quad (3.28)$$

where $M = (\ln C_1,\alpha,\beta,\gamma,\delta)^T$ and $\hat{M}$ is a vector containing the best fit parameters to the joint CP+MSP fit. For ease of computation, the PDF was approximated using a large number $N_s = 10^5$ of parameter values drawn from equation (3.28):

$$\rho_{\boldsymbol{M}} = \frac{1}{N_s}\sum_{s}^{N_s}\delta(\ln C_1-\ln C_{1,s})\delta(\alpha-\alpha_s)\delta(\beta-\beta_s)\delta(\gamma-\gamma_s)\delta(\delta-\delta_s). \quad (3.29)$$

To calculate P, equations (3.27) and (3.29) were substituted into equation (3.25).

To calculate the estimation error in P associated with the fitting error in model $\boldsymbol{M}$, we analyzed the distribution of P_i using single realizations of the

parameters to calculate $\rho_{\boldsymbol{M}}$, i.e., we substituted

$$\rho_{\boldsymbol{M},i} = \delta(\ln C_1 - \ln C_{1,i})\delta(\alpha - \alpha_i)\delta(\beta - \beta_i)\delta(\gamma - \gamma_i)\delta(\delta - \delta_i) \tag{3.30}$$

into equation (3.25) to calculate a number of realizations of the probability P_i. The standard deviation of P_i is the estimation error.

3.9 Appendix: Strength of the Gravitational Wave Background

In this section, we calculate the rms strength of the gravitational wave background in the residuals $\sigma_{\mathrm{GW},2}(T)$ for a strain amplitude $h_c(f)$. The former quantity is the strength of the GW signal accessible to pulsar timing observations and is used to estimate the sensitivity of a PTA in §3.5.

The strain amplitude is usually modeled with power-law behavior over the range of f relevant to pulsar timing observations,

$$h_c(f) = A_0 \left(\frac{f}{f_0}\right)^{\alpha}, \tag{3.31}$$

and is characterized by an amplitude A_0 at frequency f_0.

The power spectrum $P_r(f)$ of the TOA fluctuations is related to the strain amplitude $h_c(f)$ by (Hobbs et al. 2009a)

$$P_r(f) = \frac{h_c^2(f)}{12\pi^2 f^3}. \tag{3.32}$$

The rms of the residuals $\sigma_{\mathrm{GW},2}(T)$ over a time span T is related to the power spectrum of the perturbations $P_r(f)$ by

$$\sigma^2_{\mathrm{GW},2}(T) = \int_0^\infty df H(f,T) P_r(f), \tag{3.33}$$

where $H(f, T)$ is a high-pass filter that accounts for power that is removed by model fitting to the arrival times.

The rms of the residuals $\sigma_{\mathrm{GW},2}$ is most accurately determined by simulating the TOA perturbations associated with a GWB and then calculating the residual TOAs and $\sigma_{\mathrm{GW},2}$. For a gravitational wave background with $\alpha = -2/3$

$$\sigma_{\mathrm{GW},2}(T) \approx 1.3 \text{ ns } A_{0,-15} \left(\frac{T}{1 \text{ yr}} \right)^{5/3}, \tag{3.34}$$

where $A_{0,-15} = A_0/10^{-15}$ is the characteristic strain at $f_0 = 1 \text{ yr}^{-1}$ and that the high pass filter is approximately unity for $f > 1/T$ and zero for $f < 1/T$. We note the scaling with T is similar to that for a random walk in frequency (RW_1) for which $\sigma_{\mathrm{TN},2} \propto T^{3/2}$ is expected.

The GWB was simulated using a large number of gravitational waves with wave amplitude, frequency, phase, polarization, and propagating direction randomly selected from appropriate PDFs. In particular, the wave amplitude and frequency were selected from distributions consistent with Equation (3.31) using appropriate lower f_ℓ and upper frequency cut-offs. Equation (3.34) is valid for all $f_\ell \ll 1/T$. In simulations with $f_\ell = 1/(10\ T)$ we find that $\sigma_{\mathrm{GW},2}(T) \approx 1/25\ \sigma_{\mathrm{GW}}(T)$.

CHAPTER 4

ASTEROIDS AROUND MILLISECOND PULSARS: EVIDENCE FROM A MILLISECOND PULSAR AND IMPLICATIONS FOR PRECISION PULSAR TIMING

Pulsar timing measurements have revealed companions to neutron stars that include other neutron stars, white dwarfs, main-sequence stars, and planets. We demonstrate that the correlated but stochastic residual times of arrivals from the millisecond pulsar B1937+21 are consistent with the presence of an asteroid belt having a total mass $\lesssim 0.05\ M_\oplus$. Unlike asteroids in the solar system, the best fit pulsar asteroid belt extends over a wide range of radii, consistent with the absence of any shepherding companions. We suggest that any pulsar that has undergone accretion-driven spin-up and subsequently eliminated its companion may have timing precision limited by debris fragments. Millisecond pulsars with white dwarf companions are expected to have better timing precision, all else being equal, because the post-accretion system will have cleared a relatively large gap around the binary system. Observational tests of this model include searches for periodicities from individual asteroids, which are difficult, and tests for statistical stationarity that will become possible as further timing data accrue. Timing noise associated with asteroid belts may fundamentally limit the precision pulsar timing, reducing the sensitivity of pulsar timing array to gravitational waves[1].

[1]R. M. Shannon, J. M. Cordes, M. Kramer, T. J. W. Lazio, T. S. Metcalfe, & Z. Arzoumanian, to be submitted, ApJ

4.1 Introduction

Arrival time measurements of rotation-driven pulsars show time-correlated excesses after accounting for contributions from the spin-down of the pulsar, astrometric parameters, and obvious orbital motion (Cordes & Downs 1985, Hobbs et al. 2010, Chapter 3). Long period canonical pulsars (CPs) with high surface magnetic fields ($\sim 10^{12}$ G) have residuals that are likely dominated by internal spin fluctuations that are caused by some combination of magnetospheric torque fluctuations (Kramer et al. 2006a; Lyne et al. 2010) and torque pulses associated with differential rotation between the NS crust and core (Jones 1990).

Pulsars that have undergone accretion-driven spin-up and magnetic field attenuation are much more stable. The stability of these millisecond pulsars (MSPs) has lead to the discovery of the first planets outside of the solar system (Wolszczan & Frail 1992) and stringent tests of general relativity by studying the reflex motion associated with white dwarf companions (Verbiest et al. 2008). If timing precision is improved further, it will be possible to detect a gravitational wave background. Gravitational waves impart correlated time of arrival (TOA) variations on the signals from a set of MSPs that form a pulsar timing array (PTA Detweiler 1979; Jenet et al. 2005). In general the timing precision of a single object can be improved by observing the objects more frequently, with longer integration times, wider bandwidths, and higher gain telescopes, though these improvements are not limitless (Cordes & Shannon 2010).

Unfortunately, MSPs are not perfectly stable. In Figure 4.1, the timing residuals spanning $T = 19$ yr of observations of the MSP B1937+21 are displayed. The observations used to form these residuals are described further in the appendix

for this chapter in §4.8. These residuals show obvious systematic correlated variations. The root mean square value of this variation (after a second order fit that models the unknown phase, spin frequency f, and spin frequency derivative $\dot{f}$ of the pulsar, and sinusoidal modeling for astrometric and parallactic parameters) is $\sigma_{\mathrm{TN},2} = 13\ \mu$s. The residuals show a clear excess that can be interpreted in a number of ways. Contributions arise from the refraction of radio waves in the interstellar medium, but these are highly wavelength dependent and after mitigation, the timing residuals show a persistent achromatic component. Uncertainties in solar system ephemerides used to transform topocentric TOAs to the solar system barycenter cause small timing residuals with non-stationary statistics. This can be ruled out because, contrary to what would be expected, this type of excess is not observed in other pulsars (Kaspi et al. 1994). This inconsistency also rules out gravitational radiation as the source for this excess.

The residuals could be due to intrinsic timing noise that is caused by activity within the NS itself. The levels of timing noise in the two MSPs with known timing noise PSR B1937+21 and PSR B1821−24, and the upper limits from the other MSPs, suggest that there is some universality to timing noise in all rotation powered pulsars (Shannon & Cordes 2010).

This paper investigates another plausible mechanism for the correlated microsecond timing residuals in MSPs: physical displacement of the pulsar by orbital noise from circumpulsar objects, such as an ensemble of macroscopic, rocky asteroids. The residuals from PSR B1937+21 are too small and too incoherent to be associated with a few planets. There is direct evidence that planetary and protoplanetary environments exist around pulsars. There is the planetary system around the the MSP B1257+12 (Konacki & Wolszczan 2003), which con-

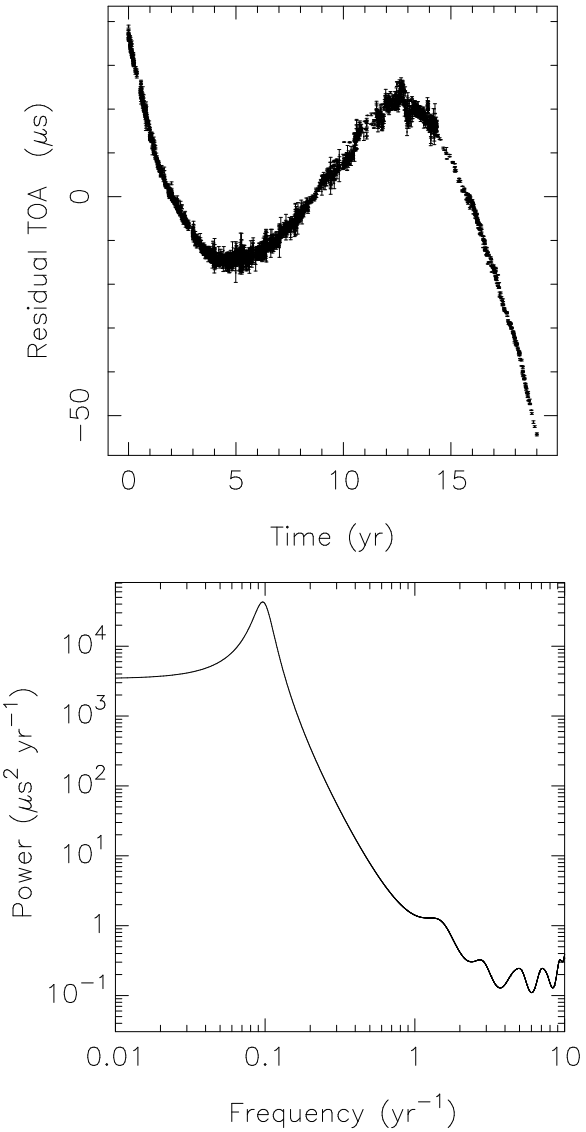

FIGURE 4.1.— Residual times of arrival (bottom panel) and maximum entropy power spectum (top panel) for PSR B1937+21. The residuals come from observations the Nançay, Effelbserg, and Westerbork radio telescopes and span $T = 19$ yr.

tains three moon to earth-mass planets in ≈ 25 to 100 day orbits, inducing rms scatter of ≈ 1 ms on the residuals TOAs. Secondly, there have been reports of a debris disk around the young magnetar 4U 0142+61 (Wang et al. 2006). The pulsar shows excess in the mid infrared that can be attributed to thermally emitting

dust heated by the central neutron star.

Many formation mechanisms have been proposed for the formation of planetary systems around pulsars. They include: (1) formation along with the progenitor, (2) formation from supernova fall back debris; or (3) formation from debris left over from an accretion phase. The second is probably relevant to the magnetar 4U 0142+61, and may also play a role of radio pulsar variability (Cordes & Shannon 2008). The last is probably relevant to PSR B1257+12, where the planetary system forms from a circumpulsar debris disk left over from an episode of accretion-driven spin-up.[2] This is then followed by (or perhaps, happens during) the evaporation of the companion by the pulsars relativistic wind.

The PSR B1937+21 system must have followed a similar path, except that it was left with a much more tenuous disk. Protoplanets formed in such a disk would be too small to force gravitational interaction after an initial runaway growth phase, and the disk would be comprised of many low-mass bodies in marginally stable orbits. The disk would extend over a wider range of orbital radii than the solar system's asteroid belt because there are no planet-mass bodies to impose radial confinement. Moreover, we assert that debris disks may be a necessary outcome of accretion driven spin-up. If this is the case, it provides a fundamental limit to pulsar stability.

We report our findings as follows: In §4.2 we discuss the perturbations to pulsar TOAs caused by asteroids belts. In §4.3 we show that many configurations of asteroid belts can be stable for the entire many Gyr lifetime of an MSP system. In §4.4, through simulation we demonstrate that there are many plausible debris disk configurations that explain the observed residuals

[2]For an alternative explanation see Miller & Hamilton (2001).

in PSR B1937+21. In §4.5 we motivate further observations that can be used to assess the plausibility of the asteroid belt model. In §4.6 we discuss implications for precision pulsar timing.

4.2 Timing Perturbations from Circumpulsar Objects

Pulsars experience reflex motion to any companion, whether it is a massive neutron star (Hulse & Taylor 1975), white dwarf (Segelstein et al. 1986), main sequence star (Fruchter et al. 1988), planet (Wolszczan & Frail 1992), or asteroid. The relative displacement of the star about its stellar barycenter (projected onto the line of sight) causes the arrival time of pulses to vary periodically.

A single object with mass m measured in $M_\oplus$ orbiting a neutron star of mass $M_{\rm NS} = 1.4\ M_\odot$ with an orbital period of P in yr, yields an rms residual TOA perturbation of

$$\begin{aligned} \delta t_2 &\approx F(P_{\rm orb}, T)\left(\frac{a \sin i}{c\sqrt{2}}\right)\left(\frac{m}{M_{\rm NS}}\right) \\ &\approx 0.85 \text{ ms } m P_{\rm orb}^{2/3} \sin i, \end{aligned} \tag{4.1}$$

where i is the inclination angle of the disk with respect to the line of sight and $F(P_{\rm orb}, T)$ is a term that accounts for the fitting for pulsar spin phase, frequency and frequency derivative, and the fitting of astrometric and parallactic terms (e.g., Demorest 2007).

If the orbital period P is less than the time span of observations T, but sufficiently different in period from $P = 1/2$ yr and 1 yr terms associated with astrometric fitting, then the perturbation in the residuals is approximately equal to the perturbation to the TOAs. If $P \geq T$, then a significant fraction of the to-

tal perturbation is removed by the fitting procedure. To properly address the effects of this fitting requires simulation which is discussed further §4.4.

For PSR B1937+21, any single orbiting companion would necessarily have a period in excess of the 19 yr data span because no obvious periodicity is seen. The total mass in an ensemble of asteroids at random orbital phases may exceed that of a single planet by several orders of magnitude because the residuals are an incoherent sum of the individual sinusoidal contributions. For $j = 1, N_a$ asteroids, the rms perturbation to the TOAs is

$$\sigma_{\rm TOA} = \left[\sum_{j=1}^{N_a} \left(\delta t_j\right)^2\right]^{1/2}, \tag{4.2}$$

where δt_j is the perturbation from a single asteroid and is given by equation (4.1).

If all asteroids have the same inclination, which would be expected if the asteroid belt has a disk origin, and the masses and semi-major axes of the asteroids are statistically independent, the rms of time time series can be expressed as

$$\begin{aligned} \sigma_{\rm TOA} &= \sqrt{N_a}\left(\frac{a_{\rm rms}\sin i}{c\sqrt{2}}\right)\left(\frac{m_{\rm rms}}{M_{\rm NS}}\right) \\ &= 0.76 \text{ ms } \left(\zeta\sqrt{N_a}\right)\left(\frac{a_{\rm rms}\sin i}{1 \text{ AU}}\right)\left(\frac{M_{\rm belt}}{1\ M_\oplus}\right), \end{aligned} \tag{4.3}$$

where $a_{\rm rms}$ is the rms semi-major axis and we have used the ratio of rms to mean mass

$$\zeta \equiv \frac{m_{\rm rms}}{\langle m\rangle} = \begin{cases} \dfrac{(2-\alpha)}{\sqrt{(3-\alpha)(1-\alpha)}}, & \alpha < 1 \\ \dfrac{(2-\alpha)}{(3-\alpha)(\alpha-1)}\left(\dfrac{m_2}{m_1}\right)^{(\alpha-1)/2} & 1 < \alpha < 2 \end{cases} \tag{4.4}$$

for a power-law mass probability density function $f_m(M) \propto m^{-\alpha}$, in the mass range m_1 to $m_2 \gg m_1$. For a wide range of parameter values $\zeta \approx 1$.

Thus to account for $\approx$ 10 microsecond residuals for PSR B1937+21, $a_{\rm rms} \sin i M_{\rm belt}/\sqrt{N_a} \approx 10^{-1.8}$. There is a clear trade off between the total mass in asteroids and the number of objects. However, the range of semi-major axes can be constrained by matching the spectral content of the residuals.

4.3 Orbital Stability and Asteroid Formation

The requirement for dynamical stability for the disk places additional constraints on the asteroidal system. For a fixed mass asteroid belt, a constraint can be placed on the number of objects in the disk. The criterion for stability based on three-body effects require that the asteroids be separated in semi-major axis Δa by

$$\Delta a/a \gtrsim 2.1(m/M_{\rm NS})^{1/3} \tag{4.5}$$

to avoid destabilizing perturbations (Gladman & Duncan 1990). For a belt of N_a objects between r_1 and r_2, letting $m \rightarrow \langle m \rangle \equiv M_{\rm belt}/N_a$ and summing δa over $N_a \gg 1$ asteroids yields

$$\begin{aligned} N_a \quad &\lesssim \left[\frac{\ln(r_2/r_1)}{2.1}\right]^{3/2} \left(\frac{M_{\rm NS}}{M_{\rm belt}}\right) \\ &\lesssim \left(\frac{M_{\rm NS}}{M_{\rm belt}}\right) \approx 683 \left(\frac{M_{\rm belt}}{M_\oplus}\right)^{-1/2} . \end{aligned} \tag{4.6}$$

We argue that in an asteroid belt formed from a disk of material much more tenuous than that from the early solar system the bodies undergo runaway growth until they reach marginal orbital stability and then they cease growing. Therefore we take equation (4.6) with equality, yielding the maximum number of asteroids for a given total mass. Substituting this expression into equation (4.3) we obtain the maximal mass asteroid belt:

$$M_{\rm belt,max} = M_{\rm NS}\left(\frac{\sqrt{2}c\sigma_{\rm TOA}}{\zeta a_{\rm rms}\sin i}\right)^{4/5}$$
$$\approx 0.051 M_\oplus \left(\frac{\sigma_{\rm TOA,\mu s}}{\zeta a_{\rm AU}\sin i}\right)^{4/5}, \quad (4.7)$$

where $\sigma_{\rm TOA,\mu s}$ is the rms perturbation in microseconds and $a_{\rm AU}$ is the rms semimajor axis in AU.

In the formation of a solar type planetary system, protoplanets undergo runaway growth until they reach a mass limited by their ability to gravitationally feed on the surrounding surface mass density (Lissauer 1987, 1993; Goldreich et al. 2004b). Slower but inexorable growth to planet-sized objects follows if perturbations induce orbit crossings. The rate of growth in this secondary phase depends on protoplanet masses, velocity dispersion, and the presence of gas to induce orbit crossings and accrete onto more massive planets.

The best fit debris disk around PSR B1937+21 is too tenuous to have formed planets. To show this we estimate the surface density of the disk Σ. For the maximal mass solution, the mean asteroid mass is $\langle m\rangle = M_{\rm belt}^{3/2}/M_{\rm NS}^{1/2} \sim 10^{-5.6}\ M_\oplus$ for the case considered above. The largest isolation mass m_H to which a protoplanet may grow during the runaway phase is the total mass contained within an orbital radial range of several Hill's sphere radii (Lissauer 1987, equation 11):

$$m_H = \frac{(4\pi B r^2\Sigma)^{3/2}}{(3M_{\rm NS})^{1/2}} \approx 10^{-2.75} M_\oplus \left(r_{\rm AU}^2\Sigma_0\right)^{3/2} \quad (4.8)$$

where $B \approx 3.5$ and $r_{\rm AU}$ is the semimajor axis in AU and Σ_0 is the surface density in g cm^{-2}. Comparison with our maximal-mass solution implies that at 1 AU, $\Sigma \approx 0.013$ g cm^{-2}, smaller by three orders of magnitude than the minimum-mass surface density (i.e., excluding volatiles) thought to be present in the solar system at the end of the runaway phase (Lissauer & Stewart 1993), and smaller

by $\gtrsim 10^4$ than in the planet forming region near the planet pulsar system PSR B1257+12 (Ruden 1993). Of course surface density at the time of planet formation may have been larger if volatiles were present, and the Hill's mass may be correlated with orbital radius and depend on the radial variation of Σ, in which case the upper bound on asteroid number based on the stability criterion would be altered. Our basic argument is unchanged, however.

Asteroid formation in the high-luminosity environment of PSR B1937+21 after reactivation of the rotation driven pulsar luminosity is a trade-off between dispersal of gas and agglomeration. Using the present-day energy loss rate of the pulsar $\dot{E} = 4\pi^2 I \nu \dot{\nu} \approx 250 L_\odot$, where I is the neutron star moment of inertia and is assumed to be 10^{45} g cm^3, the energy intercepted is sufficient to head the asteroids to a temperature

$$T(r) = 1200\text{K}\ (1-A)^{1/4} \left(\frac{L}{250 L_\odot}\right)^{1/4} \left(\frac{r}{\text{AU}}\right)^{-1/2}, \tag{4.9}$$

where A is the albedo of the material to the pulsar energy. Grain formation could have occurred outside 1 AU at pulsar turn-on, whether or not $\dot{E}$ is dominated by relativistic particle flux.

PSR B1937+21 has a spindown lifetime of $\nu/2\dot{\nu} \approx 234$ Myr, which is an upper bound on the elapsed time since the cessation of accretion. The spindown age is much longer than the expected runaway phase but short enough that the asteroidal disk we associated with timing residuals may still be evolving: slow coalescence may occur while the wind evaporates the protoplanets that are deflected to orbits near the NS.

4.4 Plausible Disk Configurations

The residual TOAs for PSR B1937+21 are dominated by low-frequency noise but contain a broad spectrum of components. To find asteroid systems that reproduce the frequency content of the data, simulations of a wide range of asteroid belt configurations were conducted. Each asteroid was assigned an orbital radius according to a probability distribution which is flat in radius (hence decreasing in asteroid surface density with radius) between inner radius r_1 and outer radius r_2. Within its orbit, each asteroid was giving a random initial phase. The masses of the objects are selected from the power law distribution defined previously. Additionally, the disks were required to satisfy the dynamical stability constraint expressed in equation (4.5).

At each time (with times matching the observing time of the actual observations), the cumulative orbital effect was calculated. To this, a random white-noise contribution of rms amplitude $\sigma_n = 1\mu$s was added to model other white noise effects, forming the simulated TOAs.

The residual TOAs were found by subtracting from the simulated TOAs a least-squared fit that models the spin down parameters (spin rate and its derivative) and sinusoids of year and half year periods to mimic the fitting for astrometric and parallactic terms, respectively.

The real and simulated data were compared using maximum entropy power spectra of the timing residuals. To find acceptable asteroidal parameters, we minimized a cost function

$$C = \frac{\sum_k \left[S_k^{(o)} - S_k^{(s)}\right]^2}{\min\left\{\sum_k \left[S_k^{(o)}\right]^2, \sum_k \left[S_k^{(s)}\right]^2\right\}}, \tag{4.10}$$

TABLE 4.1
GRID SEARCH PARAMETERS

Parameter	Description	Values
M_a	Total mass ($M_\oplus$)	0.3 0.1 0.03 0.01 0.003 0.001
N_a	Number of asteroids	3 10 30 100 300 1000
$a_{\min}$	Inner radius of asteroid belt (AU)	0.1 0.3 1.0 3.0 10.0 30.0
$a_{\max}$	Outer radius of asteroid belt (AU)	1.0 3.0 10.0 30.0 100.0
α	Spectral index of mass distribution	0.05 0.1 0.5 0.9 1.1 1.25 1.5
$M_{\min}$	Minimum mass of asteroid $M_\oplus$	10^{-6}

NOTE.—Grid Search Parameters. For each set of parameters 100 stable asteroid belt configurations were examined.

where $S_k^{(o)}$ and $S_k^{(s)}$ are the power spectra of the observed and simulated data sets respectively. The sum over frequency includes 1000 frequencies between 0.01 yr^{-1} and 10.0 yr^{-1} at 0.01 yr^{-1} intervals. We searched for the minimum-cost combinations of parameters by using a brute-force search over a grid of values for N_a, r_1, r_2, m_1, m_2, and α. The values of the parameters chosen are displayed in Table 4.1. For each set of parameters, 100 stable asteroid belt configurations were simulated.

Figure 4.2 shows the three simulated asteroid belts that most closely matched the observations. No unique combination of parameters were found that minimize the cost function. For example, the number of asteroids can vary from 10 to 1000, but the total asteroidal mass is found to satisfy $M_{\mathrm{belt}} \propto \sqrt{N_a}$, in accord with equation (4.6). We characterize the best fits according to

$$M_{\mathrm{belt}}/\sqrt{N_a} \approx 10^{-2.0\pm0.5} M_\oplus, \quad \text{with} \quad N_a \gg 10. \tag{4.11}$$

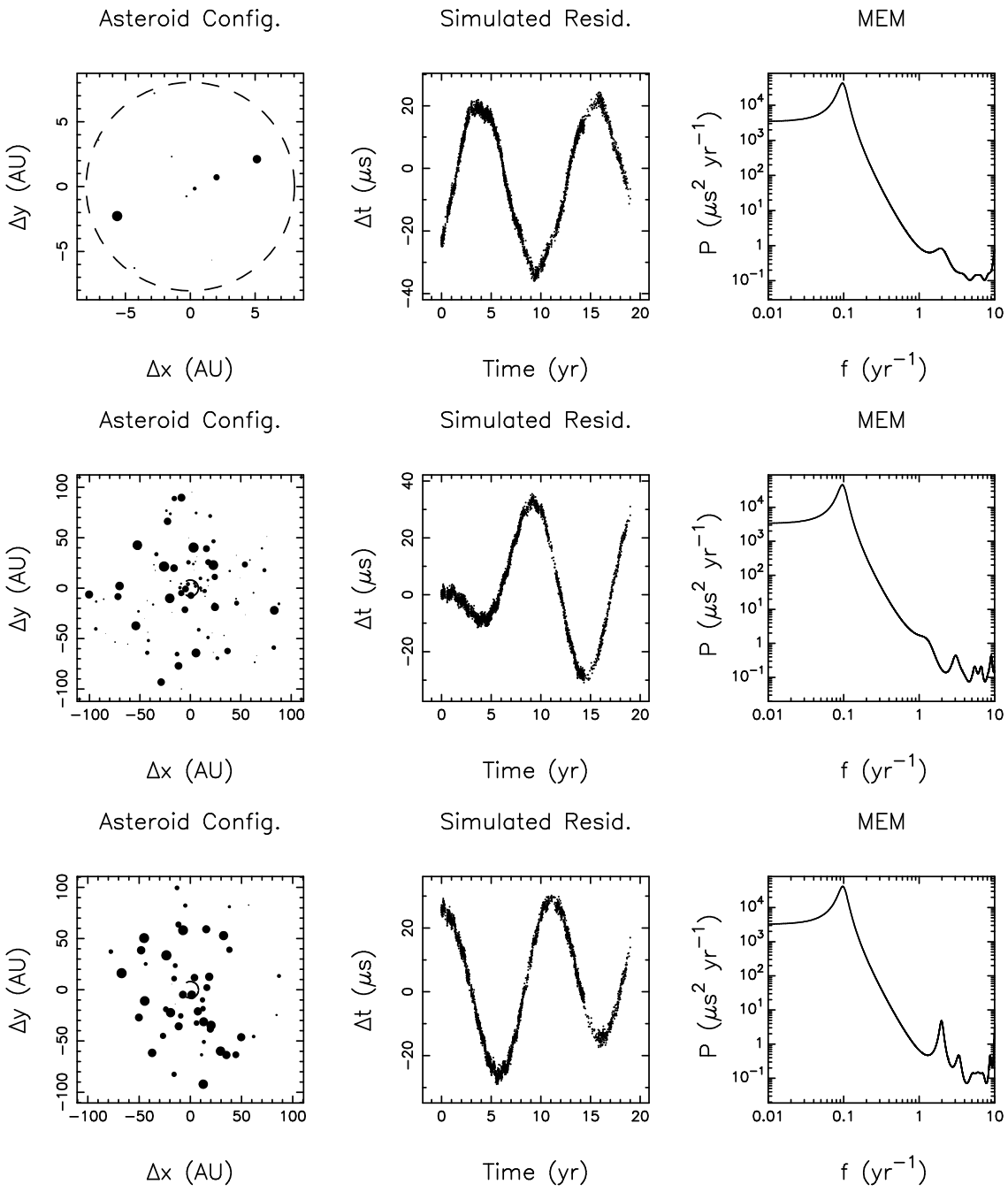

FIGURE 4.2.— Best-fit disk configurations. From the top row to the bottom row we show the three best-fit disk configurations. *Right panels:* Asteroid belt configuration at initial time in the simulation. Each asteroid is represented by a filled circle, with the size of the circle proportional to the radius of the asteroid. The open dashed circle represents the radius of an orbit with a period corresponding to the data length (19 yr). The *Center panels:* residual TOAs associated with the asteroid belt. *Left panels:* Maximum entropy power spectra for the simulated residuals (thick line) and the observed time series (thin line).

4.5 Tests of the Asteroid Belt Model

A drawback of an asteroid belt model for the origin of timing noise in PSR B1937+21 is that it is difficult, though not impossible to test. In the following subsections we first highlight tests that can be conducted using high precision pulsar timing, and then discuss tests more generic to neutron stars and radio pulsars.

4.5.1 Tests Unique to MSPs and PSR B1937+21

Periodicity in time series: A single periodicity identified within the residual time series is indicative of a single object. Because an asteroid belt contains a variety of masses, it is possible that the largest may be detectable. Two criteria arise in a Fourier spectral analysis of the residuals: the signal to noise ratio (SNR) and the frequency resolution. In a discrete Fourier transform of N data points sampled over a data span of $T > P_{\rm orb}$, SNR $= \sqrt{N}\delta t/\sigma_n$ (for SNR > 1), where δt is the amplitude of the perturbation from the single object σ_n is the rms error. Requiring SNR > 5 for detection implies that for an object to be detectable suggests that

$$ma \sin i \geq 10^{-4.3}\ (M_\oplus \cdot \mathrm{AU}) \left(\frac{\sigma_n}{0.1\ \mu\mathrm{s}}\right) \left(\frac{N}{100}\right)^{-1/2} \left(\frac{\mathrm{SNR}}{5}\right); \tag{4.12}$$

therefore individual asteroids of quite small mass in 1 AU orbits produce amplitudes that can be detected in the Fourier transform.

Resolving spectral lines associated with single asteroids are potentially more difficult, however. If asteroids comprise a marginally stable and maximally packed belt (see equation 4.5), the frequency resolution T^{-1} must be smaller than the separation of spectral lines produced by neighboring asteroids $\delta f/f =$

$(3/2)\delta a/a$, which, for a $1.4M_\odot$ neutron star works out to

$$\frac{T}{P_{\rm orb}} \gtrsim 470\left(\frac{10^{-4}}{m}\right). \tag{4.13}$$

The required frequency resolution is therefore quite difficult to satisfy, unless the asteroids belt is much more sparse than minimally required.

Stationarity in time series: If individual asteroids cannot be discriminated, the statistics of their collective behavior can be used to distinguish the asteroid model from intrinsic spin noise. Spin noise is manifested as non-stationarity in the residuals (Cordes & Downs 1985, Shannon & Cordes 2010) that can be modeled as random walks in spin phase, spin frequency, and frequency derivative or and other related non-stationary processes For these processes respectively, the rms residuals scale, proportionally to $\sigma_{\rm TN}(T) \propto T^\gamma$, with $\gamma = 1/2, 3/2, 5/2$. Most canonical pulsars show consistency with the frequency and frequency derivative spin noise, a superposition of the two, and the random walks combined with occasional discrete jumps (Cordes & Downs 1985; D'Alessandro et al. 1995). Recently Shannon & Cordes (2010) found that for rotation-powered pulsars[3] the expected rms level of timing noise is $\sigma_{\rm TN}(T) \propto T^{2.0\pm0.1}$.

Long term stationarity is not expected in asteroid belts. On time scales shorter than the largest orbital period (i.e, $T > P_{\rm orb,max}$) the residuals show non-stationary statistics because $\sigma_{\rm TN,2}$ grows as a larger portion of the amplitude of the longest period objects is manifested in the post fit residuals. The transition from non-stationary to stationary statistics can be explored by applying a variety of diagnostics to the TOAs, including the structure functions, spectral estimators, and $\sigma_{\rm TN,2}(T)$ itself. If non-stationarity persists for long periods of

[3]We distinguish rotation powered canonical pulsars and millisecond from the magnetically driven magnetars, which show excess timing noise Shannon & Cordes (2010).

time, either 1) an asteroid belt model would need to be developed that includes objects in wide, stable orbits; or 2) the debris disk origin could be ruled out.

No spectral power inside the rock line / ice line: As mentioned earlier, the spin-down luminosity of PSR B1937+21 is large. A large fraction of this material can be deposited efficiently into material surrounding the pulsar heating it up to large temperatures, which is defined in equation (4.9). For this pulsar, asteroids composed of rocks would not be expected inside 1 AU ($P_{\rm orb} \approx 0.8$ yr), assuming a melting temperature of 1200 K and complete absorption of the pulsar spin down energy ($A = 0$). Asteroids composed of ice and other refractory material would not be expected inside a radius of 16 AU ($P_{\rm orb} \approx 14$ yr), assuming a melting temperature of 300 K and complete absorption of the pulsar spin down energy. Definitively identifying power from inner regions of an asteroid belt is not as simple as identifying power at high Fourier components because spectral leakage causes power to be aliased from low fluctuation frequency to high fluctuation frequency.

No correlation between residuals and magnetospheric activity: In a study of timing noise in canonical pulsars, Lyne et al. (2010) found that for a few objects, a fraction of the timing noise is associated with changes between discrete spin down $\dot{f}$, and that these states are associated with with average pulse profiles. If *all* of the timing noise in PSR B1937+21 is associated with the this type of behavior, an asteroid belt origin would be ruled out, because reflex motion would neither cause transitions between discrete states of $\dot{f}$ nor cause this type of pulse profile variation. As discussed earlier, the levels of timing noise are consistent with what is observed in canonical pulsars (Shannon & Cordes 2010). However, given pulsar to pulsar variability in the levels of timing noise in canonical pul-

sars, some fraction or all of the observed timing noise in this PSR B1937+21 may still be associated with reflex motion.

Variations in dispersion measure: Another possible though highly unlikely approach would be to search for variations in dispersion measure (DM) due to evaporation of asteroidal material by the pulsar's relativistic wind. However complete evaporation of a 0.02 $M_\oplus$ asteroid would only contribute to DM variations of 0.02 μs at an observing frequency of 1.4 GHz, which is much smaller than the contribution to dispersion measure from the interstellar medium (Ramachandran et al. 2006). Only if the belt contained significantly more mass would DM variations be detectable.

4.5.2 Other Tests for Debris Disks around Pulsars

Infrared emission from debris: Any debris would be passively heated by the neutron stars thermal and nonthermal emission to temperatures of hundreds of Kelvin, radiating predominantly in the infrared. For this debris to be detectable, the disk would be required to have a large effective area. Infrared observations of other pulsars have placed limits of many Earth masses on circumpulsar dust disks (Lazio & Fischer 2004; Bryden et al. 2006), and large amounts of telescope time would be required to detect a debris disk around PSR B1937+21. Because PSR B1937+21 is in the Galactic plane, definitive associated of infrared emission would additionally be hindered by confusion with coincident infrared sources.

Reflections of radio emission off of asteroids: If the radio beam intersects the asteroid belt, radio emission will reflect off of any material (Phillips 1993; Cordes & Shannon 2008). In the past detection has been difficult because single-dish

instrumentation did not (and still does not) provide sufficient stability to detect faint off-pulse emission and radio interferometers were not capable of imaging pulsar fields of view with the required sub-second time resolution to gate on and off pulses. New interferometers such as the EVLA and the SKA will be capable of fast-dump imaging and it will be possible to better quantify off pulse emission. Reflected radio emission can be distinguished from magnetospheric through measurement of the degree of polarization. The former would be depolarized due to the rough surfaces of asteroid belts, while the latter would show high levels of polarization.

Confirmation of the orbital noise interpretation for PSR B1937+21 may rely on finding planets and asteroids around other pulsars and demonstrating that they are a frequent outcome of processes that lead to otherwise isolated neutron stars.

4.6 Implications: Timing Precision & Gravitational Wave Detection

As demonstrated above, MSP systems that contain a population of large, rocky objects possess poorer timing residuals. However MSPs that have large companion objects are inherently better timing systems because debris-companion interactions clear the disk of much of its mass in a short amount of time.

Debris clearing in MSP systems is analogous to late-time evolution of planetary systems that is described by Goldreich et al. (2004a). Very quickly a gap will form around the companion because net torques from the orbiting companion

move material away from its orbit. As a function of time t, the width of the gap is

$$w(t) \sim a\left(\frac{M_c}{M_{\rm NS}}\right)^{2/5} (\Omega t)^{1/5}, \tag{4.14}$$

where M_c is the mass of the companion, a is the semi-major axis of the orbit, and Ω is the orbital frequency. It is important to note that this method only opens gaps very slowly ($w \propto t^{1/5}$) and is inefficient for opening gaps in planetary systems for which the mass ratio is small. For a binary system the width $w(t)$ as a function of time is

$$w(t) \approx 2 \text{ AU } \left(\frac{M_c}{0.2 M_\odot}\right)^{2/5} \left(\frac{P_{\rm orb}}{10\ d}\right)^{2/15} \left(\frac{t}{\rm Gyr}\right)^{1/5}. \tag{4.15}$$

Inner regions of the disks can be cleared within the spindown time of the pulsar. However the outer regions are unlikely to be cleared. Pulsars that have heavier companions in wider, longer period orbits are likely to harbor smaller debris disks.

However, all systems are likely to have some form of debris disk. Assuming the disk comprises of more than a few objects it is nearly impossible to mitigate these effects. This will fundamentally limit the sensitivity of timing precision and the sensitivity of a PTA to gravitational waves. Once this limit is reached, the only way to improve the sensitivity of the PTA is to incorporate additional objects.

4.7 Conclusions

The existence of planets around two pulsars, a debris disk around another, and a possible asteroid belt around PSR B1937+21 has many implications for the

pulsar population as a whole. Protoplanetary disks around pulsars are likely to cover a wide range in density and total mass in order to have planets form in some cases but not in others.

We have shown that asteroid belts can form and persist around millisecond pulsars, and these systems can affect the timing precision at the nanosecond to microsecond level. The timing noise observed for PSR B1937+21 can be described by such a disk. Disks of lower mass may exist around other millisecond pulsars, and may have not been detected because of the insufficient timing precision. Unless the disks are populated by only a few objects, it is difficult to identify and correct for these effects. High precision timing observations of other MSPs may show unmitigatable excess associated with these disks.

4.7.1 Acknowledgements

This work made use of NASA's ADS System. This work was supported by the NSF through grant AST-0807151 and by NAIC, which is operated by Cornell University under a cooperative agreement with the NSF.

4.8 Appendix: Observations of B1937+21

In this section we describe the data and methods used to form the residual times series for PSR B1937+21 that was used in the analysis in this paper. The residuals are presented in Figure 4.1.

Observations from three telescopes were used to form the time series. In Ta-

TABLE 4.2

PSR B1937+21

Fit and data-set	
Pulsar name	B1937+21
MJD range	47517.5—54457.6
Number of TOAs	3142
RMS of the residuals (μs)	13.9
Weighted fit	N
Measured Quantities	
Right ascension, α	19:39:38.561272(18)
Declination, δ	+21:34:59.1345(4)
Pulse frequency, f (s^{-1})	641.928251153425(4)
First derivative of pulse frequency, $\dot{f}$ (s^{-2})	$-4.3312955(17)\times10^{-14}$
Dispersion measure, DM ($cm^{-3}pc$)	70.635(13)
Proper motion in right ascension, μ_α (mas yr^{-1})	−0.06(3)
Proper motion in declination, μ_δ (mas yr^{-1})	−0.40(5)
Parallax, π (mas)	−3.8(11)
Set Quantities	
Epoch of frequency determination (MJD)	47899.5
Epoch of position determination (MJD)	47500
Epoch of dispersion measure determination (MJD)	47899.5
EPHVER	5
Derived Quantities	
$\log_{10}$(Characteristic age, yr)	8.37
$\log_{10}$(Surface magnetic field strength, G)	8.61
Assumptions	
Clock correction procedure	TT(TAI)
Solar system ephemeris model	DE405
Binary model	NONE
Model version number	5.00

NOTE.— Observed and derived parameters for PSR B1937+21. For fit parameters, the ± 1σ uncertainties on the last digit are displayed in parentheses.

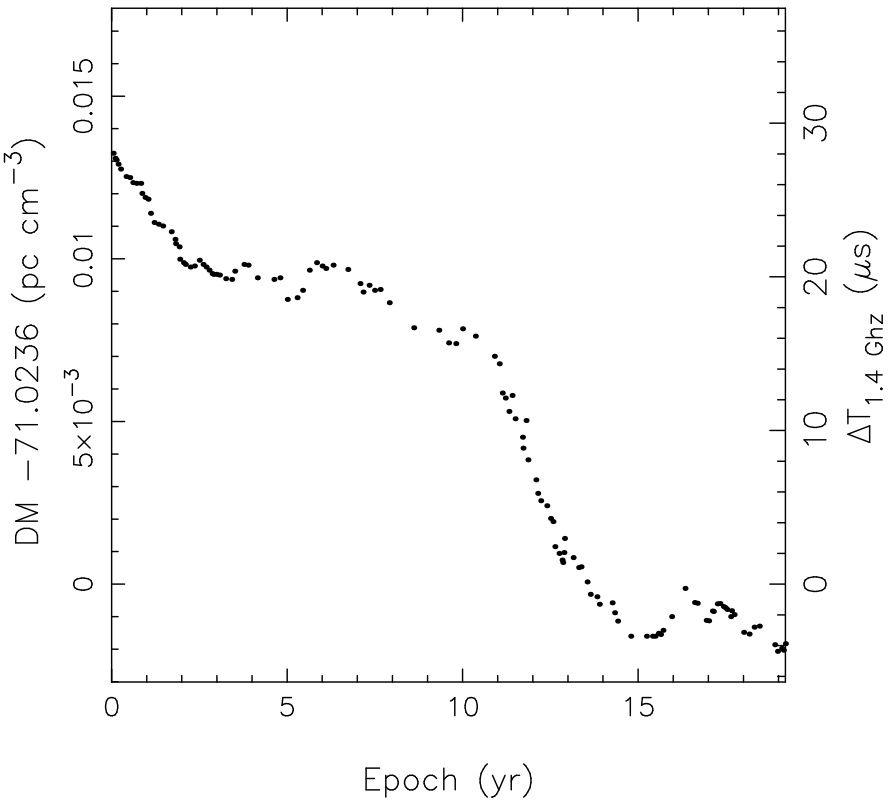

FIGURE 4.3.— Dispersion Measure of PSR B1937+21 over the observation epoch spanned by our observations. On the right vertical axis, we show the relative perturbation to 1.4 GHz observations (the typical observing frequency of the observations reported here) that would be caused by the same change in DM.

ble 4.3 we list the observations, including the observing telescope, MJD range of observations, observing span T, nominal observing frequency ν, observing backend, and total number of TOAs $N_{\rm TOA}$. Most of the observations have been used in previous studies, and references to previous published work are displayed in Table 4.3.

The TEMPO2 package (Hobbs et al. 2006) was used to model pulse TOAs. In Table 4.2 we present the ephemeris for our observations. Two notable steps were necessary to produce the best time series:

Correct for propagation effects: It is well known that it is necessary to correct for

TABLE 4.3
OBSERVATIONS

Observatory	MJD Range	T (yr)	Backend	ν GHz	N_{TOA}	Ref
Nançay	47517 – 53339	14.9	OLDSYS	1410	3200	1
Nançay	53286 – 54363	2.9	NBPP	1370	167	2
Effelsberg	50982 – 54216	8.9	EBPP	1410	187	3
Westerbork	51386 – 53456	5.7	PUMA	1380	72	3
Westerbork	53581 – 54457	2.4	PUMA2	1380	38	3
Total	47517 – 53339	19.0	···	···	3664	

NOTE.—Properties of the observations used in this analysis. We list the observatory, observation span, backend instrumentation, typical observing frequency, and references that either report previous observations or describe the instrumentation. The references listed are: (1) (Cognard et al. 1995); (2) Cognard et al. (2000); and (3) Janssen (2008).

interstellar propagation to achieve the best timing precision. Because the refractive index of the interstellar medium is radio frequency dependent, propagating radio waves at different frequencies arrive at different times and travel different paths. This is manifested as a number of different perturbations to the observed signal relative to the emitted signal. We refer the reader to Cordes & Shannon (2010) and Chapter 5 for additional discussion of the full suite of effects. At minimum it is necessary to correct for the group delay relating to the total electron content of the line of sight referred to as the the dispersion measure (DM) in the parlance of radio astronomy.

Because the observations presented here are at each epoch single frequency observations, it is necessary to use published measurements of DM to correct the TOAs. Ramachandran et al. (2006) report DM for this pulsar from the be-

ginning of our observations presented here up until MJD 52276. J. Verbiest (private communication) reports DM measurements from MJD 53082 to MJD 54528. These total DM time series for our observations is presented in Figure 4.3. The DM at our observation epochs was found though by interpolation using a cubic spline. We note that this correction method results in latent dispersion measure propagation and does not correct for higher order propagation effects.

Fit for observatory and backend offsets: It is necessary to fit for phase offsets between different telescopes and receivers, because of the relative delays in equipment and variability in the fiducial phase used to define the TOAs. All the observations were connected to the Effelsberg observations because they had the highest quality TOAs and overlapped with all of the other observations. For the overlapping interval between the Effelsberg observations and the other data sets, the phase offset (jump) was fit. To best determine the jump, harmonic whitening terms were included in the model to mitigate the effect of the timing noise (Hobbs et al. 2004). With the phase offsets set, the entire data set was modeled without the inclusion of timing noise.

CHAPTER 5

CORRECTING INTERSTELLAR PROPAGATION DELAYS IN PRECISION PULSAR TIMING OBSERVATIONS

To improve the precision of pulsar timing observations to the levels required to directly detect gravitational radiation it is necessary to correct for the propagation of radio waves through the interstellar medium beyond the typical dispersion measure correction. Here we assess most of the delays associated with interstellar propagation and present simulations that model frequency-dependent time of arrival perturbations in long term pulsar timing observations. We model the multi-frequency times of arrival and identify the strength of interstellar propagation effects with different observing configurations and a variety of scattering screen geometries. We then test the efficacy of many time-of-arrival based mitigation schemes. We show that first-order approaches that correct only for effects that scale proportional to ν^{-2} (dispersion measure-like corrections) poorly remove interstellar propagation effects resulting in residuals that contain a larger and more non-stationary residual TOAs. We find that methods that correct for effects that scale proportional for ν^{-2} variations and ν^{-X} variations, where X is between 4 and 7 (depending on the screen and observation conditions), provide the best correction to times of arrivals. The value of X varies because the line of sight and observing properties strongly affect which particular perturbation is the second strongest. We also find that there is a contribution to the TOAs that is stochastic in both frequency and time and therefore cannot be corrected using solely time of arrival information. This term is attributed to the decorrelation of propagation trajectories at widely separated frequencies. We conclude that it is important to obtain simultaneous or nearly simultaneous multi-frequency TOAs and that fitting for three unique frequency

dependencies best corrects the effects of refractive interstellar scintillation.[1]

5.1 Introduction

The regularity of the arrival times in the pulsed radio emission from pulsars has enabled many discoveries fundamental to physics and astrophysics, including stringent constraints on the divergence of gravitation from Einstein's theory of general relativity (Hulse & Taylor 1975; Kramer et al. 2006b), the discovery of the first planetary-mass objects outside of the solar system (Wolszczan & Frail 1992), and the equation of state of dense nuclear matter (Lattimer & Prakash 2007).

One interesting but presently unrealized application of pulsar timing is the direct detection of gravitational waves (GWs) and the characterization of GW-emitting sources. The quadrupolar signature of gravitational waves passing through the solar neighborhood is manifested as a unique angular signature in the TOAs from a set of ultra-stable millisecond pulsars (MSPs) that form a pulsar timing array (PTA; Detweiler 1979; Hellings & Downs 1983; Foster & Backer 1990). PTAs are sensitive to gravitational waves with periods between 1 month and 20 yr, (corresponding to frequencies between $\approx$ 2 and 400 nHz) with the sensitivity band constrained by observing cadence and timing campaign duration.

The strongest source of gravitational waves in the PTA observing band is suspected to be a stochastic background associated with merging massive black holes (Jaffe & Backer 2003). This background imparts a non-stationary (red)

[1] R. M. Shannon, J. M. Cordes, to be submitted to ApJ.

signal in the TOAs, with a characteristic root mean squared (rms) amplitude in the residual TOAs of $\approx$ 20 ns over a 5 year period (Shannon & Cordes 2010, henceforth referred to as Paper I). It is currently estimated that between 20 to 40 pulsars, with timing precision between $\approx$ 10 and 100 ns level are required to significantly detect plausible sources of gravitational radiation (Jenet et al. 2005, Paper I).

To reach the required precision and detect GWs, it is necessary to identify and correct for many perturbations to the TOAs. Some perturbations are deterministic in time, and independent of observing frequency, and can be parameterized and included in a timing model (Edwards et al. 2006). An example of this is the perturbation associated with the secular spin down of the pulsar. However, other perturbations exist that are stochastic in time and therefore cannot be corrected solely with single frequency timing information, necessitating the use of ancillary information.

Any uncorrected perturbation contributes an additional error to TOAs and decreases the sensitivity of a PTA to GWs. It is of particular interest to identify and correct non-stationary (red) perturbations because these more severely affect the sensitivity of a PTA to a stochastic gravitational wave background than stationary (white) noise (Paper I).

This work complements other recent analyses of astrophysical sources of noise in PTA observations. In Paper I, we assessed the levels of pulsar spin noise which contributes a radio-frequency independent timing error. Based on the levels of timing noise in canonical pulsars and the two MSPs that exhibit timing noise, we concluded that for many MSPs, spin noise is present at levels comparable to the GWB. In Cordes & Shannon (2010) (Paper II) we comprehen-

sively identify and the many stochastic perturbations to TOAs using a physical model for times of arrival.

One set of perturbations discussed in Paper II are associated with the propagation of radio waves through the interstellar medium (ISM). As the emitted radio emission travel from the pulsar to the earth, the propagating waves refract through the warm ionized electrons (shown in Figure 5.1), and the pulse arrival time is retarded relative to the expected arrival time in vacuum. This delay varies with time because the the sampled region of the ISM changes as the pulsar Earth line of sight with the relative motion of the Earth and the pulsar through the Galaxy.

The effects of interstellar propagation can be partially mitigated though identification and removal of RF-dependent perturbations to the TOAs, because the strength of the refraction and hence the TOA perturbation is highly frequency dependent. This is in contrast with other astrophysically interesting perturbations to TOAs that impart achromatic perturbations to TOAs like the one associated with gravitational waves.

Multi-frequency mitigation methods are presently only minimally applied in precision timing observations. It is usually assumed that chromatic variability in pulse arrival times is associated entirely with the change in the total electron content (referred to as dispersion measure, DM) of the line of sight. Under this assumption the arrival time is directly proportional to the dispersion measure and proportional to the inverse square of observing frequency. When the DM is larger, the observed pulses arrive slightly later, and vice-versa. This effect is assumed to be completely deterministic in frequency; therefore it is assumed to be sufficient to measure the pulse TOAs at two frequencies to mitigate these

DM variations. For the nearby MSPs currently incorporated in PTAs, observed at typical observing frequencies ($\approx$ 0.5 GHz to 3 GHz), DM variation delays have an rms amplitude of many microseconds. The correction for this effect has been identified as crucial to the success of PTAs (You et al. 2007).

However the approximation that the ISM is smooth is insufficient. It is well known that the warm ISM contains electron plasma density fluctuations over a wide variety of length scales and that these fluctuations cause multi-path propagation of the pulsar signal (Scheuer 1968; Rickett 1969, 1990). Thus, in addition to the DM delay there are other higher order effects that must be considered (Armstrong 1984; Cordes et al. 1986; Romani et al. 1986; Foster & Cordes 1990; Hu et al. 1991; Coles et al. 2010, henceforth referred to as C10; Paper II).

This study differs in a number of ways from the recent study in C10, and is in general a complementary analysis. C10 focus on studies of diffractive effects associated with electron density variations on small length scales that cause TOA perturbations on short time scales. Due to computational limitations (discussed below) they considered only propagation over a narrow range of frequencies. We take a complementary approach by focusing on refractive effects and limiting time and spatial resolution but enabling TOA perturbations to be studied over a wide range of frequencies.

This study extends previous studies of refractive propagation effects. Foster & Cordes (1990) investigated propagation effects using a one-dimensional screen. They suggested that there were likely significant perturbations to the pulse time of arrival associated with geometric path length variations that would not be corrected using the simple DM-correction technique. Hu et al. (1991) used a two-dimensional screen to simulate propagation effects. These

studies were conducted when there were only a few known MSPs and timing precision was much poorer. A reexamination of propagation effects is warranted because the increase in the number of known MSPs, the improvement in timing precision, and increased computation power that enables a wider range of scattering configurations to be considered.

In this paper we carefully examine slowly-varying propagation delays associated with refractive interstellar scintillation (RISS). Compared to previous studies, we examine a wider range of screen configurations and observing strategies. We quantitatively assess the efficacy of many mitigation strategies, relevant to PTAs and other long-term timing observations.

We show that for many MSPs, observed at typical observing frequencies, these effects perturb pulsar TOAs at the 10 ns to 100 ns level and contribute a non-stationary signal to pulsar arrival times. We show that these effects can be mitigated using multi-frequency timing observations, with the optimal technique dependent on the particular line of sight and other sources of TOA uncertainty in the measurements.

Our findings are outlined as followed: In §5.2 the relationship between the pulse perturbation and the the image intensity is discussed. In §5.3 a refractive screen model is motivated and an approximation for the image intensity associated with RISS is presented. In §5.4 the TOA perturbations with the refractive screen are presented. In §5.5 a series of simulations conducted to investigate refractive perturbations are presented. The details of the simulation are presented in the appendices to this chapter. In §5.6 mitigation strategies are described. In §5.7 the effectiveness of the mitigation strategies for different screen configurations is analyzed. In §5.8 observational configurations that can be used to

improve pulsar timing are investigated.

Throughout this paper *frequency* is used in two distinct contexts. Observing radio frequency is denoted ν. Fluctuation frequency, the conjugate variable to time in the spectral analysis of a time series, is denoted f.

5.2 Propagation Delays and Image Intensity

Interstellar propagation contributes both a bulk delay that retards the pulse arrival time and changes the observed shape of the pulse, which is displayed in Figure 5.1. In panel a) we show the observed TOAs are corrected to the solar system barycenter (circle S), assuming that the the radio waves propagate along a direct line of sight from the pulsar (circle P) to the Earth (circle E). Inhomogeneities in the density of warm interstellar plasma cause the radio waves to travel along an ensemble of paths constrained by a curved banana-shaped tube, denoted by the thin solid lines. In this analysis, scattering is assumed to be constrained to a thin screen located a distance sD from the Earth along the pulsar earth line of sight, where D is the pulsar distance. At the screen distance, the center of the tube is offset from the direct line of sight by an angle θ_r and has a width θ_d. Unlike the configuration displayed here, θ_g is typically larger than θ_r. The size and shape of the tube vary with frequency and time. The location of the tube, projected on the screen can also be characterized by an image intensity $B(\boldsymbol{\theta})$. In Figure 5.1, panels b-d we display schematic diagrams of the emitted pulse shape (*Panel b*), the pulse broadening function $p(t)$ (*panel c*), and the observed pulse shape (*panel d*) as a function of pulse phase $\phi = t/P$, where P is the pulsar spin period. Interstellar dispersion and the tube offset from the di-

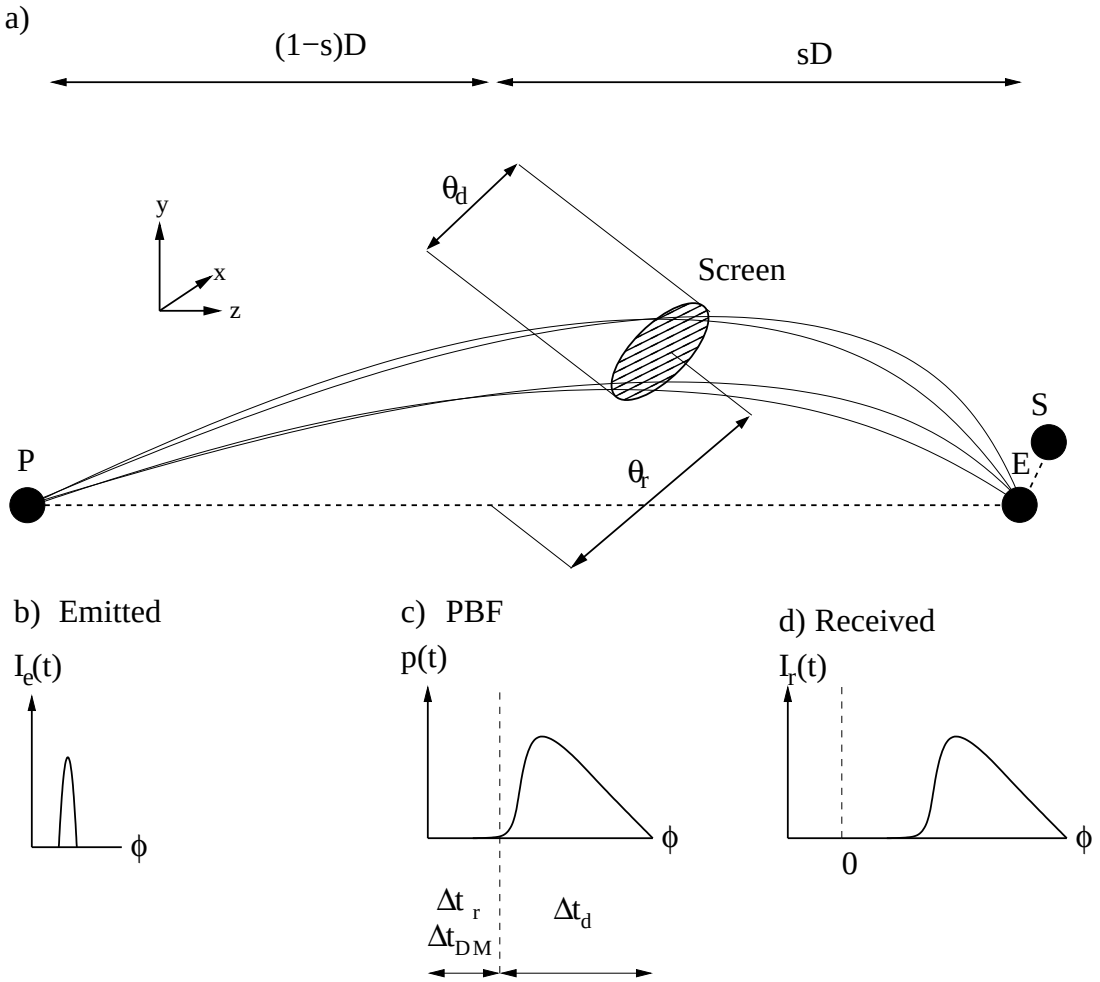

FIGURE 5.1.— *Panel a:* Propagation delay geometry. Observed TOAs are corrected to the solar system barycenter (circle S), assuming that the the radio waves propagate along a direct line of sight from the pulsar (circle P) to the Earth (circle E). In this analysis, scattering is assumed to be constrained to a thin screen located a distance *sD* from the Earth along the pulsar earth line of sight, where *D* is the pulsar distance. At the screen distance, the center of the tube is offset from the direct line of sight by an angle θ_r and has a width θ_d. Note that for clarity we have displayed a configuration with $\theta_r > \theta_d$. In most scattering configurations, the opposite is assumed to be true. The location of the tube, projected on the screen can also be characterized by an image intensity $B(\boldsymbol{\theta})$. *Panels b-d:* Schematic diagrams of the emitted pulse shape (*Panel b*), pulse broadening function $p(t)$ (*panel c*), and observed pulse shape (*panel d*).

rect line θ_r of sight impart a total delay to the pulse, respectively labeled Δt_r and $\Delta t_{\rm DM}$. The width of the tube θ_d causes the pulse to be broadened Δt_d. In general

the emitted pulse is much broader than the PBF and the net delay is the sum of the width of the PBF Δt_d, Δt_r, and $\Delta t_{\rm DM}$.

The effects of interstellar broadening are encapsulated in a pulse broadening function (PBF) $p(\tau, \nu)$, which we use synonymously with impulse response function to mean the function that accounts for both the distortion and delay to the observed pulse caused by the ISM. Using the PBF, the observed pulse $I_r(t, \nu)$ at an observation frequency of ν and pulse phase t is related to the emitted pulse $I_e t, \nu)$ by

$$I_r(t, \nu) = \int d\tau I_e(t, \nu) p(t - \tau, \nu), \tag{5.1}$$

The PBF is related to the image intensity $B(\boldsymbol{\theta})$ by (Cordes & Lazio 2001; Rickett 2006)

$$p(t, \nu) = \frac{\int d\boldsymbol{\theta} B(\boldsymbol{\theta}, \nu) \delta(\Delta t_{\theta}(\boldsymbol{\theta}, \nu) - t)}{\int d\boldsymbol{\theta} B(\boldsymbol{\theta}, \nu)}, \tag{5.2}$$

where $\Delta t_{\theta}(\boldsymbol{\theta}, \nu)$ is the net perturbation through point $\boldsymbol{\theta}$ in the image. In general, the image brightness is not directly observable because the image is very small compared to the resolution of radio telescopes. We note that equation 5.2 is valid for all scattering configurations and is merely a statement of conservation of energy, i.e, the flux in the observed pulse is equal to the flux in the image.

The shape of the observed pulse varies as the PBF changes with time. To determine the effect of the PBF on pulse arrival time it is in general necessary to perform implement a standard TOA estimation algorithm, in which the observed pulse is compared to a template (e.g., Taylor 1992). However, if the PBF is much narrower than the observed pulse, the TOA perturbation Δt is the mean of the PBF (Paper II)

$$\Delta t(\nu) = \int_0^{\infty} t p(t) dt. \tag{5.3}$$

This limit is applicable to precision timing observations because along these lines of sight, scattering is relatively weak at the typical observing frequencies [2] ($\nu \approx 0.5$ GHz to 3 GHz) and the width of the PBF is $\ll 1$ μs, is much less than the width of the most narrow ≈ 50 μs features in pulse profiles.

Substituting equation (5.2) into equation (5.3), the TOA perturbation is

$$\Delta t(\nu) = \frac{\int d\boldsymbol{\theta} B(\boldsymbol{\theta}, \nu) \Delta t_{\theta}(\boldsymbol{\theta}, \nu)}{\int d\boldsymbol{\theta} B(\boldsymbol{\theta}, \nu)}. \tag{5.4}$$

In this analysis, equation (5.4) is used to partition the propagation delay into different components, enabling the identification of unique scaling relationships in both observing frequency ν and fluctuation frequency f. Through a point on the screen $\boldsymbol{\theta}$ a sub-perturbation i contributes a net delay $\Delta t_{\boldsymbol{\theta},i}(\boldsymbol{\theta})$ and the image-averaged sub-perturbation is

$$\Delta t_i(\nu) = \frac{\int d\boldsymbol{\theta} \Delta t_{\boldsymbol{\theta},i}(\boldsymbol{\theta}, \nu) B(\boldsymbol{\theta}, \nu)}{\int d\boldsymbol{\theta} B(\boldsymbol{\theta}, \nu)}. \tag{5.5}$$

5.3 Wave Propagation and Thin Screen Scattering

At any instant the observed emission is the combination of scattered radio waves that have traveled many trajectories through a curved ellipsoidal (banana-shaped) tube displayed in Figure 5.1. The tube is characterized by an angular width θ_d, which can be related to the refractive length scale ℓ_r on the screen by $\theta_d \approx \ell_r/(sD)$, which is displayed in Figure 5.1.

Interstellar propagation effects can be divided into two classes distinguished

[2] We note there have been observations of interstellar scattering for some pulsars with lines of sight comparable to MSPs (e.g., Brisken et al. 2010) for which this limit may not be applicable; see Paper II for more details.

by different spatial scales. Density variations on small length scales (smaller than the size of the tube) are caused by the self interference of the radio emission. This interference is associated with path length differences and electron density variations along different trajectories within the tube, causing intensity variations in time and frequency. The emission shows variations in frequency because of the frequency-dependence of the phase of the electromagnetic waves and in time because of the changing pulsar Earth line of sight. These short term intensity variations are referred to as diffractive interstellar scintillation (DISS).

In addition to causing intensity variations, DISS causes time of arrival variations. Cordes et al. (1990) studied the connection between pulse times of arrival in the MSP B1937+21 on short time scales, and showed that at low observing frequencies DISS was limiting timing precision. C10 examined these effects in both simulations and observations and found in both cases there was a correlation between pulse arrival time and flux. However, in their observations of the MSP J0437−4715, the correlation between flux and TOA was orders of magnitude larger than expected. In other recent work, Hemberger & Stinebring (2008) monitored the slow pulsar B1737+13 over half a year and found that a pseudo-delay showed marked variation that, if unmitigated and present in timing array pulsars, would severely limit timing array sensitivity. However, the timing precision of the pulsar was insufficient to establish a correlation between the pseudo-delay and TOA. Between observation epochs these diffractive effects are stationary and can be treated as a white noise source.

On scales much larger than θ_d, electron density variations alter the shape of the tube and its position relative to the direct line of sight, resulting in both flux variations and changes in the characteristics of the DISS. These longer term

variations are referred to as refractive interstellar scintillation (RISS). Because these effects are caused by electron density fluctuations on scales much larger than the diffractive effects, they exhibit statistically non-stationary behavior. In the subsequent sections report on the analysis of these refractive effects.

5.3.1 Modeling the Image Intensity

In general it is necessary to model the observed radio emission by integrating over a large three dimensional space (Lambert & Rickett 1999). Because the ISM is turbulent, modeling radio wave propagation beyond second-moment statistical properties necessarily requires simulation. Unfortunately it is presently computationally prohibitive to conduct a full simulation of wave propagation because of the dynamic range necessary to model the wave propagation.

To conduct a full simulation requires the modeling of wave propagation down to the diffractive length scale ℓ_d, which is the length scale over which the ISM changes the phase of the radiowaves by $\approx \pi$ radians. For the lines of sight and observing frequencies relevant to pulsar timing, $\ell_d \approx 10^9$ cm. The largest length scales are different in each dimension of the full simulation. Along the line of sight (the z-axis of Figure 5.1), the length scale is the distance to the pulsar (nominally $\sim 10^{21}$ cm). In the direction of projected motion (the x-axis of Figure 5.1), the outer scale is the projected motion of the pulsar, ($V_p T \approx 10^{14}$ cm, for $V = 100$ km s^{-1}, and $T = 10$ yr). Perpendicular to the projected direction of motion (the y-axis of Figure 5.1), the scale refractive length scale ℓ_r (nominally 10^{13} cm for the pulsars and observing frequencies relevant here). For these typical values, to possess the required spatial dynamic range a computationally

impractical phase screen consisting of 10^{39} samples is required.

Two physically valid approximations make the simulations computationally viable. Firstly, scattering is assumed to be located in a geometrically thin phase-changing screen. Observations of diffractive intensity variations show that this is true most nearby pulsars (Stinebring et al. 2001; Cordes et al. 2006a; Putney & Stinebring 2006).

Even with this *thin screen* assumption it is unfeasible to conduct a simulation over the wide range of frequencies (a factor of 2 or greater) necessary for pulsar timing observations over the observing spans of $T = 5$ to 10 years relevant for GW detection. A computationally viable simulation of a two dimensional screen can be conducted by either reducing the total observing time and range of frequencies modeled or by neglecting diffractive effects. C10 chose to reduce both the range of frequencies modeled and total observing span. Over a narrow range of frequencies and an observing span of a few months, C10 conducted a full diffractive simulation. Because the simulations were conducted only over a narrow range of frequencies C10 assumed that dispersive delay could be perfectly corrected. This assumption is problematic and is discussed further below.

In the simulations we conduct, the screen resolution is reduced by modeling phase variations larger than the refractive length scale ℓ_r, which is much larger the diffractive scale. This enables the simulation of phase screens over a wide range of observing frequencies over $T = 10$ yr observing spans enabling a proper assessment of the nonstationarity of refractive propagation delays.

In the appendix to this chapter in §5.11, we present a model for the image intensity $B(\boldsymbol{\theta})$ that we summarize here. First, the location of unique subimages

are identified near stationary phase point. In these regions the waves can constructively interfere. Around each stationary phase point, the refractive phase is modeled using a paraboloid. It is assumed that the unmodeled diffractive phase variations follow ensemble average behavior, with a non-refracted image intensity $B_0(\boldsymbol{\theta})$. With these assumptions the wave propagation through the screen, modeled by the Kirchoff diffraction integral (KDI) can be determined and the intensity of the refracted image $B(\boldsymbol{\theta})$ is expressed as a function of the non-refracted image, with two modifications to the non-refracted image. Firstly, relative to the direct line-of-sight the image center is offset to the stationary phase point $\boldsymbol{\theta_0} = \boldsymbol{r_0}/(sD)$. Secondly, relative to the unperturbed image, the image is rotated and stretched along two principal axes. The distortion is parameterized by a 2×2 matrix $\boldsymbol{M}$. Therefore, the refracted image can be expressed as a function of the non-refracted image as

$$B(\boldsymbol{\theta}, \nu) = B_0\left(\boldsymbol{M}(\boldsymbol{\theta} - \boldsymbol{\theta_0}), \nu\right). \tag{5.6}$$

In addition to causing variable TOAs, the image shape variations cause flux variability. Relative to the non-refracted image, the flux is

$$F_{\rm rel}(\nu) = \frac{\int d\boldsymbol{\theta} B(\boldsymbol{\theta}, \nu)}{\int d\boldsymbol{\theta} B_0(\boldsymbol{\theta}, \nu)}. \tag{5.7}$$

We will also examine the correlation of this flux variability with TOA.

With this model for image intensity we can calculate the delays through the screen. Because these expressions only model paraboidal variations in refractive phase, they underestimate the strength of effects near caustics and other situations in which diffraction plays a strong role. To study these effects it is necessary to employ a diffractive simulation.

5.4 TOA Perturbations

5.4.1 Dispersive Perturbations

Through a point $\boldsymbol{\theta}$ on the screen the perturbation associated with the radiowave dispersion is

$$\Delta t_{\mathrm{DM},\boldsymbol{\theta}}(\nu) = -\frac{2\pi}{\nu}\Phi_r(\boldsymbol{\theta},\nu). \tag{5.8}$$

This perturbation is anti-correlated with the screen phase because the delay is associated with the group velocity (and not the phase velocity) of the propagating radio waves.

Averaged over the entire image, the delay is

$$\Delta t_{\mathrm{DM}}(\nu) = -\left(\frac{2\pi}{\nu}\right)\frac{\int d\boldsymbol{\theta} B(\boldsymbol{\theta},\nu)\Phi_r(\boldsymbol{\theta})}{\int d\boldsymbol{\theta} B(\boldsymbol{\theta},\nu)}. \tag{5.9}$$

This delay is both deterministically and stochastically wavelength dependent. By expanding about the direct line of sight, the different components are identified as

$$\begin{aligned}\Delta t_{\mathrm{DM}} \quad &= -\left(\frac{2\pi}{\nu}\right)\Phi_r(0) - \left(\frac{2\pi}{\nu}\right)\Phi_{\mathrm{SPP}}(0) \\ &\quad -\left(\frac{2\pi}{\nu}\right)\frac{\int d\boldsymbol{\theta} B(\boldsymbol{\theta})\left[\Phi(\boldsymbol{\theta}) - \Phi_{\mathrm{SPP}}(0) - \Phi(0)\right]}{\int d\boldsymbol{\theta} B(\boldsymbol{\theta})} \\ &= \Delta t_{\mathrm{DM}} + \Delta t_{\mathrm{DM},C} + \Delta t_{\mathrm{DM},I}. \end{aligned} \tag{5.10}$$

The first term Δt_{DM} in equation (5.10) is the group delay along the direct line of sight. It is entirely correlated between observations at different frequencies, and is completely removed by the standard DM correction scheme (You et al. 2007). The second term $\Delta t_{\mathrm{DM},C}$ is the delay through the center of the image (i.e, the

delty through the SPP). This term is not perfectly correlated between different observing frequencies because the location of the SPP varies with frequency. The third term $\Delta t_{\mathrm{DM},I}$ is associated with the averaging of the phase across the image B, and also changes with frequency and time. At lower frequencies the scattered image is larger and the delay measured across the image is averaged over a larger portion of the phase screen. The shape and the location of the image decorrelate with increasingly widely separated frequencies.

5.4.2 Geometric Delays

There are TOA variations associated with the variable path length through the refracted image that we classify as geometric perturbations. Pulse TOAs are determined at the observatory and then referred to the solar system barycenter (SSB) using a model for the position of the Earth. This correction depends on the assumed position of the pulsar, which is found to highest precision by modeling the TOAs.

To identify the delays associated with RISS, it is necessary to compare the corrected SSB arrival time in the absence and presence of the refracting screen. To calculate these delays, we define a coordinate system with the SSB at the origin, the pulsar at position $\boldsymbol{D} = D\hat{\boldsymbol{n}}$, and the earth is at time variable location $\boldsymbol{r}(t)$. For simplicity, the pulsar is assumed to be stationary.

In the absence of a refracting screen, the travel time from the pulsar to the solar system barycenter is

$$\Delta t_{\odot} = \frac{D}{c}, \tag{5.11}$$

and the time for the pulse to travel to the Earth is

$$\begin{aligned}\Delta t_{\oplus} &= \frac{1}{c}\,|\boldsymbol{D} - \boldsymbol{r}_{\oplus}| \\ &\approx \frac{D}{c}\left[1 + \frac{1}{2}\left(\frac{r_{\oplus}^2}{D^2} - \frac{2\boldsymbol{r}_{\oplus}\cdot\hat{\boldsymbol{n}}}{D}\right)\right].\end{aligned} \tag{5.12}$$

Thus in the absence of the screen a correction $\Delta t = T_{\oplus} - T_{\odot}$ is applied to properly refer the arrival times to the SSB:

$$\Delta t = -\frac{1}{c}\,(\boldsymbol{r}_{\oplus}\cdot\hat{n}) + \frac{1}{2c}\frac{r_{\oplus}^2}{D}. \tag{5.13}$$

The first term is associated with the pulsar position on the sky and results in an 1 yr periodic variation in the TOAs. The second term is associated entirely with the solar system ephemeris.

In the presence of a thin scattering screen, the path length to the Earth is increased relative to the direct line of sight. The additional travel time through a point in the screen offset $\boldsymbol{r}$ from the direct line of sight is

$$\begin{aligned}\Delta t_{\oplus,s}(\boldsymbol{r}) &= |(1-s)D\hat{\boldsymbol{n}} + \boldsymbol{r}| + |sD\hat{\boldsymbol{n}} + \boldsymbol{r} - \boldsymbol{r}_{\oplus}| \\ &\approx \frac{D}{c} + \frac{1}{2c}\left[2(\boldsymbol{r} - \boldsymbol{r}_{\oplus})\cdot\hat{\boldsymbol{n}} + \frac{r^2}{(1-s)D} + \frac{(\boldsymbol{r} - \boldsymbol{r}_{\oplus})^2}{sD}\right].\end{aligned} \tag{5.14}$$

The total geometric propagation perturbation is the difference between equations (5.14) and (5.12):

$$\Delta t_g(\boldsymbol{r}) = \frac{1}{2c}\left[2\boldsymbol{r}\cdot\hat{\boldsymbol{n}} + \frac{r^2 - 2(1-s)\boldsymbol{r}\cdot\boldsymbol{r}_{\oplus}}{s(1-s)D} + \left(\frac{1-s}{s}\right)\frac{r_{\oplus}^2}{D}\right]. \tag{5.15}$$

Substituting $\boldsymbol{\theta} = \boldsymbol{r}/(sD)$, and noting that $\boldsymbol{r}\cdot\hat{\boldsymbol{n}} \equiv 0$, the total geometric perturbation is

$$\Delta t_{g,\boldsymbol{\theta}}(\boldsymbol{\theta}) = \left(\frac{D_p}{2c}\right)\left(\frac{s}{1-s}\right)\theta^2 - \frac{1}{c}\boldsymbol{\theta}\cdot\boldsymbol{r}_{\oplus} + \left(\frac{1-s}{s}\right)\frac{r_{\oplus}^2}{cD}. \tag{5.16}$$

The first term in equation (5.16) is the geometric delay through the screen. The second term in equation (5.16) is due to incorrectly calculating the arrival time of the pulse at the solar system barycenter. The final term in equation (5.16) is nearly constant in time because the Earth's motion about the SSB is nearly circular and is henceforth ignored.

In the case of a single stationary phase point (thus a single subimage), the geometric delay averaged over the image is found by substituting equation (5.16) into equation (5.5) and integrating over $\boldsymbol{\theta}$,

$$\begin{aligned}\Delta t_g(\nu) \quad &= \left(\frac{D}{2c}\right)\left(\frac{s}{1-s}\right)\theta_0^2 - \frac{1}{c}\boldsymbol{\theta_0}\cdot\boldsymbol{r}_\oplus \\ &\quad + \frac{1}{\det \boldsymbol{M}}\left(\frac{D}{2c}\right)\left(\frac{s}{1-s}\right)\theta_d^2,\end{aligned} \tag{5.17}$$

where it is assumed that the non-refracted image is centered on the origin, i.e.,

$$\int \boldsymbol{\theta} B_0(\boldsymbol{\theta}) d\boldsymbol{\theta} = 0, \tag{5.18}$$

and θ_d^2 is the mean squared deflection angle,

$$\theta_d^2 \equiv \frac{\int \theta^2 B_0(\boldsymbol{\theta}) d\boldsymbol{\theta}}{\int B_0(\boldsymbol{\theta}) d\boldsymbol{\theta}}. \tag{5.19}$$

We note that θ_0, θ_d, and $\boldsymbol{M}$ all vary with observing frequency and time. Many of the perturbations contain terms that are at least partially stochastic.

We additionally note that the expressions derived in this section are approximated to first order in $\boldsymbol{r}_\oplus/D$. If we were to expand to second order we would find additional corrections associated with curvature of the wavefield (e.g., parallactic terms).

5.4.3 Total Delay and Scaling Laws

The total delay $\Delta t_{\rm tot}$ is the sum of equations (5.9) and (5.17). These perturbations have fluctuations that vary in both radio frequency and time. In Table 5.1 we summarize the scaling dependencies of the terms with radio frequency ν and fluctuation frequency f. We show the scalings for the image shape parameters: phase Φ, the components of the vector $\boldsymbol{\theta_0}$, and matrix $\boldsymbol{M}$. We also show the scalings for the TOA perturbations which are in general functions of these terms. To estimate the scalings we assume that the phase has power law variations (equivalent to assuming that the electron density variations follow a power law) and that its structure function can be expressed as

$$D_\Phi(\boldsymbol{b}) \equiv \langle \Phi(\boldsymbol{r})\Phi(\boldsymbol{r}+\boldsymbol{b})\rangle = \pi^2 \left(\frac{b}{\ell_d}\right)^{\beta-2}, \tag{5.20}$$

where ℓ_d is the diffractive scale.

The perturbations show three distinct scalings with radio frequency, indicating that observations at four frequencies are necessary to recover an achromatic signal of interest within the TOAs. Because some of the scalings depends on the power spectrum of the phase variations, proper correction requires that β be constrained. This can accomplished by using the TOA observations themselves (requiring observation at a fifth observing frequency), or analysis of ancillary information such as the observations of DISS or DM variation observations.

The perturbations show a wide variety of time variability because they have power spectra with spectral indexes nominally between −2 and +2. The perturbations show non-stationarity that is different than expected from the gravitational wave background, which has power spectra with spectral indices between −4 to −5, for background formed from MBH binaries (Jaffe & Backer 2003)

TABLE 5.1
RADIO FREQUENCY AND FLUCTUATION FREQUENCY SCALING LAWS

Parameter	RF	FF
	Shape	
Φ	-2	$-\beta$
θ_r ($\propto \partial\Phi$)	-2	$-\beta+2$
$\boldsymbol{C}$ ($\propto \partial^2\Phi$)	-2	$-\beta+4$
θ_d	$-\gamma$	0
	TOA Perturbations	
$\Delta t_{\rm DM}$	-2	$-\beta$
$\Delta t_{\rm DM,C}$	-24	$-\beta+2$
$\Delta t_{\rm DM,S}$	$-2-\gamma$	$-2\beta+4$
$\Delta t_{\rm Bary}$	-2	$-\beta+2$
$\Delta t_{\rm Geo}$	-4	$-2\beta+4$
$\Delta t_{\rm Diff}$	$-2-\gamma$	$-\beta+4$
	Gravitational Wave Background	
GWB	0	-4 to -5

NOTE.—Scalings laws for the strengths of different perturbations in radio frequency (RF) and fluctuation frequency (FF). The medium is assumed to have a density fluctuations with a power law density fluctuations $P_\Phi \propto q^{-\beta}$. In the top row, the scaling with respect to properties of the refracted image are displayed. In the bottom rows the scalings for the various TOA perturbations are displayed. Note that $\gamma \equiv 2\beta/(\beta-2)$.

or cosmic strings (Damour & Vilenkin 2005), respectively. The signal imparted by interstellar propagation may more strongly mimic other classes of GW emitting sources, such as single continuous wave sources, or bursts of gravitational waves (Finn & Lommen 2010; Yardley et al. 2010). Other applications of long term timing such as analysis of orbital motion of systems, system proper motion and distances (via timing parallax) are extracted from periodic components. For example, pulsar position fits is affected by the annual barycentric correction term. Mitigation strategies are discussed in detail in §5.6.

5.5 Simulating Refractive Perturbations

We conducted a series of simulations for a wide variety of screen and observations configurations to determine the strength of the propagation effects and assess the efficacy of mitigation techniques. A detailed description of the simulation implementation is presented in an appendix to this chapter in §5.12. The pulsar and earth are assumed to be static so that at at any time the phase can be expressed as $\Phi(\boldsymbol{x}, t) = \Phi(\boldsymbol{x} - s\boldsymbol{V}_p t)$.

5.5.1 Generating Phase Screens

Phase variations are modeled on a grid, with the grid size and spacing constrained by the required dynamic range of the simulation. The screen must be sufficiently large to model the largest relevant length scales. In the direction perpendicular to motion, the screen must be sufficiently large to model the image size at the lowest frequency (the frequency at which the image has the largest size). In the direction of projected motion, the screen must be sufficiently large to model the motion of the pulsar across the screen or the refractive scale at the lowest frequency, whichever is larger. The screen must have sufficient resolution to over-resolve the image at the highest observing frequency (the frequency at which the refractive scale is the smallest). Fluctuations are generated that follow a predetermined fluctuation power spectrum $P_\Phi(q)$ in the ensemble average.

Additionally, it is assumed that the outer scale of the medium $L_0 = 1/q_0$ (the length scale at which the phase variations become stationary) is larger than the

screen size $L_{\rm max} = 1/q_{\rm max}$ and the inner scale $L_{\rm in}$ is much smaller than the smallest scale of the simulation $L_{\rm min} = 1/q_{\rm min}$. To model the smoothing caused by DISS, a Gaussian low pass filter is applied to the screen in the Fourier domain $W(q) = \exp(-q^2/2q_r^2)$ where $q_r = 1/\ell_r$. In Figure 5.2 we display the schematic ensemble average power spectrum of the fluctuations and relevant lengths scales of the simulation.

5.5.2 Calculating the Perturbations

At each time and observing frequency, the refracted image $B(\boldsymbol{\theta})$ is determined by locating stationary phase points (SPPs) using a grid search. Around each of the SPP the phase Φ_r is approximated with with paraboloid. The total perturbation is found by numerically integrating Equations (5.9) and (5.17) over the scattered image formed around stationary phase points. In the simulations presented here, we assume that there is only one SPP per epoch.

5.5.3 Simulation Properties

With these simulations we investigated a variety of scattering screen and observing configurations. The simulations were based on media with fluctuations containing power-law spectra with a variety of screen strengths. The diffractive scintillation bandwidth $\Delta\nu_d$ at a reference observing frequency $\nu_{\rm REF}$ was used as a proxy for screen strength.

A wide range of observation configurations were investigated. We examined perturbations on a wide range of frequencies (enabling us also to investigate the

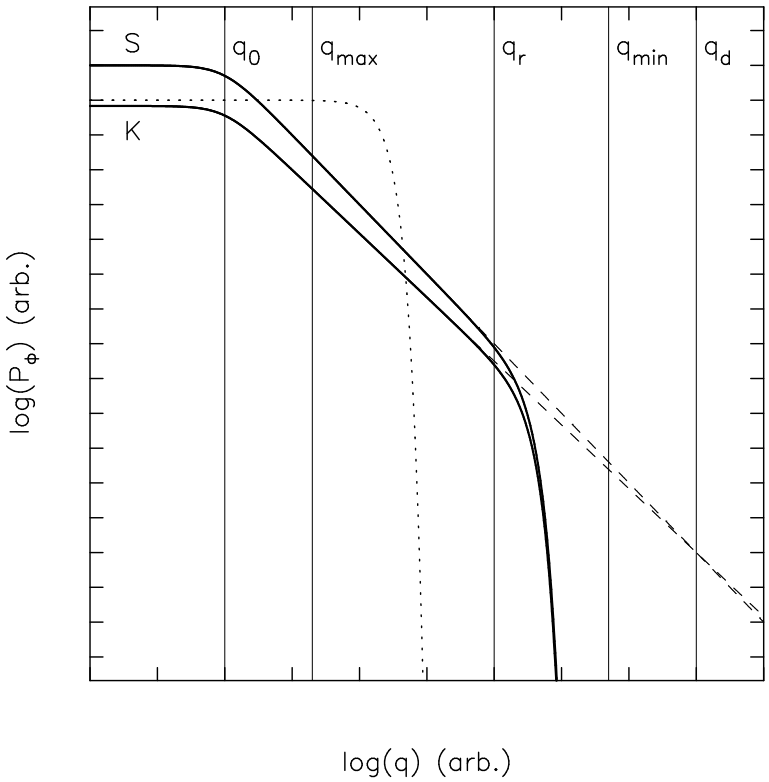

FIGURE 5.2.— Schematic power spectra $P_\phi(q)$ versus spatial frequency q for square law ($P_\phi \propto q^{-4}$, upper curve S) and Kolmogorov ($P_\Phi \propto q^{-11/3}$, lower curve K) media. The media are calibrated such that they have the same size fluctuations at the diffractive scale $\ell_d = 1/q_d$. The simulation only includes structures with between the maximum length scale of the simulation $q_{\rm max} = 1/L = 1/(V_{\rm eff}T)$, where $V_{\rm eff}$ is the effective motion of the line of sight across the screen and T is the total observing span; and the minimum length scale in the medium $q_{\rm min}$, which is the refractive scale at the highest observing frequency. While the electron density contains fluctuations over a wide range of scales (thin dashed lines), the phase fluctuations are smoothed to the refractive scale to properly model DISS smoothing (thick lines). The dotted line represents the power spectrum used for the smooth media simulations, discussed in §5.5.4.

effect of observing bandwidth), with a range of levels of white noise.

For the simulations presented here, a total of $N_{\rm TOA} = 500$ TOAs were simulated at evenly spaced intervals over $T = 5$ yr observing span. This observing span matches nominal PTA observing campaign expected to detecting stochastic GWBs with moderate confidence (paper I; Jenet et al. 2005).The TOAs were

simulated at 11 radio frequencies, with a range of total bandwidths.

Where not explicitly stated, the screen parameters are the default values listed in Table 5.4 in Appendix 5.12 and are henceforth referred to as the *standard simulation*. These simulations nominally follow the scattering properties of the well-studied MSP B1937+21. For the standard simulation, TOAs were simulated at evenly spaced frequencies from $\nu = 1$ GHz to 2 GHz. This range was chosen because it matches the $2:1$ bandwidth capability of present and near-future feeds and backends (Ransom et al. 2009) in a frequency band expected to be useful for pulsar timing. At higher frequencies pulsars are fainter and timing decrease timing precision. At lower frequencies propagation effects including both the effects discussed here and related DISS effects decrease TOA precision (Paper II).

5.5.4 Phenomenology

In this section we present some of the basic properties of the simulation. To show that the simulations are realistic, we investigate perturbations associated with smooth media (i.e., media that have perturbations at length scales much larger than ℓ_r) to demonstrate the validity of the implementation. We then examine more closely turbulent media.

Smooth Media

Smooth screens were generated in the Fourier domain. The screens were set to have correlations only on length scales $\ell_c \gg \ell_r$. Complete details of this

implementation are provided in an appendix to this chapter in §5.12.

Single realizations of TOA perturbations associated with this type of phase screen are displayed in Figure 5.3. In the leftmost panels of Figure 5.3 the perturbations associated with one realization of this type of screen media as a function of time at two widely spaced frequencies are displayed. The perturbations show fluctuations on large scales compared to the turbulent media described in the next section.

In the center column of panels in Figure 5.3, the scaling of the perturbations versus time,

$$\gamma_i(t) = \log(\Delta t_i(\nu_1)/\Delta t_i(\nu_2))/\log(\nu_1/\nu_2) \tag{5.21}$$

are displayed. The perturbations show values close to the expected scalings presented in Table 5.1. We note that when the perturbations get close to zero, the values γ diverges away from the expected value because of numerical round-off error. Even with the smooth phase screen there is a slight variation in γ for some of the terms, because at the different frequencies the SPPs are located at slightly different positions.

Using the best-fit values of γ from the center panels, the infinite frequency perturbation can be extrapolated using

$$\Delta t_{i,\infty} = \Delta t_i(\nu_1) - \left(\frac{\nu_1}{\nu_2}\right)^{\gamma} \Delta t_i(\nu_2). \tag{5.22}$$

If the perturbation can be perfectly corrected $\Delta t_{i,\infty} = 0$. For each perturbation, Δt_∞ is displayed in the rightmost column of Figure 5.3. Even in the case of smooth media, the correction is not perfect.

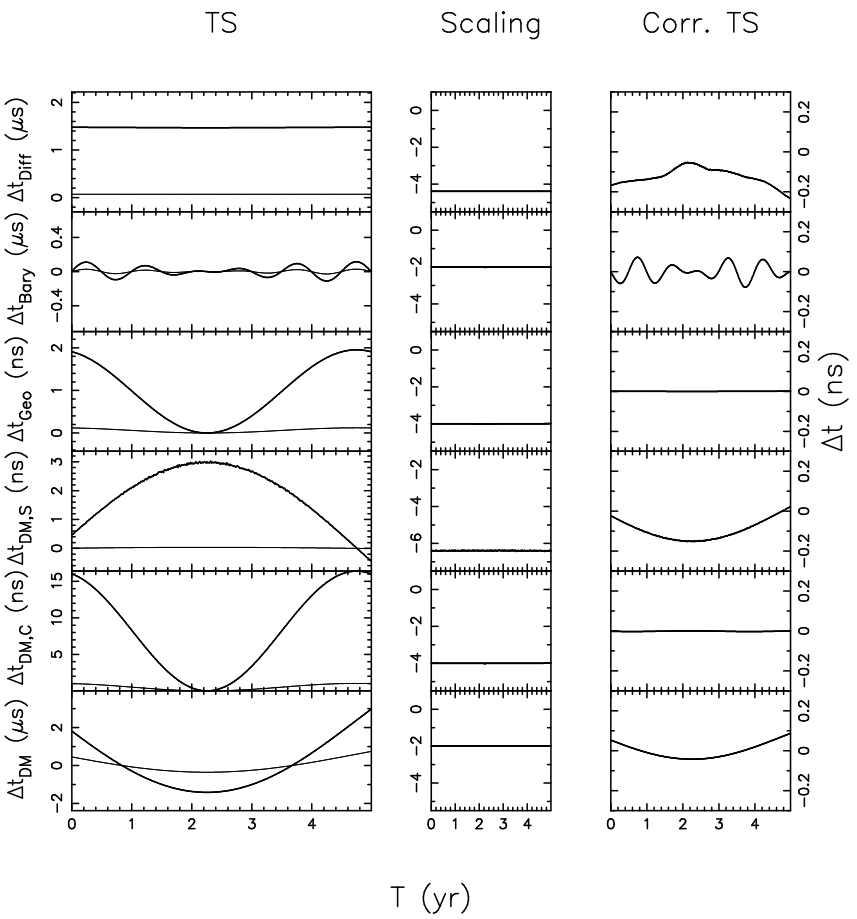

FIGURE 5.3.— Multi-frequency perturbations to times of arrival for a smooth phase screen. In the left series of panels the perturbations for both a low observing radio frequency (thick lines) and a high observing frequency (thin lines) are displayed. In the center series of panels, we show the scaling with time, which is defined in equation (5.21). In the right series of panels we show the TOAs corrected to infinite frequency, which is defined in equation (5.22), using the two frequency perturbations described shown in the left panels.

Turbulent Media

For the standard simulations single realizations of TOA perturbations at two observing frequencies are displayed in Figures 5.4 and 5.5 for a Kolmogorov-like thin screen, and 5.6 and 5.7 for a square-law like thin screen. In each case the scattering screens have the strength expected from PSR B1937+21. For each realization, the perturbations are displayed at observing frequencies of ν = 1 GHz

and ν = 2 GHz. Here we highlight a few qualitative properties of the perturbations, but note that large realization to realization variation in the strength and nature of the perturbations are exhibited because of the non-stationarity of the phase screen.

Strength and Stationarity: The root mean squared amplitude of the different perturbations range over a few orders of magnitude. The dispersion measure variations contributes a perturbation that has both the largest amplitude and the most non-stationary (i.e., most red) behavior. Most of the DM variations are correlated between observing bands. To identify the two components, we show the two terms of the dispersive delay as identified in equation (5.10): the dispersive delay through the direct line of sight $\Delta t_{\rm DM}$, through the image center $\Delta t_{\rm DM,C}$, and averaged over the image $\Delta t_{\rm DM,I}$. The barycentric correction term $\Delta t_{\rm Bary}$ shows quasiperiodic variations.

Frequency Scaling: The variations are larger and smoother at lower frequencies. The frequency scaling of the rms amplitudes of the perturbations are weaker than predicted in Table 5.1 because diffractive effects smooth and decorrelate observations.

Correlation between $\Delta t_{\rm DM,S}$ and $\Delta t_{\rm Diff}$: The dispersive delay associated with the center of the stationary phase point $\Delta t_{\rm DM,C}$ is directly correlated with the geometric delay, which was also recognized by C10 and in Paper II.

Differences between Kolmogorov and Square-Law Media: For the same scattering strength at a fixed reference frequency, the square-law like media show smoother perturbations, because the screen contains larger scale fluctuations. The barycentric correction term has a larger and more periodic component in

the square law simulation because prominent large scale structures refract the SPP farther away from the direct line of sight for longer periods of time (in some case, for many years).

Correlation between $\Delta t_{\rm Diff}$ *and Flux:* There have been previous reports of an anti-correlation between pulse arrival and refractive flux variations (Lestrade et al. 1998), and during extreme scattering events as well (Cognard et al. 1993). In the refractive simulations presented here, there is a modest correlation between flux (in the uppermost panels of s 5.4, 5.5, 5.6, and 5.7) and Δt. For square law media there is a large variation in the level of correlation from realization to realization. For Kolmogorov simulations there is a 20% to 40% anti correlation between flux and dispersive delay $t_{\rm DM}$, which is consistent with observations of B1937+21 reported by (Lestrade et al. 1998).

5.6 Mitigating Refractive Perturbations

We investigation mitigation approaches that mitigate the propagation effects using only time of arrival information. The goal of course is to determine the arrival time at the solar system barycenter in the absence of any interstellar medium. Because all propagation effects scale as power laws with negative spectral indexes with frequency, the desired arrival time is effectively the infinite frequency arrival time. Based on the power-law scalings for the perturbations derived in previous sections, an appropriate model for single epoch TOAs is

$$t(\nu) = t_\infty + \sum_{i=1}^{N_c} C_i \nu^{-X_i}, \tag{5.23}$$

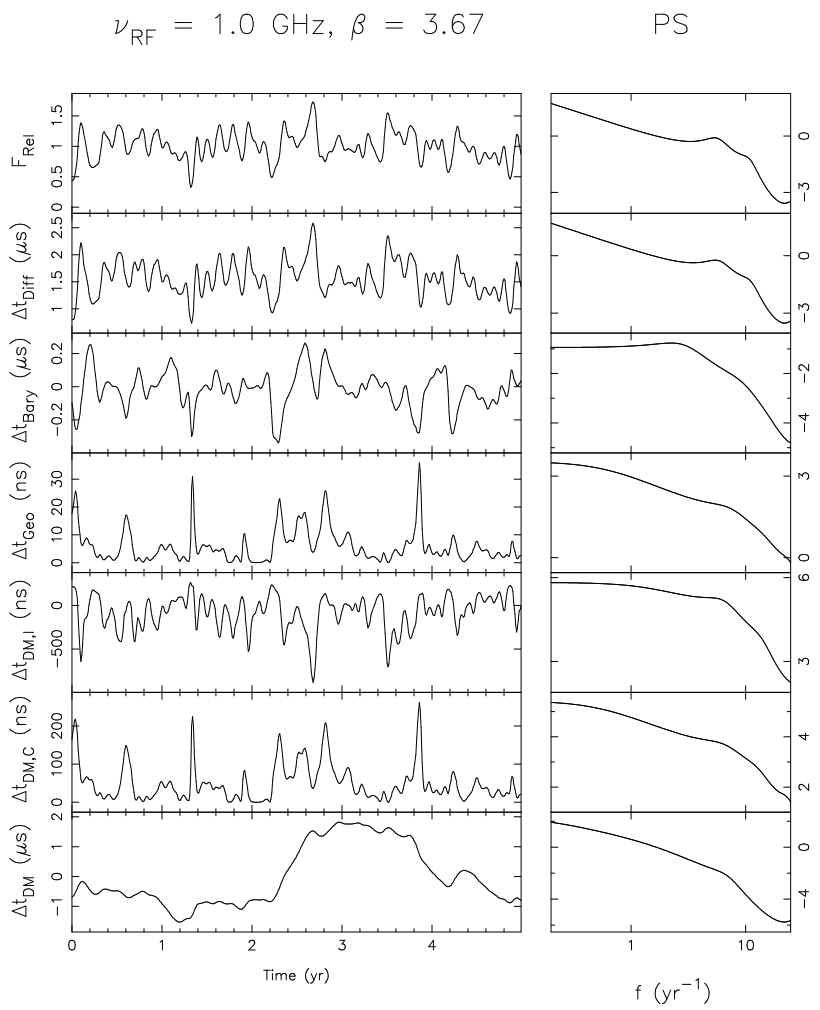

FIGURE 5.4.— Multi-frequency perturbations to times of arrival for Kolmogorov media, at observing frequencies ν_{RF} = 1.0 GHz for the same screen displayed in Figure 5.5. From bottom to top we display the dispersive perturbation through the direct line of sight Δt_{DM}, the dispersive perturbation associated with the center of the image $\Delta t_{DM,C}$, the dispersive delay associated with image averaging $\Delta t_{DM,I}$, the barycentric perturbation term Δt_{Bary}, the path length variation associate with the offset of the stationary phase point Δt_{Geo}, and the geometric perturbation associated with the averaging image Δt_{Diff}. We also display the flux, normalized to the non-diffracted flux F_{rel}. For each set of perturbations, we show perturbations and the maximum entropy power spectra. The amplitudes of the power spectra are labeled in base 10 units to the right of the plots in either μs^2 yr^{-1} of ns^2 yr^{-1}, in the same units as the in which the perturbations are expressed.

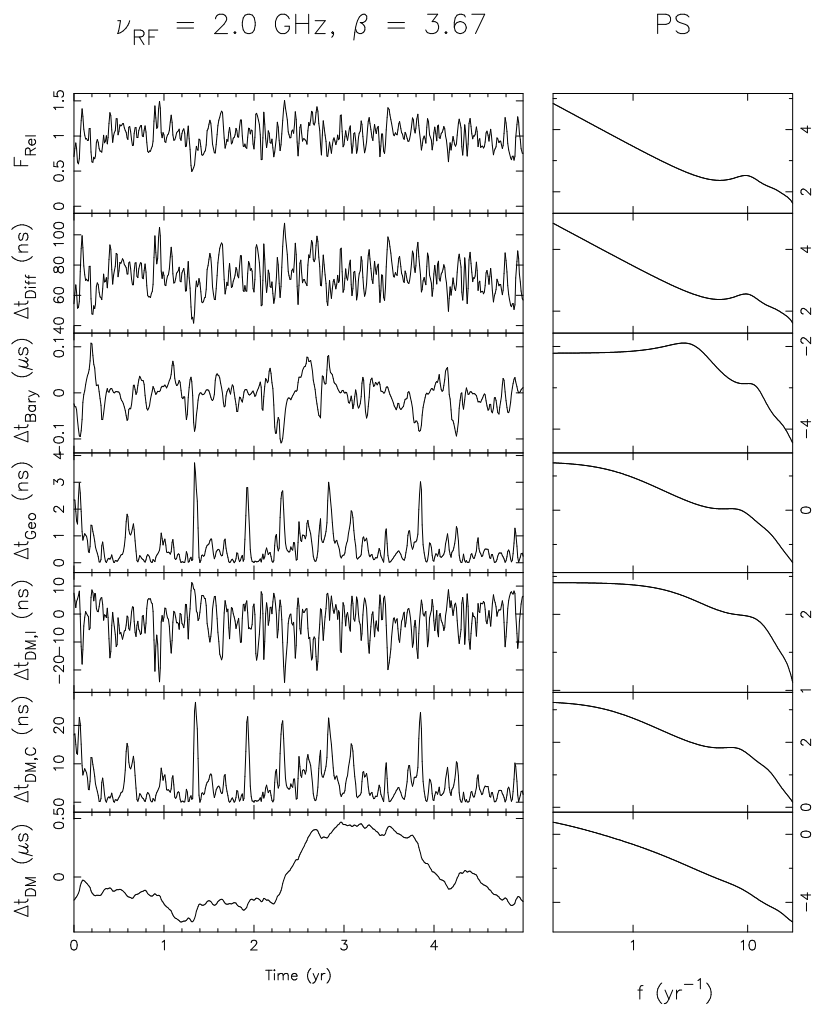

FIGURE 5.5.— Time of Arrival perturbations for a Kolmogorov media, at observing frequencies ν_{RF} = 2.0 GHz, for the same screen displayed in Figure 5.4. The plots are labeled the same as for Figure 5.4.

where t_∞ is the infinite frequency TOA; we emphasize that the goal of multi-frequency TOA fitting is to estimate this parameter.

There are five deterministic frequency scalings expected from the simulations: the achromatic term t_∞, ν^{-2}, ν^{-4}, $\nu^{\approx -4.4}$, and $\nu^{\approx -6.4}$. In the following discussion we start at the currently employed two coefficient mitigation strategy and extend to proceed to discuss higher-order strategies.

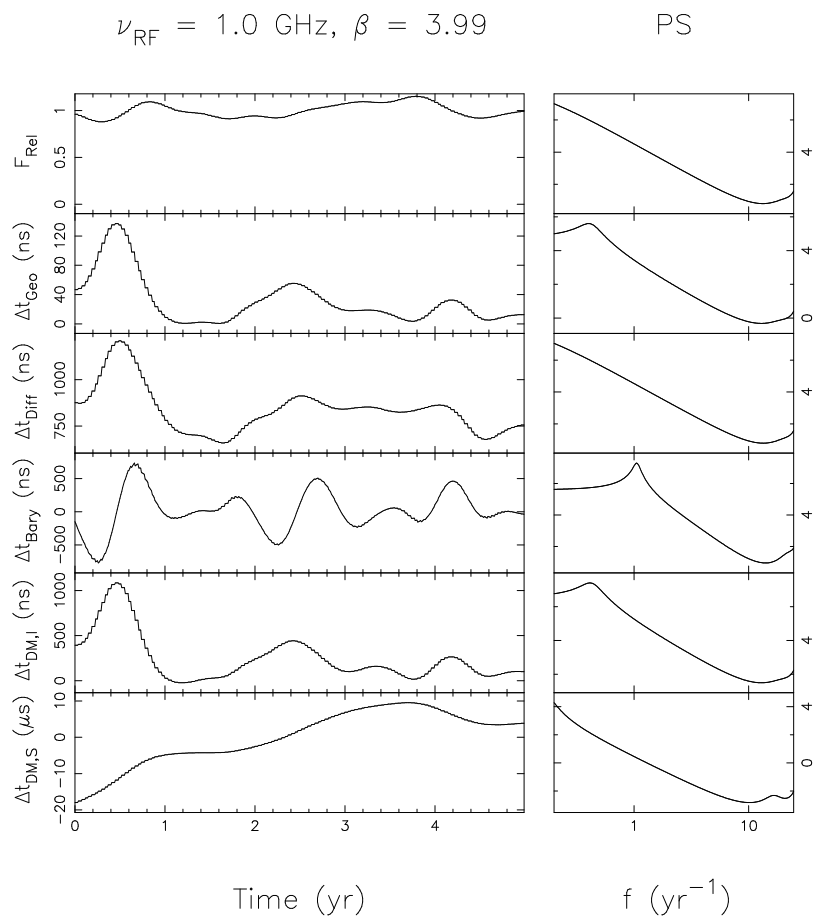

FIGURE 5.6.— Multi-frequency perturbations to times of arrival for square law-like media, at observing frequencies ν_{RF} = 1.0, for the same screen used in Figure 5.5. The plots are labeled the same as for Figure 5.4.

Two-coefficient mitigation: Presently TOA are mitigated assuming that the only propagation term is proportional to ν^{-2}. At each epoch (where we define an epoch as observations that are either simultaneous using a multi-frequency receiver, or contemporaneous using multiple observations separated by a few days), uncorrected TOAs are estimated at two widely separated frequencies. At each observing frequency ν, the TOAs $t(\nu)$ are modeled to contain two components: the infinite frequency achromatic component that potentially includes a GW perturbations and certainly other achromatic timing perturbations; and a term proportional to ν^{-2} associated mostly dispersion delay but also the

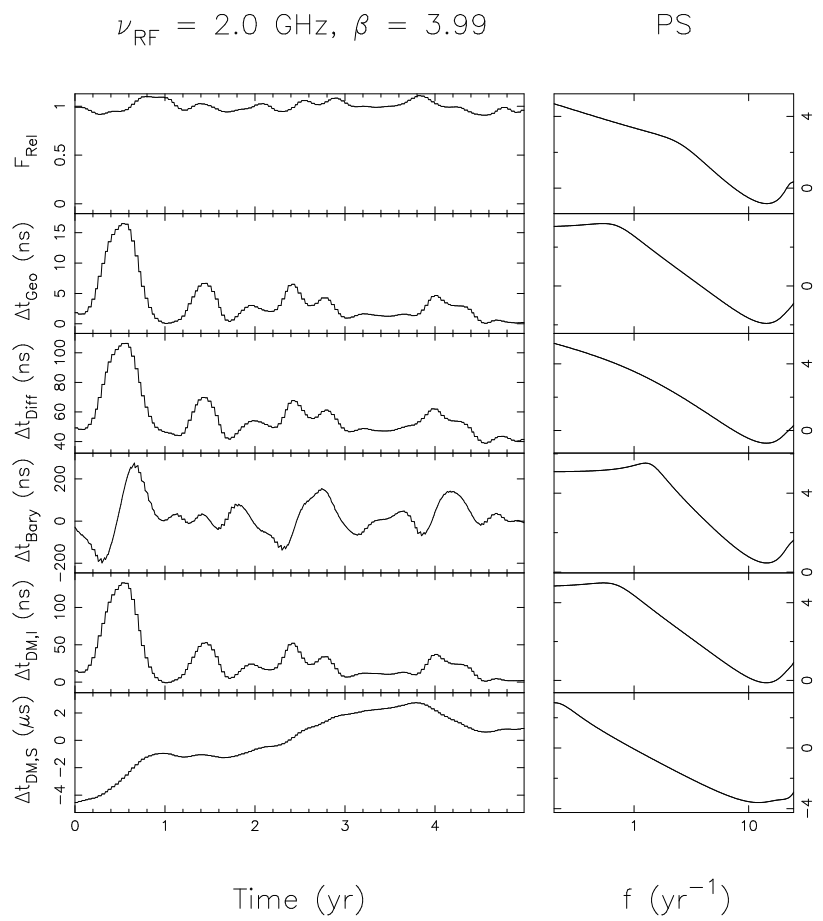

FIGURE 5.7.— Multi-frequency perturbations to times of arrival for square law-like media, at observing frequencies ν_{RF} = 2.0 GHz, for the same screen used in Figure 5.5. The plots are labeled the same as for Figure 5.4.

barycentric delay Δt_{Bary}:

$$t(\nu) = t_\infty^{(2)} + C_2^{(2)}\nu^{-2}. \tag{5.24}$$

Three-coefficient mitigation: In addition to the terms in the two-coefficient fit, a three-coefficient mitigation strategy has an additional term with frequency scaling $\propto \nu^{-X_3^{(3)}}$ with a value dependent on the line of sight configuration:

$$t(\nu) = t_\infty^{(3)} + C_2^{(3)}\nu^{-2} + C_3^{(3)}\nu^{-X_3^{(3)}}, \tag{5.25}$$

In a previous analysis, Foster & Cordes (1990) assumed $X_3^{(3)} = 4$, which assumes

that the geometric term $\Delta t_{\rm Geo}$ has the largest contribution after the dispersive delay.

Four-coefficient mitigation: Similarly, in the four coefficient model is

$$t(\nu) = t_\infty^{(4)} + C_2^{(4)}\nu^{-2} + C_3^{(4)}\nu^{-X_3^{(4)}} + C_4^{(4)}\nu^{-X_4^{(4)}}, \tag{5.26}$$

where the frequency scalings of $X_3^{(4)}$, $X_4^{(4)}$ depend on the properties of the medium.

No correction: If no chromatic terms are fit, the fitting model is formally

$$t(\nu) = t_\infty^{(0)}. \tag{5.27}$$

In subsequent analyses this uncorrected TOA will be compared to TOAs generated using other methods. This last method is not presently used for high precision timing but may be relevant if timing observations are conducted at much higher observing frequencies and DM variations are neglected.

5.7 Line of Sight dependencies

5.7.1 Optimal Mitigation Techniques

Before characterizing properties of the mitigated time series, it is necessary to establish values of the exponents that best mitigate the higher order terms. Based on the simulated perturbations, these exponents are expected to have values between 4 and approximately 7.

We considered two classes of observations: the first employs the minimal number of observation frequencies (e.g., three frequencies for the three mitiga-

tion technique) and those that used the a large number ($N_\nu = 11$) frequency channels. The former mimics the capabilities of older backends, in which timing observations were conducted with narrow bandwidths using different receivers, while the latter suitably models for modern and near-future observing systems.

Three-coefficient mitigation: We corrected times series using the three-coefficient technique with values of $X_3^{(3)}$ ranging from 3.0 to 10.0, for a large number of simulations. The average of the rms of these times series is plotted versus $X_3^{(3)}$ in Figure 5.8 for 30 realizations of both Kolmogorov-like and square-law like media using the standard simulation parameters.

For Kolmogorov-like medium, the minimum occurs at $X_3^{(3)} = 5.6$ for the three frequency and $X_3^{(3)} = 5.3$ for the eleven-frequency mitigation strategies. In both cases, the minima lie within a broad trough. The value of $X_3^{(3)}$ suggest that propagation is dominated in single realizations by either diffractive broadening of the refracted image or the offset of the image from the direct line of sight.

For the square-law like medium, the minimum occurs at $X_3^{(3)} = 4.5$, for both three-frequency fitting and $X_3^{(3)} = 4.4$ from the eleven frequency fitting. The value suggests that the second largest term is associated with the deviation of the refracted image from the line of sight.

In subsequent analysis we will use $X_3^{(3)} = 5.3$ for the analysis of Kolmogorov media and $X_3^{(3)} = 4.5$ for the square law medium.

Four-coefficient mitigation:

We conducted a grid search over distinct values of $X_3^{(4)}$ and $X_4^{(4)}$ ranging from

3.0 to 9.0 incrementing the values by 0.1. We searched for the pair ($X_3^{(4)}$,$X_4^{(4)}$) that minimized the RMS of 100 time series. For the standard simulations of square law-like media the minimum was found to occur near the edge of the simulation $(X_3^{(4)}, X_4^{(4)}) = (8.8, 9.0)$ for four frequency observations. The large values of the coefficients imply that the lowest frequency term is being mitigated. For the 11-frequency observations, the minimum was found to occur at $(X_3^{(4)}, X_4^{(4)}) = (6.1, 7.2)$ for 11-frequency observations.

For the standard simulations of Kolmogorov-like media, the minimum occurs at the edge of the simulation for four frequency $(X_3^{(4)}, X_4^{(4)}) = 6.9, 7.0)$ observations and at $(X_3^{(4)}, X_4^{(4)}) = (7.0, 7.4)$ for eleven frequency observations.

In Figure 5.8 the average RMS is plotted versus $X_4^{(4)}$. The parameter $X_3^{(4)}$ was fixed at the optimal three-coefficient model for both Kolmogorov-like and square-law like media. In the high signal to noise ratio cases presented here the approaches that use a limited number of frequencies are superior to the approaches that use a large number of frequencies. While this appears to be counterintuitive it is because the additional measurements of corrupt the estimation of t_∞, and is consistent with the parameter estimation error for t_∞ presented in equations (D11) and (D12) of Paper II.

In Table 5.2 we show the optimal scalings for selected scattering screen geometries and line of sight configurations. The optimal scalings depend on the scattering configuration because a frequency-correlated term must have a larger amplitude than any uncorrelated term across the time series. Neither three-frequency nor four-frequency mitigation techniques completely correct the time series because the perturbations contain a component that is stochastic in radio frequency.

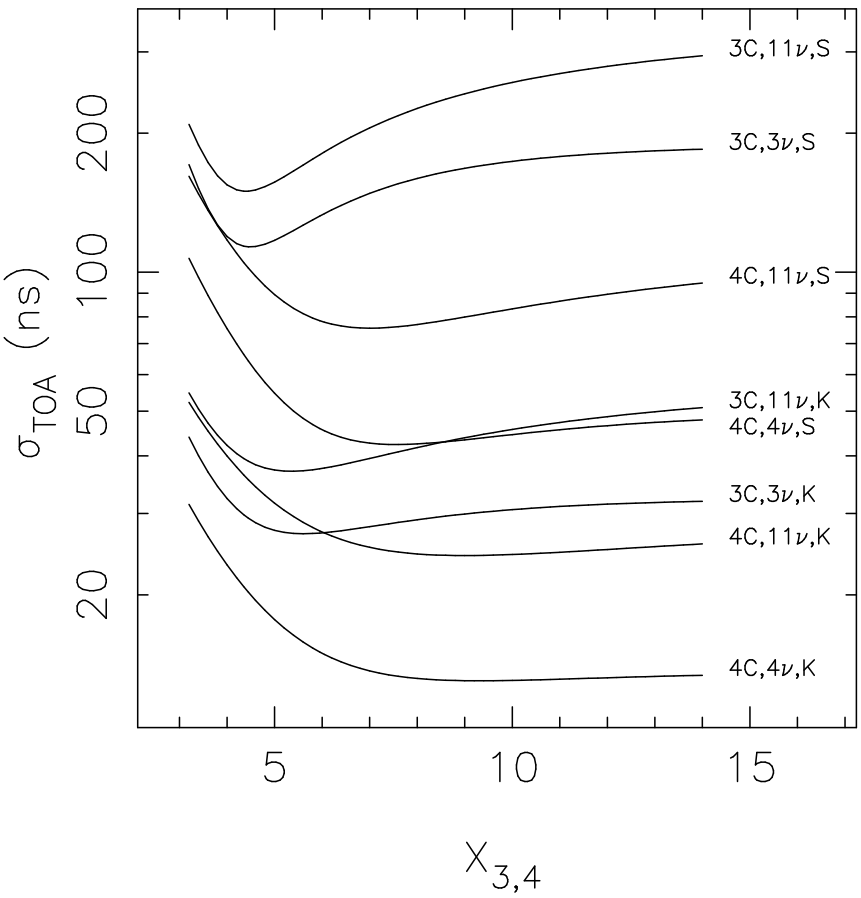

FIGURE 5.8.— Average RMS of the corrected time series $\sigma_{\rm TOA}$ versus exponential scalings of for 3-coefficient (X_3) and 4-coefficient mitigation schemes (X_4). The upper four lines, labeled *S* show the rms averaged over 30 realizations of square law-like media. The bottom four lines, labeled *K*, show the rms averaged over 30 realizations of the Kolmogorov media. Each mitigation scheme is labeled by the number of terms in the mitigation strategy and the number of frequencies channels employed. For example $3C, 11\nu$ refers to the 3-coefficient correction scheme with 11 frequency observations.

5.7.2 Corrected Time Series

In Figure 5.9 the corrected residuals for the same realizations of Kolmogorov screen as in Figure 5.4 and 5.5 are presented. In Figure 5.10 the corrected residuals for the same realizations of square-law media as in Figure 5.6 and 5.7 are presented. Three and four coefficient mitigation strategies result in smaller and

TABLE 5.2
BEST EXPONENTS

Screen Type	$3C, 11\nu$		$4C, 11\nu$		
	$X_3^{(3)}$	$\sigma_3(\mu s)$	$X_3^{(4)}$	$X_4^{(4)}$	$\sigma_4(\mu s)$
Kolmogorov-like					
1 – 2 GHz	5.3	37	7.0	7.4	23
0.5 – 2.5 GHz	6.2	107	7.2	7.6	56
Square-law Like					
1 – 2 GHz	4.4	156	5.4	5.8	74
0.5 – 2.5 GHz	4.5	438	5.4	5.8	202

NOTE.—Optimal mitigation strategies. For representative screen and observing configurations, we display the best-fit exponents X and the average rms σ of the corrected time series.

more stationary residual time series than two coefficient mitigation strategies. The benefits of three and four-coefficient correction are confirmed through analysis of a large number of realizations.

5.7.3 Dependence on Observing Span

In Figure 5.11, the rms of the residuals are plotted versus the observing span, for simulations similar to the standard simulations. The uncorrected residuals are highly nonstationary (increasing with $T_{\rm span}$). The corrected residuals (with perhaps the exception of the two coefficient residuals), are stationary after $\approx$ 0.5 year, when the time series reaches the refractive time scale.

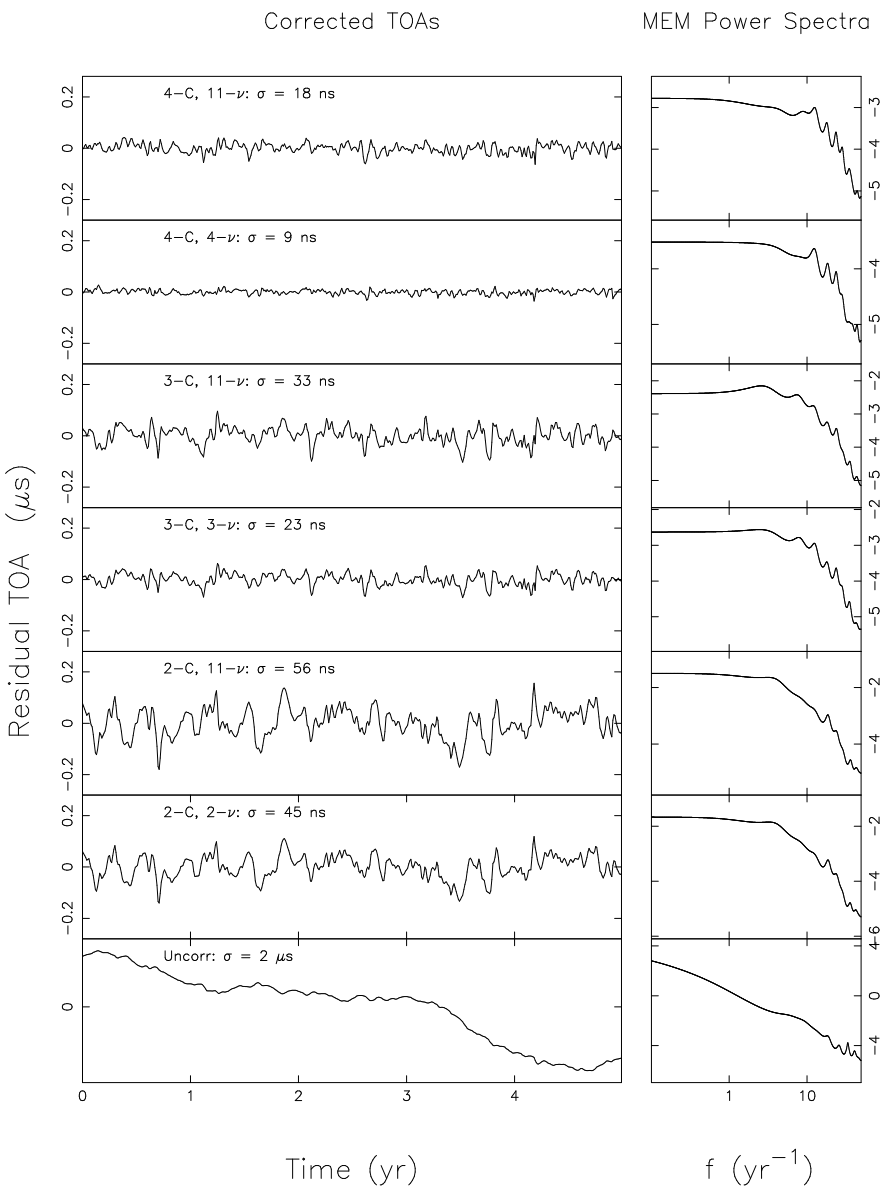

FIGURE 5.9.— Corrected TOAs for Kolmogorov-like media. These corrected TOAs correspond to the simulations presenting the perturbations displayed in Figures 5.4 and Figures 5.5. The mitigation schemes are as follows: $2C, 2\nu$: two coefficient model and two observing frequencies: 1.0 and 2.0 GHz. $3C, 3\nu$ - Three coefficients and three observing frequencies: 1.0, 1.4, and 2.0 GHz. $4C, 4\nu$: Four coefficients and four spot frequencies: 1.0, 1.4, 1.7, and 2.0 GHz. The $2C, 11\nu$ scheme, $3C, 11\nu$ scheme, and the $4C, 11\nu$ scheme use all eleven simulated frequencies and two-coefficient, three-coefficient, and four-coefficient mitigation strategies, respectively.

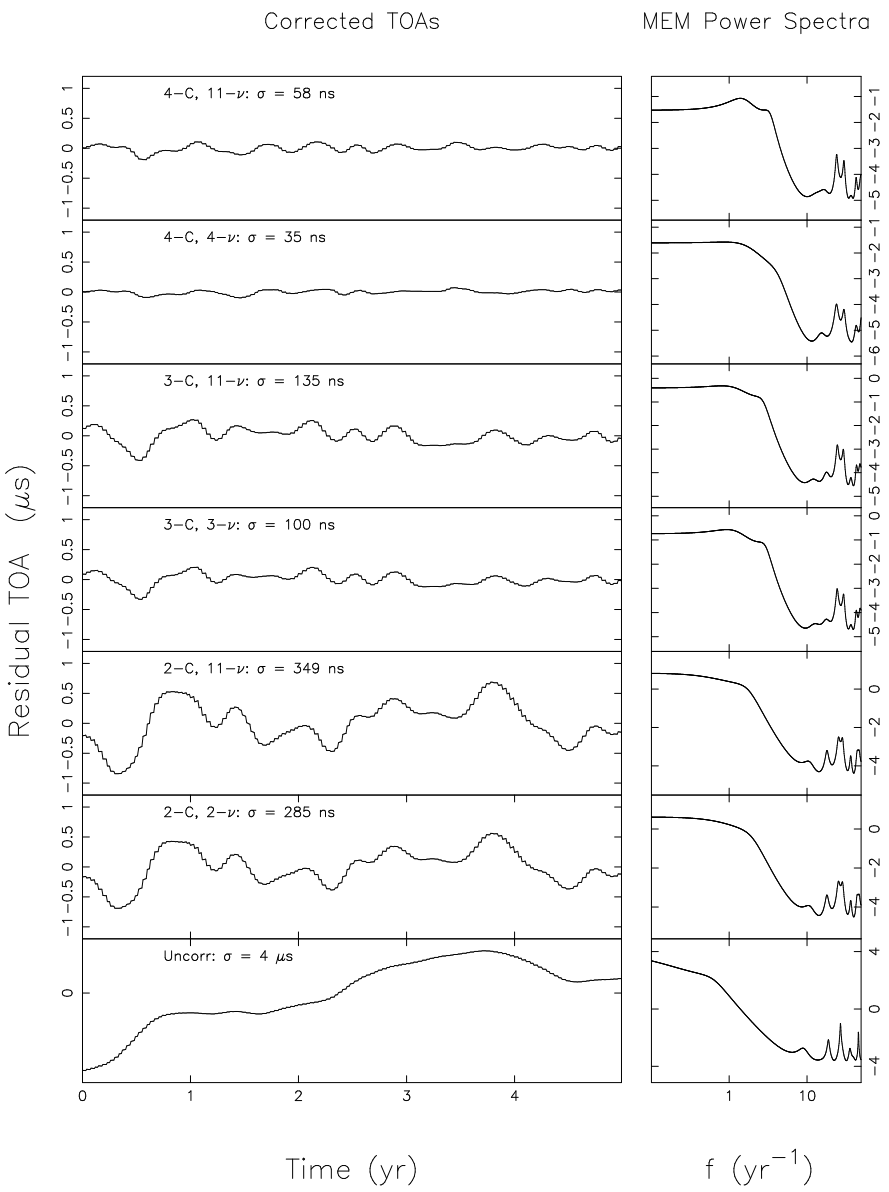

FIGURE 5.10.— Corrected TOAs for square-law like media. These corrected TOAs correspond to the simulations presenting the perturbations displayed in Figures 5.6 and Figures 5.7. The mitigation schemes are labeled using the same scheme discussed in Figure 5.10.

5.7.4 Media Type

We investigated the effect of media type on the amplitude of the residuals, for power law media with different spectral indices β, ranging from $\beta = 3.33$ to

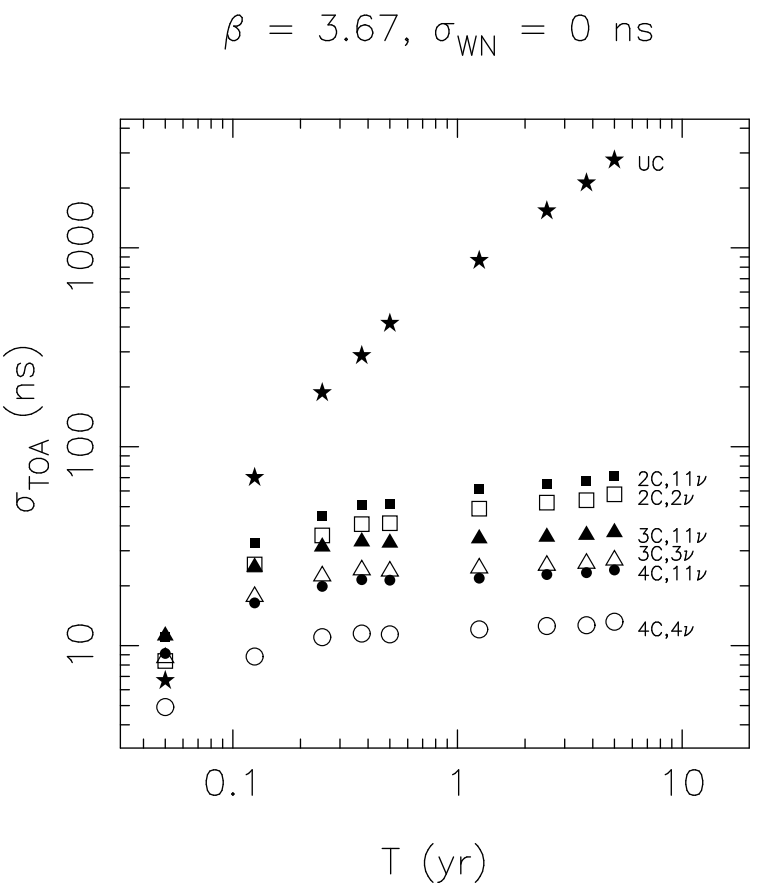

FIGURE 5.11.— RMS of the residuals $\sigma_{\rm TOA}$ versus observing span $T_{\rm span}$.

β = 3.99. In Figure 5.12 the rms of the residual time series is plotted versus β for simulations with values fixed at the standard simulation values. The time series were corrected using scalings X_3 and X_4 ideal for mitigating Kolmogorov-like media, as discussed in §5.7.1.

5.7.5 Scattering Strength

The levels of propagation noise in the corrected residuals is strongly correlated with the strength of scattering along the line of sight. Scattering strength was varied by altering the diffractive scintillation bandwidth at the reference fre-

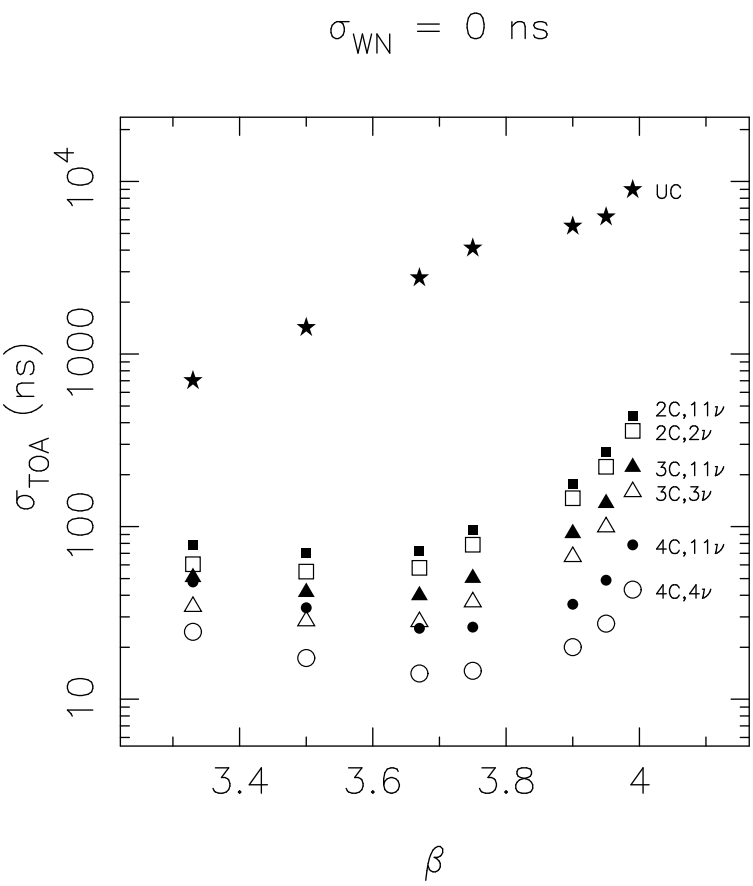

FIGURE 5.12.— RMS corrected arrival times $\sigma_{\rm TOA}$ for media with different power law indices β.

quency $\Delta\nu_d(\nu_{\rm REF})$. The average rms of the corrected time series are plotted versus $\Delta\nu_d(\nu_{\rm REF})$ in Figure 5.13.

5.7.6 Distance

In Figure 5.14 we show the rms of the corrected time series versus the distance to the pulsar D. For the uncorrected media, the rms decreases with increasing distance. However, for the corrected time series, the rms marginally increases for square law medium and is basically uncorrelated for square-law media. The rms is not strongly dependent on distance because the line-of-sight scattering

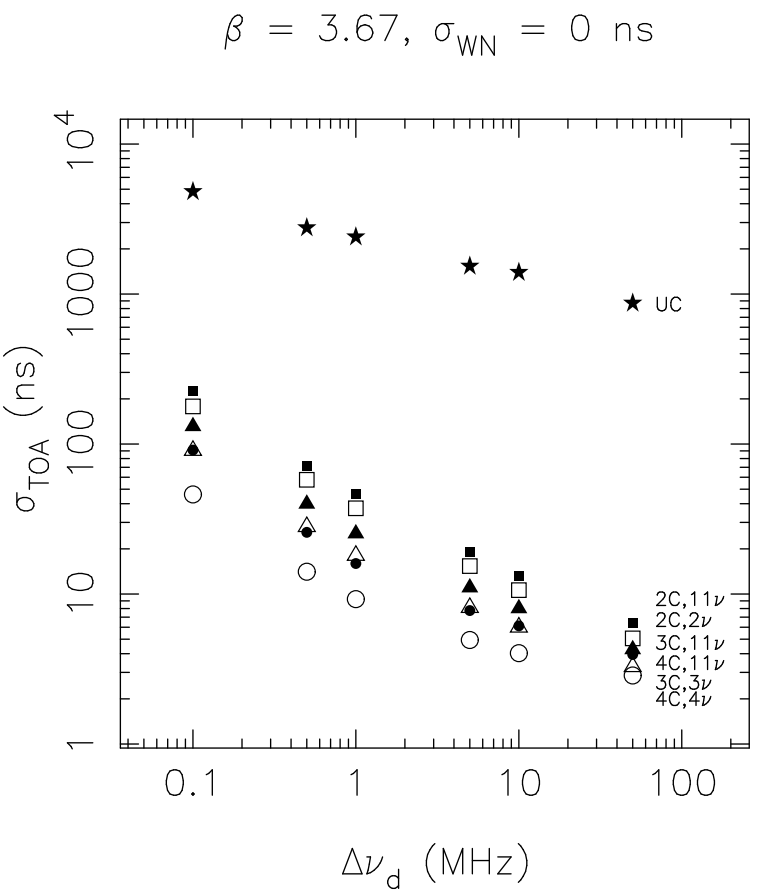

FIGURE 5.13.— Average rms of the corrected time series $\sigma_{\rm corr}$ versus diffractive scintillation bandwidth $\Delta\nu_d$ measured at 1.2 GHz, for for a Kolmogorov media (β = 3.67).

strength is absorbed in the diffractive scintillation bandwidth $\Delta\nu_d$, which itself depends strongly on the observing distance.

5.7.7 Other Line-of-Sight Dependencies

In the previous subsections, we have characterized particular line of sight properties that we suspected would cause order of magnitude variations in amplitude of the TOA perturbations. Other line of sight properties will certainly cause variations in propagation properties. For example, the pulsar space velocity V_p

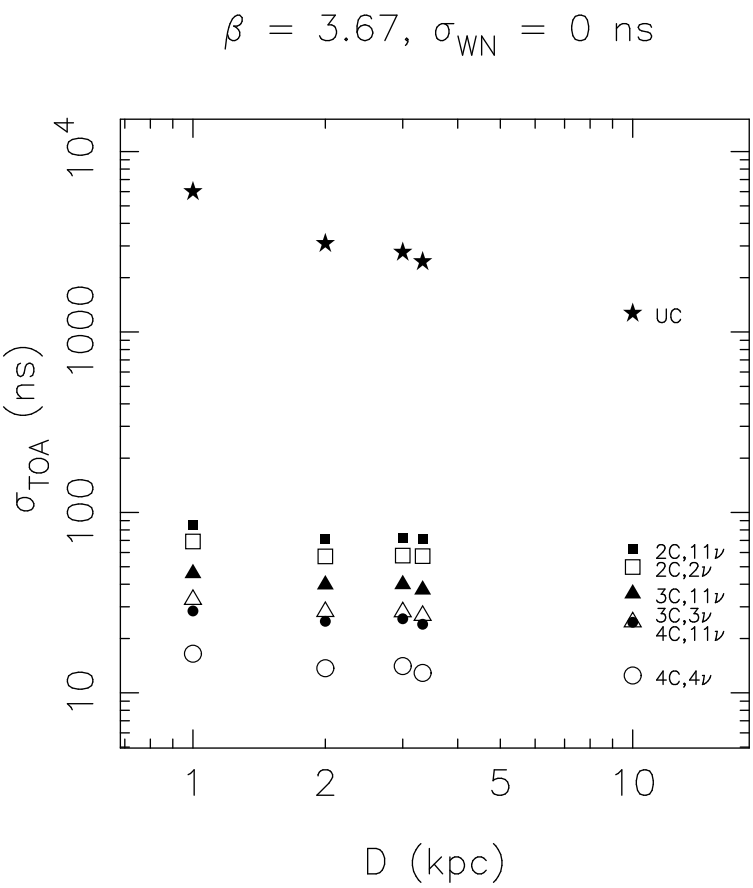

FIGURE 5.14.— Average rms of the TOAs $\sigma_{\rm TOA}$ versus pulsar distance for fixed diffractive scintillation bandwidth $\Delta\nu_d$, from 100 simulations of the same Kolmogorov medium. There is little variation in the rms of the corrected TOAs, indicating that for fixed $\Delta\nu_d$ distance does not significantly affect the amplitude of the corrected residuals.

changes the refractive time scale and the timescale for stationarity. The pulsar sky position will affect the strength of the barycentric correction term to vary, with pulsars closer the ecliptic showing larger variations. To completely assess the influence of interstellar propagation effects on the precision of individual LOSs (i.e., to determine the strength to with a factor of a few), it is necessary to incorporate these effects.

5.8 Observing Configurations

5.8.1 Additive White Noise

Other noise sources limit the ability to identify and remove interstellar propagation effects, and ultimately limit the efficacy of any correction strategy. One additional source of noise is white noise. While most commonly associated with the finite signal to noise ratio of an observation, intrinsic pulsar phase jitter and diffractive interstellar scintillation also contribute white noise to precision timing (Paper II).

To model the effects of white noise, additive Gaussian white noise was added to the simulated TOAs. For all of the simulations described below, the rms level of white noise $\sigma_{\rm WN}$ was assumed to be the same value at all frequencies. In reality, white noise will be highly chromatic because both radiometer noise and the DISS effects are frequency dependent (Paper II).

For varying levels of $\sigma_{\rm WN}$, we calculated the rms of the corrected time series for 100 realizations. For the standard simulations, the results are presented in Figure 5.15. If white noise is small relative to TOA perturbations, the three and four coefficient mitigation strategies are effective. In all cases, the three and four coefficient mitigation strategies produce stationary time series , which suggests that the time series are more amenable to additional smoothing/low-pass filtering, discussed in subsequent sections.

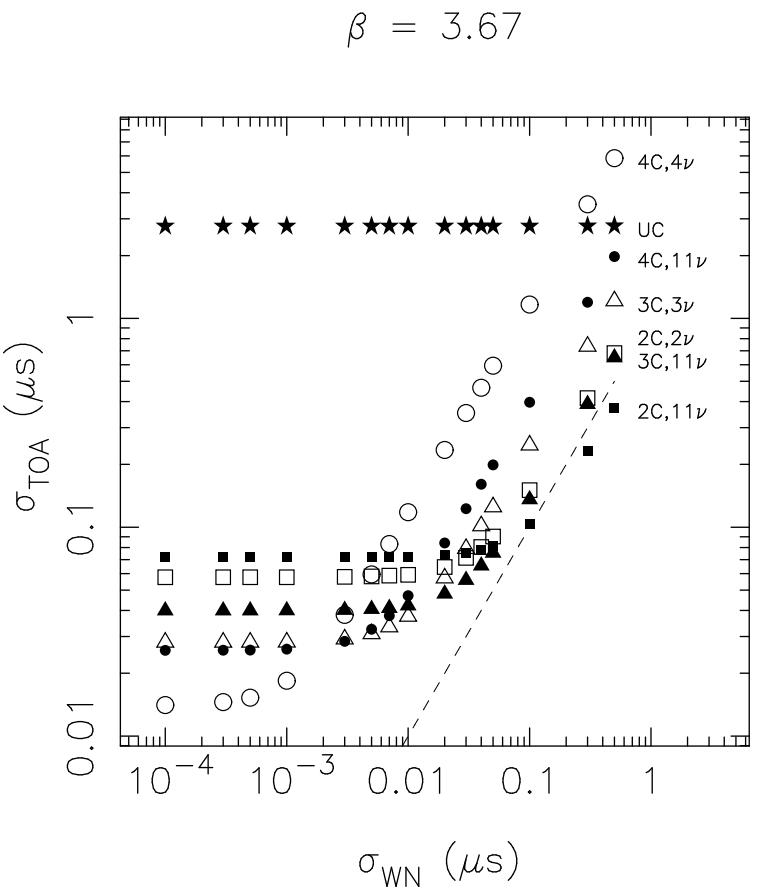

FIGURE 5.15.— RMS amplitude of the time series $\sigma_{\rm TOA}$ versus white noise levels $\sigma_{\rm WN}$ for Kolmogorov-like media. The schemes are identified by the number of coefficients used and the number of frequencies used. For example $2C, 11\nu$ is the mitigation scheme in which achromatic (ν^0) and DM-like (ν^{-2}) frequency dependencies are fit, using 11 TOAs. If there are low levels of white noise, 3 or 4 coefficients can be used in improve timing precision. If there are high levels of white noise, 2 term correction is the most effective. The dashed line is $\sigma_{\rm TOA} = \sigma_W$. When the residuals are dominated by white noise, the TOA the corrected TOAs should be proportional to this line.

5.8.2 Simultaneity of Multi-frequency Observations

In many pulsar timing experiments multi-frequency TOAs are obtained using different receivers and corrections are applied using TOAs that are not truly simultaneous but only contemporaneous. The degree of contemporaneity can differ: at some telescopes the observations occur consecutively and the observa-

tions may be only separated by ≈ 0.5 hr. At others telescopes the observations are separated by many days.

To examine this effect, we corrected simulated TOAs using random time offsets between observations at each observing frequency. The offset was drawn randomly from a Gaussian distribution with varying standard deviation $t_{\rm off}$ and rounded to the nearest observation on the grid, which has 3.7 day resolution. The effects of different mean offset $t_{\rm off}$ on the observations are displayed in Figure 5.16. We find that for all mitigation techniques, the timing precision decreases significantly when the offset between spot frequency measurements is increased.

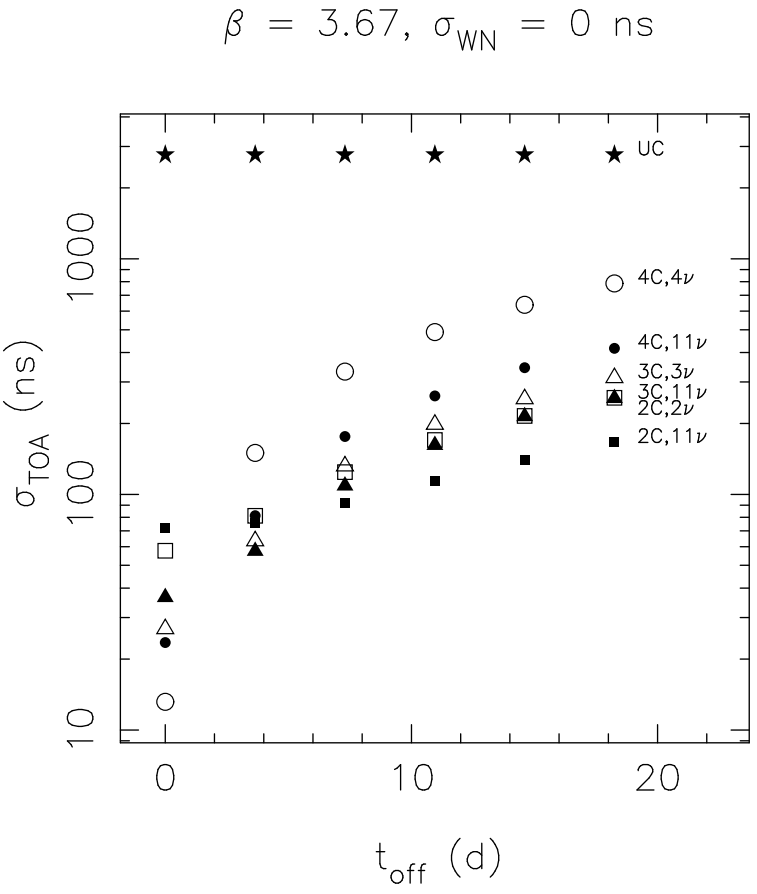

FIGURE 5.16.— RMS of the corrected for different offsets between frequency measurements for a Kolmogorov-likes (right) medium.

5.8.3 Smoothing

Smoothing the TOAs improves timing precision because it removes the high fluctuation frequency components contained in the mitigated TOAs associated with uncorrelated propagation effects and white noise. We examined the effect of smoothing using a Gaussian filter in the time domain. The filter is characterized by the half width of the filter at the $1/e$ point $t_{\rm smooth}$.

With increased smoothing the three and four-coefficient mitigation techniques significantly outperform the two-coefficient technique. We find that smoothing is equally effective when applied before or after mitigating the TOAs if the observations are simultaneous. If there is an offset between observations smoothing after fitting is far superior. In Figure 5.17 we show the average rms of the corrected TOAs versus the smoothing length, assuming that there is an average 7 day offset between observations.

Ultimately, the maximum length of the smoothing filter is limited by the properties of the detected signal of interest and the total observing span of the observations. If the goal is to detect or study a stochastic gravitational wave background or other highly non-stationary perturbations that have minimal power at high fluctuation frequency, it would be reasonable to smooth the time series to > 1 year.[3] In contrast, for detection or study periodic or bursting sources such as binary systems or individual gravitational wave sources (Finn & Lommen 2010), this type of smoothing is unfeasible.

[3] After, of course, fitting for annual and semiannual astrometric terms

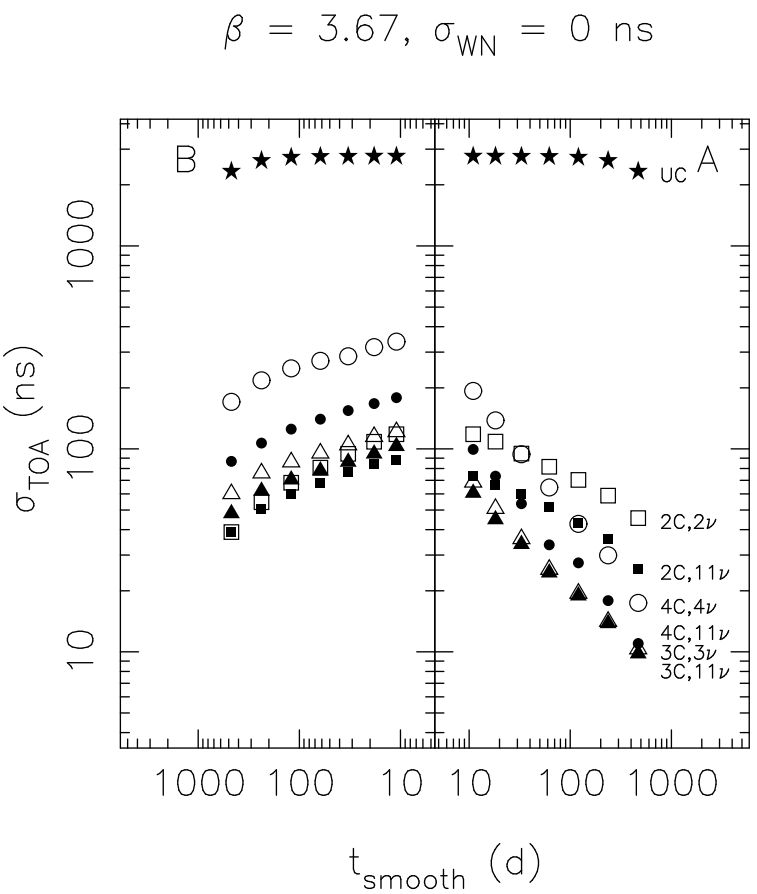

FIGURE 5.17.— RMS of the corrected TOAs for different smoothing lengths $t_{\rm smooth}$ for a Kolmogorov-like medium, assuming an average 7 day offset between multi-frequency observations. In panel *A* we show the effective RMS if the smoothing is conducted after the multi-frequency fit. In panel *B* we show the effective RMS if the smoothing is conducted before the multi-frequency fit.

5.8.4 Observing Frequency

If other sources of noise are negligible it is desirable to conduct timing observations at higher radio frequencies because all refractive propagation effects are much smaller at higher frequency. Unfortunately, nearly all pulsars are far brighter at lower radio frequencies; therefore there is a trade-off between timing uncertainties associated with radiometer noise at high frequencies and interstellar propagation noise that limits timing precision at lower frequencies, as

discussed in §5.8.1.

5.8.5 Observing Bandwidth

We studied the effects of varying observing bandwidth. With the central observing frequency set at 1.5 GHz and the number of frequency channels remaining fixed, the total bandwidth $\Delta\nu$ was varied between 0.2 GHz to 2.5 GHz.

The average rms of the corrected time series $\sigma_{\rm TOA}$ for different observing bandwidths is displayed in Figure 5.19, for both Kolmogorov-like and square law-like media, assuming no additional white noise. The benefits of including additional terms in the TOA mitigation strategy are most pronounced when wide observing bandwidths are used. The two coefficient mitigation strategy becomes less effective when wide bandwidth observations ($\Delta\nu > 1$ GHz) are conducted.

5.8.6 Variable Instrument and Observing Configurations

In the previous sections, we assumed that observing configurations were stable, by which we mean observations are conducted using the same observing bands throughout a timing campaign. In this case, the rms is not sensitive to any systematic bias in the measurement of t_∞, which does not introduce a time-variable component to the residual time series (Paper II).

Instrument configurations are likely to be variable for a number of reasons. Data from multiple telescopes are likely to be combined to improve sensitiv-

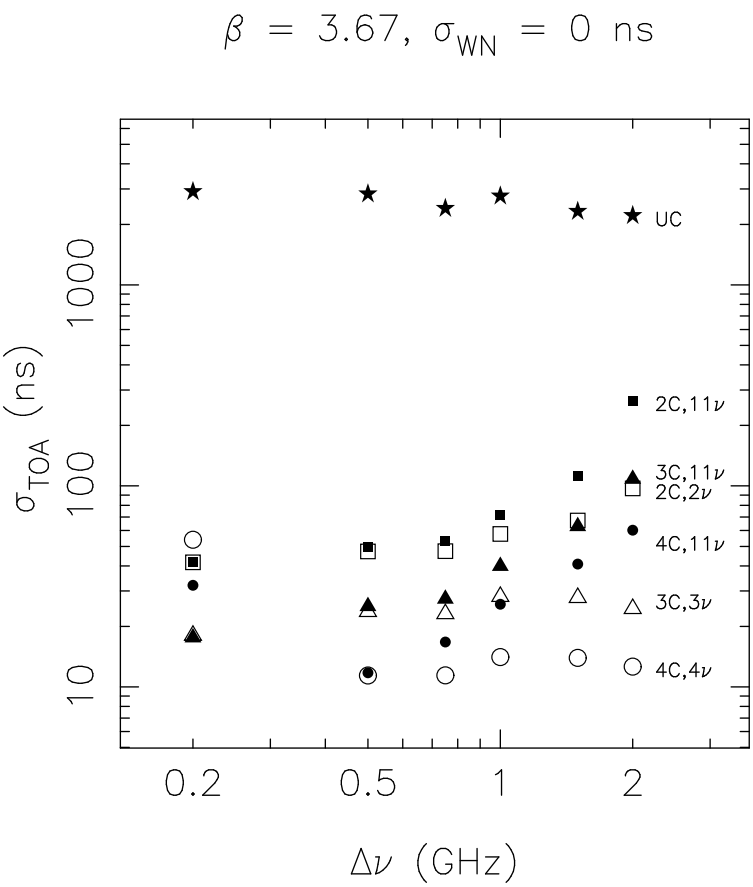

FIGURE 5.18.— Root mean square corrected arrival times $\sigma_{\rm ISS}$ for observing bandwidths $\Delta\nu_{\rm RF}$, for a Kolmogorov-like medium. The rms arrival times for all mitigation techniques times assuming additional white of $\sigma_W = 10$ ns. If the scattering is weak relative to the observing bandwidth, the ability to mitigate TOAs reduces. As a result, there will be an optimal observing bandwidth, which will depend on the strength of the scattering and other sources of noise is the times of arrival.

ity to GWs, employing different signal processing backends at different bandwidths, likely centered at different frequencies. Additionally, observing configurations at a single telescope may change because receivers and data acquisition and signal processing technology (backends) improve with the advancement digital signal processing capabilities. However, even in data sets from single telescopes using the same receivers and receiver backends, observing bandwidth can be variable. For example, frequency channels are occasionally excised

because of sporadic radio interference.

To assess the effect of instrument variability on these mitigation strategies, we simulated and corrected a series of TOAs using four observing frequencies that were taken with alternating observing bands. One observing band comprised observations at 1.0 GHz, 1.1 GHz, 1.2 GHz, and 1.3 GHz. The other observing band comprised observations at 1.7 GHz, 1.8 GHz, 1.9 GHz, and 2.0 GHz. In all other aspects the simulations followed the standard set of parameters. We compared this to a stable observing configuration, in which the four frequencies used were 1.0 GHz, 1.4 GHz, 1.7 GHz, and 2.0 GHz. In Figure 5.19 the RMS of the corrected time series is plotted versus $X_3^{(3)}$ and $X_4^{(4)}$ for both the stable observing configuration and variable observing configuration. For the four coefficient mitigation techniques we set $X_3^{(4)} = 4.4$. The variable shows a minimum at $X \approx 4.4$, which is expected from the diffractive delay term. The analysis methods here are insensitive to this term when the observing configuration does not change. This effect can potentially be mitigated if the frequency evolution of the TOA is modeled.

5.9 Prediction for PTA Pulsars

The levels of propagation noise depend most strongly on the strength of scattering in the direction of the pulsar and the chosen observing frequencies. We have demonstrate that, to first order, if the propagation noise is characterized by the observable diffractive scintillation bandwidth $\Delta\nu_d$ that the noise is independent of observing distance.

Currently 37 pulsars are being timed as part of the three pulsar timing ar-

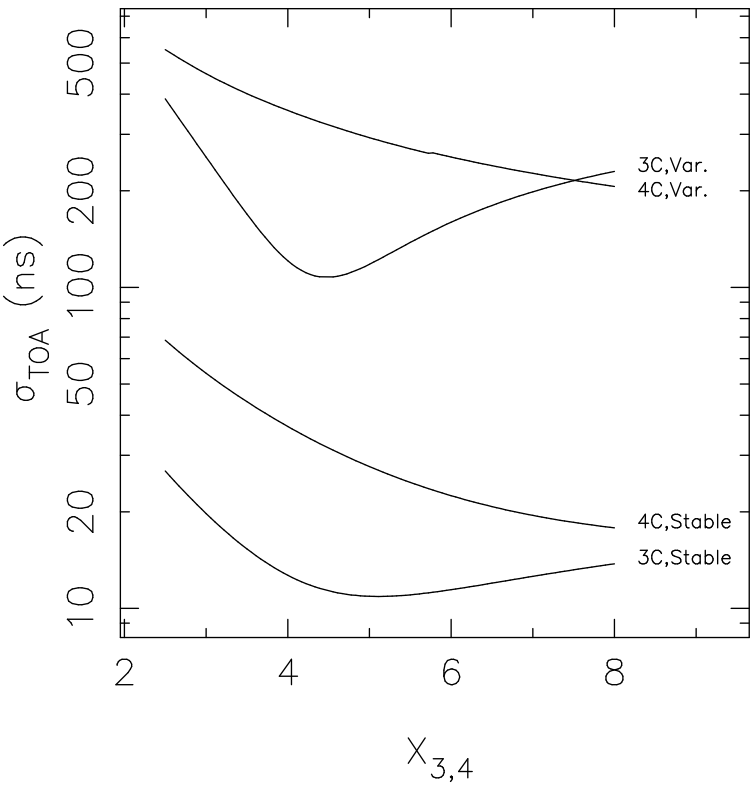

FIGURE 5.19.— Root mean square corrected arrival times $\sigma_{\rm corr}$ versus the best exponent β for stable and variable observing configurations (described in §5.8.6).

rays: the North American (NANOGrav) Array (Jenet et al. 2009), the European EPTA (Ferdman et al. 2010), and the Australian PPTA Verbiest et al. (2010) pulsar timing arrays.

In Table 5.3 we plot the estimated levels of ISM noise for these pulsars. For the strength of noise we assume that observations are conducted on observations at 1-2 GHz, assuming that the white noise amplitude is 50 ns for each TOA at each observing frequency. We have assumed that the media is Kolmogorov.

Because the levels of scattering vary between objects, the expected levels of timing noise vary markedly over these objects. For many objects two frequency approaches are likely to be sufficient. For more scattered objects, three coeffi-

cient approaches are necessary.

However as discussed in Chapter 2, additional pulsars are needed to make a highly significant detection of the gravitational waves and perform subsequent characterization New pulsars are likely to be more distant and more scattered. In addition, new pulsars are likely to be fainter. Given pulsars are brighter at lower frequencies, it may be necessary to observe fainter, more distant objects in frequency bands where scattering is stronger.

5.10 Conclusions

We have assessed the strength of refractive interstellar propagation effects through a series of simulations. Below our findings are summarized:

Multi-frequency observations can be used to correct refractive propagation effects: While for some nearby weakly scattered pulsars it is sufficient to correct only for ν^{-2} perturbations, for other pulsar timing precision requires to correct for ν^{-2} and ν^{-X}-like terms. In addition this higher order correction produces corrected time series with more stationary residuals.

The optimal observing bandwidth depends on the line of sight: When the total observing bandwidth widens, the arrival times become less correlated and correction becomes less effective. When the total observing bandwidth is narrow, higher order corrections cannot be resolved from the frequency dependent terms.

There is residual timing error, even after optimal mitigation: TOAs contain a component that is stochastic in frequency that cannot be mitigated solely with TOA

information.

Low pass filtering the time series improves timing precision: After two coefficient or three coefficient mitigation the residual time series contain an unmitigated component that can be removed by smoothing or low pass filtering.

To best mitigate TOAs, simultaneous or near simultaneous observations are preferable: If simultaneous or near-simultaneous observations are not feasible, TOAs can be improved by smoothing the corrected time series, but not the uncorrected time series.

Changes in observing configurations cause systematic variations in the TOAs: If only two or a few observing configurations are used, it may be sufficient to fit for an arbitrary phase offset between the two time series.

Optimal observing strategies will be line of sight dependent: To obtain the best residuals, it is necessary to tailor observing strategies to each line of sight.

In the future, the simulation methods presented here will be extended to more complex (two-dimensional) scattering geometries, e.g. anisotropic media. We will also include the effect of pulse profile evolution, which can will systematically affect TOAs (Ahuja et al. 2007).

It is also imperative to conduct full diffractive simulations over a wide range of frequencies to examine diffractive effects and model pulse profiles in a way consistent with current pulsar timing methodology. These simulations can also be used to analyze the role that other diagnostics of interstellar propagation (such as Dynamic spectra) in mitigation (Walker & Stinebring 2005; Hemberger & Stinebring 2008).

It is necessary to classify the lines of sight to all MSPs because of the strong LOS dependencies of the strength of scattering effects. To complete this classification, it is necessary to form high-quality dynamic spectra for all PTA pulsars at many epochs at many observing frequencies.

5.10.1 Acknowledgements

We thank Bill Coles, Rick Jenet, Barney Rickett, and Dan Stinebring for useful discussions. We additionally thank Bill Coles and Barney Rickett for providing us with a preprint of C10 in advance of publication. This work made use of NASA's ADS system and the ANTF pulsar catalogue (Manchester et al. 2005). This work was supported by the NSF through grant AST-0807151 and by NAIC, which is operated by Cornell University under a cooperative agreement with the NSF.

5.11 Appendix: Refracted Image Shape

In the simulations presented in this paper, the image intensity $B(\boldsymbol{\theta})$ is used to connect the refractive phase screen to the propagation delay, because it is easily computed. The image intensity is then determine used to determine the perturbation associated with the screen by weighting the delay through any position by the image intensity, as expressed in equation (5.4).

Electron density fluctuations on large scale refract, focus and defocus radiation from a pulsar producing variations in the flux density and arrival time. *Large* is defined relative to the scale $D\theta_d$ that is larger than the Fresnel scale

TABLE 5.3
STRENGTH OF PROPAGATION EFFECTS

Pulsar Name	$\Delta\nu_d$ (MHz)	$\sigma_{\rm RISS}$ (ns)	Ref
J0030+0451	182.9	0.11	1
J0437−4715	236.0	0.08	2
J0613−0200	1.0	20.52	2
J1012+5307	117.9	0.17	3
J1022+1001	188.6	0.11	2
J1024−0719	176.8	0.11	2
J1045−4509	0.0	420.01	2
J1455−3330	117.9	0.17	4
J1600−3053	0.1	359.68	2
J1603−7202	3.2	6.28	2
J1640+2224	18.3	1.09	5
J1643−1224	0.0	978.98	2
J1713+0747	52.4	0.38	2
J1730−2304	6.3	3.19	2
J1732−5049	1.9	10.45	2
J1744−1134	150.9	0.13	2
B1821−24	0.0	1607.46	2
B1855+09	4.6	4.34	2
J1909−3744	88.2	0.23	2
B1937+21	1.2	16.23	2
J2019+2425	13.4	1.50	6
J2124−3358	593.6	0.03	2
J2129−5721	905.1	0.02	2
J2145−0750	133.2	0.15	2
J2317+1439	34.4	0.58	6

NOTE.—Estimated strength of scattering effects for current PTA pulsars, assuming observations are conducted using the standard observing procedure. We list the diffractive scintillation bandwidth $\Delta\nu_d$ scaled to 1.2 GHz assuming Kolmogorov power law medium, using published estimations of this parameter, when available. References are: 1., Nicastro et al. (2001); 2. C10; 3., Lange et al. (2001); 4., Bhat & Gupta (2002); 5., Bogdanov et al. (2002); 6., Johnston et al. (1998);

$\approx \sqrt{\lambda D}$ by the same factor that the Fresnel scale is larger than the diffraction scale $\approx \lambda\theta_d$ (Rickett 1990). While an acceptable model for electron density variations is one with a continuum of length scales, it is useful to separated large and small scales, which we do here. The Kirchoff diffraction integral for the scalar wavefield has an integrand $\exp[i\Phi(\boldsymbol{x}, \boldsymbol{x}')]$, where $\boldsymbol{x}$ and $\boldsymbol{x}'$ are both two dimensional vectors transverse to the line of sight that reside on the observer plane and the screen plane, respectively. The total phase $\Phi = \phi_g + \phi_r + \phi_d$, is comprised of a geometric term

$$\phi_g(\boldsymbol{x}, \boldsymbol{x}') = k\left[\frac{x'^2}{sD} + \frac{|\boldsymbol{x} - \boldsymbol{x}'|^2}{(1-s)D}\right], \tag{5.28}$$

a refractive term ϕ_r from large scale variations, and a diffractive term ϕ_d from small scale variations. We have denoted the earth-pulsar distance as D the earth-screen distance as sD, and the earth pulsar distance $(1-s)D$.

In the absence of the refractive term, the scattered wavefield of a point source is described by an ensemble average image intensity $B_0(\boldsymbol{\theta})$, where $\boldsymbol{\theta} = \boldsymbol{x}'/sD$. Refraction is included as a quadratic surface centered on a stationary phase point (SPP) $\bar{\boldsymbol{x}}'$ on the screen corresponding to an angle $\bar{\boldsymbol{\theta}}$:

$$\phi_r(\boldsymbol{x}') = \phi_r(\bar{\boldsymbol{x}}') + \boldsymbol{A} \cdot (\boldsymbol{x}' - \bar{\boldsymbol{x}}') + (\boldsymbol{x}' - \bar{\boldsymbol{x}}') \cdot \boldsymbol{C}(\boldsymbol{x}' - \bar{\boldsymbol{x}}'), \tag{5.29}$$

where $\boldsymbol{b}$ is a 2-dimensional vector that describes the phase gradient about the SPP and $\boldsymbol{C}$ is a 2×2 matrix that describes the curvature about the SPP.

By consolidating linear and quadratic terms, and solving the Kirchoff diffraction integral, the refraction-distorted image can be expressed as a function of the

non-distorted image:

$$B(\boldsymbol{\theta}) = B_0(\boldsymbol{M}(\boldsymbol{\theta} - \bar{\boldsymbol{\theta}})), \tag{5.30}$$

where $\boldsymbol{M} = \boldsymbol{U}^{\dagger}\boldsymbol{\gamma}_2^{-1}\boldsymbol{U}$, $\boldsymbol{\gamma_2}$ is a 2×2 diagonal matrix that describes the refractive *gains* along the major and and minor axes of the distortion and $\boldsymbol{U}$ is a 2×2 matrix that diagonalizes $\boldsymbol{C}$, i.e., a rotation matirx that defines the orientation of the major and minor axes of the paraboloid relative to the coordinate system.

In practice we do not solve for $\boldsymbol{b}$ and $\boldsymbol{C}$ at the stationary phase points, but at points on the grid of the phase screen. The stationary phase point is located at the region where the total phase gradient is zero.

$$\boldsymbol{\nabla}\Phi_{\text{tot}}(\boldsymbol{x'}) = \boldsymbol{\nabla}\left(\phi_r + \phi_g\right) = 0, \tag{5.31}$$

where the second term in equation (5.31) is the geometric phase associated with path length differences through the screen.

The location of the SPP can be found by substituting equation (5.29) into equation (5.31). Because the resulting equations are linear in x' and y', there is a unique solution,

$$x' = \frac{cd - ae}{be - c^2} \text{ and } y_r = \frac{ac - bd}{be - c^2}, \tag{5.32}$$

where

$$\begin{aligned} a \quad &= A_x - C_{xx}x_0 - C_{xy}y_0, \;\; b = \frac{k}{s(1-s)D} + C_{xx}, \;\; c = C_{xy} \\ &d = A_y - C_{yy}x_0 - C_{xy}y_0, \;\; \text{and } e = \frac{k}{s(1-s)D} + C_{yy}. \end{aligned} \tag{5.33}$$

In angular units, the SPP is located at

$$\theta_{r,x} \quad = \frac{x_r}{sD}, \theta_{r,y} = \frac{y_r}{sD}. \tag{5.34}$$

The matrix $\boldsymbol{M}$ describes the warping of the image is expressed as

$$\boldsymbol{M} = \begin{bmatrix} G_x \cos^2\alpha + G_y \sin^2\alpha & (G_x - G_y)\cos\alpha\sin\alpha \\ (G_x - G_y)\cos\alpha\sin\alpha & G_x \sin^2\alpha + G_y \cos^2\alpha \end{bmatrix}, \tag{5.35}$$

where α is the rotation angle of major of curvature relative to the x axes,

$$\alpha = \frac{1}{2}\tan^{-1}\left(-2C_{xy}/(C_{xx} - C_{yy})\right), \tag{5.36}$$

and $G_{x,y}$ are the refractive gains along the major and minor axes,

$$G_x = \left(1 + \frac{s(1-s)D}{kC'_{xx}}\right)^{-1}, G_y = \left(1 + \frac{s(1-s)D}{kC'_{yy}}\right)^{-1}. \tag{5.37}$$

The curvature along the major and minor axes are C_{xx} and C_{yy}:

$$C'_{xx} = C_{xx}\cos^2\theta + 2C_{xy}\cos\theta\sin\theta + C_{yy}\sin^2\theta \tag{5.38}$$

$$C'_{yy} = C_{xx}\sin^2\theta - 2C_{xy}\cos\theta\sin\theta + C_{yy}\cos^2\theta. \tag{5.39}$$

5.12 Appendix: Simulations

In this appendix we describe simulations that were used to model the perturbations to pulse times of arrival (TOAs) through refractive phase screens. The implementation is outlined below and detailed in the following subsections:

1. Define the properties of the scattering screen and the observations (Appendix 5.12.1): The strength of propagation effects are highly line of sight dependent. Therefore, it is first necessary to define the properties of the scattering screen and the location and velocity of the pulsar. The strength of the effect are also dependent on the choice of observational frequencies

2. Generate the reference phase screen $\Phi_{\rm ref}(\boldsymbol{x}, \nu_{\rm ref})$. (Appendix 5.12.2): As a proxy for electron density variations that govern radio wave propagation, the phase screen at the highest observing frequency is used to construct the phase screens at all observing frequencies because it requires the finest resolution.

3. Generate phase screens $\Phi(\boldsymbol{x}, \nu)$ *for the observing frequencies* (Appendix 5.12.3): Relative to the reference phase screen, the other phase screens at lower frequencies have larger and smoother phase variations. These screens are formed by rescaling the phase and low-pass filtering the reference phase screen $\Phi_{\rm ref}$.

4. Calculate propagation delays through the phase screens (§5.4 of the main text): For each time and at each frequency, the refractive propagation delays, identified in §5.2, are calculated.

5. Add additional perturbations to the TOAs. Other sources of noise are added to the TOAs to properly assess the efficacy of mitigation techniques. In this paper the only other noise source is additive white noise.

6. Mitigate TOAs (§5.6 of the main text): We mitigate the propagation effects using a variety of a TOA-based methods. The properties of the corrected TOAs are quantified by the rms and the spectral properties of the corrected time series. This is described in §5.6 of the main text.

5.12.1 Characterizing the Scattering Screen

The phase screens are simulated on rectangular grid so that each time t and position $\boldsymbol{x}$, the phase is calculated as $\Phi(\boldsymbol{r}, t; \nu) = \Phi(x_i - sV_{\rm eff}t, y_i; \nu)$. We have set x to be the direction of effective motion $V_{\rm eff} = sV_p$, where s is the fractional distance earth screen distance, and bulk motion of the screen and Earth are assumed to be negligible. The direction y is of course perpendicular to motion.

In order to estimate the strength of the propagation effects, a number of quantities need to be defined: the geometry of the observer-pulsar-scattering screen system, the nominal strength of the scattering screen, and the observing frequencies. The full list of these quantities is presented in Table 5.4.

Calibrating the screen and screen structure: As a proxy for scattering strength, we use the scintillation decorrelation bandwidth $\Delta\nu_d(\nu_{\rm ref})$ at a reference frequency $\nu_{\rm ref}$. This quantity is chosen because it is both directly observable and often reported in the literature, and is directly related to other properties of the scattering screen (Cordes et al. 1986; Romani et al. 1986).

The structure of the fluctuations in the phase screen is characterized by the power spectrum of the electron density and phase fluctuations $P_{n_e} \propto P_\Phi(\boldsymbol{q})$ is used, where $\boldsymbol{q}$ is spatial frequency, i.e., the Fourier conjugate to screen position $\boldsymbol{x}$. In most of the simulations we assume that the phase fluctuations follow a power law with power law $P_\Phi \propto q^{-\beta}$ over the scales of interest here, which appears to be a reasonable assumption (Rickett 1990). For most lines of sight β is between 11/3 (Kolmogorov) and 4 (square law). However, to demonstrate that our simulations are properly behaving we simulated a smooth screen by assuming the power spectrum was a one-sided Gaussian ($P_\Phi \propto \exp[-q^2/2q_c^2]$).

Relevant length scales and numerical screen size: The screen dimensions are set by the resolution and size requirements. The relevant length scales are the diffractive length scale $\ell_d(\nu)$, the refractive length scale $\ell_r(\nu)$ and the projected distance the pulsar moves along the screen L_x.

At each observing frequency, these length scale are derived from the frequency dependent decorrelation bandwidth $\nu_d\nu$. For power-law media with β between 3 and 4, the decorrelation bandwidth relative to reference frequency is

$$\Delta\nu_d(\nu) = \Delta\nu_{d,\mathrm{ref}} \left(\frac{\nu}{\nu_{\mathrm{ref}}}\right)^{2\beta/(2-\beta)}. \tag{5.40}$$

Following the expressions in Hu et al. (1991), the diffractive scale on the screen plane is

$$\ell_d(\nu) = \pi^{(6-\beta)/(\beta/2-1)} \sqrt{\frac{s(1-s)cD\Delta\nu_d(\nu)}{2\nu^2}}, \tag{5.41}$$

and the refractive scale on the screen plane is

$$\ell_r(\nu) = \left[\frac{(\beta-2)}{4(4-\beta)}\right]^{1/2} \frac{csD}{\nu\ell_d(\nu)}. \tag{5.42}$$

The screen is set to have grid sizes Δx and Δy that are both a factor M_i smaller than the smallest length scale in the simulation, which is the refractive scale at the highest frequency ν_h:

$$\Delta x = \Delta y = \frac{\ell_r(\nu_h)}{M_i}. \tag{5.43}$$

In the direction of motion, the largest scale is usually the projected distance the pulsar moves across the screen[4] sV_pT, where T is the the total observing

[4]In cases where the projected distance is small, or the lowest observing frequency is exceptionally low, the refractive scale may be larger. In this case L_x follows the form of Equation (5.45).

span. To mitigate the effects of periodic boundary conditions associated with Fourier domain generation of the fluctuations (see discussion below), the length of the screen in the x direction is a factor $M_{o,x}$ larger than the projected distance:

$$L_x = M_{o,x} s V_p T. \tag{5.44}$$

In the direction perpendicular to motion, phase screen is set to be larger than the refractive scale at the lowest frequency by a factor M_o:

$$L_y = M_{o,y} \ell_r(\nu_L). \tag{5.45}$$

Putting this together, the screen has dimensions

$$N_x = \frac{L_x}{\Delta x} = M_{o,x} M_i \frac{s V_p T}{\ell_r(\nu_h)} \tag{5.46}$$

and

$$N_y = \frac{L_y}{\Delta y} = M_{o,y} M_i \frac{\ell_r(\nu_L)}{\ell_r(\nu_H)}. \tag{5.47}$$

TABLE 5.4
SIMULATION PARAMETERS

Parameter	Name	Default Values	Comment
	Observation Parameters		
N_ν	Number of observing frequencies	11	
$\nu_{i,\mathrm{RF}}$	Radio observing frequencies	1.0 to 2.0 GHz	
$\sigma_{\mathrm{WN}}(i_\nu)$	White noise level at frequency $\nu(i_\nu)$	50 ns at all ν	
	Pulsar Parameters		
D	Distance to pulsar	3 kpc	
(λ, b)	Pulsar position	$(0, 0)$	Ecliptic Coordinates (lat., long)
V_p	Pulsar Velocity	100 km s^{-1}	
Ψ	Velocity Position Angle	0.5	Relative to coordinate system locally.
	Screen Parameters		
β	Index of power spectrum of density fluctuations	3.67 or 3.99	Kolmogorov or Square-law
ν_{ref}	Reference frequency	1.2 GHz	
$\Delta\nu_d(\nu_{\mathrm{ref}})$	Diffractive scintillation bandwidth	0.5 MHz	Measured at reference frequency
s	Fractional distance to screen	0.5	
	Screen Quantization		
M_i	Screen Resolution Multiplier		Fraction of $\ell_r(\nu_{\mathrm{max}})$
$M_{o,x}$	Screen size multiplier, x-direction		Multiples of $\ell_r(\nu_{\mathrm{min}})$
$M_{o,y}$	Screen size multiplier, y-direction		

NOTE.—Parameters that need to be defined to execute simulations.

5.12.2 Generating the Reference Phase Screen

The reference phase screen is generated in the Fourier domain and then transformed into spatial domain using a fast Fourier transform (FFT):

$$\Phi(\boldsymbol{r_p}) = \sum_q \tilde{\Phi}(\boldsymbol{q_q}) \exp\left(i\boldsymbol{r_p} \cdot \boldsymbol{q_q}\right). \tag{5.48}$$

The phase screen represents one realization of random medium. It is assumed that the screen has a well defined power spectrum[5].

To generate a single realization, complex (Gaussian) white noise w_q is multiplied by an appropriate filter function $F(\boldsymbol{q})$:

$$\tilde{\Phi}(\boldsymbol{q_q}) = w_q F(\boldsymbol{q_q}). \tag{5.49}$$

The form of the filter is set by requiring that the power spectrum of the fluctuations follow ensemble average behavior:

$$\langle P_\Phi(\boldsymbol{q})\rangle = \langle \tilde{\Phi}(\boldsymbol{q})\tilde{\Phi}^*(\boldsymbol{q})\rangle. \tag{5.50}$$

By substituting Equation (5.49) into Equation (5.50), the relationship between P_Φ and f is found to be:

$$P_\Phi(\boldsymbol{q}) = \langle w_q^2\rangle F^2(\boldsymbol{q}) \propto F^2(\boldsymbol{q}). \tag{5.51}$$

Two types of phase screens were generated. Smooth screens were generated using

$$F(\boldsymbol{q}) = \exp\left(-\frac{q^2\ell_c^2}{2}\right), \tag{5.52}$$

[5]We note that it is sufficient for the power spectrum to be defined over the observing region. For example, over a finite time (or a finite region of space) many non-stationary processes have well defined ensemble average power spectra, but over infinite time or space they have divergent (infinite) power spectra.

whereℓ_c is the characteristic length scale for the fluctuations in phase. For the screen to be smooth $\ell_c \gg \ell_r$.

Turbulent phase screens that show phase fluctuations with power law behavior $P_\Phi \propto q^{-\beta}$ were also generated. In these cases, an appropriate filter is $F(q) = q^{-\beta/2}$.

Because the phase is real-valued in the spatial domain, its Fourier transform $\tilde{\Phi}$ is Hermitian. Recognizing Hermiticity in equation (5.48), the discrete Fourier transform is

$$\Phi(\boldsymbol{x}_p) = \sum_q F(\boldsymbol{q_q}) \left[a_q \cos(\boldsymbol{x_p} \cdot \boldsymbol{q_q}) + b_q \sin(\boldsymbol{x_p} \cdot \boldsymbol{q_q}) \right], \tag{5.53}$$

where a_q and b_q are real random variables with the properties $\langle a_p a_q \rangle = \langle b_p b_q \rangle = \sigma^2 \delta_{pq}$, and $\langle a_p b_q \rangle = 0$, where the angled brackets ($\langle , \rangle$) indicate the ensemble average value of the interior quantity.

5.12.3 Generating the Phase Screens

All the phase screens are generate from the same template. This template serves as a proxy for modeling the originating electron density variations. In practice this template phase screen is the highest frequency phase screen because it requires the highest spatial resolution.

The strength of the screen at all observing frequencies is set with the phase structure function:

$$D_\Phi(\boldsymbol{b}) = \langle \Phi(\boldsymbol{r}) \Phi(\boldsymbol{r} + \boldsymbol{b}) \rangle. \tag{5.54}$$

For power law media, the structure function is defined as

$$D_\Phi(b) = \pi^2 \left(\frac{b}{\ell_d}\right)^{\beta-2}, \tag{5.55}$$

where $\beta = 11/3$ for Kolmogorov media and $\beta = 4$ for square law media.

Using the discrete representation of phase (see Equation 5.50), the structure function of the simulated phase screen is

$$D_\Phi(\boldsymbol{b}) = 2\sigma^2 \sum_q F^2(\boldsymbol{q}_q)\left[1 - \cos(\boldsymbol{q}_q \cdot \boldsymbol{b})\right]. \tag{5.56}$$

The screen is normalized on the scale of the smallest resolution element, and σ is chosen such that

$$\sigma = \left[\left(\frac{\pi^2}{2}\right)\frac{D_\Phi(\Delta x/\ell_d)}{\sum_q F(q)^2(1-\cos(\boldsymbol{q}_q \cdot \boldsymbol{b}))}\right]^{1/2}. \tag{5.57}$$

To mimic diffractive smoothing of the phase screen, a filter $G(q)$ is applied in the Fourier domain to smooth the phase screen. The phase screen is smoothed to the refractive scale at a spatial frequency of $q_c = 1/\ell_r(\nu)$ using a Gaussian weighting scheme:

$$G(\boldsymbol{q}) = \exp\left[\frac{q^2}{2q_c^2}\right]. \tag{5.58}$$

Therefore, the phase at frequency ν is

$$\Phi(\boldsymbol{r_p}; \nu) = \left(\frac{\nu}{\nu_{\text{ref}}}\right)^{-1} \sum_q G(\boldsymbol{q}_q)\tilde{\Phi}_r(\boldsymbol{q}_q)\exp\left[-i\boldsymbol{q}_q \cdot \boldsymbol{r_p}\right]. \tag{5.59}$$

CHAPTER 6

MULTI-FREQUENCY PRECISION TIMING OF THE MILLISECOND PULSAR J1713+0747

The detection of gravitational waves using a pulsar timing array requires the ability to determine pulsar times of arrival to unprecedented precision. We have conducted a systematic multi-frequency timing campaign of the highly stable millisecond pulsar J1713+0747. Here we report the initial findings of this campaign. We show that the pulsar shows short term ($\leq$ 10 s) TOA variations that are likely associated with pulse jitter. These variations are shown to be independent of frequency and signal to noise ratio; therefore the only way to reduce this effect is to increase the numbers of pulses averaged. We investigate the efficacy of multi-frequency fitting to mitigate TOA variations. Though the pulsar is only weakly scattered there are hints that frequency dependent time of arrival modeling can produce higher quality TOAs. For other pulsars that are more strongly scattered these effects may be more important[1].

6.1 Introduction

The detection of gravitational waves using a pulsar timing array requires the ability to determine pulse times-of-arrival (TOAs) to unprecedented timing precision. The precision of pulsar timing is at minimum limited by radiometer noise of the telescope receiver system. In this case, it estimated that a modestly significant ($\lesssim 4\sigma$) detection of a stochastic gravitational wave background can be achieved by observing 20 to 40 pulsars over 5 to 10 years (Jenet et al. 2005).

[1]R. M. Shannon, J. M. Cordes, P. B. Demorest, T. J. W. Lazio, D. J. Nice, & D. R. Stinebring, to be submitted, ApJ.

If the only form of noise is radiometer noise, sensitivity of observations can be increased by increasing observation bandwidth, increasing observing time, increasing telescope telescope sensitivity (increasing gain, or decreasing system temperature). However, there are undoubtedly other contributions that affect the timing precision of pulsars and limit the sensitivity of pulsar timing to gravitational waves (Cordes & Shannon 2010).

In order to better quantify sources of noise in precision timing measurements, a unique timing campaign of the very stable millisecond pulsar J1713+0747 was conducted with the Arecibo 305-m telescope[2]. The details of the observations are described in §6.2.

Here we present two preliminary studies of these observations. In the first study, presented in §6.3, short term (intra-observation) contributions to TOA perturbation are examined. We identify a component to TOA perturbation that is independent of the signal to noise ratio and correlated over the entire radio frequency bandwidth accessible, suggesting strongly that the contribution is associated with stochastic pulse profile variations commonly referred to as pulse phase jitter.

In the second study, presented in §6.4, multi-frequency correction techniques are explored. We show that multi-frequency fitting drastically improves the timing precision, and hints that refractive interstellar scintillation is contributing to timing errors.

[2]The Arecibo Observatory is part of the National Astronomy and Ionosphere Center, which is operated by Cornell University under a cooperative agreement with the National Science Foundation.

6.2 Observation and Analysis Procedure

The pulsar J1713+0747 was observed with the 305−m Arecibo telescope at nine epochs spread over approximately six months. This particular pulsar was chosen because it has the best long term timing precision in the Arecibo declination range (P. Demorest et al., in preparation). Each epoch consisted of observations during two consecutive transits of the pulsar in four different receiver bands: 327 MHz, 430 MHz, L-band, and S-band, with slightly less than half a transit (50 min) of observations at each frequency. In order to sample TOA perturbations on a variety of time scales (in particular variations due to the ISM), a variable observing cadence was used, increasing exponentially in spacing up to monthly sampling. A list of observation days and approximate amount of on-source time on each day is displayed in Table 6.2. Observations were recorded with multiple backends simultaneously in order to both conduct high time-resolution observations (amenable to precision timing) and high frequency resolution observation (amenable to observations of pulsar dynamic spectra fundamental to understanding interstellar propagation effects). The results here employ only the ASP precision timing backend (Demorest 2007), which performs real time coherent dedispersion and folding at the pulsar period, producing pulse profiles for all four Stokes parameters. Folded pulse profiles were produced for 10 s intervals for sub-bands with 4 MHz bandwidth. Examples of a extremely high SNR pulsars are displayed in Figure 6.1.

On one transit, the pulsar was observed with the 327 MHz and 430 MHz receivers. The 327 MHz employs a hybrid receiver that outputs circular polarization from a native linear feed, with system temperature typically $T_{\rm sys} > 170$ K. The 430 MHz feed has native circular polarization and $T_{\rm sys} \approx 100$ K. Due to

the computational limitations associated with real-time dedispersion of low-frequency observations, ASP observations were limited to 24 MHz bandwidth. At 430 MHz, the ASP backend recorded the entire 20 MHz front-end bandwidth.

On the other transit, the pulsar was observed with the L-band wide and S-band low receivers. With the ASP backend 64 MHz of bandwidth was typically recorded, centered at 1410 MHz and 2350 MHz, respectively, for L-band and S-band observations. The L-band receiver detects linear polarization and typically has $T_{\rm sys} \approx 30$ K. The S-band receiver detects linear polarization and typically has $T_{\rm sys} \approx 30$ K. These observing frequencies were set to match the observing frequencies of the other long term timing projects conducted at the observatory.

The `ASPFitsReader` pipeline was used to generate calibrated pulse profiles and generate TOAs (Ferdman 2008). Polarization calibration and absolute flux calibration were completed by comparing a pulsed signal generated by a noise diode while the telescope was pointed on and off a calibrator source and on a pulsar. The radio galaxy CTD 93 was the chosen to be the calibrating source because it is known to be both unpolarized and have little flux variability (Shaffer et al. 1999). The receivers were calibrated for differential gain and non-orthogonality of the polarization feeds but not for elliptical polarization.

TOAs were produced by cross correlating comparing the total intensity pulse profiles to template in the Fourier domain using the algorithm presented in (Taylor 1992). Templates for each observing band were generated by from high-signal observations of the pulsar co-added from another observing program conducted using the same backend instrumentation (M. Gonzalez, private communication). The same template for each channel within the band was used. Examples of observed integrated pulse profiles are presented in in Figure

6.1.

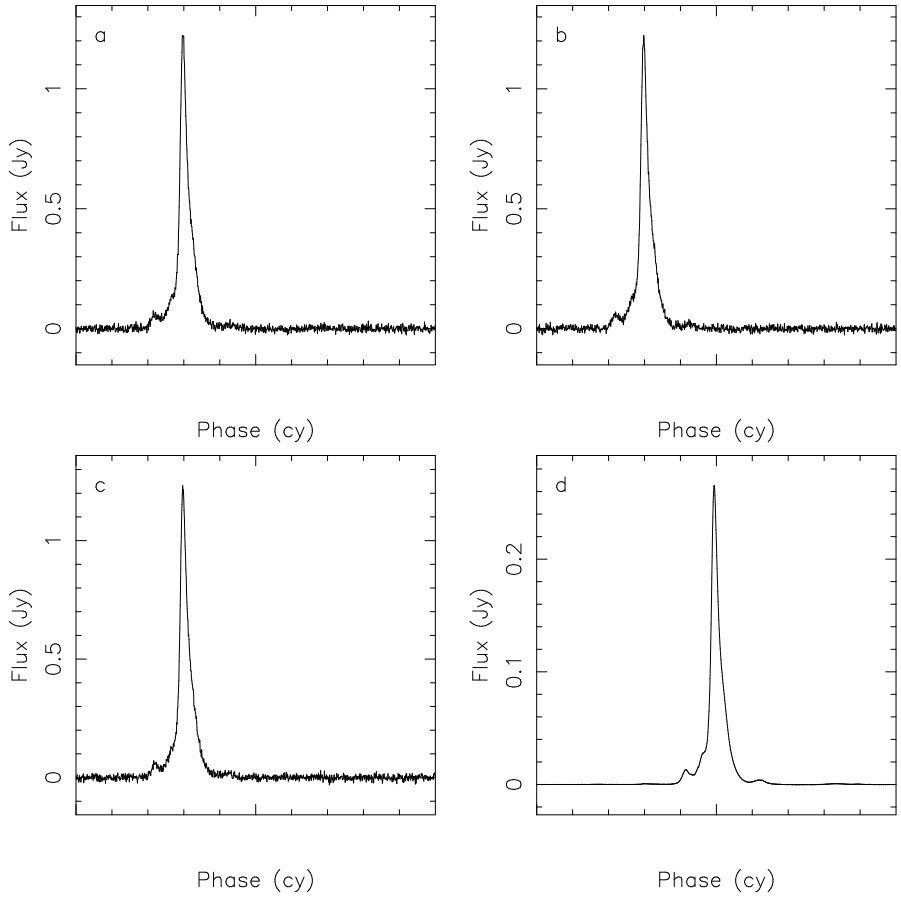

FIGURE 6.1.— L-band Pulse profiles for J1713+0747. In panels a-c we show the average pulse profiles for 10-s integrations. In panel d we show the template pulse profile.

6.3 Short Term Variations and Evidence for Jitter in PSR J1713+0747

In Figure 6.2 residual TOAs are displayed for L-band observations from MJD 54978 and for S-band observations from MJD 54983. These days were chosen because the pulsar showed particularly high SNR in the respective bands. On MJD 54978 the pulsar was about a factor of 5 brighter than usual in the L-band observations, because refractive and diffractive interstellar scintillation

enhanced the flux. These levels of flux variation are not seen in the S-band observations. While there are hints of intra-channel correlation in the TOAs it is not significant. From the histogram of the TOAs (right panels of Figure 6.2, the distribution appears to be remarkably Gaussian.

The relationship between timing error and the signal to noise ratio of the observation was examined using a wide range of SNR, with SNR defined as the ratio of the peak pulse flux to the rms off-pulse flux. The procedure for determining the rms error is as follows: For each frequency channel the TOAs were subdivided into different ranges of SNR. Within these ranges of SNR, the rms of the TOAs were calculated.

Observations from all of the frequency channels were combined to increase the range of SNR. In L-band observations, diffractive interstellar scintillation modulates the intensity of the pulsar with a characteristic frequency scale of $\Delta\nu_d \approx 30$ MHz on time scales of $\Delta t_d \approx 30$ min. To further increase the range of SNR investigated, observations from two epochs (the high SNR epoch and a second epoch where the pulsar flux was approximately its average value) were combined. The results are displayed in Figure 6.7. If radiometer noise was the only source of error in TOA estimation, the rms error would decrease $\propto \mathrm{SNR}^{-1}$ for all SNR. The dashed line shows this trend, derived by simulating the TOA estimation process using the template profile. When the SNR is low, the observations follow this trend; however, at high SNR the rms stays constant, indicating that timing error is not being limited by SNR. For the S-band observations, the signal to noise ratio is not sufficiently high to identify an excess at the level seen in the L-band observations.

There are two forms of timing error that can contribute to the saturation ob-

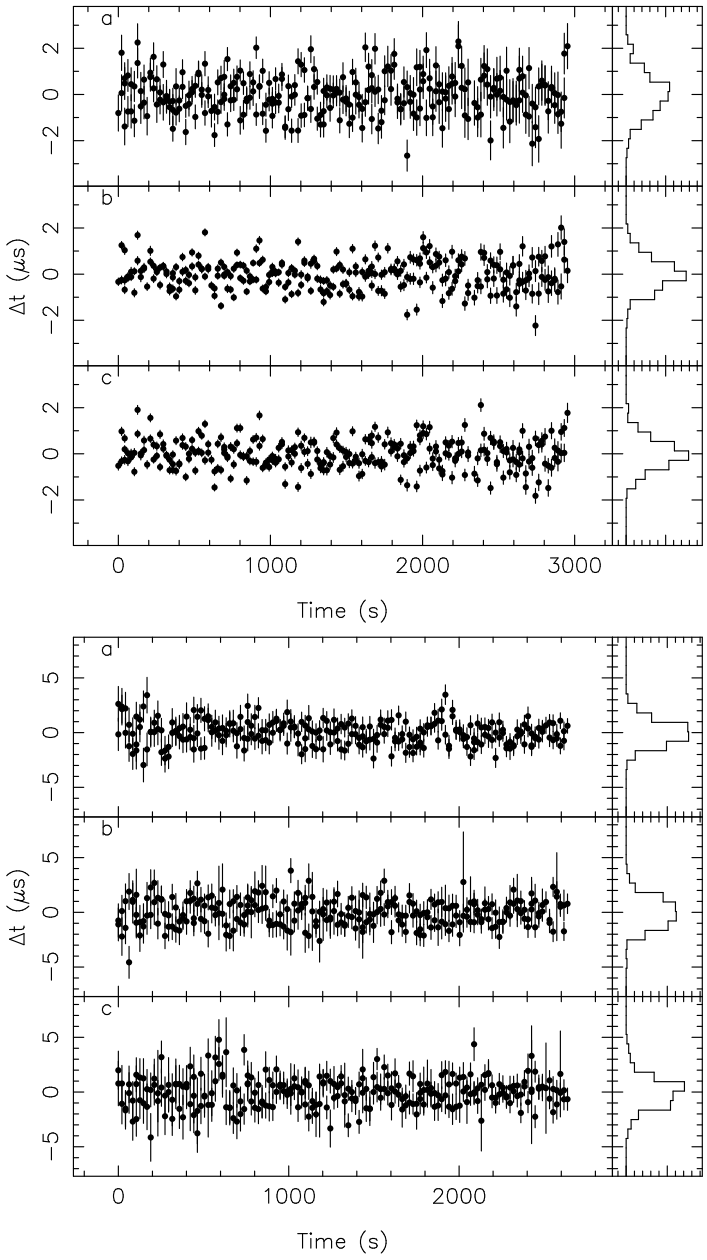

FIGURE 6.2.— TOAs for single epoch L-band (top panels) and L-band (bottom panels) observations. For each band we show TOAs at there sub-bands. For the L-band observations these correspond to observations at 1382 MHz (series a), 1410 MHz (series b), and 1430 MHz (series c). For S-band observations the three panels correspond to 2326 MHz, (series a), 2342 MHz (series b) and 2370 MHz (series c). To the right of each series of TOAs we show a histogram of the TOAs.

served in Figure 6.7. Diffractive interstellar scintillation (DISS) modulates the pulse on short time scales ands contributes an uncorrelated (white noise-like)

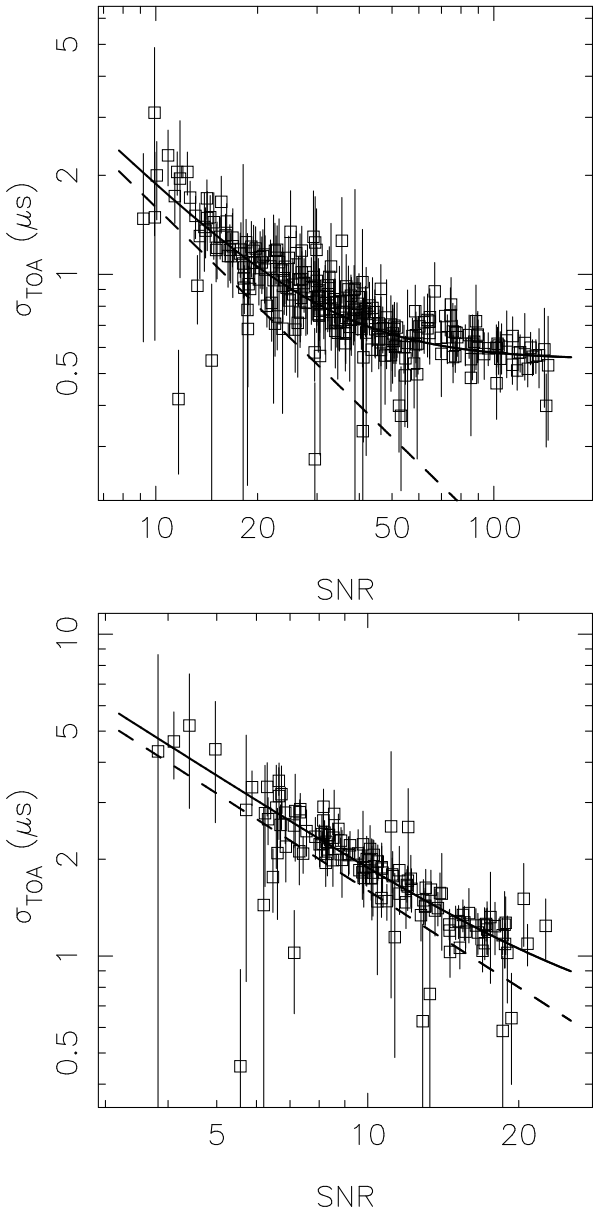

FIGURE 6.3.— RMS residuals $\sigma_{\rm TOA}$ versus signal to noise ratio (SNR) for 10 sec L-band (top) and S-band (bottom) observations of PSR J1713+0747. The dashed line shows the scaling expected for the rms if the error is entirely associated with radiometer noise ($\sigma_{\rm TOA} \propto {\rm SNR}^{-1}$. The solid line shows the scaling expected if the rms has a jitter component (which would not vary with pulse phase) and a radiometer component. For L-band observations, the timing precision is clearly limited by some form of noise that is independent of SNR. For S-band observations, the SNR is never sufficiently high to significantly identify the component at the levels observed in the L-band observations.

perturbation to pulse arrival times independent of the SNR. This form of uncertainty has been seen in observations of another (more highly scattered) MSP, PSR B1937+21 (Cordes et al. 1990; Jenet & Gil 2004). DISS is ruled out as the source of noise because the variations are highly correlated and of the same amplitude in each sub-band, whereas DISS is highly frequency dependent. In Figure 6.4 we show the arrival times as a function of frequency for three consecutive pulses. While there is structure in the TOAs at different observing bands, the residuals between different channels are highly correlated. This correlation can be seen through analysis of the correlation of a large number of TOAs between different frequency channels. In Figure 6.5 we display a scatter plot of the residual TOAs $\Delta t_{\rm toa}$ for three different pairs of channels, showing the very strong inter-channel correlation.

Additional evidence suggesting that against a DISS origin for the timing error comes from the lack of correlation between SNR and absolute time of arrival. Coles et al. (2010) recently reported the correlation between SNR and time of arrival on the diffractive times scale in both simulations and in observation for the PSR J0437−4715. However the observed correlation was orders of magnitude larger than was predicted from the simulation. The bottom panels of Figure 6.7 show a scatter plot between SNR and Δt in two frequency bands, using the same data used in Figures 6.5 and 6.6 and show no evidence for correlation between SNR and TOA.

The most plausible source for the observed timing error is pulse jitter. Pulse jitter is thought to arise from intrinsic modulation of the radio emission region. To produce jitter, either the location of the emitting region moves stochastically in pulse longitude, or the relative amplitude of different emitting components

varies. Pulse jitter has been observed in all pulsars, with the possible exception of the main component of PSR B1937+21. In time-like units the rms associated with jitter is quantified as (Cordes & Downs 1985; Cordes & Shannon 2010)

$$\sigma_J = w_{\mathrm{eff},i} f_J \sqrt{1 + m_I^2} \tag{6.1}$$

where $w_{\mathrm{eff},i}$ is the intrinsic pulse width, f_J is the jitter parameter and models the rms shift of the emitted pulse (in units of the intrinsic pulse width), and m_I is the amplitude modulation index. Based on the data presented in Figure 6.8, and assuming $w_{\mathrm{eff},i} = 600$ μs and $m_I = 1$, the jitter parameter $f_J = 0.35$. The value of the jitter parameter isconsistent with values observed in many canonical pulsars and other millisecond pulsars.

6.4 Multi-Frequency TOA Corrections

It is current practice in precision pulsar timing observation to conduct observations at two widely space frequencies. Using these TOAs, the arrival time is modeled as containing a frequency dependent component associated with the column density of electrons in the ISM (the dispersion measure) and the infinite frequency TOA that is indepdent of interstellar propagation:

$$t(\nu) = t_\infty + C_{\mathrm{DM}} \nu^{-2}. \tag{6.2}$$

It is essential to correct for this effect because from epoch to epoch the column density of electron changes (effectively altering the value of 6.2), at the many microsecond levels for nearby pulsars observed in the 1 GHz to 2 GHz range (Ramachandran et al. 2006; You et al. 2007; Chapter 5; Cordes & Shannon 2010).

However, there are other time variable effects associated with the ISM

(Cordes & Shannon 2010; Chapter 5). In the spirit of assessing the strength of these effects, we applied multi-frequency correction schemes discussed in Cordes & Shannon (2010) and Shannon & Cordes (2010). At a single epoch, the delays associated with interstellar propagation were modeled by

$$t(\nu) = t_\infty + \sum_i^{N_c} C_i \nu^{-\beta_i}. \tag{6.3}$$

While models of interstellar propagation predict particular values of β_i (i.e., angular wander of the pulsar image geometrical delays scales proportional to ν^{-4}), the β_i were treated as free parameters. As noted in Cordes & Shannon (2010) that if additional terms are included in the model t_∞ that lie below white noise levels, the fit performance degrades.

Analysis was conducted on residual TOAs after a model fit. We did not fit for the pulsar spin properties but we did examine the role of profile evolution using different modeling techniques by modeling phase offsets (known as *jumps* in pulsar timing parlance) in the observations. The first technique is to assume that there are no modeled offsets. This would be true if the pulse profile did not evolve significantly. The second method is to only fit for phase offsets between the different receivers, subsequently referred to as *band jumps*. This is valid if the major source of offset was associated with different delays associated with the receivers (for example different cable lengths). The third method is to fit for offsets between all frequency channels, which we subsequently referred to as *channel jumps*. This is the most general situation and would model any stationary frequency-dependent TOA variation, whether it is intrinsic to the pulsar.

Using the initial ephemeris as a starting point, we used TEMPO2 to solve for the offsets and produce residual TOAs. The quality of fit was the weighted rms of the corrected time series (the rms of t_∞), weighted by the standard error in

t_∞ derived from the least squares fit. The results of the correction methods are summarized in Table 6.1.

In Figure 6.9 the residual TOAs for the observations of PSR J1713+0747 are displayed including the fit for channel offsets. There is a slight trend in the residuals over the observing span. In Figure 6.10 we show best fit curves for three epochs versus frequency for the channel offset fit. The residual time of arrival versus ν^{-1}, which enables the modeled infinite frequency arrival time to be displayed on the plot. In Figure 6.11 we show the performance of the fits versus the value of the exponent used for all the three frequency fitting models observed.

In the cases where jumps are included in the model, fitting increases the weighted rms. In the cases where jumps are not included, fitting improves the rms.

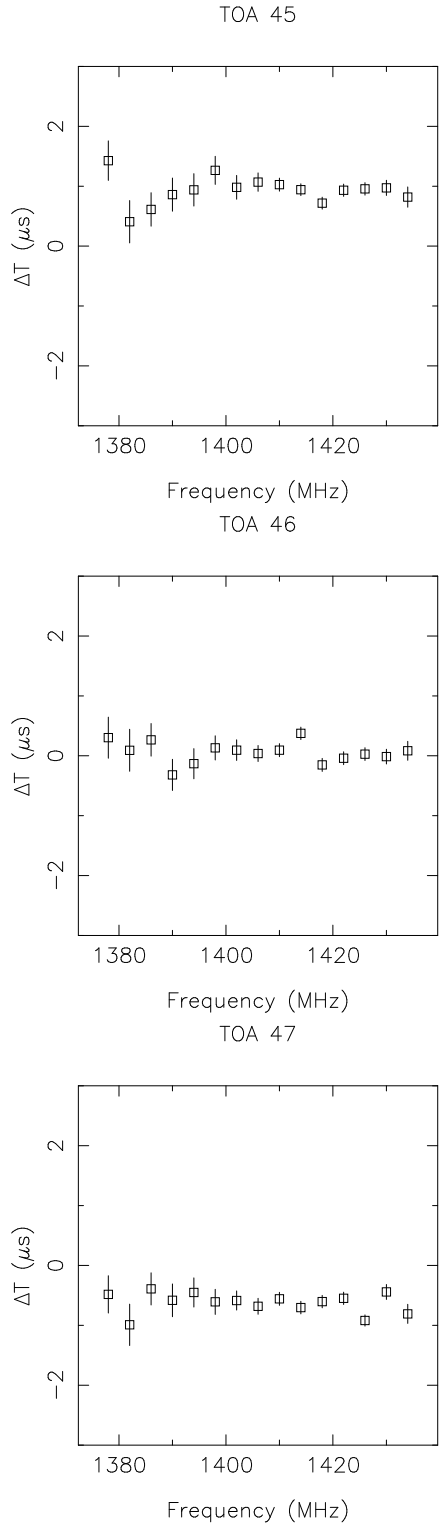

FIGURE 6.4.— Residual TOA versus frequency for consecutive 10-s sub-integrations. There is a systematic offset of the TOAs.

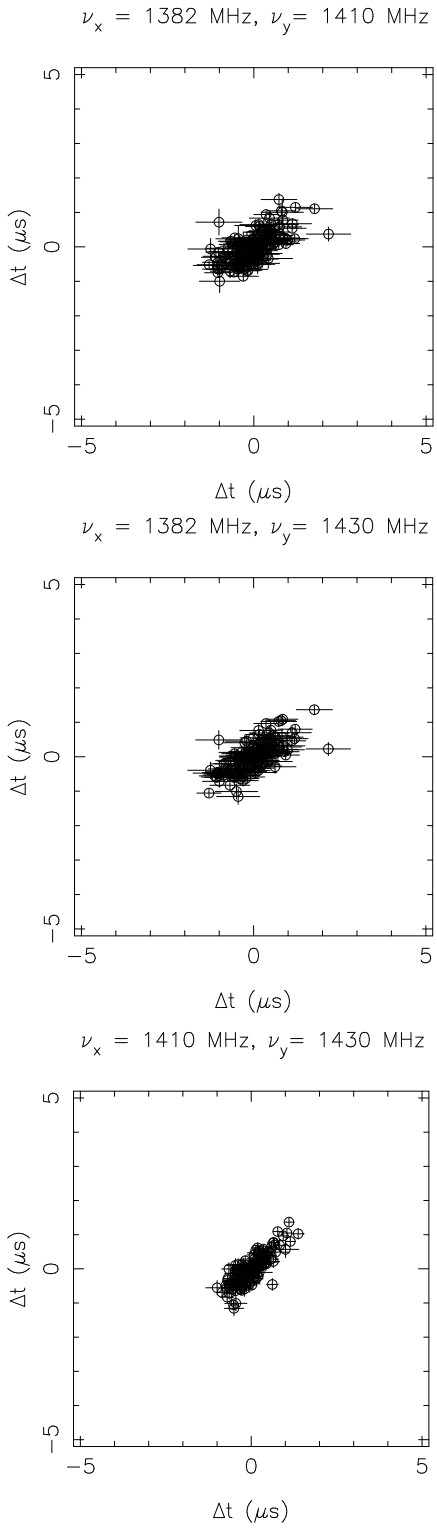

FIGURE 6.5.— Correlation of TOAs between select L-band channels. The error bars represent the $1-\sigma$ template fitting errors.

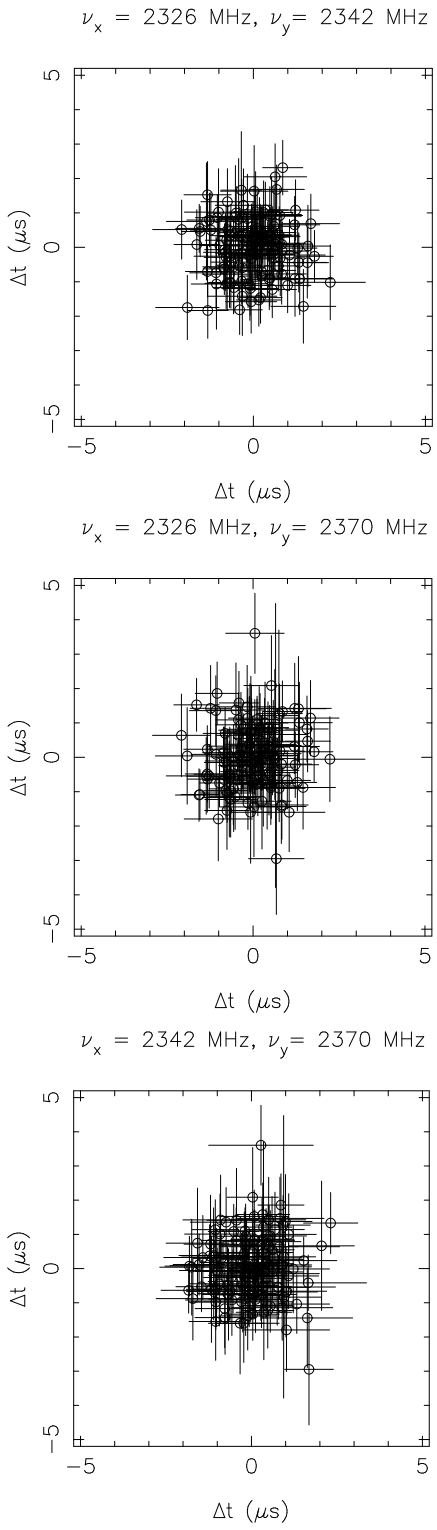

FIGURE 6.6.— Correlation of TOAs between select S-band channels. The error bars represent the $1-\sigma$ template fitting errors.

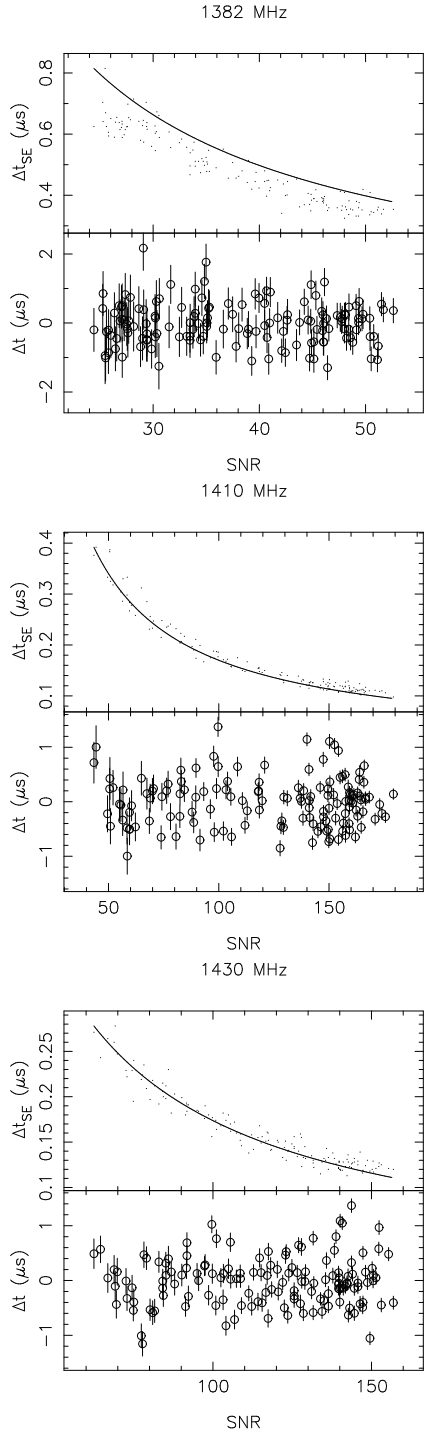

FIGURE 6.7.— *Top panels:* Signal to noise ratio versus rms standard error for observations in three frequency channels within L-band. The standard error follows the expected scaling relation with signal to noise ratio (solid line). *Bottom panels:* SNR versus time of arrival. For these observations the correlation between SNR and TOA is constrained to be < 0.1.

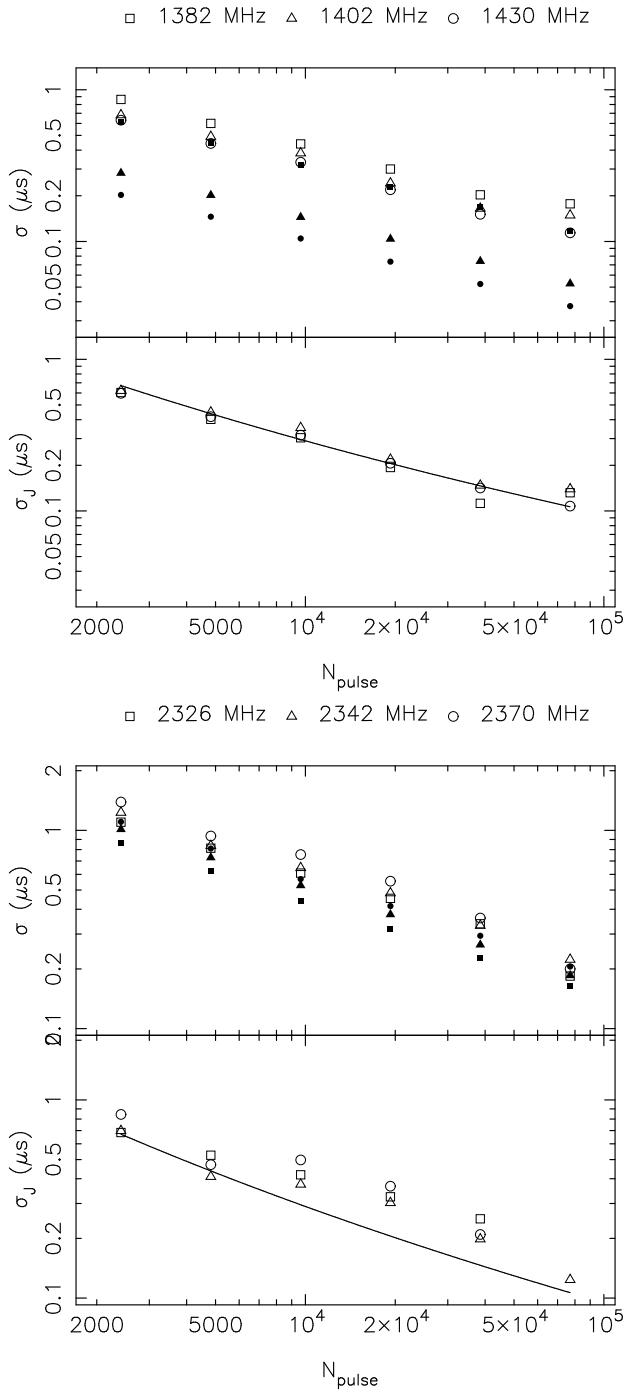

FIGURE 6.8.— *Top panels:* Observed RMS (unfilled marks) and expected RMS (filled marks) versus the average number of points, for L-band (left) and S-band (right) observations. *Bottom panels:* Quadratic different between observed and expected levels of noise for L-band (left panels) and S-band (right panel) observations. The line is a fit to the L-band data.

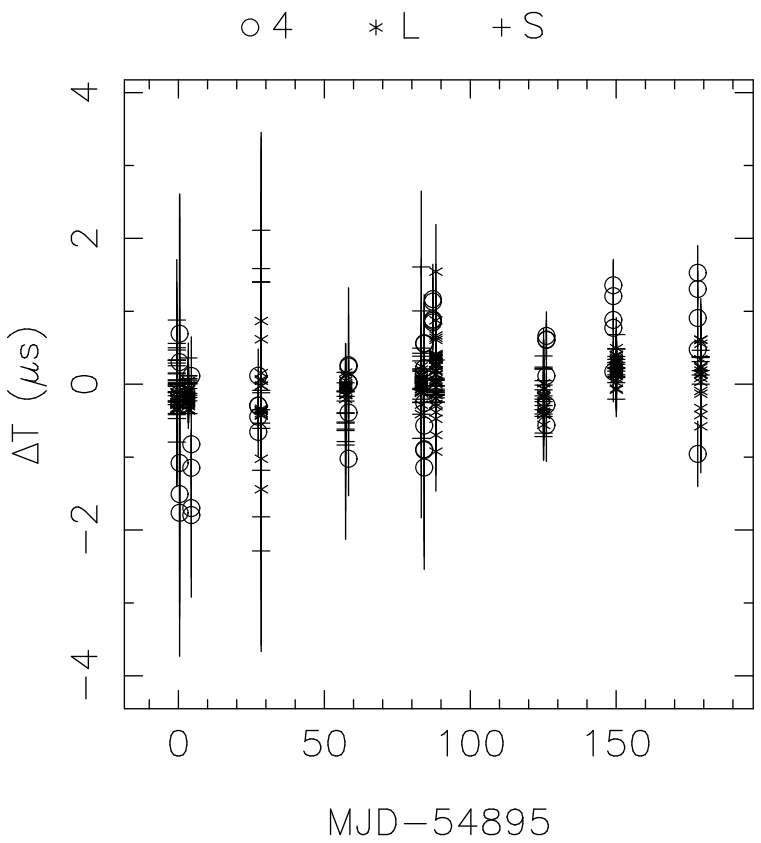

FIGURE 6.9.— Residual TOAs for PSR J1713+0747. The different symbols represent the residual TOAs at the different offset and are labeled above the plot, with 4 corresponding the 430 *MHz* observations, *L* representing L-band observations and *S* representing S-band observations.

In Table 6.1 the corrected values are displayed. There are a number of different ways to model frequency offsets. We compare fits in which we have fit for frequency arbitrary phase offsets between all the frequency channels.

6.5 Discussion and Conclusions

Jitter contributes a white noise element to pulsar TOAs. Unlike other forms of white noise, such as radiometer noise, jitter can only be mitigated by averaging over a larger number of pulses. Some of the observations here have sufficient

TABLE 6.1
EFFICACY OF MITIGATION METHODS

	4+L+S	L+S
	No Jumps	
No mitigation	1.265	1.255
ν^{-2}	1.742	1.109
ν^{-X}	0.809 (3.0)	1.101 (1.6)
$\nu^{-2} + \nu^{-X}$	1.091 (1.2)	0.953 (10.0)
	Band Jumps	
No mitigation	0.013	0.013
ν^{-2}	0.038	0.059
ν^{-X}	0.013 (7.4)	0.057 (2.7)
$\nu^{-2} + \nu^{-X}$	0.064 (2.8)	0.055 (10.0)
	Channel Jumps	
No mitigation	0.041	0.041
ν^{-2}	0.097	0.248
ν^{-X}	0.038 (3.4)	0.131 (10.0)
$\nu^{-2} + \nu^{-X}$	0.213 (10.0)	0.231 (10.0)

NOTE.—Efficacy of mitigation methods using different timing models and different band selection.

signal to noise that singles pulses would be detected (with SNR ≈ 3).

Refractive propagation delays can potentially be mitigated through multi-frequency time of arrival analysis. We have attempted to improve using multi-frequency TOAs. In fact, we find that higher order techniques *increase* residual TOAs most likely because white noise-like TOA errors are limiting the sensitivity to higher order refractive effects.

TABLE 6.2
OBSERVATIONS OF PSR J1713+0747

Epoch (MJD)	Band	Time (min)	Band	Time (min)
54891	...	...	L	25
54892	430	43	327	43
54894	S	40	L	40
54895	430	40	327	20
54898	S	60	L	60
54899	430	45	327	45
54906	...	...	L	35
54907	430	45	327	45
54922	430	55	327	55
54923	S	60	L	45
54952*	S	60	L	55
54953*	430	55	327	55
54978*	S	35	L	55
54979*	430	55	327	55
54982*	430	55	327	60
54983*	S	45	L	50
55020	S	50	L	65
55021	430	50	327	60
55044	430	60	327	70
55045	S	60	L	70
55077	430	60	327	70
55078	S	60	L	60

NOTE.—Observations. Total observation time depended on equipment start-up time. Observing time varied due to telescope allocation, calibration time, and system failure. On days marked by an asterisk, due to node failure, ASP bandwidth was limited to 60 MHz Bandwidth in *L*-band and 20 MHz in 327 MHz band

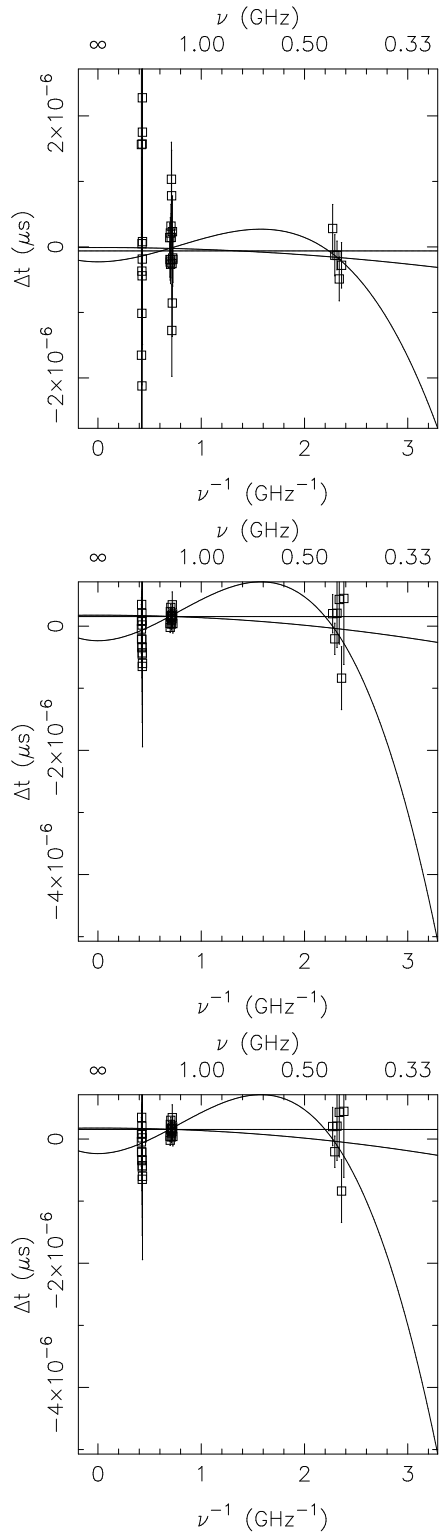

FIGURE 6.10.— Frequency dependent TOAs for three epochs. Note the abscissa is ν^{-1} and infinite arrival time is $\nu^{-1} = 0$. The fits assume exponential scaling $\beta = 3$.

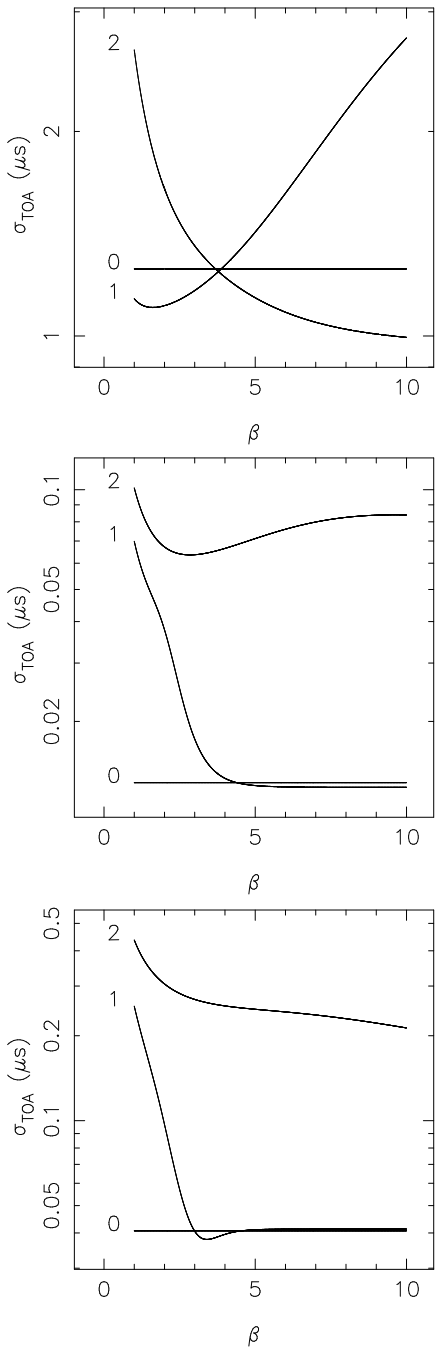

FIGURE 6.11.— RMS versus value of β for J1713+0747, for fits with no jumps (top panel), band jumps (middle panel) and channel jumps (bottom panel). See the main text for description of these techniques.

6.5.1 Acknowledgements

Travel support for conducting the observations was provided by NAIC. We thank A. Venkataraman, P. Freire, and in particular T. Ghosh for assistance in conducting the observations. We thank R. Ferdman, I. Stairs, and colleagues for developing the `ASPFitsReader` software that was used in this analysis.

CHAPTER 7

LOCATING PULSAR EMISSION REGIONS USING INTERSTELLAR SCINTILLATION

Radio emission regions in pulsar magnetospheres appear to reside in the relativistic flow above the magnetic polar cap at altitudes of 1 to 100 stellar radii. However published constraints on the pulse-phase resolved locations and sizes of emission regions are few in number and inconsistent. We present several methods that use interstellar scattering-induced structure in dynamic spectra to map emission regions as a function of spin phase and apply them to observations of two pulsars, PSRs B0834+06 and B1133+16. We use a two-dimensional correlation analysis of dynamic spectra to identify spatial offsets between emission regions, and parabolic arcs in the secondary spectra (the power spectra of the dynamic spectra) to place further limits on the shapes and locations of emission regions. For PSR B1133+16, the resolving power is low and no differential effects are seen across pulse phase, placing both upper bounds on emission region sizes and also on instrumental effects that could decorrelate dynamic spectra. For PSR B0834+06, the resolving power is much higher. Upper bounds on the shift of the cross-correlation function from zero time lag limit any spatial offset parallel to the pulsar's space velocity. We identify a decorrelation of the phase-resolved dynamic spectrum that can be attributed to the extension of the emission region in the direction transverse to the pulsar's space velocity. Structure in the secondary spectrum also supports this interpretation. Relative to the pulsar, the emission regions are extended in spin longitude but unresolved in latitude. If the magnetic field is dipolar, we estimate the emission altitude to be

$\sim$ 15% of the light cylinder radius.[1]

7.1 Introduction

In the standard description of pulsar (PSR) emission (e.g., Sturrock 1971; Ruderman & Sutherland 1975; Arons & Scharlemann 1979; Cheng et al. 1986), particles are accelerated to relativistic energies in regions with large voltage drops ($\sim 10^{12}$ V) in the magnetosphere of the neutron star (NS). These particles pair produce and form a secondary plasma in which instabilities generate the observed coherent radio emission. The radiation is by necessity relativistically beamed along or nearly along magnetic field lines that guide the particle flow. Due to the curvature of the field lines, each pulse component is beamed from a different location, with the amount of separation dependent on the altitude of emission, which is shown in Figure 7.1.

While this standard picture provides a reasonable framework, the exact configuration of the magnetosphere and the nature of the radio emission process are poorly constrained. For example, there is great uncertainty in the density of the magnetospheric plasma in the open field line region where pulsar emission likely occurs. The plasma plays a crucial role in the pulsar emission as it both sets the altitude of emission and the strength of refractive effects at higher altitudes (Barnard & Arons 1986; Lyubarskii & Petrova 1998; Petrova 2001).

Direct studies of the pulsar emission region are difficult as pulsar magnetospheres are far too small to be resolved with ground-based radio interferometers. The magnetosphere of even the nearest pulsar at $\sim$ 0.1 kpc is only about

[1]Ryan M. Shannon, James M. Cordes, Walter F. Brisken & Jean-Pierre Macquart, to be sumbitted to ApJ

10 μas in size, and the emission region, likely located deep within the magnetosphere, is substantially smaller. However, the interstellar scintillation (ISS) phenomenon provides an effective interferometeric baseline that can exceed 1 AU, yielding the spatial resolution required to probe deep within the pulsar magnetosphere and into the emission region. As part of an effort to determine the nature of the radio pulse emission process, we have used interstellar scintillation to study the emission regions of PSR B0834+06.

In §7.2 we discuss our observations. In §7.3 we review the methods of interstellar interferometry and develop new techniques that can be used to deduce source size and structure from the parabolic arcs in the secondary spectrum. In §7.4, we present studies of PSR B0834+06 conducted at the Green Bank Telescope[2]. In §7.5 we discuss the constraints on the emission region size for PSR B1133+16 which also to limit systematic effects in our observations of PSR B0834+06. In §8.5 we discuss the implications of our results and suggest future observational strategies. In the following discussion we will be using phase in two contexts. We will use pulse phase ϕ synonymously with pulse component to describe the portion of the pulse studied. We will use Φ to represent the phase of propagating radio waves.

[2]National Radio Astronomy Observatory is a facility of the National Science Foundation operated under cooperative agreement by Associated Universities, Inc.

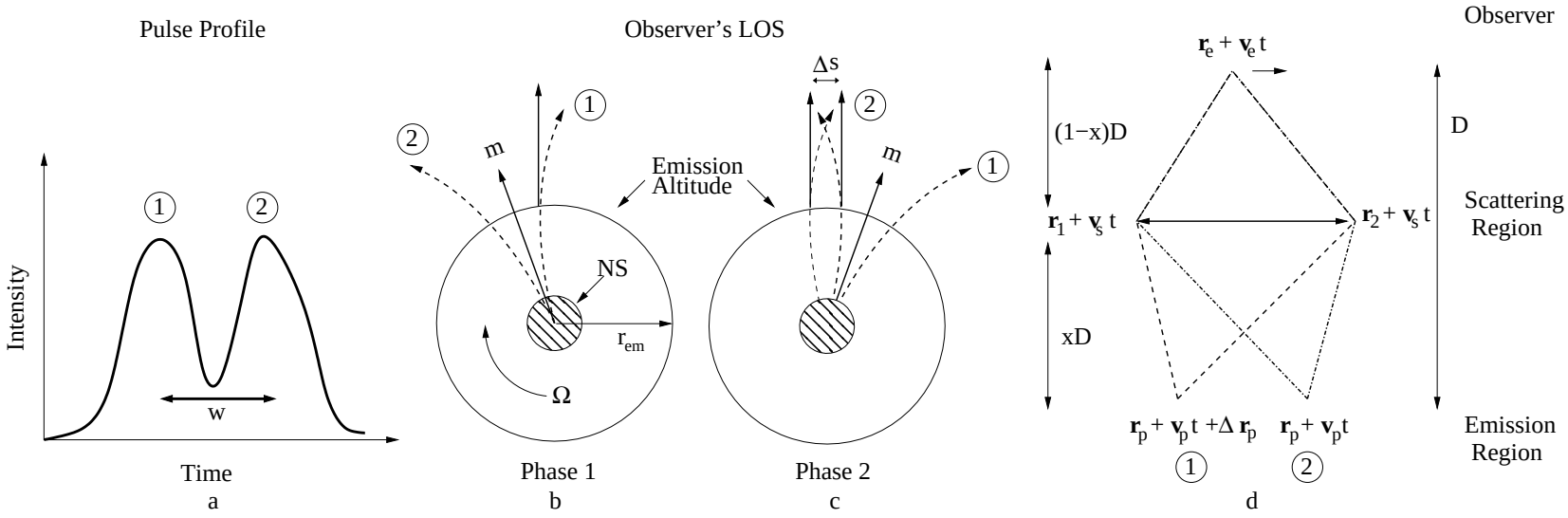

FIGURE 7.1.— Emission and Scattering Geometries. Panel *a* shows a schematic pulse profile, labeling fiducial components 1 and 2, separated by time w and phase $\Delta\theta = 2\pi w/P$, where P is the pulse period. Panels *b* and *c* show the magnetosphere geometry when components 1 and 2, respectively, are beamed in the direction of the observer. The dashed lines show the magnetic field lines along which components 1 and 2 are beamed. If the magnetic field is dipolar, the emitting regions are offset by a separation $\Delta s = r_{\rm em}\Delta\theta/3$, where $r_{\rm em}$ is the emission altitude, as the components are beamed along field lines with different curvature. Panel *d* shows the scattering geometry between two points in a scattering screen. The pulsar is at transverse position $\mathbf{r_p} + \mathbf{v_p}t$, the scattering points $\mathbf{r_1}$ and $\mathbf{r_2}$ are co-moving at velocity $\mathbf{v_s}$, and the observer is at position $\mathbf{r_e}$, moving at velocity $\mathbf{v_e}$. Radio waves from the two points in the screen scatter toward the observer and interfere at the observer's position. The observed intensity is determined by the phase difference between the two paths, which depends on observing frequency and the path length difference. The path length difference changes with time, thus intensity modulations are observed in both time and frequency. If the emission regions for different pulse components are spatially offset, the relative phases difference for the pulse components will be different, and both will show intensity modulations. The observed structures in the dynamic spectrum (DS, see main text) are caused by scattering through more complicated screen geometries that follow the same principle.

7.2 Observations

Observations of PSRs B0834+06 and B1133+16 were made on 12 November 2005 at the 100 m Green Bank Telescope with 327 MHz central frequency and 32 MHz bandwidth, recording left and right circular polarizations using a Mark-5 baseband recorder[3]. The data consist of 8 independent streams sampled every 62.5 ns with 2-bit representation.

Using pulsar timing ephemerides, the data were divided into equal portions of pulse phase containing a fixed number of samples. Fourier analysis implies that the maximum pulse phase resolution (in time units) δw and best frequency resolution $\delta\nu$ satisfy the uncertainty relation $\delta w \delta\nu = 1$. The versatility of the baseband recording technique was exploited by analyzing the data with a number of different frequency and time resolutions. A lower frequency resolution analysis used 48k point fast Fourier transforms (FFTs), corresponding to 3.1 ms phase resolution and 326 Hz frequency resolution. For a higher frequency resolution analysis, we used 130k point FFTs resulting in 8.2 ms phase resolution and 122 Hz frequency resolution. Power spectra ($|\mathrm{FFT}|^2$) were used to form the raw spectrum for each phase, $F(\nu;\phi)$. After incoherently correcting for interstellar dispersion, a large portion ($\sim$ 40%) of off pulse phase $F(\nu;\phi_{\mathrm{off}})$ was used to correct for gain variations across the bandpass to form a calibrated dynamic spectrum: $S(\nu;\phi) = (F(\nu;\phi) - F(\nu;\phi_{\mathrm{off}}))/F(\nu;\phi_{\mathrm{off}})$. The phase-resolved spectra for a fixed number of individual pulses (4 or 8, depending on the analysis) were co-added, and the series of spectra over the $\approx$ 7 ks observation of each pulsar formed phase-resolved dynamic spectrum (DS) $S(\nu,t;\phi)$, which is the basis of of our analysis. The dynamic spectrum for PSR B0834+06 can be seen in Figure

[3] `http://www.haystack.mit.edu/tech/vlbi/mark5/`

7.2. It shows fine structure indicative of scattering over large baselines.

The power spectrum of the DS is the secondary spectrum (SS): $\tilde{S}_2(f_\nu, f_t; \phi) = |\mathrm{FT}[S(\nu, t; \phi)]|^2$, where the delay f_ν is conjugate to frequency, and the fringe frequency f_t is conjugate to time. Parabolic arcs are observed in the secondary spectrum of most nearby, bright pulsars (Stinebring et al. 2001; Hill et al. 2005; Putney & Stinebring 2006). The parabolic morphology is explained by a geometric model (Walker et al. 2004; Cordes et al. 2006a) in which regions of significant power within the SS identify specific angular separations within a scattering region contributing to the modulation of the dynamic spectrum. The central core of the scattered brightness distribution interferes with the wings that extend over much larger angles (Hill et al. 2005). As fringe frequency scales linearly with angular separation and delay scales quadratically with separation, power is concentrated along a parabola. Reverse arclets are formed by interference between substructure in the image and the core, and have been observed in the SS of many pulsars (i.e., Hill et al. 2005) and identified in simulations of anisotropic scattering media (Walker et al. 2004; Coles et al. 2005). A composite secondary spectrum for our observations of PSR B0834+06 is seen in Figure 7.3. This high signal-to-noise SS was formed by combining the SS of the entire pulse with 122 Hz frequency resolution. The power profile along the arcs is shown in the outer panels of the figure. The SS shows a strong main arc composed of many reverse arclets.

The most striking feature in the secondary spectrum is an island arclet, highlighted by the arrow in Figure 7.3. The arclet is the result of interference between the main image (which forms the central region of the main parabola) and a faint sub-image. Another prominent property of this secondary spectrum is the un-

usual distribution of power in the main arc. The main arc extends farther to positive fringe frequencies but is brighter at negative fringe frequencies. This is attributed to a large-scale phase gradient in the scattering,e.g., the image of the pulsar is refracted such that the core of the image offset from the direct line-of-sight (Cordes et al. 2006a). A final notable property of the SS is the relative concentration of the power close to the main parabola. If the interfering components were distributed more istoproically throughout a scattering screen, significant power would be expected above the main arc and arclets would be less prominent. A detailed analysis of the screen structure is presented in Brisken et al. (2010).

7.3 Interstellar Interferometry

While it is possible for scattering to occur along the entire line of sight between the pulsar and the Earth, observations suggest that for many pulsars, including the pulsars studied here (Stinebring et al. 2001; Putney & Stinebring 2006), scattering is located in geometrically thin screens. While other configurations such as geometrically thick media have been considered (Lee & Jokipii 1975; Lambert & Rickett 1999; Cordes et al. 2006a), we focus our attention on the thin-screen geometry applicable the observations presented here. We define the thin screen as being located a distance xD from the pulsar and $(1 - x)D$ from the observer scatters the pulsar's radiation. The interference of waves traveling along the ensemble of paths (shown in Figure 7.1, panel d) results in the observed intensity variations which are manifested in the dynamic spectrum $S(\nu, t; \phi)$. Most previous studies have relied on correlation analyses of the dynamic spectra. In §7.3.1, we review correlative methods and the inconsistent results previously obtained

using this method. In §7.3.2 we develop tools to use the secondary spectrum (SS) to infer source size and structure.

7.3.1 Correlation Analyses of Dynamic Spectra

A common approach for quantifying the differences between the DS of the pulsar signal in pulse phases ϕ_1 and ϕ_2, is to calculate the two dimensional cross correlation function (CCF) C in frequency lag $\Delta\nu$ and time lag τ:

$$C(\Delta\nu, \tau; \phi_1, \phi_2) = \langle (S(\nu, t; \phi_1) - \bar{S}(\phi_1))(S(\nu + \Delta\nu, t + \tau, \phi_2) - \bar{S}(\phi_2)) \rangle, \quad (7.1)$$

and the correlation coefficient,

$$\rho(\Delta\nu, \tau; \phi_1, \phi_2) = \frac{C(\Delta\nu, \tau; \phi_1, \phi_2)}{\sqrt{C(\Delta\nu, \tau; \phi_1, \phi_1) C(\Delta\nu, \tau; \phi_2, \phi_2)}}, \quad (7.2)$$

where $\bar{S}(\phi)$ is the average flux density of pulse component ϕ, and angled brackets ($\langle , \rangle$), indicate averages over time and frequency.

In order to estimate source structure, the general properties of the scattering screen must be quantified, which is accomplished by determining the size and shape of the central peak of the autocorrelation function (ACF) $C(\Delta\nu, \tau; \phi, \phi)$. The width of the peak along along the frequency-lag axis ($\tau = 0$) is the scintillation bandwidth $\nu_{\rm ISS}$. The width of the peak along the time-lag axis ($\Delta\nu = 0$) is the scintillation decoherence time $t_{\rm ISS}$, and the width of the peak along the frequency lag axis is the decoherence bandwidth $\delta\nu_{\rm ISS}$. Following standard convention $\nu_{\rm ISS}$ is the half width at the $1/e$ point, and $t_{\rm ISS}$ is the half width at half the maximum. Models based on the propagation of plane or spherical waves through a turbulent plasma (see Rickett 1990, and references within for a review) are used to connect screen structure to the observed properties of the DS. The plasma

is assumed to have density fluctuations that follow a power law index α, with scattering along most pulsar lines of sight showing values between 3 and 4. The properties of the scintillation can be found by fitting one-dimensional autocorrelation functions in time A_t and frequency A_ν to functions to the form expected for a power-law medium,

$$A_t(\tau;\phi) = C(\tau,0;\phi,\phi) = D\exp[-(\tau/t_{\rm ISS})^{\alpha-2}] \tag{7.3}$$

$$A_\nu(\Delta\nu;\phi) = C(0,\Delta\nu;\phi,\phi) = D\exp[-(\Delta\nu/\nu_{\rm ISS})^{(\alpha-2)/2}]. \tag{7.4}$$

With the general properties of the scattering screen quantified, we proceed to show how the CCF can be used to estimate properties of the emission region. For additional details we refer the reader to Cordes (2000a).

Offset of the CCF: If pulse emission regions are offset in the direction of motion of the pulsar-observer line-of-sight, there will be a corresponding offset Δt of the peak correlation. Such motion is a combination of the motion of the pulsar, the earth, and the ISM. From this offset the parallel separation $\Delta r_\parallel$ can be inferred (Cordes 2000a):

$$\Delta r_\parallel \approx v_p \Delta t = \ell_d \frac{\Delta t}{t_{\rm ISS}}. \tag{7.5}$$

Here we have assumed that the effective velocity is dominated by the the pulsar velocity v_p, which is justified as pulsar motions exceed 100 km s^{-1}, and earth and screen motions are typically$\sim$ 10 km s^{-1}. The isoplanatic scale of diffraction ℓ_d is the characteristic size of the diffracted image projected onto the plane of the source:

$$\ell_d \approx v_p t_{\rm ISS} = 2^{-1/(\alpha-2)} \sqrt{\frac{(\alpha-1)cD\nu_{\rm ISS}}{4\pi(1-x)\nu^2}} \tag{7.6}$$

Decorrelation of the CCF: If the emission regions are separated in any direction, the scattering geometry and observed intensity modulations will differ,

causing a decorrelation of the DS. For a medium containing power-law turbulence, an offset of distance Δr in any direction will cause zero-lag decorrelation (Cordes et al. 1983)

$$\Delta r = \ell_d \left(-\ln[\rho(0,0;\phi_1,\phi_2)]\right)^{1/(\alpha-2)}. \tag{7.7}$$

This correlation analysis was used by Cordes et al. (1983) to set upper limits of $\approx 10^8$ cm for the separation of the two main components for both PSR B0525+21 and PSR B1133+16. Smirnova et al. (1996) observed four pulsars (PSRs B0834+06, B1133+16, B1237+25, and B1919+21) at 100 MHz, and studied both decorrelation and peak correlation offset. From studying the decorrelation, they found emission region sizes of $\approx 10^9$ cm, which corresponded to an emission altitude close to the light cylinder. From studies of the offset in time lag, they found sizes parallel to pulsar motion that were smaller by a factor of ten than those from the decorrelation.

Multiple Image Events: Another approach can be used during unique episodes of scattering, in which the modulation is not caused by core-wing scattering, but by the interference of two distinct sub-images (Wolszczan & Cordes 1987). This situation is an extreme case of the island arclet we observe in the SS of PSR B0834+06. In these instances, an offset in peak correlation in frequency lag (Cordes et al. 1986) will be associated with a separation of emitting components

$$\Delta r \approx \frac{x}{1-x}\left(\frac{cD}{r_2 - r_1}\right)\left(\frac{\delta\nu}{\nu}\right) f_\nu, \tag{7.8}$$

where f_ν is the modulation rate in frequency. Wolszczan & Cordes (1987) estimated the separation in the direction of the subimage baseline for PSR B1237+25 to be $\sim 10^8$ cm, while Gupta et al. (1999) estimated the separation of pulse components for PSR B1133+16 to be $\sim 3 \times 10^7$ cm.

Intensity Demodulation: The degree of intensity modulation dynamic spectra can also be used to estimate source region size. If a pulsar is unresolved by the scattering region, the intensity modulations within the DS will be 100%, but if the emission regions are extended, the intensity modulation of the scintillation will be less than 100%. Gwinn et al. (1997, 2000) estimated the size of the emission region of the Vela pulsar (PSR B0833−45) at different frequencies by using the strength of the intensity modulations to infer total source size of 4×10^7 cm at 2 GHz. However, it has been suggested that this effect is instrumental in nature (Cordes 2000b).

The results of previous studies, listed in Table 7.1, yield results inconsistent with each other. Most studies applied one of two techniques, and none have analyzed the arcs in secondary spectrum. Additionally, inferred emission altitudes contradict those based on other methods, like aberration-retardation (Cordes 1978; Gupta & Gangadhara 2003; Johnston et al. 2007). However, these latter methods are highly dependent on models of magnetosphere structure.

7.3.2 Arcs in Secondary Spectra

In this section, we present new techniques to study pulsar emission regions that are applied to secondary spectra. First, we develop a model to explain the properties of the SS. Because the interference is explained by geometric path length differences with little contribution from dispersion delays, the phase difference $\Delta\Phi$ between paths is directly proportional to the path length differences between a pair of rays ΔD, $\Delta\Phi = 2\pi\nu\Delta D/c$, as seen in Figure 7.1, panel d. For paths originating at position $\mathbf{r_p}$ and observed at position $\mathbf{r_e}$, through screen po-

TABLE 7.1
CONSTRAINTS ON PULSAR EMISSION REGIONS

PSR	ν (GHz)	Dir.	δr (cm)	$R_{\rm em}$ (cm)	$R_{\rm em}/r_{\rm LC}$	Ref
B0525+21	0.43	tot	$\lesssim 10^{7.9}$	$\lesssim 10^{9.0}$	≤ 0.06	1
B0823+26	0.10	$\parallel$	$10^{8.0}$	$10^{9.5}$	1.2	4
B0834+06	0.10	$\parallel$	$10^{7.8}$	$10^{9.5}$	0.5	4
	0.10	tot	$10^{9.7}$	$10^{9.7}$	0.8	5
	0.33	tot	$10^{7.8}$	$10^{8.9}$	0.2	8
	0.33	$\parallel$	$\lesssim 10^{5.7}$	$\leq 10^{7.9}$	≤ 0.02	8
B0833−45	2.30	tot	$10^{7.6}$	$10^{7.6}$	0.09	7
B1133+16	0.10	tot	$10^{7.5}$	$10^{8.7}$	0.09	3
	0.10	$\parallel$	$10^{7.7}$	$10^{8.9}$	0.2	4
	0.10	tot	$10^{9.3}$	$10^{9.3}$	0.4	2
	0.33	$\parallel$	$10^{7.5}$	$10^{8.5}$	0.05	6
	0.43	tot	$\lesssim 10^{8.0}$	$\lesssim 10^{9.5}$	$\lesssim 0.09$	1
B1237+25	0.10	tot	$10^{9.5}$	$10^{9.5}$	0.5	5
	0.43	$\parallel$	$10^{8.0}$	$10^{8.9}$	0.12	2
B1919+21	0.10	$\parallel$	$10^{8.0}$	$10^{9.5}$	0.5	4
	0.10	tot	10^{10}	10^{10}	1.6	5

NOTE.—Emission region sizes, altitudes, and upper limits calculated using interstellar interferometry. Column ν shows the observation frequency. Measurements types of labeled in column *Dir* are either of total size (labeled by *tot*) or of size parallel to effective pulsar-observe motion, indicated by $\parallel$. Emission altitudes are given in physical units and as a fraction of the light cylinder radius $r_{\rm LC} = cP/2\pi$, where P is the pulse spin period. References (1) Cordes et al. (1983), (2) Wolszczan & Cordes (1987), (3) Smirnov & Shishov (1989), (4) Smirnova (1992), (5) Smirnova et al. (1996), (6) Gupta et al. (1999), (7) Gwinn et al. (2000), and (8) This work.

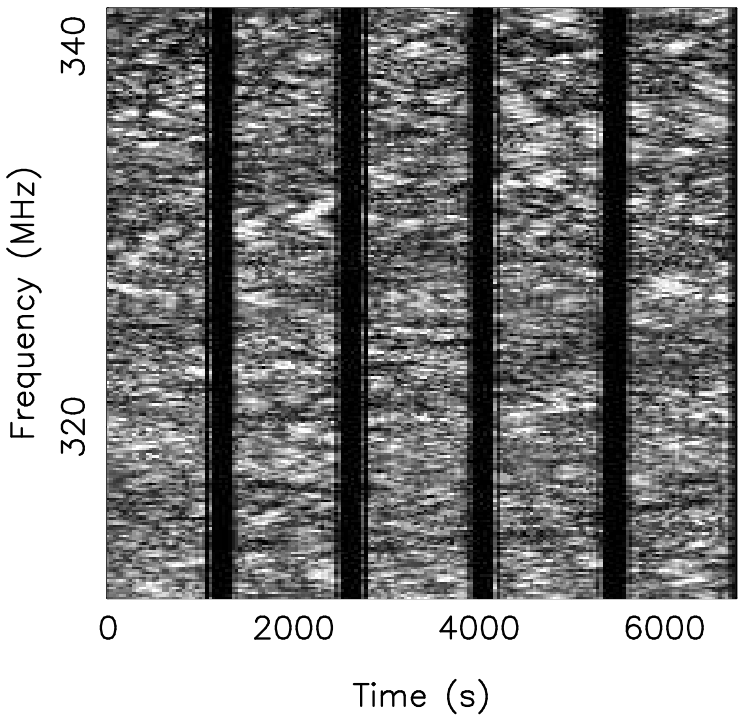

FIGURE 7.2.— The dynamic spectrum (DS) for PSR B0834+06, displayed in linear gray scale. The large vertical bands at times ≈ 1400 s, 2800 s, 4200 s, and 5400 s are gaps in the data set. Other less pronounced time-to-time fluctuations are due to intrinsic pulse amplitude modulations, such as pulse drifting an nulling, as only four pulses were averaged to form each pixel in the dynamic spectrum. These intensity variations are associated with previously observed nulling and drifting (Rankin & Wright 2007).

sitions $\mathbf{r_1}$ and $\mathbf{r_2}$, the phase difference is

$$\Delta\Phi = \frac{\nu}{2cD_{\rm eff}}[|\mathbf{r_2} + \mathbf{v_s}t|^2 - |\mathbf{r_1} + \mathbf{v_s}t|^2 - 2\,(\mathbf{r_2} - \mathbf{r_1}) \cdot ((1-x)(\mathbf{r_p} + \mathbf{v_p}t) + x(\mathbf{r_e} + \mathbf{v_e}t)]. \quad (7.9)$$

Interference from a pair of components will cause sinusoidal modulation in the intensity, contributing a delta function at a particular fringe frequency f_ν and delay f_t. The delay and fringe frequency are found by performing a Taylor expansion of equation 7.9 about time t and central frequency ν, respectively,

$$\begin{aligned} f_t &= \frac{\partial\Delta\Phi}{\partial t} = \frac{\nu}{2cD_{\rm eff}}\,(\mathbf{r_1} - \mathbf{r_2}) \cdot \mathbf{V}_{\rm eff} \\ f_\nu &= \frac{\partial\Delta\Phi}{\partial \nu} = \frac{1}{2cD_{\rm eff}}\left[r_1^2 - r_2^2 - 2(1-x)(\mathbf{r_1} - \mathbf{r_2}) \cdot \mathbf{\Delta r_p}\right], \end{aligned} \quad (7.10)$$

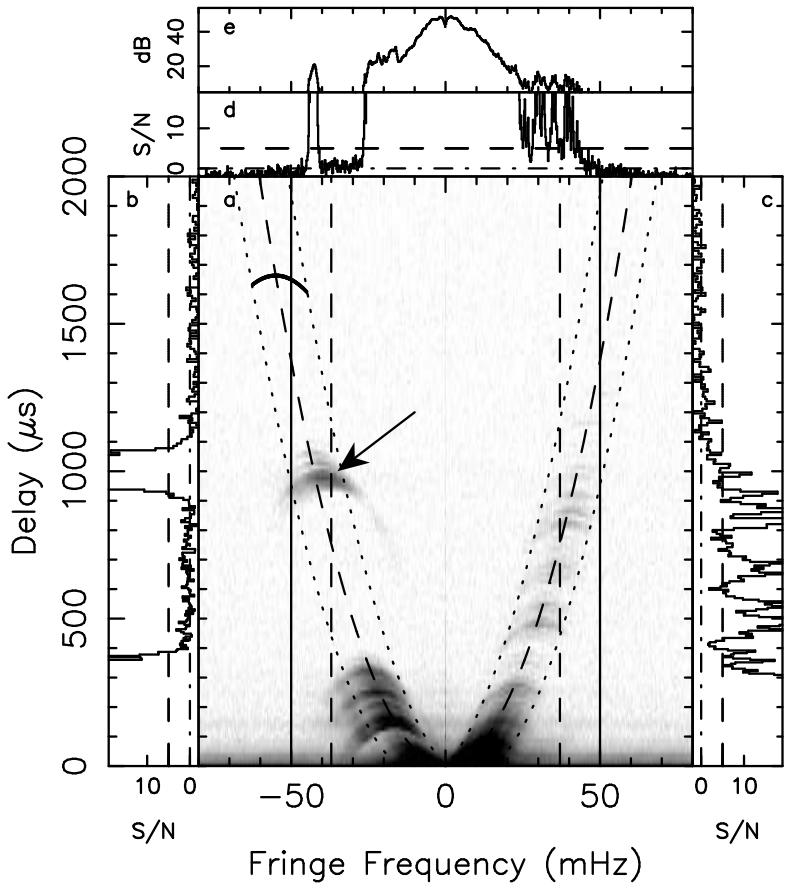

FIGURE 7.3.— The combined secondary spectrum. A logarithmic gray scale is used. The dashed parabola is the center of the arc. The dotted parabolas indicate the region used to calculate the arc profiles of the outer box. The solid inverted parabolas centered at $f_t = -55$ MHz is the template used to estimate the arclet profile. The arcs cut off above $f_t \approx 68$ mHz, setting a limit on the size of the entire emission region of $\Delta D/\ell_d \leq 0.5$. The vertical dashed lines indicates where $f_t \Delta t_{\rm ISS} = 1$, and demarcate the region for which the SS fiducially has higher resolving power than the DS. The arrow points to a particularly strong arclet. *Outer panels:* profile of arc strength. Panels b, c, and d show the profile in linear in scale measured in signal-to-noise ratio. The dash-dot line is the mean off-arc level, and the dashed line is 5σ above the mean value. Panel e shows the entire dynamic range in dB above the noise floor, showing 40 dB of dynamic range in the SS. The rest of the panels concentrate on the lower signal-to-noise features, and show the extent to which arclets can be observed.

where $\mathbf{V}_{\rm eff} = (1-x)\mathbf{v_p} + x\mathbf{v_e} - \mathbf{v_s}$ is the effective velocity, $\mathbf{\Delta r_p}$ is the offset in the pulsar plane, and single dish observations are assumed (i.e., no spatial offsets at the earth-end). With this model in mind, we discuss how the distribution of

power in pulse phase resolved secondary spectra can be used to constrain the shape and spatial separations of emitting regions.

Cutoff of the Main Arc: If the background source is sufficiently extended, the main arc will cut off (Cordes et al. 2006a). This is analogous to the roll-off of the visibility function due to finite source sizes in conventional interferometry. If a source is extended, the cumulative phase from different parts of the emitting region exceed some critical amount $\Phi_c \approx 1/2\pi$, the waves will not add up coherently, and intensity modulation will be suppressed. The phase difference is proportionally greater in portions of the scattering screen farther from core of the image, resulting in a cut-off of the arcs at high fringe frequencies and delays. The source size ΔR_s at which the arcs will cut off is

$$(\mathbf{r_2} - \mathbf{r_1}) \cdot \mathbf{\Delta R_s} > \lambda D_{\rm eff} \Phi_c. \tag{7.11}$$

The cut-off of the main parabola in fringe frequency $f_{t,c}$ sets a size limit parallel to pulsar motion

$$\Delta r_{s\|} \leq \Phi_c \frac{V_{\rm eff}}{(1-x) f_{t,c}} \approx \Phi_c \frac{v_p}{f_{t,c}}. \tag{7.12}$$

In the case that the pulsar motion dominates the effective velocity, the size limit is independent of screen location along the line of sight.

Power distribution in the main arc: Further constraints can be placed by studying the distribution of power inside the main parabola. The delay axis ($f_t = 0$) defines the line $r_{2\|} - r_{1\|} = 0$. The amount of power inside the main parabola constrains the interference in the direction perpendicular to $\mathbf{V}_{\rm eff}$. Assuming core-wing scattering, the extent of the wings along the $f_t = 0$ axis is

$$\Delta r_{s\perp} \leq \Phi_c \sqrt{\frac{c D_{\rm eff}}{2(1-x)^2 \nu^2 f_{\nu,c}}}. \tag{7.13}$$

Positions of arclets: By comparing the relative position of features in the SS between different pulse phases, the relative locations of source emission regions can be identified. These features include reverse arclets, which are formed by the interference of particularly bright structures within the wings and the core. If emitting regions are spatially separated, the arclets would be observed at different positions in phase-resolved secondary spectra[4]. The fringe rate f_t, which is only sensitive to the relative positions of interfering components, does not change if the position of the background source is altered. However, the delay f_ν changes by an amount

$$\Delta f_\nu = \frac{-2\pi(1-x)}{cD_{\rm eff}}(\mathbf{r_1} - \mathbf{r_2}) \cdot \mathbf{\Delta r_p}. \tag{7.14}$$

If a change in delay is observed equation 7.14 can be inverted to infer the relative offset of the emitting regions.

Phase in the cross spectrum: The phase in the cross spectrum can be used to infer source offset. The cross spectrum is defined as

$$\tilde{C}(f_\nu, f_t; \phi_1, \phi_2) = \tilde{S}(f_\nu, f_t; \phi_1)\tilde{S}^*(f_\nu, f_t; \phi_2), \tag{7.15}$$

such that $\tilde{C}(f_\nu, f_t; \phi, \phi) = \tilde{S}_2(f_\nu, f_t; \phi)$. In Appendix 7.7, we show the phase difference $\Delta\Phi$ between scattering regions offset by $\mathbf{\Delta r_p}$ at the pulsar and observers offset by $\mathbf{\Delta r_e}$ can be recovered from the argument of $\tilde{C}(f_\nu, f_t; \phi_1, \phi_2)$:

$$\arg\left[\tilde{C}(f_\nu, f_t; \phi_1, \phi_2)\right] = \Delta\Phi = \frac{\nu}{cD_{\rm eff}}(\mathbf{r_1} - \mathbf{r_2}) \cdot \left[(1-x)\mathbf{\Delta r_p} + x\mathbf{\Delta r_e}\right]. \tag{7.16}$$

There would be a phase difference associated with the transverse separation of the antennas $\mathbf{\Delta r_e}$ (observed in multi-station interferometric observations,

[4]This is analogous to previous observations that showed that over time scales of weeks, long-lived features in the secondary spectrum changed positions as would be expected from the changing pulse-screen-observer geometry (Hill et al. 2005)

Brisken et al. 2010) but also in the pulsar's emission region $\mathbf{\Delta r_p}$. In single dish observations, a phase offset $\Delta\Phi$ would be indicative of a spatial offset $\Delta r_\parallel$ in the direction parallel to effective motion:

$$\Delta r_\parallel = \frac{v_p}{f_t}\frac{\Delta\Phi}{2\pi}. \tag{7.17}$$

If pulse components were sufficiently separated, we would expect to see a phase gradient along the arcs in the secondary spectrum.

7.4 PSR B0834+06

The isoplanatic diffraction scale ℓ_d at the epoch of observation for PSR B0834+06 was $\approx 4 \times 10^8$ cm, the number of independent scintles in the observation was large, and, as shown below, sub nano-arcsecond resolution was achieved. The estimates of source size are based on a distance inferred from modeling the total electron density along the line of sight (0.64 ± 0.08 kpc, Cordes & Lazio 2002), and the measured proper motion ($\mu = 51 \pm 3$ mas yr^{-1}, Lyne et al. 1982), because there is not presently a parallactic distance to this object. Hence, the estimates of the size of the emitting region are directly proportional to this distance. The effect of the Earth's motion on the effective velcoity is small at the epoch of observation, increasing the effective velocity from 174 km s^{-1} to 180 km s^{-1}, and shifting its direction by 3°.

We cross-correlated the DS from each pair of on pulse phases (components 6-15 in Figure 7.4, top). We found no significant offset of the CCF in either time lag or frequency lag for any pulse phases. From the offset in time lag, we can set a 5σ upper limit on source offset in the direction parallel to the effective velocity of $\Delta r_\parallel \leq 5 \times 10^6$ cm, discussed further in Appendix 7.8.

TABLE 7.2
SCINTILLATION PROPERTIES

	$t_{\rm ISS}$ (s)	$\nu_{\rm ISS}$	ℓ_d cm	α	N_s
B0834+06	28	8 kHz	4×10^8	3.5	6900
B1133+16	170	1690 kHz	1×10^{10}	3.3	12

NOTE.—$t_{\rm ISS}$ is the (1/e) decay time of the intensity ACF, $\nu_{\rm ISS}$ is the half width half maximum frequency bandwidth of the intensity ACF; ℓ_d is the isoplanatic diffractive scale, i.e., the diffractive scale in the scattering screen projected onto the image (pulsar) plane; α is the parameter describing the shape of the decay, and the structure of the turbulent medium; and N_s is the approximate number of scintles in the data set.

We find significant variation of the cross correlation coefficient ρ across pulse phase. To mitigate decorrelation caused by low signal to noise near filter edges, we only included the inner half of each sub-band. We observed a high level of correlation between nearby pulse phases but a lower level between more distant pulse phases that is inconsistent with unity, as seen in Figure 7.4 and 7.5. The correlation decreases monotonically across pulse phase and does not depend on the signal-to-noise ratio of the pulse component suggesting a gradual shift in the positions of the pulse components. In Appendix 7.8 we show correlation is consistent with marginal offsets pulse phases and we construct a self-consistent map of the locations of the pulsar emission regions. The expected variance in the correlation coefficient is approximately

$$\sigma_\rho^2 \approx 1/N_s + 1/N_p(S/N)^{-4} \tag{7.18}$$

where the first term is the estimation error due to the finite number of scintles $N_s \approx (1 + 0.1\Delta\nu/\nu_{\rm ISS})(1 + 0.1\Delta T/t_{\rm ISS})$ (Cordes 1986), and the second term is due to the finite signal to noise, where S/N is the signal-to-noise ratio in a single pixel of the DS and N_p is the total number of pixels. PSR B0834+06 is a very bright pulsar at the observing frequency and this first term is expected to dominate the uncertainty, with the exception of the band edges. To test if this a reasonable value for the variance, we subdivided the data set into ten equal portions in time calculated the correlation coefficient for each, and that the variance of these measurements agreed with what would be expected from equation 7.18. We rule out gross systematic sources of decorrelation as nearly identical observations of PSR B1133+16 do not show the same effect (see §7.5).

To determine the extent of the arcs and the size of the emitting region, we formed a high signal to noise secondary spectrum by adding the phase-resolved SS together as shown in Figure 7.3. We suggest that the thinness of the main arc can be caused by the extension of source emitting region in a direction transverse to proper motion. Near the delay axis ($f_t = 0$) the power in the secondary spectrum falls off to background levels near $f_\nu = 20$ μs. Assuming interference is suppressed when the phase varies by $\Phi_{c,1}$ radians, we use equation 7.13 to set a cutoff of $\Delta r_\perp \leq 3 \times 10^8$ cm $f_{\nu,20}^{-1/2}\Phi_{c,1}$, which is comparable to the estimated separation of emission components from the previously described correlation analysis.

We attempted to determine if the arclets changed positions across pulse phase. For the secondary spectrum of each pulse phase, we calculated power in an arclet template centered on the locus of the main arc, for many many positions along the main arc. The arclet template and the power within the arclet

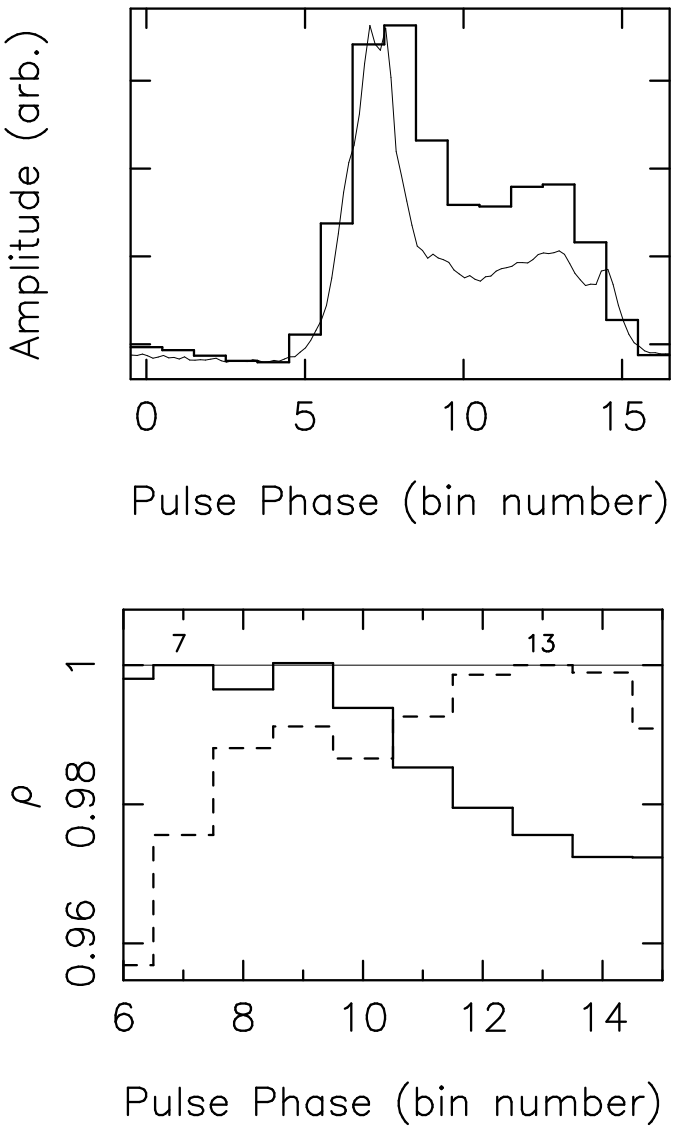

FIGURE 7.4.— *Top:* Average pulse profile for pulsar B0834+06. Components 6-15 were included in the correlation study, encompassing 33 ms (9°) of pulse phase. Over plotted is a pulse profile with much higher phase resolution. *Bottom* Correlation coefficients relative to pulse phases 7 (solid line) and 13 (dash-dotted line). The thin horizontal line is 100% correlation.

template along the arc is seen in the outer panels of Figure 7.3. For each pulse phase, we cross-correlated these the profiles and attempted to measure a shift in the position along the arc. We found no significant changes in the position of the arclets and set a less constraining upper limit than that derived by other

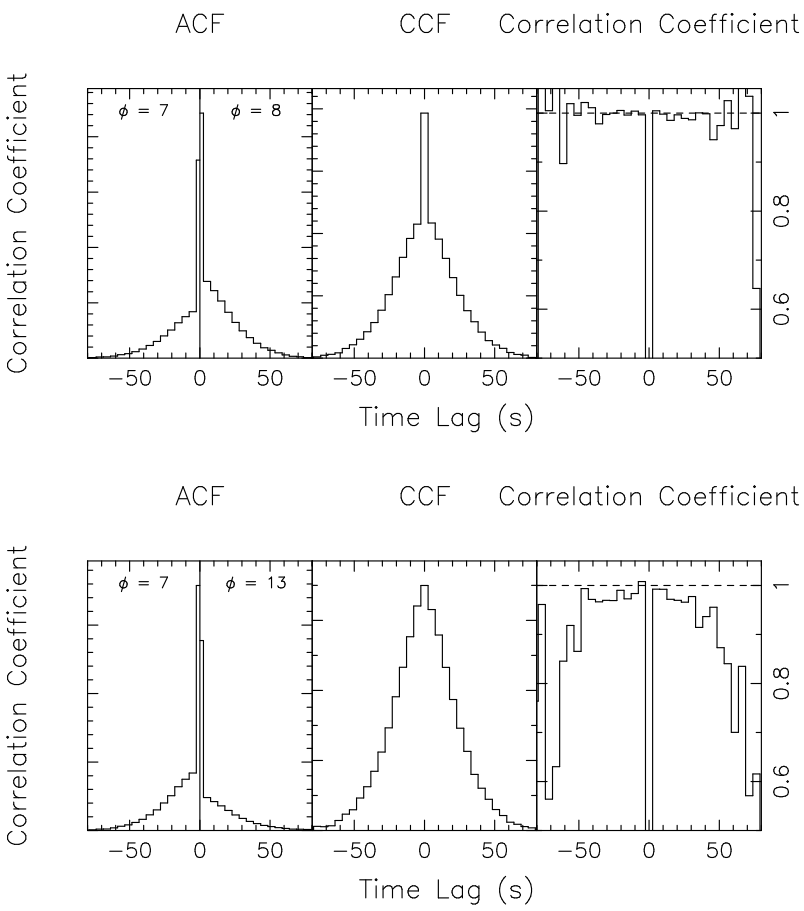

FIGURE 7.5.— Time decorrelation for two nearby pulse phases using only the inner 50% of each bandpass. The top series is for nearby pulse phases 7 and 8, and the bottom series is for more distant pulse phases 7 and 13. In each series, the right panel shows the ACF for pulse phases, with the zero lag spike. The center panel shows the CCF. The ACF and CCF panels are scaled to the same arbitrary units. The right panel shows the correlation coefficient. The dashed horizontal line is 100% correlation.

methods. In different scattering configurations or higher signal-to-noise observations, this technique could be used to effectively quantify the subtle changes in the secondary spectrum expected from emission region offset

Using the cross spectra analysis we were able to constrain source separation to comparable levels to the correlation analysis, providing a direct connection between two different methods. We measured the phase variations in the cross

spectrum: $\Phi(f_\nu, f_t; \phi_1, \phi_2) = \arg(\tilde{C}(f_\nu, f_t; \phi_1, \phi_2))$. Along the parabolic arc, where the signal to noise is the highest, no net change in phase was observed, but the root-mean-square phase can be used to constrain source separation. To determine the significance of an upper limit, we model the Fourier transform of the DS, $\tilde{S}(f_\nu, f_t; \phi) = FT[S(\nu, t; \phi)]$ as containing a deterministic component $g \exp i\Phi$ and complex noise n_ϕ.

$$\tilde{S}(f_\nu, f_t; \phi) = g(f_\nu, f_t; \phi) \exp[i\Phi(f_\nu, f_t; \phi)] + n_\phi \tag{7.19}$$

The phase difference between components ϕ_1 and ϕ_2 is

$$\begin{aligned} \Delta\hat{\Phi} &= \Phi(f_\nu, f_t; \phi_2) - \Phi(f_\nu, f_t; \phi_1) \\ &= \arg(\tilde{S}(f_\nu, f_t; \phi_2)\tilde{S}^*(f_\nu, f_t; \phi_1)) \\ &= \arg(\tilde{C}(f_\nu, f_t; \phi_1, \phi_2)) \end{aligned} \tag{7.20}$$

The noise n_ϕ is zero-mean white noise with independent real and imaginary components with variance σ_ϕ^2. We simulate $\Delta\Phi$ using the model in equations 7.19 and 7.20 to determine the estimation error in $\Delta\hat{\Phi}$.

We can estimate $g(f_\nu, f_t; \phi)$ and σ_ϕ by measuring the secondary spectrum on and off the arc.

$$|\tilde{S}(f_\nu, f_t; \phi)|^2 = \hat{g}^2(f_\nu, f_t; \phi) + 2\hat{\sigma}_\phi^2, \tag{7.21}$$

To determine σ_ϕ, we observe an off-arc portion of the arc where $\hat{g}^2(f_\nu, f_t; \phi) = 0$, and determine the on-arc gain $\hat{g}^2(f_\nu, f_t; \phi)$ by inverting equation 7.21.

With these estimates, we calculate expected values of the phase offset $\Delta\Phi = \Phi_2 - \Phi_1$. If $g = 0$, Φ is distributed uniformly over all angles between -180° and 180°. For on-arc ($g > \sigma_\phi$) portion of the cross-transform, with no spatial offset of the emission regions ($\Delta r_p = 0$), Φ would have a zero mean distribution with a

smaller variance. If there is significant offset of the emission regions ($\Delta r_p = 0$) we would expect non-zero mean value of Φ. By binning the secondary spectrum, the variance is reduced and $\Delta\Phi$ approaches Gaussian statistics. We set an upper limit $\Delta\Phi \leq 1.7^\circ$ with the feature at $f_t \approx +15$ mHz, $f_\nu \approx 300$ μs. This yields a 5σ upper limit of 5×10^6 cm on the separation in the parallel direction, which is consistent with the limits set with the correlation analysis.

We can place additional limits on source extension by analyzing the map of the scattering regions presented[5] in (Brisken et al. 2010). By correlating the received signals from Arecibo, Westerbork and Green Bank Telescopes, they were able to identify the positions of features with respect to the celestial coordinate system. They found that the main arc was formed by scattering between a central core and a highly anisotropic linear halo, aligned 25° west of north. The feature was measureable to 22 mas from the central core. Additionally, they found that the prominent island arclet was formed by scattering between a core and a prominent feature offset significantly from the linear halo. The feature is 142° west of north, and is 28 mas from the central core. The fact that the linear feature and the island arclet are nearly orthogonal to each other allows constraints on source size to be placed in nearly orthogonal directions. Converting equation 7.11 to an angular form, we find

$$\Delta R_f \leq \frac{\lambda x \Phi_c}{\theta_f} \tag{7.22}$$

Where ΔR_f is the extent of the source in the direction of a feature located in the halo at angular extent θ_f from the core of the image. We find that the source size is limited to $10^{7.7}\Phi_c/1$ rad cm in the direction of the main arc, and $10^{7.6}\Phi_c/1$ rad cm in the direction of the arclet.

[5]We have used single-station data from their VLBI observations.

The observed intensity variations encode both the structure of the scattering screen and the background source and must be distinguished in concert. An example of how source shape and screen shape can equally affect the observed intensity modulations is shown schematically in Figure 7.6. For the background pulsar, we consider configurations in which each pulse component is 1) point-like; 2) extended in the direction of effective motion without changing position across pulse phase; and 3) extended in the direction of effective motion. In addition, we consider cases in which the pulse components are i) not spatially separated; ii) separated in the direction of effective motion; and iii) separated in direction perpendicular to pulsar motion. We consider a screen that forms a scattered brightness distribution that is a) isotropic, b) extended in the direction parallel to effective motion, and c) extended in the direction perpendicular to effective motion. The lack of shift of the CCF, lack of phase difference in the cross-spectrum, and the length of the main arcs severely constrain component separation in the direction of effective motion. The asymmetry in the secondary spectrum suggests that the scattering screen is either extended in the direction of effective motion, or the source is extended in the direction transverse to pulsar motion. In Appendix 7.8 we argue that the observed decorrelation is due to the marginal resolution of the pulse emission region. In Figure 7.7 in the appendix in §7.8 we present a map showing the estimated positions of each pulse component. Assuming a dipolar field, the emission altitude is 9×10^8 cm or 15% of the light cylinder radius. While it is also possible that the decorrelation is caused by shape changes (with or without change in pulse location) across pulse longitude, in this case, we would expect pulse components arising from comparable portions of the pulse profile (for example, the peaks of the double conal profile, Rankin 1993) to be more highly correlated, and to observe non-monotonic

changes in decorrelation.

Previous observations of pulse polarization also constrain emission geometry. These observations suggest that the magnetic pole of the axis passes to within 3° of the line of sight, and that the projected angular momentum and velocity vectors are offset from one another by only 16° ± 7° (Johnston et al. 2007). In this situation, as the pulsar beam crosses the line of sight the displacement of the magnetic axis (as show in Figure 7.1, panel d) is expected to be predominantly in the direction transverse to pulsar motion.

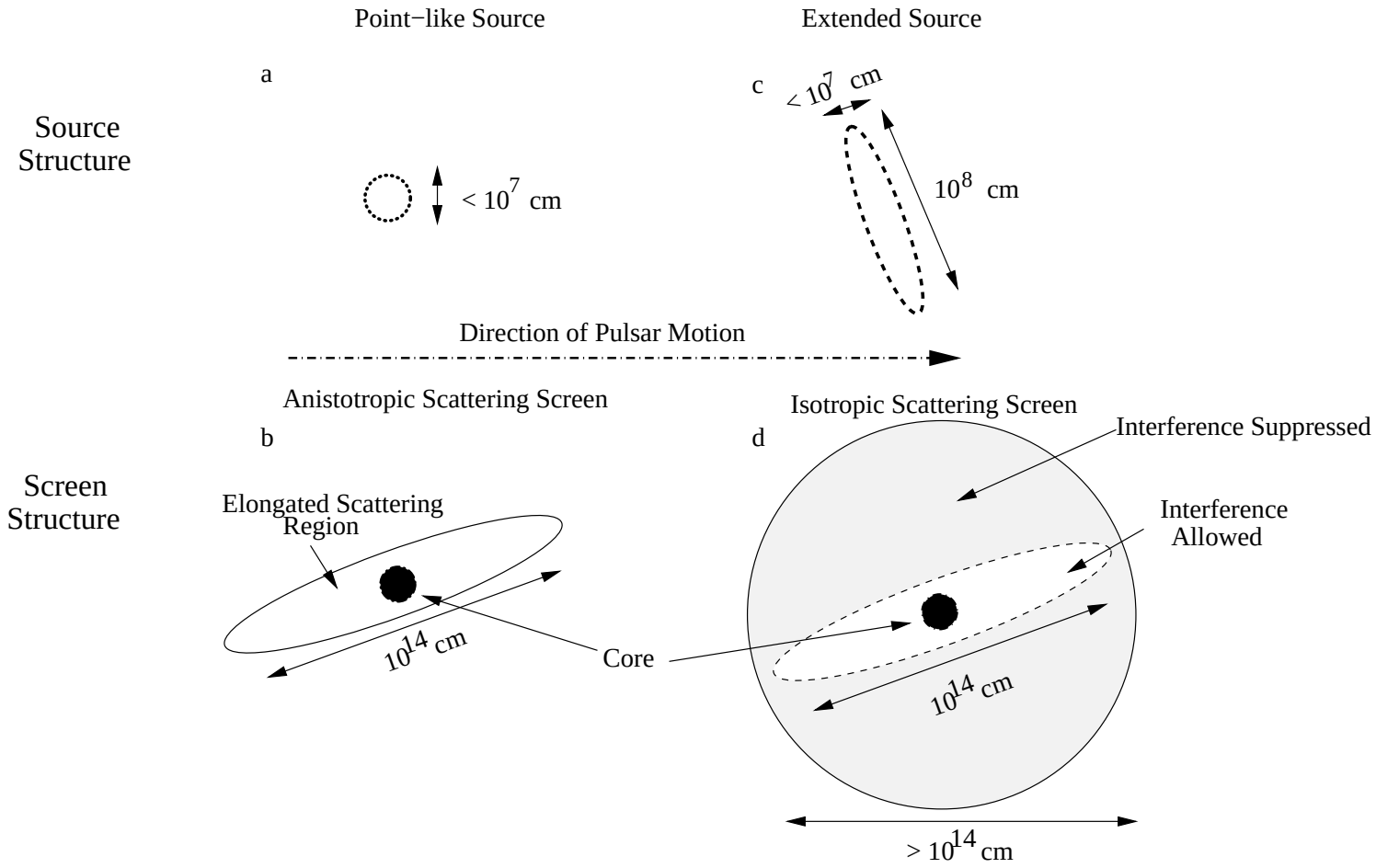

FIGURE 7.6.— Two source-screen configurations that would produce similar intensity modulations. The first, shown in the left panels, the source size is effectively point like (panel *a*), and the interference is constrained by the properties of the scattering screen (panel *b*). In the right panels, we consider a emitting region is extended. The emitting region is extended farther in one direction than another(panel *c*). The scattering screen (panel d) is not necessarily anisotropic, but interference is suppressed along the direction of extended emission, resulting in an interfering region identical that in panel *b*.

7.5 PSR B1133+16

The scattering conditions were unfavorable for high resolution observations of PSR B1133+16 during the epoch of observation. In the high signal-to-noise ratio limit, the resolving power is $\Delta r_{\rm UL} \approx \ell_d/\sqrt{N_s}$. As both ℓ_d and $1/\sqrt{N_s}$ scale strongly with the size of the scintles, the structures in the DS of PSR B1133+16 have considerably lower resolving power compared to the narrower structures of PSR B0834+06. We found neither significant decorrelation across pulse phase nor significant offset in any of the cross-correlation functions. The spatial extent of the emission region is constrained to $\delta r \lesssim r_{\rm LC} \approx 10^{9.5}$ cm.

7.6 Discussion

A complete strategy for using interstellar scintillation to resolve pulsar magnetospheres has been presented. We have summarized methods for studying the dynamic spectrum and presented new diagnostics of the secondary spectrum.

We have located the emission region within the magnetosphere of PSR B0834+06, by marginally resolving the emission region in the direction perpendicular to pulsar proper motion, and placed strong limits on the size of the emission region in the direction parallel to pulsar motion. This is consistent with the pulsar angular momentum and velocity being aligned, as is deduced from polarization and proper motion studies (Rankin 2007; Johnston et al. 2007).

Our conclusions can be tested by future observations. If further observations have similar resolving power but no evidence for an elongated scattered image, we would conclude that the shape of the scattered image was associ-

ated with an episode of unusual scattering in the ISM and not intrinsic source structure. Previous observations of PSR B0834+06 (Hill et al. 2003; Cordes et al. 2006a) cannot be used to test our observations, because they do not probe to sufficiently large resolution. Additionally, we predict that pulsars for which there is angular-momentum velocity alignment (Rankin 2007; Johnston et al. 2007) the emission region would be extended in the direction perpendicular to pulsar proper motion, and the arcs would be the thinnest.

In addition to follow-up observations of PSR B0834+06, lower frequency observations (100-200 MHz) are desirable, because for any given pulsar, the resolving power of the ISM is greater, the altitude of emission is expected to be higher, and the emission region size is expected to be larger. New facilities in this wavelength regime such as LOFAR and the low frequency component of the SKA will expand number of pulsars for which this technique can be employed. Currently, use of this technique is limited to observations of nearby pulsars at low frequencies ($\sim$ 300 MHz), because source brightness limits study to nearby pulsar. For these nearby sources, sufficient scattering strength to resolve emission regions is found only at low frequencies. In the future, larger radio telescopes like the mid frequency component of the SKA will allow study of more distant at higher frequencies.

7.6.1 Acknowledgements

This work was supported by the National Science Foundation at Cornell through grants AST 0206036 and AST 0807151. This research has made use of NASA's Astrophysics Data System Bibliographic Services and the ATNF Pulsar

Catalogue[6] (Manchester et al. 2004).

7.7 Appendix: The Generalized Cross Spectrum

In this appendix we will demonstrate that the cross correlation function (CCF) of the dynamic spectrum $C(\Delta\nu, \tau; \mathbf{\Delta r_e}, \mathbf{\Delta r_p})$ and its Fourier transform $\tilde{C}(f_\nu, f_t; \mathbf{\Delta r_e}, \mathbf{\Delta r_p})$ contain phase information that can be used to infer geometric properties of the pulsar-scattering-region-Earth system. This result generalizes the derivation of the cross-correlation function and secondary spectrum presented in Cordes et al. (2006a) to include offset of both the observer and the pulsar emission region:

$$C(\Delta\nu, t; \mathbf{\Delta r_e}, \Delta\mathbf{r_p},) = \langle \Delta I(\mathbf{r_e}, \mathbf{r_p}, \nu) \Delta I(\mathbf{r_e} + \mathbf{\Delta r_e}, \mathbf{r_p} + \mathbf{\Delta r_p}, \nu + \Delta\nu) \rangle. \tag{7.23}$$

As intensity is the square of the electric field ϵ, C is a fourth moment of the electric field. All the spatial quantities are varying time, as the source, screen and observer have independent motion, and the time scales of this variation are much slower than the reciprocal bandwidth. For conciseness of notation, the time dependence will be introduced below.

In the strong scattering limit, the phase perturbation of the electric field is large and the real and imaginary components of the field are statistically independent, zero mean quantities. In this limit, equation 7.23 can be expressed as a product of second moment quantities:

$$C(\Delta\nu; \mathbf{\Delta r_e}, \Delta\mathbf{r_p}) = |\Gamma(\mathbf{\Delta r_e}, \Delta\mathbf{r_p}, \Delta\nu)|^2, \tag{7.24}$$

[6] `http://www.atnf.csiro.au/research/pulsar/psrcat`

where

$$\Gamma(\mathbf{\Delta r_e}, \Delta \mathbf{r_p}, \Delta\nu) = \langle \epsilon(\mathbf{r_e}, \mathbf{r_p}, \nu)\epsilon^*(\mathbf{r_e} + \mathbf{\Delta r_e}, \mathbf{r_p} + \mathbf{\Delta r_p}, \nu + \Delta\nu)\rangle. \tag{7.25}$$

We will assume that the scattering occurs in a thin screen a distance xD from the pulsar and a distance $(1-x)D$ from the observer, as seen in Figure 7.1, panel d. In this case, the observed electric field can be expressed using the Kirchoff diffraction integral

$$\epsilon(\mathbf{r_e}, \mathbf{r_p}, \Delta\nu) = \frac{1}{i\lambda D_{\rm eff}} \int d\mathbf{r_s} B(\mathbf{r_s}) \exp\left(-2\pi i \Phi(\mathbf{r_s}, \mathbf{r_e}, \mathbf{r_p}, \nu)\right), \tag{7.26}$$

where $B(\mathbf{r_s})$ is the scattered brightness distribution, and is a random variable connecting the stochastic scattering processes to the observed scintillation. Substituting equation 7.26 into equation 7.25, we find

$$\begin{aligned}
&\langle \epsilon(\mathbf{r_e}, \mathbf{r_p}, \nu)\epsilon^*(\mathbf{r_e} + \mathbf{\Delta r_e}, \mathbf{r_p} + \mathbf{\Delta r_p}, \nu + \Delta\nu)\rangle = \qquad (7.27)\\
&\quad \frac{\nu^2}{c^2 D_{\rm eff}^2} \exp\left[-i\frac{\Delta\nu D}{c}\right] \exp\left[\frac{-i(\nu+\Delta\nu)}{2cD_{\rm eff}}\left((1-x)\Delta r_p^2 + x\Delta r_e^2\right)\right]\\
&\quad \times \int d\mathbf{r_1} d\mathbf{r_2} \langle B(\mathbf{r_1}) B(\mathbf{r_2})\rangle \exp\left\{\frac{i\nu}{2cD_{\rm eff}}\left[r_1^2 - r_2^2 - 2\mathbf{r_2}\cdot\left((1-x)\mathbf{\Delta r_p} + x\mathbf{\Delta r_e}\right)\right]\right\}\\
&\quad \times \exp\left\{-\frac{i\Delta\nu}{2cD_{\rm eff}}\left[r_2^2 - 2\mathbf{r_2}\cdot\left((1-x)\mathbf{\Delta r_p} + x\mathbf{\Delta r_e}\right)\right]\right\}. \qquad (7.28)
\end{aligned}$$

Assuming the brightness distribution is stationary,

$$\langle B(\mathbf{r_1}) B(\mathbf{r_2})\rangle = \langle B^2(\mathbf{r_1} - \mathbf{r_2})\rangle \delta(\mathbf{r_1} - \mathbf{r_2}), \tag{7.29}$$

we integrate equation 7.26 over $\mathbf{r_2}$ to find

$$\begin{aligned}
&\langle \epsilon(\mathbf{r_e}, \mathbf{r_p}, \nu)\epsilon^*(\mathbf{r_e} + \mathbf{\Delta r_e}, \mathbf{r_p} + \mathbf{\Delta r_p}, \nu + \Delta\nu)\rangle = \qquad (7.30)\\
&\quad \frac{\nu^2}{c^2 D_{\rm eff}^2} \exp\left[-i\frac{\Delta\nu}{cD}\right] \exp\left[\frac{-i(\nu+\Delta\nu)}{2cD_{\rm eff}}\left((1-x)\Delta r_p^2 + x\Delta r_e^2\right)\right]\\
&\times \int d\mathbf{r_1} \langle B^2(\mathbf{r_1})\rangle \exp\left[-\frac{i\nu}{cD_{\rm eff}}\mathbf{r_1}\cdot\left((1-x)\mathbf{\Delta r_p} + x\mathbf{\Delta r_e}\right)\right]\\
&\quad \times \exp\left\{-\frac{i\Delta\nu}{2cD_{\rm eff}}\left[r_1^2 - 2\mathbf{r_1}\cdot\left((1-x)\mathbf{\Delta r_p} + x\Delta\mathbf{r_e}\right)\right]\right\},
\end{aligned}$$

where $\langle B^2(\mathbf{r_1})\rangle$ is the rms brightness distribution. We now explicitly define the time dependence by substituting $\mathbf{\Delta r_e} \rightarrow \mathbf{\Delta r_e} + (\mathbf{v_e} - \mathbf{v_s})\tau$ and $\mathbf{\Delta r_p} \rightarrow \mathbf{\Delta r_p} + (\mathbf{v_p} - \mathbf{v_s})\tau$. Additionally, we define the effective velocity $\mathbf{V} = (1-x)\mathbf{v_p} + x\mathbf{v_e} - \mathbf{v_s}$, and assume $r_1 \gg \Delta r_e, r_p, V\tau$. We then substitute 7.30 into equation 7.24 to find the ensemble-averaged CCF

$$
\begin{aligned}
C(\Delta\nu, \tau; \mathbf{\Delta r_e}, \mathbf{\Delta r_p}) &= \Gamma(0,0,\Delta\nu;\tau)\Gamma^*(\mathbf{\Delta r_e}, \mathbf{\Delta r_p}, \Delta\nu; \tau) = \\
&\int d\mathbf{r_1} d\mathbf{r_2} \langle B^2(\mathbf{r_1})\rangle\langle B^2(\mathbf{r_2})\rangle \exp\left[-\frac{2i\pi\nu}{cD_{\text{eff}}}(\mathbf{r_1}-\mathbf{r_2})\cdot\mathbf{V}\tau\right] \exp\left[-\frac{\pi i \Delta\nu}{cD_{\text{eff}}}\left(r_1^2 - r_2^2\right)\right] \\
&\times \exp\left\{\frac{2\pi i}{cD_{\text{eff}}}(\mathbf{r_1}-\mathbf{r_2})\cdot\left[(1-x)\mathbf{\Delta r_p} + x\mathbf{r_e}\right]\right\}, \qquad (7.31)
\end{aligned}
$$

and the cross-spectrum is

$$
\begin{aligned}
\tilde{C}(f_\nu, f_t; \mathbf{\Delta r_e}, \mathbf{\Delta r_p}) &= \int d\Delta\nu d\tau \Gamma(0,0,\Delta\nu;\tau)\Gamma^*(\mathbf{\Delta r_e}, \mathbf{\Delta r_p}, \Delta\nu;\tau)\exp\left[2\pi i\left(f_\nu\Delta\nu + f_t\tau\right)\right] \\
&= \int d\mathbf{r_1} d\mathbf{r_2} \langle B^2(\mathbf{r_1})\rangle\langle B^2(\mathbf{r_2})\rangle \exp\left\{\frac{2\pi i}{cD_{\text{eff}}}(\mathbf{r_1}-\mathbf{r_2})\cdot\left[(1-x)\mathbf{\Delta r_p} + x\mathbf{r_e}\right]\right\} \\
&\times \delta\left(f_t - \frac{\nu}{cD_{\text{eff}}}(\mathbf{r_1}-\mathbf{r_2})\cdot\mathbf{V}\tau\right)\delta\left(f_\nu - \frac{\Delta\nu}{2cD_{\text{eff}}}\left(r_1^2 - r_2^2\right)\right) \qquad (7.32)
\end{aligned}
$$

As the only complex quantity is the exponential factor, we identify the phase in the cross-spectrum as

$$
\Delta\Phi(f_\nu, f_t; \mathbf{\Delta r_e}, \mathbf{\Delta r_p}) = \frac{2\pi}{cD_{\text{eff}}}(\mathbf{r_1}-\mathbf{r_2})\cdot\left[(1-x)\mathbf{\Delta r_p} + x\mathbf{\Delta r_e}\right], \qquad (7.33)
$$

where the delta functions in equation 7.32 identify the baselines within the scattered brightness distribution contributing at a particular fringe frequency and delay.

7.8 Appendix: Locating Emission Components

To determine if the observed decorrelation of the DS of PSR B0834+06 is associated with the physical separation of emission components, we combine the ob-

servational evidence and attempt to produce a self-consistent map of the emission region. Using the correlation coefficients ρ_{ij} and the time offsets τ_{ij} between all pulse phases i and j, it is possible to reconstruct a two dimensional map of the pulsar emission region. Defining the list of two dimensional positions of the N pulse phases as $\{\mathbf{r}\} = \{\mathbf{r_1}, \mathbf{r_2}, ..., \mathbf{r_N}\}$, the expected decorrelation is

$$\log|\rho_{ij}| = (|\mathbf{r_i} - \mathbf{r_j}|/\ell_d)^{1/(\alpha-2)}, \tag{7.34}$$

and the expected time offset is

$$\tau_{ij} = \frac{r_{i\|} - r_{j\|}}{V_{\rm eff}}, \tag{7.35}$$

where we have used $\|$ to indicate the component of $\boldsymbol{r}_i$ in the direction of effective motion. For the N pulse phases observed, there are $N(N-1)/2$ measured correlations. As there are two degrees of freedom for the spatial positions of each pulse component, in all cases where the pulse is subdivided into at least 6 phase bins, the system is over constrained.

We define a simulated set of positions for the N pulse phases as $\{\hat{\mathbf{r}}\} \equiv \{\hat{\mathbf{r}}_\mathbf{1}, \hat{\mathbf{r}}_\mathbf{2}, ..., \hat{\mathbf{r}}_\mathbf{N}\}$. The non-normalized probability density as

$$\log P(\{\hat{\mathbf{r}}\}) = -\sum_{ij}\left[\frac{(\hat{\rho}_{ij} - \rho_{ij})^2}{2\sigma_\rho^2} + \frac{(\hat{\tau}_{ij} - \tau_{ij})^2}{2\sigma_\tau^2}\right], \tag{7.36}$$

where we have used σ_ρ, and σ_τ are the measurement uncertainties, $\hat{\rho}_{ij}$ and $\hat{\tau}_{ij}$ are estimates based on the values of $\{\hat{\mathbf{r}}\}$, and ρ_{ij} and τ_{ij} are the measured values.

A Metropolis-Hastings procedure was used to estimate the source positions as brute-force integration was computationally infeasible due to the high dimensionality of $\{\hat{\mathbf{r}}\}$. An initial set of positions $\{\hat{\mathbf{r}}\}_1$ was drawn from a Gaussian distribution with zero mean and standard deviation $\sigma_{r,i}$ to approximately match the average separation separation between the pulse components $\sigma_{r,i} = 0.2\ell_d$. From these positions an initial set of probabilities $\log P(\{\hat{\mathbf{r}}\}_1)$ was calculated.

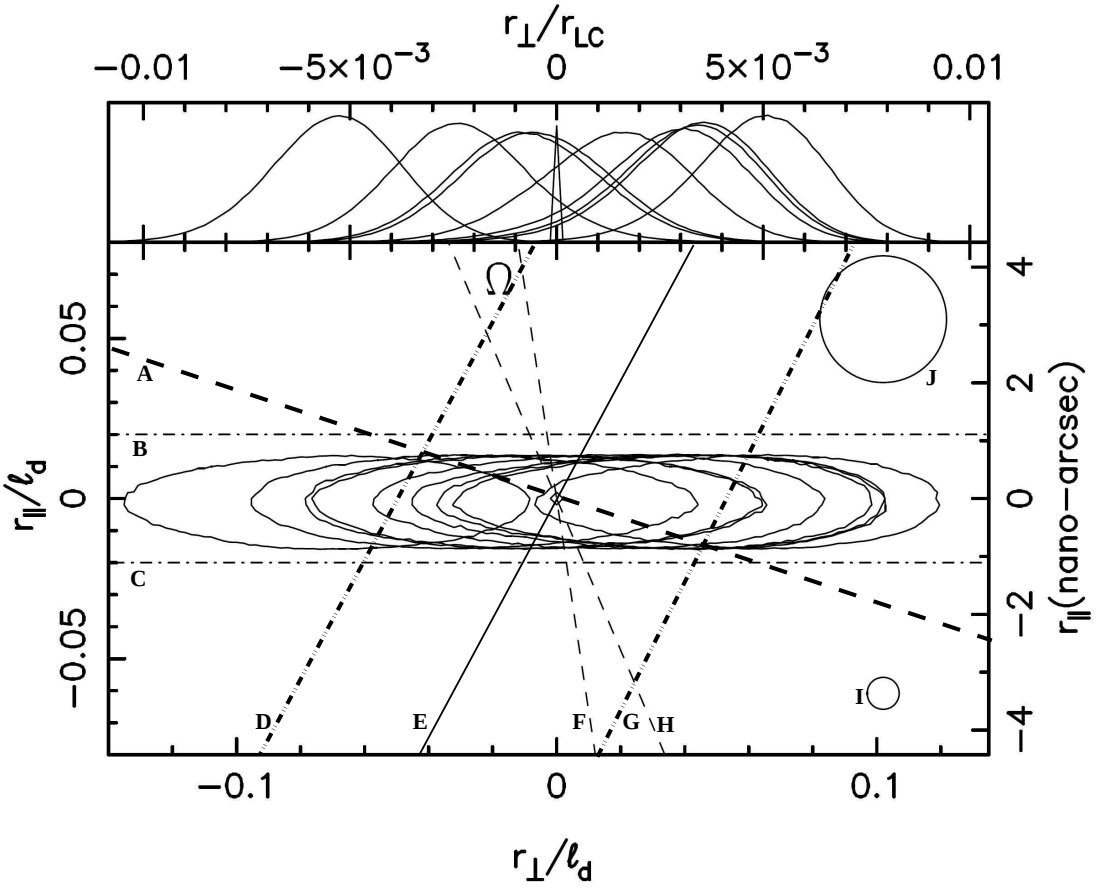

FIGURE 7.7.— *Lower Panel:* Constraints on the emission region of PSR B0834+06. The contours identify where the probability density decreases to 1% of its peak value, and represent pulse components 6 to 15, from left to right, relative to phase bin 10. Dashed line *A* indicates the direction over the pulsar beam travels across the line of sight. The horizontal dashed-dot lines (*B* and *C*) indicate the contraints on emission separation in the direction parallel to pulsar motion, from the lack of shift of the CCF and lack of observed phase variation in the cross-spectrum. Solid angled line *E* indicates the relative direction of the screen image, based on interferometric observations by (Brisken et al. 2010). Dashed double-dotted lines *D* and *G* indicate constraints on the pulsar image based on the observed interference of the island and main images. The nearly vertical dashed lines (*F* and *H*) indicate the possible orientation of the projected angular momentum axis Ω, based on radio polarization observations. The circle in the upper right corner labeled *J* indicates the effective resolving power from the correlation coefficient alone. The circle labeled *I* in the bottom right corner is the estimated size using the altitude measured using abberation-retardation methods by Johnston et al. (2007) assuming a dipolar field geometry. *Upper Panel:* Marginalized probability densities for the pulse components along direction perpendicular to pulsar motion.

After the initial set of positions was generated an iterative random walk was conducted. For each iteration, a new set of random positions $\{\hat{\mathbf{r}}\}_2$ was generated by perturbing the previous set $\{\hat{\mathbf{r}}\}_1$ by a much smaller amount: $\{\hat{\mathbf{r}}\}_2 = \{\hat{\mathbf{r}}\}_2 + \{\mathbf{\Delta r}\}$. For the second set of points $\log P(\{\hat{\mathbf{r}}\}_2)$ was calculated. If $\log[P(\{\hat{\mathbf{r}}\}_2)] - \log[P(\{\hat{\mathbf{r}}\}_1)] > \log s$ (where s is drawn from the uniform (0,1) distribution) the position was switched. Otherwise the position stayed the same. The perturbation sizes $\{\mathbf{\Delta r}\}$ were drawn from a normal distribution with $\sigma_{r\perp} = 0.01\ell_d$, and $\sigma_{r\|} = 0.005$, chosen so the switching rate was about 0.25. A large number of iterations were completed in order to estimate the source positions and their uncertainties.

The results of the Monte Carlo integration are displayed in Figure 7.7. In the direction parallel to effective motion, there is no observed source offset. By combining the results from all pairs of pulse phases we set a highly constraining offset of $\Delta r_{\|} \leq 2\times10^{-3}\, r_{\rm LC}$. In the perpendicular direction, the estimated positions of the pulsar show monotonic changes, with neighboring components showing significant overlap in the position of pulse components. In addition to this map we produced maps with higher and lower pulse phase resolution, which were consistent with the map shown in Figure 7.7.

CHAPTER 8

A SEARCH FOR DEBRIS AROUND FOUR VARIABLE PULSARS

After a supernova explosion a modest amount of material falls back to form a disk surrounding the resultant neutron star. The material aggregates into rocky debris and the disk remains stable for the entire 10 Myr lifetime of a canonical radio pulsar. We have developed a model that unifies different classes of radio variability observed in many older pulsars. Rocky material migrates inwards from a debris disk and is ablated inside the pulsar magnetosphere. This material alters the electrodynamics in the magnetosphere and causes both the observed quiescent and bursting states observed in nulling pulsars, intermittent pulsars, and rotating radio transients; and changes in pulse profile in mode changing pulsars. With this model in mind, we searched for debris disks around three nulling pulsars and one intermittent pulsar that were the best candidates to host debris disks detectable by the Spitzer *IRAC* camera. Disk luminosities and upper limits set debris migration rates and hence the role debris can play in altering pulsar emission. For three objects, we find sources that are coincident with the radio pulsar position. However, because of the density of stars in the fields of view coupled with the modest resolution of the telescope, we can not rule source confusion as the source of these objects. For all objects we set total mass limits of $\leq 10^{-2}\ M_{\oplus}$ of material assuming material properties similar to that of the Solar system. Compact debris disks around pulsars will certainly be detected with next generation infrared facilities such as the James Webb Space Telescope, providing insight into post-main sequence stellar evolution and potentially pulsar magnetospheric physics[1].

[1]R. M. Shannon, J. M. Cordes, T. J. W. Lazio, M. Kramer, A. G. Lyne, to be submitted ApJ.

8.1 Introduction

During the formation and evolution of a neutron star (NS), there are three scenarios in which it can acquire circumstellar material that may form a debris disk, an asteroid belt, or even planets.

In the first scenario, the progenitor star possessed a debris disk and the disk survives the supernova explosion and remains gravitationally bound to the NS. However, given many NS are born with large space velocities and disks around progenitor stars are likely to be very tenuous, it is likely that this mechanism can not form large disks. The amount of material depends on the supernova explosion asymmetry and the kick velocity of the NS which can exceed 10^3 km s^{-1}.

In the second scenario, a metal-rich fallback material accumulates around the NS shortly after its birth. Recently Wang et al. (2006) found an excess of infrared emission from the young anomalous X-ray pulsar (AXP) 4U 0142+61 that they attribute to a cool debris disk formed from supernova fallback material. These observations corroborate work suggesting that supernova ejecta with insufficient energy to escape will form a compact disk whose lifetime will exceed the radio-emitting lifetime $\sim 10 - 100$ Myr of a typical pulsar (Menou et al. 2001; Lu & Cheng 2002; Ekşİ & Alpar 2005; Cordes & Shannon 2008).

The third occurs only for NS that remain in binaries, accrete material from a low-mass companion, and then evaporate the companion (sometimes completely) with remnant material forming orbital debris disk. Three planets have been detected around the millisecond pulsar B1257+12 (Konacki & Wolszczan 2003). These planets were most likely formed from evaporated material from a companion. There is a radio pulsar that was previously observed as a low

mass X-ray binary confirming the connection between the two classes of objects (Archibald et al. 2009; Wang et al. 2009).

Disks around pulsars may be detectable through pulsar timing, a technique which is sensitive to reflex orbital motion of the pulsar and was used to establish the existence of planets around PSR B1257+12. Current pulsar timing observations indicate that individually detectable planets around pulsars are rare. However, many pulsars show long-term non-stationary variations in the arrival times of the pulses at an rms level of 0.1 to 1 ms over $\sim$ 10 year time scales that could be due, in part, to the cumulative reflex motion from an ensemble of orbiting objects with total mass of order 0.1 to 1 $M_{\oplus}$. Strikingly, this value is comparable to that seen in the disk around 4U 0142+61 ($\sim$ 10 $M_{\oplus}$) and only somewhat above the upper limit set by Spitzer observations of PSR B1257+12 (10^{-2} $M_{\oplus}$ Bryden et al. 2006).

Additional empirical evidence for orbital debris comes from radio pulsar fluctuations. Nulling pulsars (NPs) are a well detected class of pulsars that show sudden cessation of radio emission for durations of seconds to hours (Backer 1970).

Recent work has revealed intermittent pulsars (IPs), pulsars that shut off for days or weeks and turn on at quasi-periodic intervals to produce otherwise normal pulses. Remarkably, the spindown rate caused by magnetospheric torques increases by about 50% when the pulsar is on, suggesting that radio emission is related to currents that cause the torques (Kramer et al. 2006a).

Mode changing pulsars show discontinuous changes in pulse shape. The different modes are typically accompanied by different changes in flux density.

The time scale for mode changes is typically minutes to hours. Recent work suggests that some pulsars show much more subtle mode changing over years and that the mode changing is connected torque variations undoubtedly connected to the pulsar magnetosphere (Lyne et al. 2010).

Rotating Radio Transients (RRATs) are objects that turn on for only an occasional pulse period but otherwise are quiet (McLaughlin et al. 2006). RRATs show bursts of radio emission consisting of one or more narrow pulses with widths $\sim$ 2 to 30 ms with long intervals between bursts, minutes to hours or longer. However, sustained observations demonstrate that pulse arrival times are periodic suggesting that like pulsars they are spinning objects, with periods $\sim 0.2 - 5$ s.

Cordes & Shannon (2008) provide a unified explanation for radio intermittency by invoking orbital debris as a trigger for either inducing or quenching radio emission. A general argument favoring an extrinsic trigger is that otherwise similar pulsars (e.g., objects that have similar spin periods P and spindown rates, $\dot{P}$, implying similar spin ages $P/2\dot{P}$, and surface magnetic field, $B \propto \sqrt{P\dot{P}}$) show radically different modulations of their radio emission (Biggs 1992).

Another argument follows from the 30-day quasi-periodicity of the bursts seen from the first reported IP, PSR B1931+24. An orbital clock mechanism is a natural explanation for the long time scales and quasi-periodicities of the observed phenomena can be explained if a larger orbiting object stimulates stochastic bombardment of the pulsar's magnetosphere by smaller objects, whose effects need not be strictly periodic. PSR B1931+24 is not unique; there are now four other IPs identified in long-term monitoring with the Lovell Telescope at Jodrell Bank.

A striking feature of NPs, IPs, mode changing pulsars, and RRATS is that transitions between states on-to-off, off-to-on, or mode-to-mode are rapid. This is consistent with what we expect from the poisoning of a pulsar's magnetosphere by extrinsic material. The spinning magnetic field generates large voltage drops across so-called gaps in which accelerated particles can, in turn, generate secondary electron-positron ($e^{\pm}$) pairs. For canonical pulsars (10^{12} G and $\sim$ 1 s spin period) the voltage drop is 10^{12} V. In most pulsar models, this is a self-regulating process: charged particles extracted from the NS crust reduce the voltage drop: too many will shut off the acceleration. Pairs appear to be necessary for radio emission, producing radiation beams that parallel the current flow near the magnetic axes of the NS. To maintain steady beams of current and radiation, the magnetosphere must be in a near-vacuum state. Accreting particles will short out the voltage drop and shut off the beams. Conversely, for a NS with too low a magnetic field and/or spin rate, the beams are quiescent unless an external trigger of seed charges temporarily re-activates the production of $e^{\pm}$ pairs. In the debris-intrusion model extrinsic material can both temporarily shuts off radio emission in some objects (NPs) and stimulate radiation in others (IPs and RRATs).

The size and configurations of circum-neutron star debris disks are expected to widely vary: much less in cases where the NS outran potential fallback material or when a young, short-period pulsars evaporate or disperse debris material on a short time scale. Significant debris is expected if a pulsar is born with a relatively long period or if its radiation beam does not illuminate the debris disk. Indeed, nulling is more prominent in pulsars with emission beams that are closer to the spin axis (Cordes & Shannon 2008). Modeling of supernova fallback suggests that at least 10 $M_{\oplus}$ of material can remain in a compact (10^{11} cm)

disk (Menou et al. 2001). This is far more than needed to electrodynamically perturb a pulsar to produce the above-mentioned effects.

As a conservative ansatz, consider a minimal disk with total mass of $10^{-4} M_{\oplus}$ orbiting a NS with surface temperature of 10^5 K; the minimal disk extends from the pulsar light cylinder (LC) radius, $r_{\rm LC} = cP/2\pi \sim 10^{10}$ cm to a distance a factor of ten larger, consistent with models of SN fallback disks.

The minimal disk is sufficient to disrupt a pulsar's electrodynamics if inward transport of disk objects is efficient. Transport into the pulsar magnetosphere is via collisional migration or, more likely in a sparse disk, radiation driven migration from the Yarkovsky effect (Nesvorný & Bottke 2004). Disks can of course be more massive and more luminous than our minimal disk.

Though these disks are faint they are observable through a number of methods. They can potentially be detected through their thermal emission. The disks are irradiated by the pulsar, either by its thermal surface emission, or a relativistic wind.

There have been studies searching for debris disks around both the old MSPs A lot of attention has been placed on the planet pulsar system PSR B1257+12 because it is already known to contain few $M_{\oplus}$ of material (in the form of planets). Lazio & Fischer (2004) unsucessfullly searched for debris disks around the MSP.

There have been searches for debris disk associated with supernova fallback from the youngest pulsars as well (Hulleman et al. 2004). We note that there have been suggestions that this emission could originate in the pulsar magnetosphere (Beloborodov & Thompson 2007).

There have been few studies of objects at intermediate ages and magnetic field strengths. Notably, Rea et al. (2010) searched for emission from two RRATs at near-IR wavelengths (1.0 μm to 2.5 μm). For RRAT J1317−5759 no infrared emission was detected. For RRAT J1819−1458, infrared emission was detected in the direction of the pulsar. However, they could not rule out chance coincidence for the source. Rea et al. (2008) unsuccessfully searched for an optical companion to the intermittent pulsar B1931+24.

In §8.2 we present two distinct models for debris disks that are used in analysis of the observations presented here. In §8.3 we discuss the target selection methodology and observing and reduction procedures used. In §8.4 we discuss the specific observations and identify potential infrared counterparts and constrain disk flux and disk mass. In §8.5 we discuss the results and the prospects future observations for identifying debris disks around neutron stars and pulsars.

8.2 Disk Models

We consider two different classes of models of debris disks. The first class assumes that the debris disk is optically thin, analogous to the Solar system asteroid belt or the rings around Saturn. In this case, the fluence of the disk is independent of the observing geometry. We discuss this model further in §8.2.1.

In the second class, the disk is optically thick and similar to debris disks around a main sequence stars. This class of disk is comprised of much smaller dust particles. In this case, the observed luminosity is highly dependent on the viewing geometry. We discus this model further in §8.2.2.

In both cases the disks are compact and unresolvable. It is also important to note that in both cases the debris is far more luminous than neutron star at infrared wavelengths because the much larger radiating area of the disk negates the higher temperature of the neutron star. Assuming the NS radiates like a perfect black body in infrared wavelengths, its flux is

$$S_* = 10^{-3.4}\ \mu\text{Jy}\ T_5 \lambda_{-4}^{-2} R_6^2 d_{\text{kpc}}^{-2}, \tag{8.1}$$

where the NS temperature is $10^5\ T_5$ K, the NS radius is $10^6 R_6$ cm, the NS is 1 d_{kpc} kpc distant, and the observing wavelength is 10 λ_{-4} μm. As will be presented our observations are sensitive to $\sim 10\ \mu$Jy emission.

8.2.1 Asteroid Belt

One model we consider is a debris disk comprising large macroscopic rocky objects. We assume that the disk has uniform surface density and that material properties are independent of location. We additionally assume that constituent objects (grains, rocks, asteroids) have sizes that follow a power-law distribution (i.e., $\rho \propto R^{-b}$ with an index $b > 1$) extending from a minimum size R_1 to maximum size R_2. The fraction of rocks with sizes between R_a and $R_a + dR_a$ is

$$f(R_a)dR_a = (b-1)\frac{R_2^{b-1}R_1^{b-1}}{R_2^{b-1} - R_1^{b-1}} R_a^{-b} dR_a. \tag{8.2}$$

The disk is modeled to have an inner radius r_1 and outer radius r_2, with total mass M_a.

The number of asteroids per unit surface area of the disk is

$$n = \frac{3}{4\pi}\frac{4-b}{b-1}\frac{M_a}{\rho(r_2^2 - r_1^2)}\frac{R_2^{b-1}R_1^{b-1}}{R_2^{b-1} - R_1^{b-1}}\frac{1}{R_2^{4-b} - R_1^{4-b}}, \tag{8.3}$$

where the mass density ρ of all the asteroids is assumed to be the same. For a size distribution following a collisional distribution $b = 7/2$ (Dohnanyi 1969), equation (8.2) simplifies to

$$f(R_a)dR_a = \frac{5}{2} R_1^{5/2} R_a^{-7/2} dR_a. \tag{8.4}$$

Assuming $R_2 \gg R_1$, $r_2 \gg r_1$, and the collisional power law, the density of the disk is

$$n = \frac{3}{20\pi^2} \frac{1}{r_2^2} \frac{M_a}{\rho R_1^2} \sqrt{\frac{R_1}{R_2}}. \tag{8.5}$$

In subsequent sections, scaling relationships are developed in comparison with what we refer to as *the standard disk* that has a mass $M_a = 10^{-4} M_{a,-4} M_\oplus$; inner radius $r_1 = 10^{10} r_{1,10}$ cm; outer radius $r_2 = 10^{-2} r_{2,-2}$ AU $= 1.5 \times 10^{11} r_{2,-2}$ cm; and is a distance $d = d_{\rm kpc}$ kpc from the observer. We assume that the rock size distribution has a minimum size of $R_1 = 10^{-2} R_{1,-2}$ cm and a maximum size $R_2 = 10^4 R_{2,4}$ cm, and follows a collisional power law distribution ($b = -7/2$).

Material surrounding the NS is in thermal equilibrium with its surroundings, heated by the radiation emitted by the NS. If directed towards the disk, the beamed magnetospheric radiation would heat the debris. However, the thermal emission from the NS surface also provides heating of the disk and is independent of disk-beam geometry.

For a disk radiated by the NS thermal emission, most of the heating will be associated with far-ultraviolet and soft X-ray emission. The asteroid belt disk that is discussed in this section is optically thin. As a result the absorbed flux is independent of height within the disk and the observed flux will be independent of viewing geometry.

In this case, the equilibrium temperature of an asteroid in the disk is

$$T_a^4(r) = (1-A)\left(\frac{R_*}{2r}\right)^2 T_*^4, \tag{8.6}$$

where A is the albedo of the material. Combining the contribution from all of the asteroids in the disk, the flux density a distance d from the debris disk is

$$S_\nu = 2\pi \int_{r_1}^{r_2} \int_{R_1}^{R_2} dR_a n(r) f(R_a) S_\nu(r,d), \tag{8.7}$$

where $S_\nu(r,d)$ is the expected flux density from an asteroid, which is assumed to be black body emission. Using the model distribution the observed spectral energy distribution is

$$S_\nu = \frac{45}{16\pi^5} \frac{\sigma_{\rm SB}(1-A)T_*^4}{\nu} \frac{R_*^2}{d^2} \frac{M_a}{\rho r_2^2 \sqrt{R_1 R_2}} \int_{x_1}^{x_2} dx \frac{x^2}{e^x - 1}, \tag{8.8}$$

where

$$x_{1,2} = (h\nu/kT_*)/(1-A)^{1/4} \sqrt{2r_{1,2}/R_*}. \tag{8.9}$$

The peak flux occurs at a wavelength $\lambda_{\rm peak} \approx 21\mu m T_5^{-1}(1-A)^{-1/4} R_6^{1/2} (r_{2,-2} r_{1,10})^{1/4}$. The integral in equation (8.8) is ≈ 3 for standard parameters. It could be as high as ≈ 6 for disks that extend to asymptotically large distances, and will be much smaller for narrower disks. However, without the presence of large shepherding bodies, extended disks are expected. For the standard disk the peak flux density is

$$S_\nu \quad = 10^{-0.7} \mu{\rm Jy}\, d_{\rm kpc}^{-2} T_5^3 R_6^{3/2} M_{a,-4} R_{1,-2}^{-1/2} R_{2,4}^{-1/2} r_{1,10}^{1/4} r_{2,-2}^{-7/4} \rho_0^{-1} \left(\frac{1-A}{0.5}\right) \tag{8.10}$$

8.2.2 Dusty Disk

The optically thick model we use was developed by Vrtilek et al. (1990). This disk was used by Wang et al. (2006) to model the candidate dust disk surround-

ing the AXP 4U0142+61. This model follows previous work by Shakura & Sunyaev (1973) with the extra assumption that disk heating is dominated by X-ray flux from the central star and that the vertical structure of the disk is isothermal.

In this case, the temperature profile of the disk can be solved analytically as function of the distance r to the neutron star,

$$T(r) = \left[\frac{\sqrt{k/\mu m_H} L_X \omega}{4\pi\sigma GM} \right]^{2/7}, \tag{8.11}$$

where $\omega(r)$ is the angular velocity of the orbiting material, L_X is the NS luminosity, k is Boltzmann's constant, μ is the molecular weight of the constituent gas and m_H is the mass of hydrogen.

Substituting $\omega = \sqrt{GM/r^3}$, and assuming that the star luminosity is dominated by its thermal emission (i.e., $L_X = 4\pi R_{\rm NS}^2 \sigma T_{\rm NS}^4$) equation (8.11) can be re-expressed as

$$\begin{aligned} T(r) &= \left[\sqrt{\frac{k}{\mu m_H GM r^3}} R_{\rm NS}^2 T_{\rm NS}^4 \right]^{2/7} \\ &= 235 \text{ K} \left(\frac{r}{r_{\rm LC,1}} \right)^{-3/7} \left(\frac{T}{10^5 \text{ K}} \right)^{8/7}, \end{aligned} \tag{8.12}$$

where we have assumed the NS radius is $R_{\rm NS} = 10^6$ cm, the NS mass is $M_{\rm NS} = 1.4 M_\odot$, and have scaled the distance r relative to the NS light cylinder, i.e., $r_{\rm LC,1} = c\, P/(2\pi)$ assuming the pulsar has a spin period of $P = 1$ s.

We note that for the same radius, the temperature of the optically thick disk is much cooler than the optically thin disks.

The total flux of the disk is

$$F_\nu = \frac{2\pi}{D^2} \int_{r_i}^{r_o} r dr B_\nu(T(r)) \chi(r), \tag{8.13}$$

where r_i and r_o are the inner and outer radii of the disk, respectively, and $\chi(r)$ describes the inclination of the disk with respect to the line of sight. For the remaining discussion, we will assume that the disk is face-on [2] (i.e., $\chi(r) \equiv 1$).

8.3 Reduction Procedures

We observed 4 variable pulsars: two pulsars that show normal nulling behavior, one pulsar that shows extreme nulling behavior, and final one that shows extreme mode changing behavior. The specific properties of the objects are discussed in the next section.

The objects were selected using the asteroid-injection model, which allows us to estimate disk mass from the radio variability. We assume that if pulsar variability is caused by complete modulation of the pulsar current (i.e., the Goldreich-Julian current I, Goldreich & Julian 1969). NS with larger modulations of I have large accretion rates and hence come from larger disks.

The pulsars were observed with *Spitzer* space telescope's *IRAC* Camera in the 4.5 μm and 8.0 μm channels at single epochs in mid to late 2008. This observation configuration was chosen because it maximized the throughput of the observations in the wavelength ranges to which *Spitzer* is most sensitive to compact circumpulsar debris disks.

Integration times were chosen that would enable us to set comparable limits on the size and configuration of the debris disk for all the objects, based on inference from the radio variability. Observations were dithered to avoid satura-

[2] A more general expression for $\chi(r)$ can be found in equation (13) of Perna & Hernquist (2000).

tion from both zodiacal and Galactic backgrounds and to mitigate pixel-to-pixel response variation of the detectors.

The observations were processed using the `Mopex` tools developed by the staff at the Spitzer Science Center to analyze data for the `IRAC` and `MIPS` instruments. For each pulsar, a mosaicked image was generated from individual stack of exposures using the `Mosaic` pipeline.

The `Apex` pipeline was used to perform point sources extraction on the stack of exposures. Aperture photometry on the background subtracted mosaicked image was used to estimate the flux of the sources in the field surrounding the pulsar.

8.3.1 Setting Upper Limits and Detection Confidence

One of the fundamental limitations of the observations is confusion within the field of view because of the high source density coupled with the relatively low spatial resolution of the telescope. The detection significance was assessed through analysis of the statistical properties of the sources in the the field of each pulsar.

Probability that sources are coincident: If the offset between the radio position and the infrared source in right ascension is $A = \alpha_{\rm radio} - \alpha_{\rm IR}$ and in declination is $D = \delta_{\rm radio} - \alpha_{\rm IR}$, the probability that the infrared source and radio pulsar are coincident is

$$P_C \approx \frac{1}{2\pi\sigma_\alpha\sigma_\delta}\int_{|\Delta\alpha|>A} d\Delta\alpha \exp\left[-\left(\frac{\Delta\alpha^2}{2\sigma_\alpha^2}\right)\right]\int_{|\Delta\delta|>D} d\Delta\delta \exp\left[-\left(\frac{\Delta\delta^2}{2\sigma_\delta^2}\right)\right],$$

where

$$\sigma_\alpha = \sqrt{\sigma^2_{\alpha,\mathrm{radio}} + \sigma^2_{\alpha,\mathrm{IR}}} \tag{8.14}$$

and

$$\sigma_\delta = \sqrt{\sigma^2_{\delta,\mathrm{radio}} + \sigma^2_{\delta,\mathrm{IR}}} \tag{8.15}$$

are the quadrature sums of the positional uncertainties in right ascension and declination, respectively, which are assumed to be independent.

Chance overlap for a detected source: In the region surrounding the pulsar (typically an area of 100 × 100 pixels, which works out to an area of $A_S = 1.4{\times}10^4$ arcsec^2), N_S sources are found that exceed the flux of the observed source F_{min}. The uncertainty in the position of the source is the combined uncertainty of the radio position and the candidate source position, added in quadrature. This uncertainty can be converted into an area A_{err}. The expected number of sources that fall within the region of the source is

$$\lambda(F > F_{\mathrm{obs}}) = N_S \left(\frac{A_{\mathrm{err}}}{A_S}\right). \tag{8.16}$$

The number of sources within A_{err} is expected to follow a Poisson probability density function (PDF); therefore the probability that at least one source has overlap with the observed source is

$$P_{\mathrm{OL}}(N > 0) = 1 - P(N = 0) = \exp\left[-N_S \left(\frac{A_{\mathrm{err}}}{A_S}\right)\right]. \tag{8.17}$$

The probability defined in equation (8.17) is used in subsequent sections to assess the likelihood that a detected source is the result of chance overlap.

Upper limits on source fluence: To place upper limits in cases where there were no sources present in the fields, we set uppper limits based on sources that were detected at a signal to noise ratio of 3, as defined in the Apex pipeline.

TABLE 8.1
OBSERVED PULSARS

PSR	ν (s^{-1})	$\dot{\nu}$ (10^{-15} s^{-2})	$\dot{E}$ ($L_\odot/10^{-3}$)	D (kpc)	Epoch MJD	T_{exp}
B0031−07	1.06	−0.5	5.5	1.0	54699	120×30 s
J0623+0341	1.63	−2.3	38	2.0	54773	240×30 s
B0826−34	0.54	−0.3	1.6	0.5	54594	130×12 s
B1133+16	0.84	−2.6	22	0.4	54631	120×30 s

NOTE.—For each pulsar, the spin frequency ν, spin frequency derivative $\dot{\nu}$, spin down luminosity $\dot{E}$, and nominal distance D are listed. We also list the observation epoch, and exposure time T_{exp}. We have assumed that the spin down luminosity of the NS is $\dot{E} = 4\pi^2 I \nu \dot{\nu} = 0.01 Ł_\odot\ I_{45} \nu_0 \dot{\nu}_{-15}$, where the moment of inertia is $I = 10^{45} I_{45}$ g cm^3 .

8.4 Observations and Results

Relevant properties of the observed pulsars are listed in 8.1. Our findings are summarized in Table 8.2 and discussed in the following subsections.

8.4.1 The Extreme Mode Changing Pulsar B0826−34

PSR B0826−34 shows extreme mode changing behavior with a spin frequency of $\approx$ 0.5 Hz. It was initially classified as a nulling pulsar (Durdin et al. 1979) though further observations indicate that supposedly quiescent mode contains pulsed flux that has 2% of the fluence of the bright state (Esamdin et al. 2005). The bright state is typically comprised of several thousand pulses sequentially followed by long durations in the faint state, which can last up to 8 hr. The

TABLE 8.2
CANDIDATE PROPERTIES

Parameter	Radio	IRAC 4.5	IRAC 8.0
	PSR B0826−34		
α	08:28:16.62(16)	08:18:16.40(11)	···
δ	−34:17:07(3)	−34:17:08(1)	···
P_C	···	0.5	···
P_{OL}	···		···
F_ν (μJy)	···	24 ± 0.4	< 13
	PSR J0623+0341		
α	06:23:46.756(9)	00:23:46.61(8)	···
δ	+03:40:04.9(4)	+03:40:03(1)	···
P_C	···	0.5	···
P_{OL}	···		···
F_ν (μJy)	···	15.9 ± 0.1	< 15
	PSR B0031−07		
α	00:34:08.8748(1)	00:34:08.82(10)	00:34:09
δ	−07:21:53.483(2)	−07:21:51.1(1.7)	-07:21:50
P_C	···	0.1	1.0
P_{OL}	···	0.12	0.2
F_ν (μJy)	···	12.4 ± 0.2	8.2 ± 0.4
	PSR B1133+16		
α	11:36:03.143(1)	···	···
δ	+15:51.12.837(2)	···	···
F_ν (μJy)	···	< 6	< 13

NOTE.—Properties of candidate sources for observed pulsars. The uncertainties for the radio pulsar positions includes contributions in both the position and the proper motion, projected from onto the observing epoch. For the infrared sources, the source right ascension is α, and declination δ are measured at the observation epoch in the J2000 coordinate system. P_C is the probability that the infrared source is coincident with the radio pulsar, P_{OL} is the probability of chance coincidence, F_ν is the flux of the source.

pulsar is in the faint state 70% of the time. Its distance is estimated to be 0.5 kpc based on measurements of electron density along the line of sight and a model of Galactic structure (Cordes & Lazio 2002).

The most precise position estimate for PSR B0826−34 comes from pulsar timing presented in (Hobbs et al. 2004). Because of large levels of timing noise, the position and proper motion are poorly constrained.

X-ray observations of the pulsar have yielded an upper limit of $10^{-4.5} L_{\odot}$ (Gil et al. 2008). Assuming that the luminosity is associated with blackbody emission, the surface temperature is constrained to $T_{\rm NS} < 10^{5.1}$ K.

In Figure 8.1, the IRAC 4.5 μm and 8.0 μm images of the field surrounding the pulsar are displayed. The radio position error for the object is denoted by the ellipse. A bright star near the pulsar introduces some artifacts, particularly in the 4.5 μm image. However, these artifacts do not overlap with the expected position of the pulsar.

There is a candidate source coincident with the pulsar in the 4.5 μm image. The source has a flux of 24 ± 0.4 μJy and is detected at a SNR of 42. In the region surrounding the pulsar there are 0.012 sources per square arcsecond detected with a signal to noise ratio greater than that of the observed source. The chance probability of an overlapping source is estimated to be 0.47. In the 8 μm image, there are no candidate sources. We set an upper limit for the 8 μm emission of 13 μJy, which corresponds to an SNR = 5 in the region surrounding the pulsar.

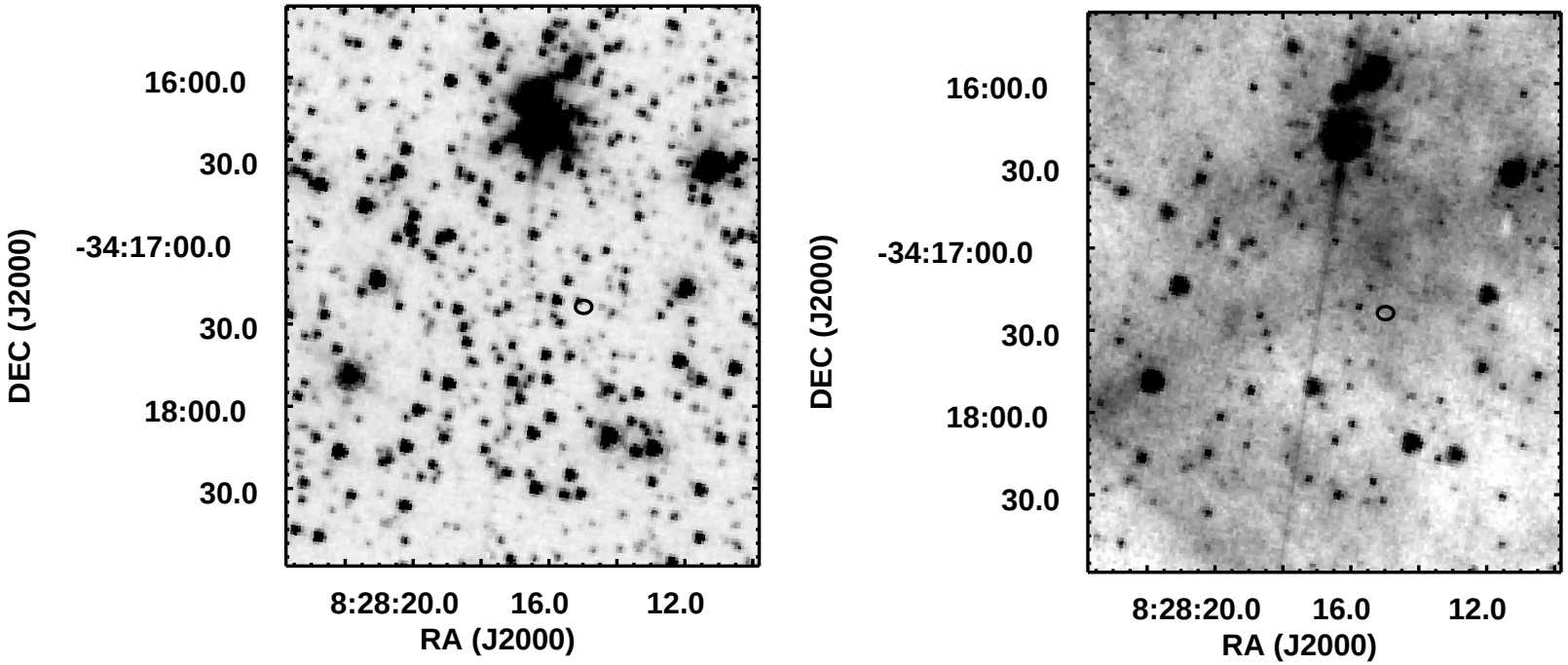

FIGURE 8.1.— Field surround PSR B0826−34 in 4.5 μm (left panel) and 8.0 μm (right panel) bands. The ellipse denotes the 2 − σ positional uncertainty of the pulsar. The candidate source can be found at the center of the ellipse.

In Figure 8.2 we show constraints on the brightness of the PSR B0826−34 system and models for plausible disk configurations that satisfy these constraints. For the 4.5 μm observations the flux of both the candidate source and an upper limit (assuming the candidate source is not associated with the pulsar) are displayed. Given the flux of the source in the 4.5 μm image and the upper limit in the 8 μm image suggest that the source is blue, we conclude that the source is most likely a field star.

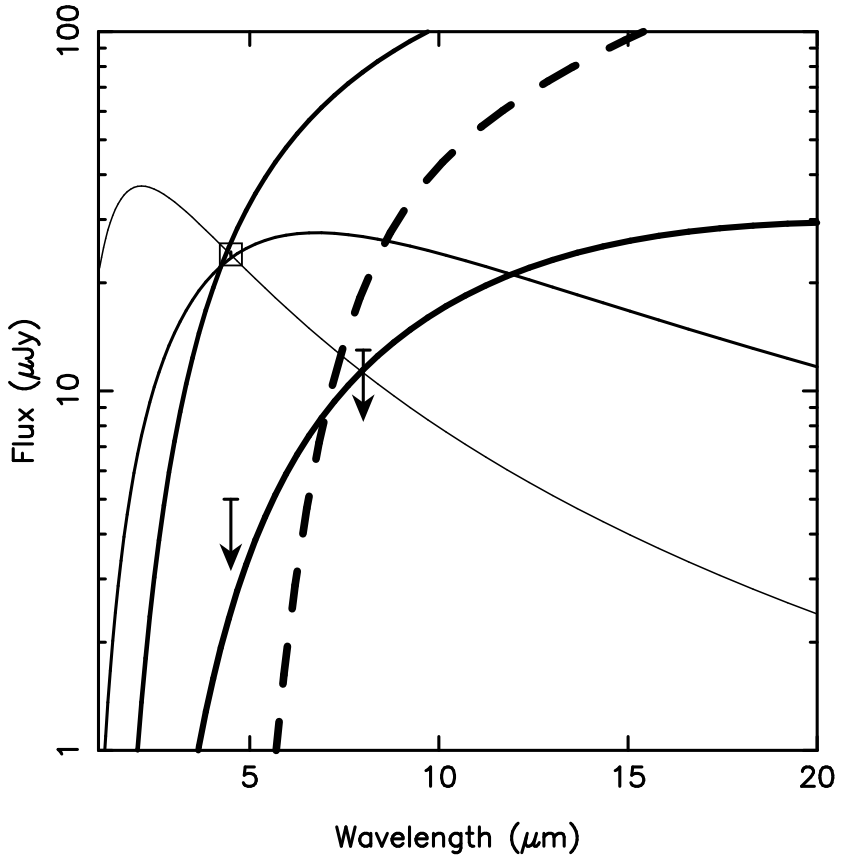

FIGURE 8.2.— Debris disk models for PSR B0826−34. The solid lines represent optically thin models. From thinnest to thick line width, the models plotted are respectively $T_{\rm NS} = 10^6$ K, $M_D = 10^{-5.5}\ M_\oplus$; $T_{\rm NS} = 10^{5.5}$ K, $M_D = 10^{-3.5}\ M_\oplus$; $T_{\rm NS} = 10^5$ K, $M_D = 10^{-1.9}\ M_\oplus$; and $T_{\rm NS} = 10^5$ K, $M_D = 10^{-2.1}\ M_\oplus$ **check this**. The dashed line represents optically thick models with a neutron star with temperature $T_{\rm NS} = 10^{5.8}$ K.

8.4.2 Intermittent Pulsar: J0623+0341

PSR J0623+0341 is a recently discovered intermittent pulsar with a spin frequency of $\approx$ 1.6 Hz. It shows bursts of radio emission that are 30 − 60 s in duration separated by $\approx$ 1 hr. Based on the column density of electrons and an electron density model of the Galaxy (Cordes & Lazio 2002) the intermittent pulsar is 2.0 kpc distant. The pulsar is located towards the Galactic anticenter.

In Figure 8.3 we show the 4.5 μm and 8.0 μm images of the field surrounding PSR J0623+0341. The mosaicked images show artifacts associated with bright stars in the field. A source is found in the 4.5 μm image that is marginally consistent with the pulsar position. We do not find any sources in the 8.5 μm image that are consistent with the pulsar position. In Table 8.2 the properties of the candidate source are listed.

In Figure 8.4 we show constraints on the brightness of the PSR J0623+0341 system and plausible disk configurations that satisfy these constraints.

8.4.3 Nulling Pulsar: B0031−07

PSR B0031−07 has s spin frequency of $\approx$ 1.1 Hz and exhibits long bursts and nulls: Huguenin et al. (1970) found that the typical group of pulses contains 30 to 100 pulses, the delay between groups ranging from fifty to several hundred pulse periods. At decameter wavelengths there have reports of exceptionally bright giant pulse emission (Kuzmin & Ershov 2004).

Based on trigonometric parallax derived from radio interferometric observations, the pulsar is 1.0 kpc distant and has well constrained position and proper

motion (Chatterjee et al. 2009).

In Figure 8.5, the *IRAC* 4.5 μm and 8.0 μm images of the field surrounding the pulsar are displayed. The location of the pulsar is also displayed, but the positional uncertainty is too small to be observed. The position and proper motion of the pulsar are based on pulsar timing observations.

In Table 8.2 we summarize the properties of the candidate pulsar. There is a point source in the 4.5 μm image that is consistent with the position of the pulsar. The source was detected with a signal to noise ratio of 58 and has a flux of 12.4 ± 0.2 μJy. There is a low significance source detected in the 8 μm image that is consistent with the pulsar position. The flux of this source has a signal to noise ratio of 3 and a very poorly constrained position.

In Figure 8.6 we show constraints on emission from the PSR B0031−07 system and the SEDs of plausible disks that satisfy these constraints. For the 4.5 μm we plot both the flux of the possible source and a derived upper limit. For the 8 μ we plot the flux of the candidate source.

8.4.4 Nulling Pulsar: B1133+16

PSR B1133+16 has a spin frequency of 0.8 Hz and nulls approximately 15% of the time. There has been recent suggestions that the nulling is quasi-periodic (Herfindal & Rankin 2007), with a period of a few hundred pulse periods, which, if driven by an orbiting body corresponds to an orbital radius within the pulsar magnetosphere. Orbiting debris may be able to withstand the outer magnetosphere of this object, but only for very short times (Cordes & Shannon 2008).

Herfindal & Rankin (2007) suggest that quasiperiodicity is associated with the *carousel* rotation of emission patches about the magnetic axis. The mechanism that causes this carousel motion is unclear. One possible mechanism is the so called $E \times B$ drift (Ruderman & Sutherland 1975); however the drift rate of this pulsar and most other pulsars is incongruous with the rate expected from this model.

The pulsar has been detected in soft X-rays with Chandra, with power law (magnetospheric) and polar cap (thermal, $T \approx 10^{6.2}$ K fitting the observed spectra equally well (Kargaltsev et al. 2006). There has additionally been a claimed detection of the pulsar in optical bands (Zharikov et al. 2008). Radio VLBI observations of this object indicate that it is 0.4 kpc distant and place strong constraints on its position and proper motion (Brisken et al. 2002).

In Figure 8.7 we show display the IRAC images of the field surrounding the pulsar. We also indicate the position of the pulsar. No point sources are found that are consistent with the position of the pulsar.

In Figure 8.8 we plot the observed constraints on the emission from the B1133+16 system and curves showing the brightness for plausible disks surrounding these systems. We place constraints on the nominal disk masses of 10^{-6} $M_{\oplus}$ to 10^{-3} $M_{\oplus}$ for asteroid belt like disks. If the nulling was associated with a body orbiting inside or near the pulsar magnetosphere, it would be too faint to be detected in infrared wavelengths.

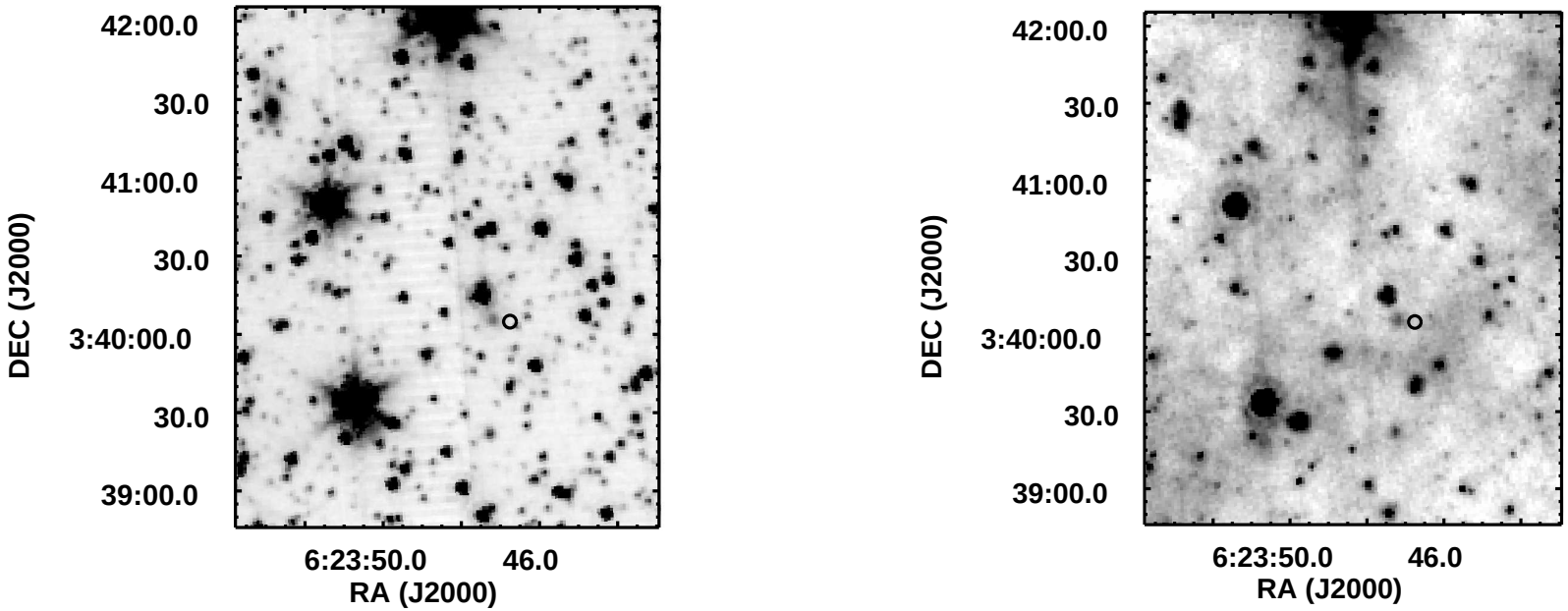

FIGURE 8.3.— The field surrounding PSR J0623+0341 in the IRAC 4.5 μm (left panel) and 8.0 μm (right panel) bands. The circle indicates the position of the pulsar but does not reflect the uncertainty in the radio pulsar position, which is too small to display.

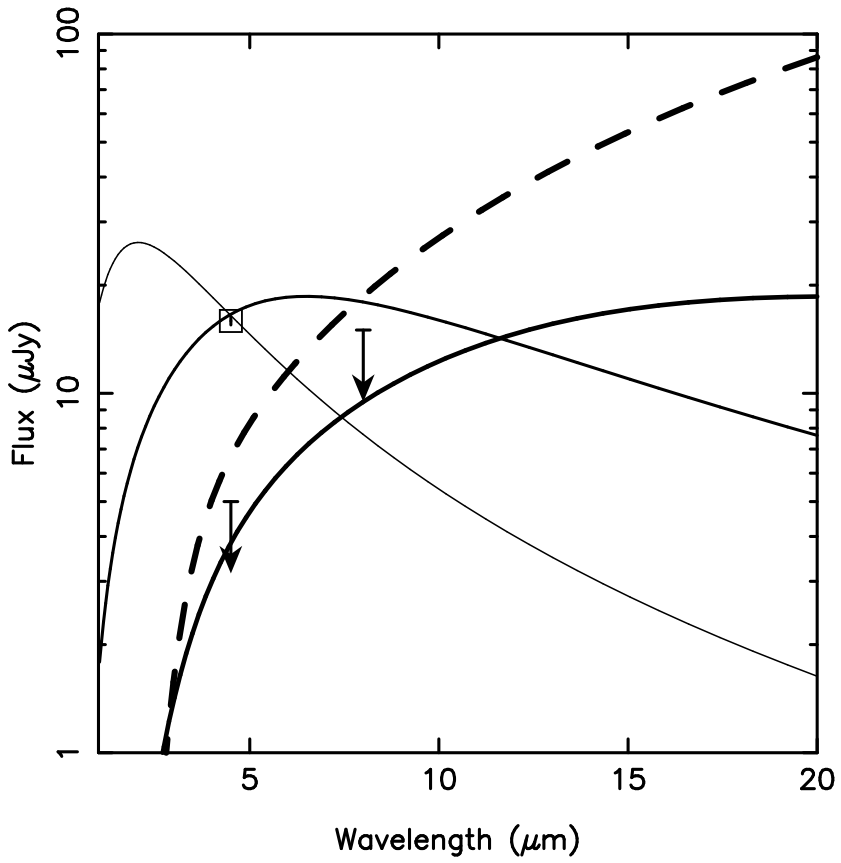

FIGURE 8.4.— Debris disk models for PSR J0623+0341. The solid lines represent the optically thin models. From thinnest to thickest line width, the models plotted are respectively $T_{\rm NS} = 10^6$ K, $M_D = 10^{-5}\ M_\oplus$; $T_{\rm NS} = 10^{5.5}$ K, $M_D = 10^{-3}\ M_\oplus$; and $T_{\rm NS} = 10^5$ K, $M_D = 10^{-2}\ M_\oplus$. The dashed line represents an optically thick disk assuming $T_{\rm NS} = 10^5$ K.

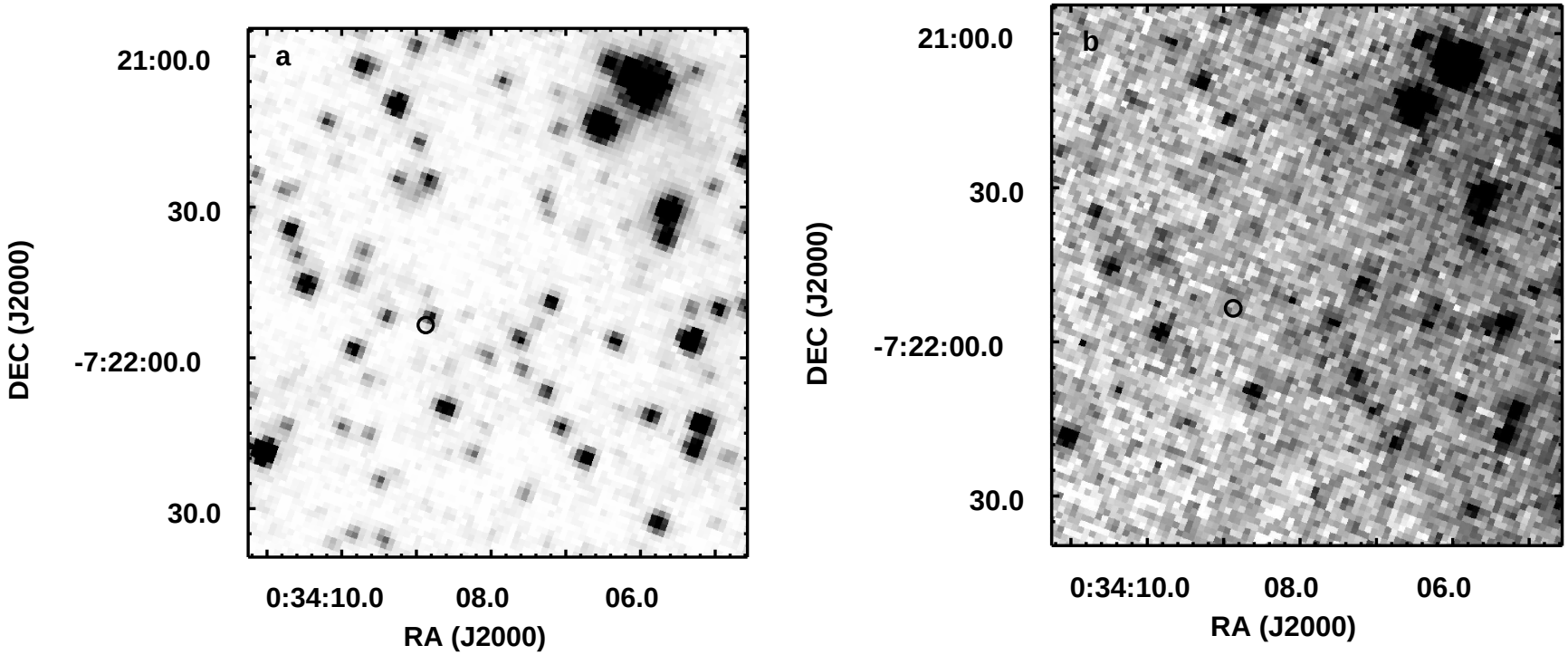

FIGURE 8.5.— The field surrounding PSR B0031−07 in the 4.5 μm (left panel) and 8 μm (right panel) *IRAC* bands. The center of the circle is the position of the radio pulsar. The uncertainty in the position is too small to display.

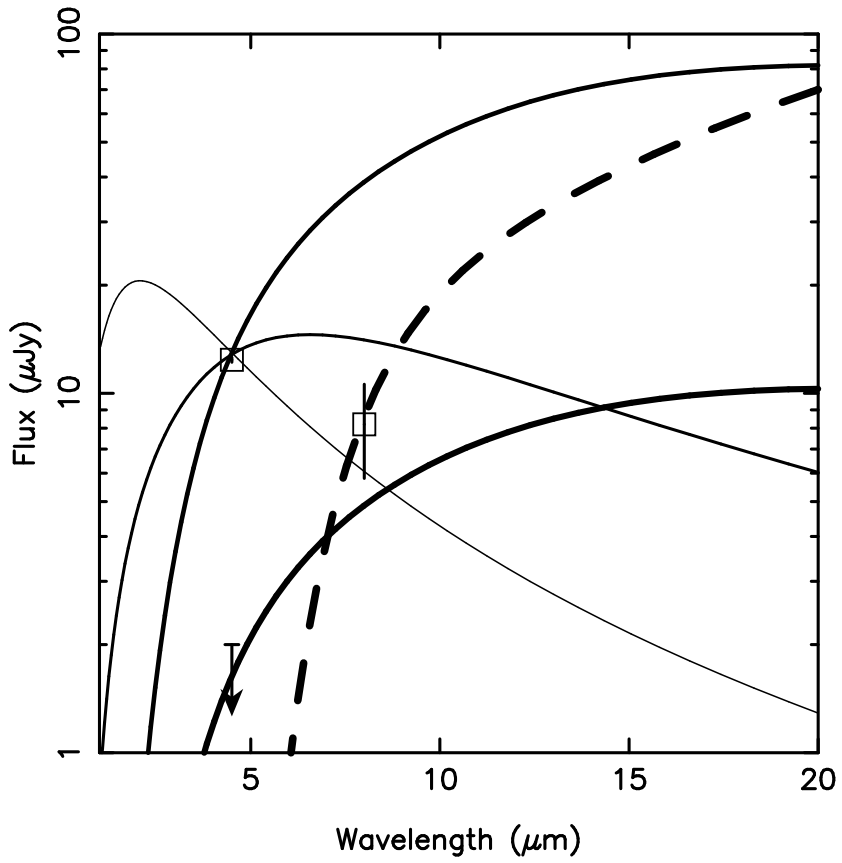

FIGURE 8.6.— Debris disk models for PSR B0031−07. The solid lines represent optically thin models. From thinnest to thickest line widths, the models are respectively $T_{\rm NS} = 10^6$ K, $M_D = 10^{-5.0}\ M_\oplus$; $T_{\rm NS} = 10^{5.5}$ K, $M_D = 10^{-4.9}\ M_\oplus$; $T_{\rm NS} = 10^5$ K, $M_D = 10^{-2.8}\ M_\oplus$; and $T_{\rm NS} = 10^5$, $M_D = 10^{-3.7}\ M_\oplus$. The dashed line represents an optically thick disk model with $T_{\rm NS} = 10^{5.8}$ K.

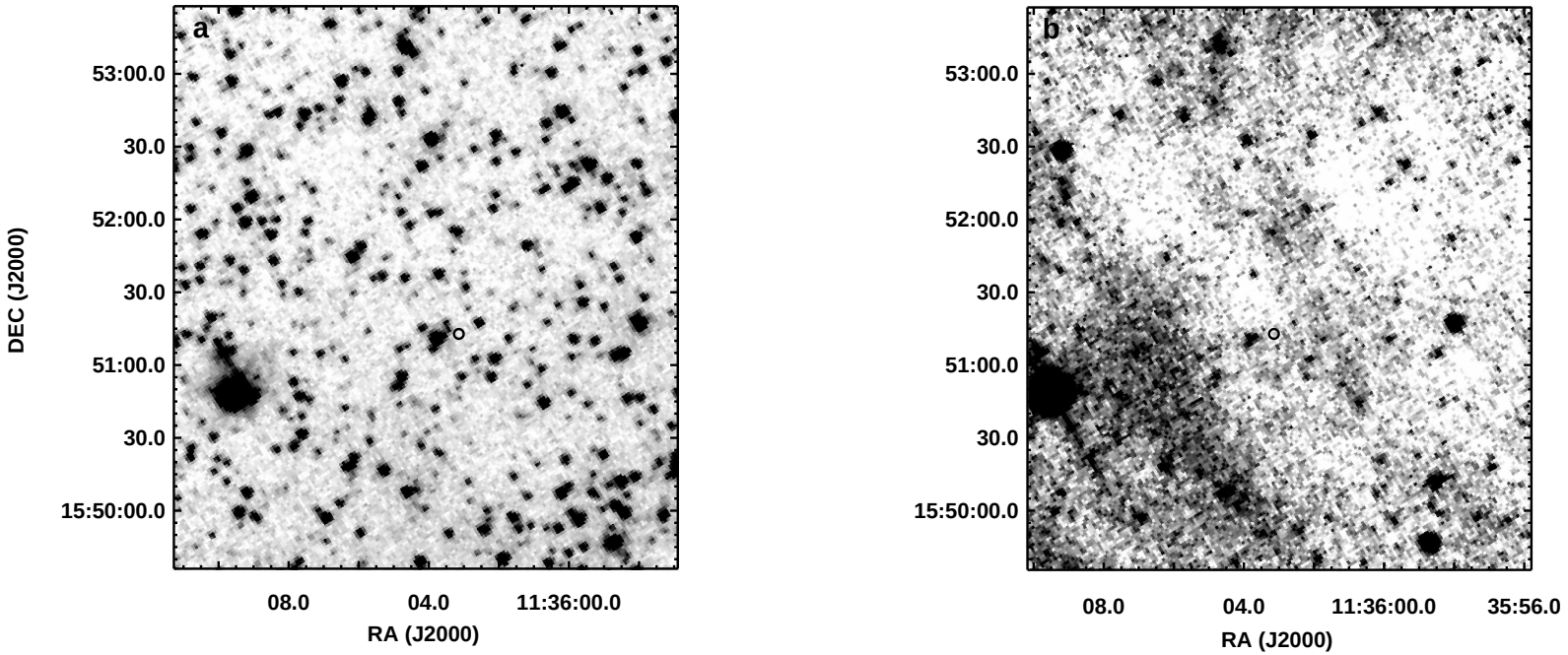

FIGURE 8.7.— Field surround PSR B1133+16 in 4.5 μm (left panel) and 8.0 μm (right panel) bands. The circle marks the position of the pulsar at the observation epoch. Because the position of the pulsar is known very accurately, the radio uncertainty of the pulsar is too small to be displayed on the plot.

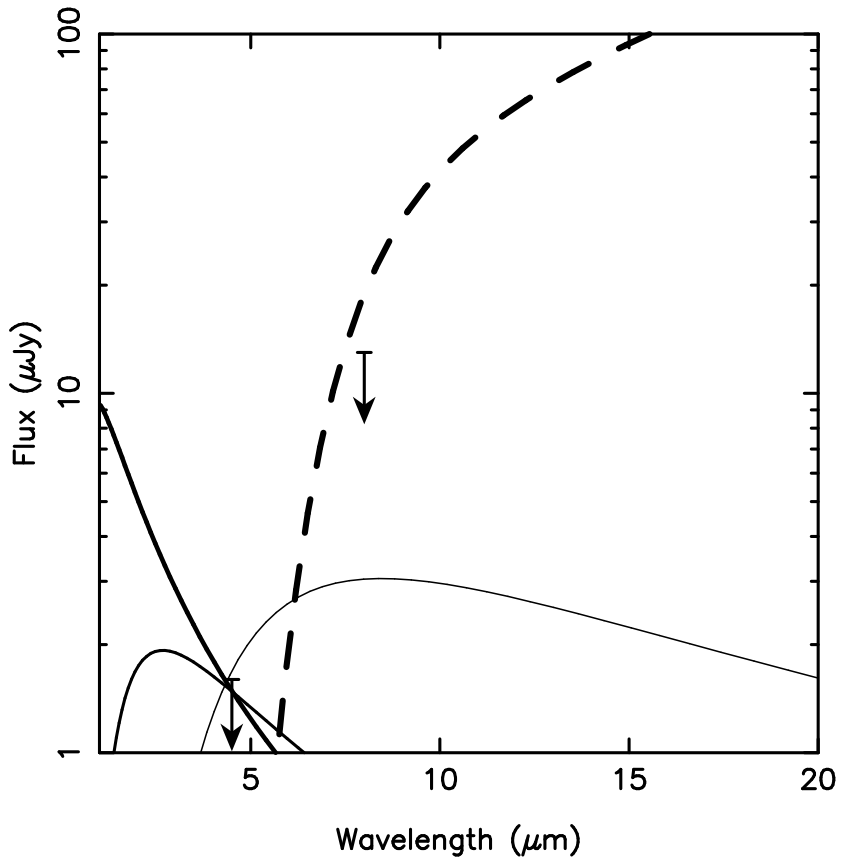

FIGURE 8.8.— Debris disk models for PSR B1133+16. The solid lines represent optically thin debris disk models. From thickest to thinnest line width, the the models are respectively, $T_{\rm NS} = 10^6$ K, $M_D = 10^{-5.6}\ M_\oplus$; $T_{\rm NS} = 10^{5.5}$ K, $M_D = 10^{-4.8}\ M_\oplus$; and $T_{\rm NS} = 10^5$ K, $M_D = 10^{-3.1}\ M - \oplus$. The dashed line indicates an optically thick disk model with $T_{\rm NS} = 10^{5.8}$ K.

8.5 Discussion and Conclusions

No definitive detections of debris disks were made with these observations. For a few sources, candidate infrared counterparts were found. However, high probabilities for source confusion and spectral indices inconsistent with the debris disk model make it likely that the candidates are stars along the line of sight.

Near future facilities will enable detection or place strong constraints of circumpulsar debris. Next generation space telescopes will have larger apertures comes better sensitivity and higher angular resolution. This angular resolution could mitigate source confusion present in the *Spitzer* observations.

Another possibility would be to search for reflected radio emission off of the pulsars. Radio waves would be efficiently scattered off of any macroscopic material with size greater than the observing wavelength (Phillips 1993; Cordes & Shannon 2008). Scattered flux would be extended over all of pulse phase for extended disks, and, unlike pulsar radio emission, would be unpolarized. Searching for off pulse radio emission is a possibility. It is difficult to accomplish with single dish telescopes because instrumental instabilities make it difficult to establish zero baseline. With next generation interferometers such as the EVLA it will be possible to detect form phase resolved images of the pulsar and search for non-polarized emission in an off-pulse window.

8.5.1 Acknowledgements

This work is based on observations made with the Spitzer Space Telescope, which is operated by the Jet Propulsion Laboratory, California Institute of Technology under a contract with NASA. Support for this work was provided by NASA through an award issued by JPL/Caltech. This work made use of NASA's ADS System and the ATNF Pulsar Catalogue (Manchester et al. 2005).

CHAPTER 9

CONCLUDING REMARKS AND PLANS FOR FUTURE WORK

This dissertation presents a wide range of studies that examine the relationships between pulsars and their environments. Here we discuss directions to further our understanding of pulsars and their environments.

9.1 Reconcile the Diversity of Timing Noise

In Chapter 3 we connect timing noise across the pulsar population using residual by analyzing how the rms residuals vary with pulsar properties (spin frequency and spin frequency derivative) and observing span. The motivation for this analysis that the rms of the timing noise (or figures related to it) are commonly published in the literature. This analysis could be improved through a more detailed analysis of times series. It is imperative to understand the time evolution of timing noise. Studies of individual time series would enable stronger constraints on the time variability of timing noise for individual pulsars. This would be particularly useful in understanding the level of stationarity of timing noise, enabling confirmation of recent anecdotal evidence that timing noise is to a large degree stationary (Lyne et al. 2010).

9.2 Constrain Circumpulsar Debris Disks

There is undoubtedly matter orbiting pulsars, and a fraction of it is likely aggregated into rocky macroscopic bodies. This material fundamentally limits timing precision because it cannot be realistically mitigated (Chapter 4). It can

plausibly affect pulsar radio emission (Cordes & Shannon 2008), though direct evidence is still lacking (Chapter 8).

The properties of debris disks can be constrained through detailed studies of pulsars known to harbor debris disks, such as the 4U0142+61 system. This magnetar shows a pronounced mid-infrared excess associated with either a dust disk (Wang et al. 2006) or perhaps magnetospheric emission (Beloborodov & Thompson 2007). If the infrared emission is caused by a dust disk, spectral signatures associated with its constituent material (such as iron oxides) would show up in narrow band photometry or low resolution spectroscopy. Magnetospheric origin would cause the emission to be highly polarized and lack narrow-band spectral features. In addition, polarization observations can potentially be used to measure the density of material in the pulsar magnetosphere (Shannon & Heyl 2006).

Secondly sensitive near-future telescopes can be leveraged to better probe these systems. As discussed in Chapter 8, infrared observations (with JWST) and radio observations (with the EVLA or the SKA) provide orders of magnitude improvement in constraining debris disk configurations.

Theoretically, a closer examination of the role of the pulsar wind in affecting circumpulsar debris is warranted. For example, it is important to understand the role the pulsar wind plays in driving migration of planet and asteroidal mass systems, analogous to the role of the wind from protostars in driving planet migration (Lovelace et al. 2008).

9.3 Develop and Implement Improved Strategies for Mitigating Interstellar Propagation Effects

Interstellar propagation affects pulsar timing at the 10 ns to 100 ns level for many current pulsars included in a pulsar timing array, observed at standard timing radio frequencies.

In Chapter 5, the simulations presented modeled only large scale (refractive) phase variations in the interstellar medium over a limited range of scattering screen configurations. It is important to incorporate more realistic models of interstellar propagation effects. For example it is imperative to incorporate smaller scale (diffractive) variations. In addition, it is essential to simulate a more diverse range of lines of sight, by incorporating media that have show highly anisotropic scattering (indicative of highly anisotropic scattering structure) or large scale inhomogeneities.

The work presented in Chapter 5 uses only time of arrival information to mitigate interstellar propagation effects. Future work should investigate the use of ancillary information derived from dynamic spectra.

The diversity of lines of sight can be studied through observations of bright canonical pulsars with comparable scattering to many pulsar earth lines of sight. Though these observations cannot be used to directly study TOA variations due to interstellar propagation effects[1], canonical pulsars are much brighter, making high dynamic range observations of pulsar dynamic spectra feasible. Features

[1]Wide pulses, pulse jitter, and large levels of timing noise limit timing precision achievable with canonical pulsars (typically 100 ms per TOA) to levels much larger that the perturbations expected from interstellar propagation (typically 100 ns)

in these dynamic spectra are easier to analyze. An example of this type of observation can be seen in observation of Figure 9.1, which shows observations of the canonical pulsar B1737+13. The secondary spectrum is anisotropic between positive and negative fringe frequency, suggesting that the structure is refracted far from the direct line of sight.

There has been recent excitement about phase retrieval algorithms in mitigating propagation effects (e.g., the cyclic spectroscopy method, P. Demorest & M. Walker, submitted). The utility of these methods in a realistic observing environment need to be examined. For example, the limitations of this methodology by finite signal to noise ratio of observations, pulse jitter, and pulse profile evolution with frequency need to be explored.

9.4 Understand Single Pulse Structure in Millisecond Pulsars

In Chapter 6 we showed that instrinsic pulse instability was limiting timing precision. What is causing this instability? Can it be corrected? For emission altitude variation (associated perhaps with a change in the magnetospheric plasma density) would cause both changes in pulse shape and changes in arrival time.

Regardless of the nature of physical nature of the shape variations, if a strong correlation can be identified between pulse shape and arrival time, a corrector can be developed.

While this corrector could be implemented in profiles averaged N pulses, single pulses are better because the effects are not averaged out by $1/\sqrt{N}$, so the nature of the variability can be better understood. The viability of single

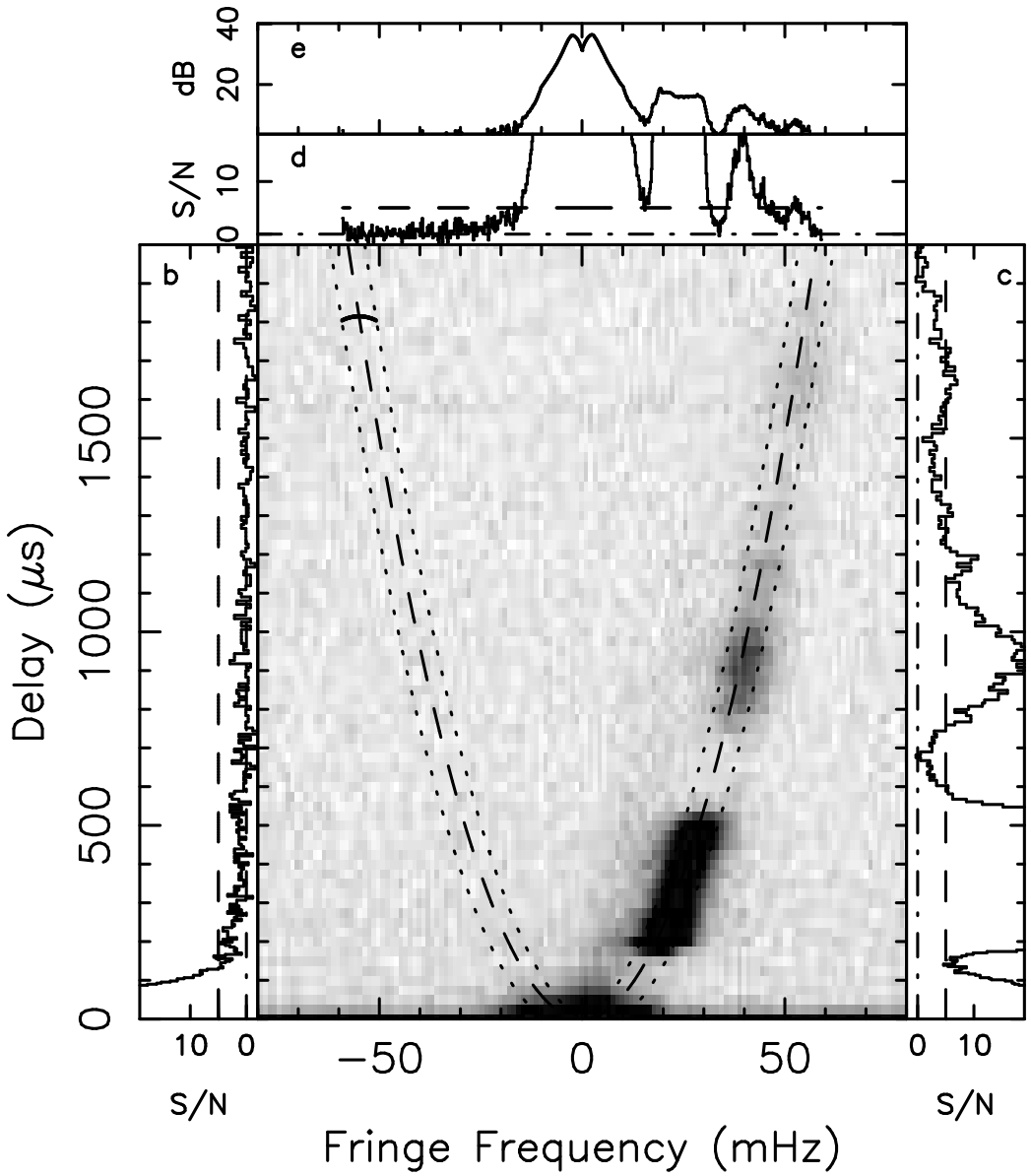

FIGURE 9.1.— *Center Panel:* Secondary spectrum for the canonical pulsar B1737+13, observed at 302 MHz to 352 MHz with the Arecibo telescope. The structure in the spectrum indicates that the pulsar is highly scattered, indicating that the pulsar. *Side and top panels:* the intensity profile along the main arc. Panels b and c show the power in linear scale for each side of the parabola.

pulse observations of many millisecond pulsars is questionable because of their low luminosity. For a few relatively bright MSPs, it may be necessary to select observing frequencies at which the pulsar shows strong scintillation, and

leverage these intensity variations to find a day (or sub-band) at which the intensity is sufficiently high to detect single pulses, likely with modest signal to noise ratio. For example, companion WAPP data to some of the observations of PSR J1713+0747 presented in Chapter 6 (particularly L-band observations) may be suited for this type of study.

9.5 Realistically Assess the Sensitivity of a Pulsar Timing Array

The results presented in Chapter 2 show the most optimistic sensitivity for a PTA. These results form a very preliminary assessment of the requirements for PTA observations. They suggest that if timing noise is present more pulsars observed and higher throughput can both improve the sensitivity of the timing array.

It is therefore important to examine the sensitivity of real detection statistics. Sensitivity needs to be assessed in the context of more a more realistic dectection statistic that incorporates the angular correlation. As part of this effort we are developing web-based tools that can be used to assess the sensitivity a pulsar timing array[2].

A direct detection of GWs with a PTA will bring a lot of excitement. However because of the gravity of the situation it also will bring skepticism. This skepticism can be ameliorated if sound detection methodology is implemented. Presently detection methodology is focused on low significance detection of the

[2] `http://arcc.phys.utb.edu/nano_sandbox/index.php`

GWB. At higher significance levels, diagnostics can be implemented that enable checks to ensure that whatever was *detection* was of gravitational waves passing through the solar neighborhood and not some other spurious signal.

9.6 Map the Emission Regions of More Pulsars

The techniques for resolving pulsar magnetospheres described in Chapter 7 can be used on other pulsars. Candidate pulsars for these techniques are with large magnetospheres, relatively nearby (luminous with magnetospheres with large angular extent), with relatively high degrees of scattering. We have observations archived at the Cornell Center for Advanced Computing of such pulsars from the Arecibo 305-m and Green Bank 100-m telescopes that are amenable to such analysis, such as the observations of the canonical pulsar B1737+13 presented in Figure 9.1.

BIBLIOGRAPHY

Ahuja, A. L., Mitra, D., & Gupta, Y. 2007, MNRAS, 377, 677

Allen, B., & Romano, J. D. 1999, PRD, 59, 102001

Anholm, M., Ballmer, S., Creighton, J. D. E., Price, L. R., & Siemens, X. 2009, PRD, 79, 084030

Archibald, A. M., et al. 2009, Science, 324, 1411

Armstrong, J. W. 1984, Nature, 307, 527

Arons, J., & Scharlemann, E. T. 1979, ApJ, 231, 854

Arzoumanian, Z., Nice, D. J., Taylor, J. H., & Thorsett, S. E. 1994, ApJ, 422, 671

Backer, D. C. 1970, Nature, 228, 42

Backer, D. C., & Hellings, R. W. 1986, ARAA, 24, 537

Barnard, J. J., & Arons, J. 1986, ApJ, 302, 138

Bell, J. F., Bailes, M., Manchester, R. N., Lyne, A. G., Camilo, F., & Sandhu, J. S. 1997, MNRAS, 286, 463

Beloborodov, A. M., & Thompson, C. 2007, ApJ, 657, 967

Bhat, N. D. R., & Gupta, Y. 2002, ApJ, 567, 342

Biggs, J. D. 1992, ApJ, 394, 574

Bogdanov, S., Pruszyńska, M., Lewandowski, W., & Wolszczan, A. 2002, ApJ, 581, 495

Boynton, P. E., Groth, E. J., Hutchinson, D. P., Nanos, Jr., G. P., Partridge, R. B., & Wilkinson, D. T. 1972, ApJ, 175, 217

Brisken, W. F., Benson, J. M., Goss, W. M., & Thorsett, S. E. 2002, ApJ, 571, 906

Brisken, W. F., Macquart, J., Gao, J. J., Rickett, B. J., Coles, W. A., Deller, A. T., Tingay, S. J., & West, C. J. 2010, ApJ, 708, 232

Bryden, G., Beichman, C. A., Rieke, G. H., Stansberry, J. A., Stapelfeldt, K. R., Trilling, D. E., Turner, N. J., & Wolszczan, A. 2006, ApJ, 646, 1038

Camilo, F., et al. 2007, ApJ, 663, 497

Champion, D. J., et al. 2005, MNRAS, 363, 929

—. 2010, ApJL, 720, L201

Chatterjee, S., et al. 2009, ApJ, 698, 250

Cheng, K. S. 1987, ApJ, 321, 805

Cheng, K. S., Ho, C., & Ruderman, M. 1986, ApJ, 300, 500

Chukwude, A. E. 2007, Chinese Journal of Astronomy and Astrophysics, 7, 521

Cognard, I., Bourgois, G., Lestrade, J., Biraud, F., Aubry, D., Darchy, B., & Drouhin, J. 1993, Nature, 366, 320

—. 1995, A&A, 296, 169

Cognard, I., Lestrade, J., Backer, D. C., Ray, P. S., Foster, R. S., & Cadwell, B. J. 2000, in Astronomical Society of the Pacific Conference Series, Vol. 202, IAU Colloq. 177: Pulsar Astronomy - 2000 and Beyond, ed. M. Kramer, N. Wex, & R. Wielebinski, 55

Coles, W. A., McLaughlin, M. A., Rickett, B. J., Lyne, A. G., & Bhat, N. D. R. 2005, ApJ, 623, 392

Coles, W. A., Rickett, B. J., Gao, J. J., Hobbs, G., & Verbiest, J. P. W. 2010, ApJ, 717, 1206

Cordes, J. M. 1978, ApJ, 222, 1006

—. 1980, ApJ, 237, 216

—. 1986, ApJ, 311, 183

—. 2000a, astro-ph/0007231

—. 2000b, astro-ph/0007233

Cordes, J. M., Boriakoff, V., & Weisberg, J. M. 1983, ApJ, 268, 370

Cordes, J. M., & Downs, G. S. 1985, ApJS, 59, 343

Cordes, J. M., & Helfand, D. J. 1980, ApJ, 239, 640

Cordes, J. M., & Lazio, T. J. W. 2001, ApJ, 549, 997

—. 2002, astro-ph/0207156

Cordes, J. M., Pidwerbetsky, A., & Lovelace, R. V. E. 1986, ApJ, 310, 737

Cordes, J. M., Rickett, B. J., Stinebring, D. R., & Coles, W. A. 2006a, ApJ, 637, 346

Cordes, J. M., & Shannon, R. M. 2008, ApJ, 682, 1152

—. 2010, ApJS, submitted

Cordes, J. M., Wolszczan, A., Dewey, R. J., Blaskiewicz, M., & Stinebring, D. R. 1990, ApJ, 349, 245

Cordes, J. M., et al. 2006b, ApJ, 637, 446

D'Alessandro, F., McCulloch, P. M., Hamilton, P. A., & Deshpande, A. A. 1995, MNRAS, 277, 1033

D'Alessandro, F., McCulloch, P. M., King, E. A., Hamilton, P. A., & McConnell, D. 1993, MNRAS, 261, 883

Damour, T., & Vilenkin, A. 2005, PRD, 71, 063510

Demorest, P. B. 2007, PhD thesis, University of California, Berkeley

Demorest, P. B. 2008, in http://www.nanograv.org/presentations/IPTA/PTA_Workshop_Demorest.pdf

den Hartog, P. R., Kuiper, L., Hermsen, W., Kaspi, V. M., Dib, R., Knödlseder, J., & Gavriil, F. P. 2008, A&A, 489, 245

Detweiler, S. 1979, ApJ, 234, 1100

Dewey, R. J., & Cordes, J. M. 1989, in Timing Neutron Stars, ed. H. Ögelman & E. P. J. van den Heuvel, 119

Dib, R., Kaspi, V. M., & Gavriil, F. P. 2008, ApJ, 673, 1044

Dohnanyi, J. W. 1969, JGR, 74, 2531

Durdin, J. M., Large, M. I., Little, A. G., Manchester, R. N., Lyne, A. G., & Taylor, J. H. 1979, MNRAS, 186, 39P

Edwards, R. T., Hobbs, G. B., & Manchester, R. N. 2006, MNRAS, 372, 1549

Ekşİ, K. Y., & Alpar, M. A. 2005, ApJ, 620, 390

Esamdin, A., Lyne, A. G., Graham-Smith, F., Kramer, M., Manchester, R. N., & Wu, X. 2005, MNRAS, 356, 59

Ferdman, R. 2008, PhD thesis, University of British Columbia

Ferdman, R. D., et al. 2010, Classical and Quantum Gravity, 27, 084014

Finn, L. S., & Lommen, A. N. 2010, ApJ, 718, 1400

Foster, R. S., & Backer, D. C. 1990, ApJ, 361, 300

Foster, R. S., & Cordes, J. M. 1990, ApJ, 364, 123

Foster, R. S., Lyne, A. G., Shemar, S. L., & Backer, D. C. 1994, AJ, 108, 175

Fruchter, A. S., Stinebring, D. R., & Taylor, J. H. 1988, Nature, 333, 237

Gavriil, F. P., & Kaspi, V. M. 2002, ApJ, 567, 1067

Gil, J., Haberl, F., Melikidze, G., Geppert, U., Zhang, B., & Melikidze, Jr., G. 2008, ApJ, 686, 497

Gladman, B., & Duncan, M. 1990, AJ, 100, 1680

Goldreich, P., & Julian, W. H. 1969, ApJ, 157, 869

Goldreich, P., Lithwick, Y., & Sari, R. 2004a, ApJ, 614, 497

—. 2004b, ARAA, 42, 549

Gotthelf, E. V., Gavriil, F. P., Kaspi, V. M., Vasisht, G., & Chakrabarty, D. 2002, ApJL, 564, L31

Gupta, Y., Bhat, N. D. R., & Rao, A. P. 1999, ApJ, 520, 173

Gupta, Y., & Gangadhara, R. T. 2003, ApJ, 584, 418

Gwinn, C. R., et al. 1997, ApJL, 483, L53

—. 2000, ApJ, 531, 902

Hankins, T. H., Kern, J. S., Weatherall, J. C., & Eilek, J. A. 2003, Nature, 422, 141

Harding, A. K., Shinbrot, T., & Cordes, J. M. 1990, ApJ, 353, 588

Helfand, D. J., Taylor, J. H., Backus, P. R., & Cordes, J. M. 1980, ApJ, 237, 206

Hellings, R. W., & Downs, G. S. 1983, ApJL, 265, L39

Hemberger, D., & Stinebring, D. R. 2008, ApJL, 674, L37

Herfindal, J. L., & Rankin, J. M. 2007, MNRAS, 380, 430

Hill, A. S., Stinebring, D. R., Asplund, C. T., Berwick, D. E., Everett, W. B., & Hinkel, N. R. 2005, ApJL, 619, L171

Hill, A. S., Stinebring, D. R., Barnor, H. A., Berwick, D. E., & Webber, A. B. 2003, ApJ, 599, 457

Hobbs, G., Lyne, A. G., & Kramer, M. 2010, MNRAS, 402, 1027

Hobbs, G., Lyne, A. G., Kramer, M., Martin, C. E., & Jordan, C. 2004, MNRAS, 353, 1311

Hobbs, G., et al. 2009a, MNRAS, 394, 1945

Hobbs, G. B., Edwards, R. T., & Manchester, R. N. 2006, MNRAS, 369, 655

Hobbs, G. B., et al. 2009b, Publications of the Astronomical Society of Australia, 26, 103

Hotan, A. W., Bailes, M., & Ord, S. M. 2006, MNRAS, 369, 1502

Hu, W., Stinebring, D. R., & Romani, R. W. 1991, ApJL, 366, L33

Huguenin, G. R., Taylor, J. H., & Troland, T. H. 1970, ApJ, 162, 727

Hulleman, F., van Kerkwijk, M. H., & Kulkarni, S. R. 2004, A&A, 416, 1037

Hulse, R. A., & Taylor, J. H. 1975, ApJL, 195, L51

Hurley, K., et al. 2005, Nature, 434, 1098

Jacoby, B. A., Bailes, M., van Kerkwijk, M. H., Ord, S., Hotan, A., Kulkarni, S. R., & Anderson, S. B. 2003, ApJL, 599, L99

Jaffe, A. H., & Backer, D. C. 2003, ApJ, 583, 616

Janssen, G. 2008

Jenet, F. A., Anderson, S. B., & Prince, T. A. 2001, ApJ, 546, 394

Jenet, F. A., & Gil, J. 2004, ApJL, 602, L89

Jenet, F. A., Hobbs, G. B., Lee, K. J., & Manchester, R. N. 2005, ApJL, 625, L123

Jenet, F. A., Lommen, A., Larson, S. L., & Wen, L. 2004, ApJ, 606, 799

Jenet, F. A., et al. 2006, ApJ, 653, 1571

—. 2009, astro-ph/0909.1058

Johnston, S., Kramer, M., Karastergiou, A., Hobbs, G., Ord, S., & Wallman, J. 2007, MNRAS, 381, 1625

Johnston, S., Nicastro, L., & Koribalski, B. 1998, MNRAS, 297, 108

Jones, P. B. 1990, MNRAS, 246, 364

Kaplan, D. L., & van Kerkwijk, M. H. 2005, ApJL, 628, L45

Kargaltsev, O., Pavlov, G. G., & Garmire, G. P. 2006, ApJ, 636, 406

Kaspi, V. M., Gavriil, F. P., Chakrabarty, D., Lackey, J. R., & Muno, M. P. 2001, ApJ, 558, 253

Kaspi, V. M., Taylor, J. H., & Ryba, M. F. 1994, ApJ, 428, 713

Konacki, M., & Wolszczan, A. 2003, ApJL, 591, L147

Kramer, M., Lyne, A. G., O'Brien, J. T., Jordan, C. A., & Lorimer, D. R. 2006a, Science, 312, 549

Kramer, M., et al. 2006b, Science, 314, 97

Kuzmin, A. D., & Ershov, A. A. 2004, A&A, 427, 575

Lambert, H. C., & Rickett, B. J. 1999, ApJ, 517, 299

Lange, C., Camilo, F., Wex, N., Kramer, M., Backer, D. C., Lyne, A. G., & Doroshenko, O. 2001, MNRAS, 326, 274

Lattimer, J. M., & Prakash, M. 2007, Phys.Rep., 442, 109

Lazaridis, K., et al. 2009, MNRAS, 400, 805

Lazio, T. J. W., & Fischer, J. 2004, AJ, 128, 842

Lee, L. C., & Jokipii, J. R. 1975, ApJ, 202, 439

Lestrade, J., Rickett, B. J., & Cognard, I. 1998, A&A, 334, 1068

Lissauer, J. J. 1987, Icarus, 69, 249

—. 1993, ARAA, 31, 129

Lissauer, J. J., & Stewart, G. R. 1993, in Astronomical Society of the Pacific Conference Series, Vol. 36, Planets Around Pulsars, ed. J. A. Phillips, S. E. Thorsett, & S. R. Kulkarni, 217–233

Lommen, A. N. 2002, PhD thesis, University of California, Berkeley

Lovelace, R. V. E., Romanova, M. M., & Barnard, A. W. 2008, MNRAS, 389, 1233

Lu, Y., & Cheng, K. S. 2002, Chinese Journal of Astronomy and Astrophysics, 2, 161

Lyne, A., Hobbs, G., Kramer, M., Stairs, I., & Stappers, B. 2010, Science, 329, 408

Lyne, A. G., Anderson, B., & Salter, M. J. 1982, MNRAS, 201, 503

Lyubarskii, Y. E., & Petrova, S. A. 1998, A&A, 333, 181

Manchester, R., Hobbs, G., Teoh, A., & Hobbs, M. 2004, astro-ph/0412641

Manchester, R. N. 2008, in http://www.nanograv.org/presentations/IPTA/PTA_Workshop_Manchester.ppt

Manchester, R. N. 2009, in Proc. IAU General Assembly

Manchester, R. N., Hobbs, G. B., Teoh, A., & Hobbs, M. 2005, AJ, 129, 1993

Matsakis, D. N., Taylor, J. H., & Eubanks, T. M. 1997, A&A, 326, 924

McLaughlin, M. A., et al. 2006, Nature, 439, 817

—. 2009, MNRAS, 400, 1431

Menou, K., Perna, R., & Hernquist, L. 2001, ApJ, 559, 1032

Miller, M. C., & Hamilton, D. P. 2001, ApJ, 550, 863

Nesvorný, D., & Bottke, W. F. 2004, Icarus, 170, 324

Nicastro, L., Nigro, F., D'Amico, N., Lumiella, V., & Johnston, S. 2001, A&A, 368, 1055

Ord, S. M., Jacoby, B. A., Hotan, A. W., & Bailes, M. 2006, MNRAS, 371, 337

Perna, R., & Hernquist, L. 2000, ApJL, 544, L57

Petrova, S. A. 2001, MNRAS, 324, 931

Phillips, J. A. 1993, in ASP Conf. Ser. 36: Planets Around Pulsars, ed. J. A. Phillips, S. E. Thorsett, & S. R. Kulkarni, 321–325

Putney, M. L., & Stinebring, D. R. 2006, Chinese Journal of Astronomy and Astrophysics Supplement, 6, 233

Ramachandran, R., Demorest, P., Backer, D. C., Cognard, I., & Lommen, A. 2006, ApJ, 645, 303

Rankin, J. M. 1993, ApJS, 85, 145

—. 2007, ApJ, 664, 443

Rankin, J. M., & Wright, G. A. E. 2007, MNRAS, 379, 507

Ransom, S. M., Demorest, P., Ford, J., McCullough, R., Ray, J., DuPlain, R., & Brandt, P. 2009, in American Astronomical Society Meeting Abstracts, Vol. 214, American Astronomical Society Meeting Abstracts, 605.08

Rea, N., et al. 2008, MNRAS, 391, 663

—. 2010, astro-ph/1003.2085

Rickett, B. 2006, Chinese Journal of Astronomy and Astrophysics Supplement, 6, 020000

Rickett, B. J. 1969, Nature, 221, 158

—. 1990, ARAA, 28, 561

Romani, R. W., Narayan, R., & Blandford, R. 1986, MNRAS, 220, 19

Ruden, S. P. 1993, in Astronomical Society of the Pacific Conference Series, Vol. 36, Planets Around Pulsars, ed. J. A. Phillips, S. E. Thorsett, & S. R. Kulkarni, 197–215

Ruderman, M. A., & Sutherland, P. G. 1975, ApJ, 196, 51

Scheuer, P. A. G. 1968, Nature, 218, 920

Segelstein, D. J., Rawley, L. A., Stinebring, D. R., Fruchter, A. S., & Taylor, J. H. 1986, Nature, 322, 714

Sesana, A., & Vecchio, A. 2010, PRD, 81, 104008

Shaffer, D. B., Kellermann, K. I., & Cornwell, T. J. 1999, ApJ, 515, 558

Shakura, N. I., & Sunyaev, R. A. 1973, A&A, 24, 337

Shannon, R. M., & Cordes, J. M. 2010, ApJ, accepted

Shannon, R. M., & Heyl, J. S. 2006, MNRAS, 368, 1377

Smirnov, T. V., & Shishov, V. I. 1989, Soviet Astronomy Letters, 15, 191

Smirnova, T. V. 1992, Soviet Astronomy Letters, 18, 392

Smirnova, T. V., Shishov, V. I., & Malofeev, V. M. 1996, ApJ, 462, 289

Smits, R., Kramer, M., Stappers, B., Lorimer, D. R., Cordes, J., & Faulkner, A. 2009, A&A, 493, 1161

Splaver, E. M. 2004, PhD thesis, Princeton University

Stinebring, D. R., McLaughlin, M. A., Cordes, J. M., Becker, K. M., Goodman, J. E. E., Kramer, M. A., Sheckard, J. L., & Smith, C. T. 2001, ApJL, 549, L97

Sturrock, P. A. 1971, ApJ, 164, 529

Taylor, J. H. 1992, Royal Society of London Philosophical Transactions Series A, 341, 117

Taylor, J. H., & Weisberg, J. M. 1982, ApJ, 253, 908

Thereau, G. 2008, in http://nanograv.org/presentations/IPTA/PTA_Workshop_Theureau.pdf

Urama, J. O., Link, B., & Weisberg, J. M. 2006, MNRAS, 370, L76

van Haasteren, R., Levin, Y., McDonald, P., & Lu, T. 2009, MNRAS, 395, 1005

van Leeuwen, J., & Stappers, B. W. 2010, A&A, 509, A7

van Straten, W. 2006, ApJ, 642, 1004

Verbiest, J. P. W. 2009, PhD Thesis, Swinburne University, arXiv:0906.4246

Verbiest, J. P. W., et al. 2008, ApJ, 679, 675

—. 2009, MNRAS, 400, 951

—. 2010, Classical and Quantum Gravity, 27, 084015

Vrtilek, S. D., Raymond, J. C., Garcia, M. R., Verbunt, F., Hasinger, G., & Kurster, M. 1990, A&A, 235, 162

Walker, M. A., Melrose, D. B., Stinebring, D. R., & Zhang, C. M. 2004, MNRAS, 354, 43

Walker, M. A., & Stinebring, D. R. 2005, MNRAS, 362, 1279

Wang, Z., Archibald, A. M., Thorstensen, J. R., Kaspi, V. M., Lorimer, D. R., Stairs, I., & Ransom, S. M. 2009, ApJ, 703, 2017

Wang, Z., Chakrabarty, D., & Kaplan, D. L. 2006, Nature, 440, 772

Wolszczan, A., & Cordes, J. M. 1987, ApJL, 320, L35

Wolszczan, A., & Frail, D. A. 1992, Nature, 355, 145

Woods, P. M., et al. 2000, ApJL, 535, L55

Yardley, D. R. B., et al. 2010, MNRAS, 407, 669

You, X. P., et al. 2007, MNRAS, 378, 493

Zharikov, S. V., Shibanov, Y. A., Mennickent, R. E., & Komarova, V. N. 2008, A&A, 479, 793

Zou, W. Z., Wang, N., Wang, H. X., Manchester, R. N., Wu, X. J., & Zhang, J. 2004, MNRAS, 354, 811